The extracellular matrix and angiogenesis

Two aspects that define cardiovascular health and disease

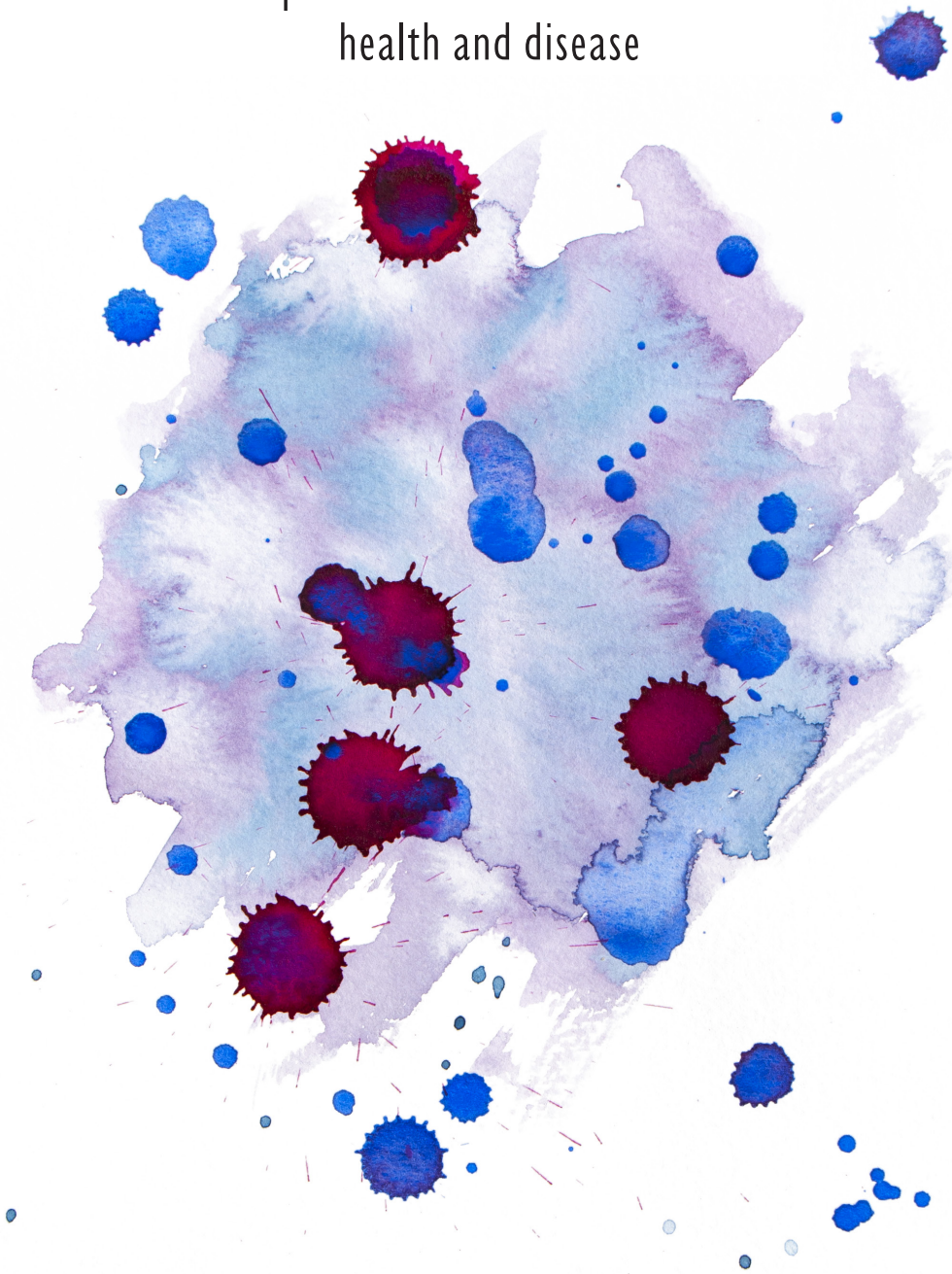

Laura Louzao Martinez

The extracellular matrix and angiogenesis

Two aspects that define cardiovascular health and disease

Laura Louzao Martinez

The extracellular matrix and angiogenesis
Two aspects that define cardiovascular health and disease

Cover design: Joint effort by Femke van Rhijn-Brouwer and Laura Louzao Martinez
Lay-out: Laura Louzao Martinez
Printed by: Ipskamp Printing

ISBN: 978-94-028-1871-0

Financial support by the Dutch Heart Foundation and the Dutch Kidney Foundation for the publication of this thesis is gratefully acknowledged.

The extracellular matrix and angiogenesis

Two aspects that define cardiovascular health and disease

De extracellulaire matrix en angiogenese

Twee aspecten die cardiovasculaire gezondheid en ziekte definiëren

(met een samenvatting in het Nederlands)

Proefschrift

ter verkrijging van de graad van doctor aan de Universiteit Utrecht
op gezag van de rector magnificus, prof.dr. H.R.B.M. Kummeling,
ingevolge het besluit van het college voor promoties
in het openbaar te verdedigen op
dinsdag 28 januari 2020 des middags te 4.15 uur

door

Laura Louzao Martinez

geboren op 13 november 1989
te Arnhem

Promotor:
Prof. dr. M.C. Verhaar

Copromotor:
Dr. K.L. Cheng

Table of contents

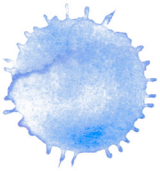

Chapter 1

Introduction and thesis outline

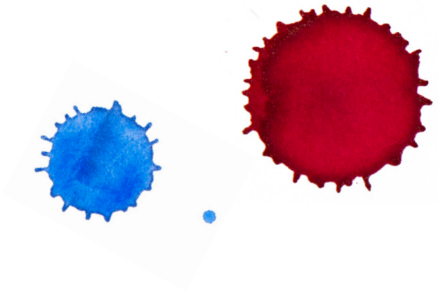

CELL JUNCTIONS AND CARDIOVASCULAR HEALTH

In multicellular organisms, a crucial role of the plasma membrane is to combine groups of cells with related specializations into tissues. Specific areas of the plasma membrane, called cell junctions, contain multiprotein complexes that facilitate structural support and cell-cell connections. These specific structures are formed between cells or anchor cells to components of the extracellular matrix (ECM), a complex meshwork of fibrous proteins and polysaccharides in which cells are embedded. These interactions not only allow the formation and maintenance of distinct tissues, but also the transfer of bidirectional information between the interior and the exterior of cells. Such information transfer is essential for many biological processes, including cell survival, proliferation, differentiation and migration[1-3]. Therefore, it is not surprising that defective cell junctions contribute to a wide variety of diseases[4-7].

Three main classes of cell junctions are prominent features of tissues in vertebrates. Gap junctions are specialized connections that form a narrow pore in the plasma membrane, permitting the rapid diffusion of small molecules and ions between adjacent cells. By this means, gap junctions provide metabolic and electrical coupling of cells. For example, the rapid movement of ions through gap junctions is important for cardiac tissue to beat in rhythm[8]. While gap junctions are involved in cellular communication, tight junctions and anchoring junctions are key for providing structural cohesion. Tight junctions are connected areas between plasma membranes of neighboring cells, forming a strong seal in between. In this way, they regulate the paracellular permeability and subsequently preserve the transcellular transport. Tight junctions are particularly important for maintaining the blood-brain barrier and the intestinal epithelial barrier[9,10]. Anchoring junctions are strong plasma membrane connections that mechanically attach the cytoskeleton of a cell to either neighboring cells or to the ECM, thereby providing stability and rigidity to tissues. Collectively, anchoring junctions and tight junctions support tissue integrity by holding cells together, provide resistance to mechanical forces and restrict the flow of molecules between cells.

Tight junctions and anchoring junctions are organized into three main structures: (1) Transmembrane adhesion proteins that connect the lateral surface of a cell to neighboring cells and the basal surface of a cell to the ECM. Examples include claudins, cadherins and integrins. (2) Intracellular adaptor proteins that

connect these adhesion proteins to cytoskeletal filaments and signaling molecules. Examples include catenins, vinculin, paxillin, and α-actinin among many others. (3) The cytoskeleton itself that aids in maintaining the cell shape and acts as a mechanosensor. In addition to adhesion and adaptor proteins, many anchoring junctions include intracellular signaling proteins that enable a downstream signaling cascade to reach the cell interior. While tight junctions are located just beneath the apical surface and are particularly important for the integrity of epithelia, anchoring junctions are widely distributed along the plasma membrane and are present in many epithelial and non-epithelial cells.

Anchoring junctions can be classified into two main forms, each involved in a distinct type of adhesion: (1) cell-matrix adhesion and (2) cell-cell adhesion (Figure 1). The interaction of cells with proteins in the extracellular environment or directly with neighboring cells is essential for cardiovascular development and health.

Cell-matrix adhesion

Cell-matrix adhesion is a key force-sensing interaction of a cell with the surrounding ECM that controls the cell's shape, behavior and fate[11]. Two main types of cell-matrix adhesion anchoring junctions have been identified, characterized by specific cytoskeletal anchors: (1) hemidesmosomes that are restricted to epithelial cells and anchor their intermediate filaments to the underlying basal lamina and (2) focal adhesions (FAs) that are more widely distributed in animal tissues and anchor the actin filaments of cells to the surrounding ECM (Figure 1).

Due to their widespread distribution among cardiovascular tissues and their importance in regulating tissue homeostasis in critical cell processes, including cell adhesion, proliferation and migration, the next section will focus on focal adhesions.

The molecular players of focal adhesions

FAs form a bridge between the cytoskeleton and the ECM, transferring mechanical forces and regulatory signals between them. More specifically, they anchor bundles of actin filaments through a large intracellular adaptor complex that consists of many different proteins. Characteristic adaptor proteins are vinculin, talin, paxillin, tensin, α-actinin and filamin. Many intracellular signaling proteins, such

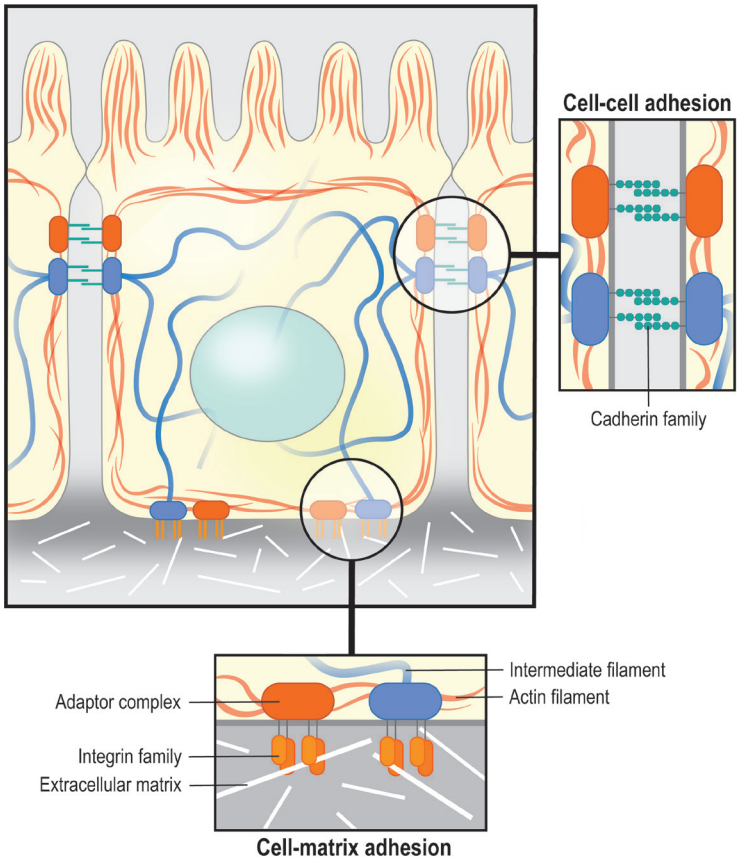

Figure 1. Schematic overview of anchoring junctions. Adaptor complexes (solid ovals) contain several different components linking the cell interior to the cell exterior. Actin filaments are shown in red and intermediate filaments are shown in blue. Cell-cell adhesion: transmembrane adhesion proteins from the cadherin family (green) form a link between neighboring cells and their cytoskeleton. Adherens junctions (lateral red solid ovals) link actin filaments, while desmosomes (lateral blue solid ovals) link intermediate filaments between cells. Cell-matrix adhesion: transmembrane adhesion proteins form the integrin family (orange) form a link between cells and the underlying extracellular matrix. Focal adhesions (basal red solid ovals) link the actin filaments, while hemidesmosomes (basal blue solid ovals) link intermediate filaments to the extracellular matrix.

as the focal adhesion kinase (FAK), associate with this multiprotein complex[12,13]. ECM components that anchor to FAs include fibronectin, laminin, vitronectin and various collagens.

The intracellular adaptor complex and specific ECM components are connected via transmembrane adhesion proteins. A major class of these adhesion proteins

is the family of integrins. Each individual integrin consists of two main parts: an α- and a β-subunit. A single β-subunit can interact with multiple α-subunits, allowing various integrin combinations with different binding affinities for ECM ligands. In vertebrates, the integrin family is composed of 18 types of α-subunits and 8 types of β-subunits that can assemble into 24 different heterodimers[14]. Some integrin subunits are ubiquitously expressed, while others are expressed in a tissue- or process-specific manner. For example, the β1-subunit is ubiquitously expressed and is the most commonly found subunit in integrin heterodimers, whereas the β6-subunit is only expressed during wound healing[15,16]. Integrins bind to specific short amino acid sequences within ECM proteins and these ligand-binding properties together with subunit composition classify them into four subgroups: (1) RGD-recognizing receptors that bind the specific RGD motif present in fibronectin among others, (2) laminin-binding receptors, (3) leukocyte-specific receptors and (4) collagen-binding receptors that recognize the specific GFOGER motif present within various collagens (Figure 2).

Integrins are more than solely an adhesive link, they are bi-directional signaling receptors that mediate signals to and from cells. The inside-out signaling mainly acts to bring integrins into the active state. These signaling pathways from the cytoplasm alter the structure of integrins and consequently their extracellular ligand-binding specificities. Upon ligand-binding, integrins undergo conformational changes. They cluster at the plasma membrane and interact with the FA adaptor complex using their cytoplasmic tails. This outside-in signaling influences the cytoskeleton and associated intracellular signaling pathways. In this way, FAs play an important role in both controlling cell shape and behavior and sensing the environment[14,16,17].

The importance of integrins is highlighted by the phenotypic defects seen in integrin knockout mice. Deletion of individual integrin subunit genes generally leads to embryonic or early postnatal mortality. This is due to developmental problems of specific organs, such as kidney and lung (α3 and α8)[18,19], placenta and heart (α4)[20], blood vessels (αv and β8)[21] and lymphatic vessels (α9)[22]. Deletion of the β1-subunit gene gives rise to the most severe phenotype, as it results in failure of the gastrulation phase[23]. Integrin knockout mice that do survive embryonic development exhibit multiple phenotypes due to the divergent roles that integrins play. For example, deletion of the α1-subunit alters cell adhesion, absence of the

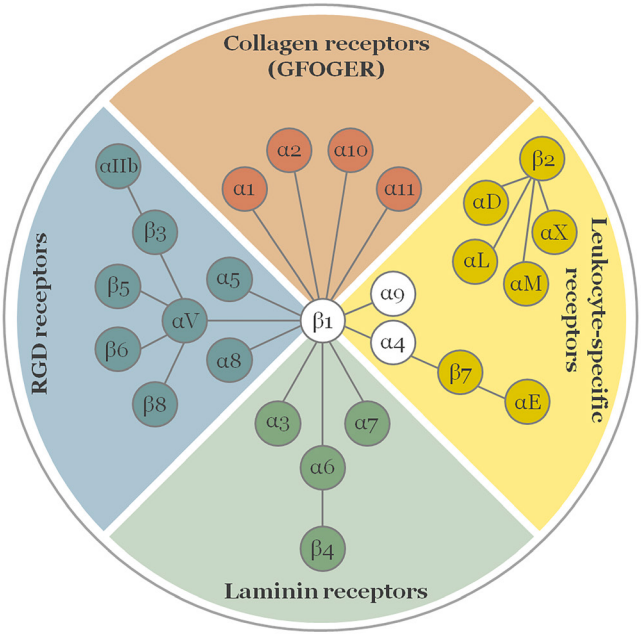

Figure 2. Overview of the integrin family and their interactions. In vertebrates, the integrin family contains 24 heterodimers. They are classified into four subgroups based upon their ligand-binding properties and subunit composition and are colored and arranged accordingly: (1) RGD-recognizing receptors that bind the RGD motif (blue), (2) collagen-binding receptors that recognize the GFOGER motif (orange), (3) leukocyte-specific receptors (yellow) and (4) laminin-binding receptors (green). Integrin subunits connected by a line represent heterodimeric α-β binding partners.
(Figure adapted from Hynes and Naba 2012[32]).

α7-subunit causes muscular dystrophy and β3-deficient mice exhibit defects in platelet aggregation[24-26]. Anti-β3 antibodies are being used in the clinic to prevent thrombosis[27], further emphasizing the importance of integrins in both health and disease. Other FA proteins are essential for embryonic development as well. Disruption of the talin gene arrests mouse development at the gastrulation stage[28], vinculin knockout results in early heart and brain defects[29] and both paxillin and FAK are essential for normal mesodermal movement, neural tube formation and early vascular expansion[30,31]. A common feature of all these knockout phenotypes is altered cell-matrix adhesion, resulting in abnormal cell spreading and migration. Due to its importance, FA dynamics in cell migration has been extensively studied.

FAs are stable in adherent stationary cells, while in migrating cells this stability is altered. Stable cells can transform into motile cells during development,

wound healing and certain pathologic conditions (e.g. metastatic cancer). During cell migration, FAs are constantly being assembled and disassembled as the cell establishes new contacts with the ECM at the leading edge and removes old contacts at the trailing edge. In more detail, small and transient adhesions, called focal complexes (FCs), are initially formed at the leading edge of a cell to mediate the attachment of extending lamellipodia with the ECM. These FCs consist of integrins and some adaptor proteins. However, many of these FCs fail to mature in FAs and are disassembled as the lamellipodia withdraw. Some FCs do mature into larger and more stable FAs by recruiting additional adaptor proteins, thereby preventing the leading edge from retracting. This maturation of FCs into FAs is highly dependent on the process of retrograde actin flow. Actin polymerizes at the leading edge to extend lamellipodia forward and this meshwork of actin filaments flows back along the membrane towards the cell body. FCs maturing at the leading edge anchor the flowing actin filaments and elongate in the direction of the actin flow, eventually forming contractile actomyosin bundles that terminate in FAs called stress fibers. FAs remain stationary with respect to the ECM and the cell uses them as an anchor to push or pull itself forward. During this movement, the retrograde actin flow changes from being driven by actin polymerization to myosin-based contraction of stress fibers. As the cell moves along its chosen path, the FAs move closer to the trailing edge where they are eventually disassembled to promote both retraction of the cell rear and forward cell movement[16,33,34]. The ability of a cell to migrate corresponds to a delicate balance between mechanical forces generated by the actin cytoskeleton and the resisting forces generated by cell adhesions. Cells cannot migrate if they are either adhered too strongly or not adhered at all to the ECM. Thus, the fastest migration occurs at an intermediate rate of adhesion, coordinated by transient FAs with a rapid turnover of structural components.

Cell migration is regulated by three members of the Rho family of GTPases: Cdc42, Rac1 and RhoA. Signals from the ECM are transmitted to Cdc42. Activation of this GTPase orients the cell and stimulates the appearance of filopodia through actin polymerization. Active Cdc42 will also ensure asymmetry of Rac1 and RhoA in the oriented cell. Concentrated Rac1 in the front induces the formation of the leading edge by stimulating the appearance of lamellipodia through the assembly of FCs and actin filaments. Vice versa, concentrated RhoA towards the cell rear induces membrane retractions through actomyosin contraction, as high RhoA levels

stimulate the transition of FCs into FAs anchored to stress fibers. Subsequently, downstream signaling of the RhoA-axis mediates adhesion disassembly needed for complete membrane retraction[16,33,35].

Thus, each distinct step in FA dynamics is controlled by a unique Rho GTPase and is marked by specific adaptor proteins, making these proteins ideal markers to monitor the degree of adhesion in both stable and migrating cells. In chapters 2 and 3 of this thesis, these markers have been used to unravel the involvement of selected ECM proteins in cell-matrix adhesion.

The extracellular matrix and its properties

A key step in the evolution of multicellular organisms was the emergence of genes coding for structural and functional proteins that can be secreted by cells into the extracellular space to help them organize into tissues. Many of these ECM molecules originated during early metazoan evolution and have remained highly conserved ever since[36]. The necessity of the ECM for multicellular life is still evident in modern embryonic development. For example, laminin is already expressed at the 16-cell stage, followed by collagen type IV expression in the early blastocyst[37].

In addition to the ECM being an adhesive substrate for cell attachment and migration, it also provides structural and mechanical support and sequestrates biochemical cues, such as growth factors. The main structural and most abundant protein in the vertebrate ECM is collagen, which accounts for nearly 90% of the dry weight of most tissues[38]. The collagen superfamily comprises of 28 members characterized by a triple helix composed of α-chains[39]. Based on their supramolecular assemblies, collagens can be divided into various subfamilies. The most abundant and widespread collagen family is represented by the fibril-forming collagens. Type I fibrils represent more than 90% of the organic mass of bone and together with type III fibrils are the main collagen found in tendons, skin, ligaments, cornea and many interstitial connective tissues. Type II and XI collagens are mostly found in the fibrillar matrix of cartilage and type V fibrils contribute to the structural scaffold of bone. Fibril-associated collagens, including types as IX, XII and XIV collagens, associate as single molecules with large collagen fibrils. Type IV collagens contain a more flexible triple helix and assemble into meshworks restricted to basement membranes[40]. Collagens also associate with other major ECM fibers, such as elastin. These elastin fibers are needed for elasticity and

resilience of tissues that undergo repeated stretch[41].

Other abundant structural ECM molecules are proteoglycans, which are scattered among the collagen fibrils in nearly all connective tissues. Proteoglycans are glycoproteins with covalently attached glycosaminoglycan chains (GAGs; repeating disaccharide polymers with attached anionic groups). Because of these GAG chains, proteoglycans are highly negatively charged, allowing them to sequester water and divalent ions. These properties of proteoglycans provide connective tissues with hydration and swelling pressure to withstand compressional forces[32]. For example, in the renal glomerular basement membrane, perlecan has a role in glomerular filtration[42]. In addition, the negative charge makes it possible for GAGs to bind growth factors and even protect them from degradation, providing a matrix-bound growth factor reservoir[43]. While collagens and proteoglycans provide structure and space-filling functions, other glycoproteins are needed to reinforce the network[32]. These adhesion molecules bind to and cross-link cellular receptors and other ECM components. For example, fibrillins provide a scaffold for the deposition of elastin, which is essential for the formation and integrity of elastic fibers[41]. Other important glycoproteins are laminins, which are major components of the basement membrane, and fibronectin, a known ligand for many integrins. Fibronectin is also known for its ability to bind specific growth factors, such as vascular endothelial growth factor (VEGF)[44].

An important aspect of the ECM is that the structure is highly dynamic. The proteins and the fibrils into which they assemble are constantly being modified. Many ECM components, including collagens, laminins and fibronectin can be cross-linked by disulfide bonding or by the action of transglutaminases, lysyl oxidases and hydroxylases[32]. Proteolytic enzymes modify the ECM as well. In fact, the processing of collagens by procollagen propeptidases is a requirement for polymerization. Many other proteolytic enzymes, including matrix metalloproteases (MMPs) and elastases, play a key role in ECM turnover and the release of sequestrated growth factors[32].

Resident cells of each tissue are responsible for the composition and structural integrity of the surrounding ECM, making it a tissue-specific 3D scaffold in which cells are embedded. This unique ECM composition is generated during early embryonic development, where ECM remodeling accompanies the migration and

differentiation events guiding cell division and the subsequent formation of distinct tissues and organs[45]. Loss-of-function studies highlight the importance of the ECM during development, as genetic deletion of specific proteins, such as fibronectin, elastin, fibrillins, laminins and collagens, often cause embryonic or early postnatal mortality[46]. The production and deposition of ECM components by resident cells continues throughout life and influence many biological processes, including cell migration, adhesion, proliferation and differentiation[47-49].

Use of tissue-specific extracellular matrix components in tissue engineering

Due to its evolutionarily conserved composition and impact on both embryonic development and cellular homeostasis, the ECM represents an ideal scaffolding system for tissue engineering. This field of research uses a combination of cells and a scaffolding system based on biomaterials and bioactive factors to improve or replace biological tissues or to implement in complex *in vitro* 3D cell models. Not only is the native ECM inherently bioactive, it is also biocompatible with cells. Selection of the appropriate matrix for tissue engineering is crucial, as it will profoundly affect cell viability and behavior. Often used natural matrices for 3D cell culture are hydrogels based on endogenous ECM components, such as collagen, fibrin and gelatin, or matrigel, which is a mixture rich in ECM proteins derived from mouse stromal tumors[50-52]. However, these ECM matrices are not tissue-specific nor do they focus on specific matrix factors for guiding the desired cell behavior. Improved matrices, such as synthetic matrices containing tissue-specific ECM components, appear to hold the best potential for mimicking the desired physiological setting. In order to create such a scaffolding system, it is necessary to fully characterize the unique and complex ECM composition of specific organs and tissues.

For unraveling the renal ECM, several studies have focused on the glomerulus, the filtering unit of the kidney. Together, they identified a highly connected glomerular ECM network comprising of almost 200 different structural and regulatory proteins, with distinct contributions by podocytes and glomerular endothelial cells[53-57]. These studies demonstrated that the composition of the glomerular ECM is far more complex than initially anticipated. Research until now focused on mapping the adult human renal ECM. However, the developing kidney undergoes extensive ECM remodeling associated with the assembly and growth

of specific nephron segments[58], matching with the microenvironment needed in 3D cell constructs. In **chapters 2 and 3** of thesis, the differences between the developing fetal and the more static mature human ECM were characterized from both the kidney and renal artery. The resulting tissue-specific catalogues give important insights into ECM structure and function and enables a more detailed investigation of promising renal ECM components and their potential use in scaffolding systems. A critical difference found is the abundance of Elastin Microfibril Interfacer 1 (EMILIN1) in the fetal ECM of both tissues. EMILIN1 is a glycoprotein that is located in elastic fibers at the interface between elastin and the surrounding microfibrils[59]. It is suggested that EMILIN1 plays an important role in the development of elastic tissues, including large blood vessels and the heart[60]. Furthermore, the chemical structure of EMILIN1 hints towards cell adhesive capacities[61,62]. Indeed, a link between EMILIN1 and renal cell-matrix adhesion was found and is described in this thesis.

Aberrant extracellular matrix remodeling in disease

The ECM is tightly regulated by a delicate balance between synthesis, degradation, reassembly and chemical modifications[45]. These complex processes need to be tightly regulated in order to maintain tissue homeostasis, especially during growth and repair. Indeed, dysregulation of ECM remodeling, either abnormal breakdown or excessive production, is associated with the development and progression of numerous pathological conditions.

Abnormal ECM breakdown mediated by proteolytic enzymes causes tissue destruction and releases sequestered bioactive molecules from the ECM. For example, high levels of MMP1 expression in the heart results in collagen loss and diminished contractility that leads to cardiac dysfunction[63]. Upregulation of MMP9 during cancer formation releases sequestered vascular VEGF from the ECM, thereby triggering the angiogenic switch[64]. Excessive ECM production and deposition without equally balanced degradation can result in fibrosis, where normal tissue is lost in an ongoing scarring process. During this process, fibroblasts are stimulated to continuously secrete precursors of ECM components, such as collagen fibers, GAGs and elastic fibers, as a last attempt to maintain structural integrity. A potent stimulator of fibrosis is the activation of the TGF-β pathway. TGF-β induces the translocation of the SMAD complex into the nucleus, where it directly enables the transcription of many ECM-related genes, such as *COL1A1* and

COL3A1[65]. In addition, the ECM itself actively participates in stimulating excessive ECM production by fibroblasts in a positive feedback loop[66]. In patients with scleroderma, increased fibronectin fragments in the circulation stimulate collagen production, ultimately leading to fibrosis[67]. This aberrant healing process can become so severe that it leads to organ failure.

A myriad of diseases are characterized by fibrosis at the end stage, including dilated cardiomyopathy (DCM). This heart muscle disease is characterized by the dilation of the left ventricle and presence of ventricular systolic dysfunction[68,69]. Myocardial fibrosis is a major feature of DCM[70-72] and therefore it is inevitable that complex ECM remodeling is involved in DCM onset and progression. Increasing our understanding on aberrant ECM remodeling in DCM could be important for the identification of future targets for treatment or prognostic markers. Here, the focus should not merely lie on structural ECM components, but on biochemical cues as well, which can regulate many biological processes. **Chapter 4** of this thesis focuses on the changes in ECM composition in DCM. Next to summarizing the existing literature, a catalogue of ECM genes associated with DCM was created using published transcriptome-based datasets. The resulting catalogue of ECM changes expands the fundamental knowledge about aberrant ECM remodeling in DCM.

Cell-cell adhesion

Cell-cell adhesion forms a continuum between cells and their linked cytoskeleton, providing them with mechanical support and positional information. Two main types of cell-cell adhesion anchoring junctions have been identified, characterized by specific cytoskeletal anchors: (1) desmosomes that are restricted to cells experiencing extreme mechanical stress, such as cardiomyocytes and epithelial cells, and anchor the intermediate filaments of neighboring cells together and (2) adherens junctions (AJs) that are found in epithelial and endothelial cells and anchor the actin filaments of neighboring cells together (Figure 1).

Due to their widespread distribution among cardiovascular tissues and their importance in regulating tissue homeostasis in critical cell processes including barrier function, cell proliferation and migration, the focus of the next section will lie on adherens junctions.

The molecular players of adherens junctions

AJs serve as a bridge connecting the cytoskeleton of neighboring cells, allowing them to respond to biochemical or mechanical stimuli. These responses include cell division and shape changes in pre-existing tissues and attachment of migrating cells during their first encounter in developing tissues[7]. In more detail, AJs anchor bundles of actin filaments through an intracellular adaptor complex that is composed of the following three main proteins: p120-catenin, α-catenin and either β- or γ-catenin. The adaptor complexes of neighboring cells are connected via transmembrane adhesion proteins. A major class of these adhesion proteins found in AJs is the family of cadherins.

The adhesive function of cadherins relies upon the formation of homodimers, where clusters of cadherins interact with similar clusters on a neighboring cell. The extracellular homophilic domain contains five cadherin repeats that are linked by Ca^{2+} binding sites[73]. In the absence of Ca^{2+}, the rigid conformation needed for dimerization is lost. Binding of p120-catenin to the juxtamembrane portion of the cadherin intracellular domain stabilizes the complex by preventing cadherin internalization. In addition, p120-catenin regulates small GTPases, including members of the Rho family of GTPases that are involved in actin reorganization[73]. The cadherin complex is directly linked to the actin cytoskeleton through a bridge formation consisting of α-catenin and either β- or γ-catenin, depending on the cadherin type. The cadherin cytoplasmic tail binds to β- or γ-catenin, which in turn binds to α-catenin. F-actin is one of the binding partners of α-catenin, thereby tethering the cadherin complex to actin filaments that originate from the underlying cortical actin belt[74] (Figure 3). These cytoskeleton rearrangements near the developing AJ strengthen cell-cell adhesion. Usually, the boundaries between adjacent cells display a stable linear morphology needed to maintain tissue integrity. These stable AJs are supported by the cortical actin belt, providing a strong barrier. However, AJs are highly dynamic and reorganize continuously in response to external or internal stimuli. These linear AJ can then convert into discontinuous AJ with reduced cell-cell adhesion, characterized by the appearance of stress fibers and radial junctions where the cadherin complex aligns with the end of these fibers. Discontinuous junctions are characteristic for an activated cell layer, for example a permeable endothelium allowing leukocyte diapedesis or the neoplastic transformation of epithelial tissue[75,76].

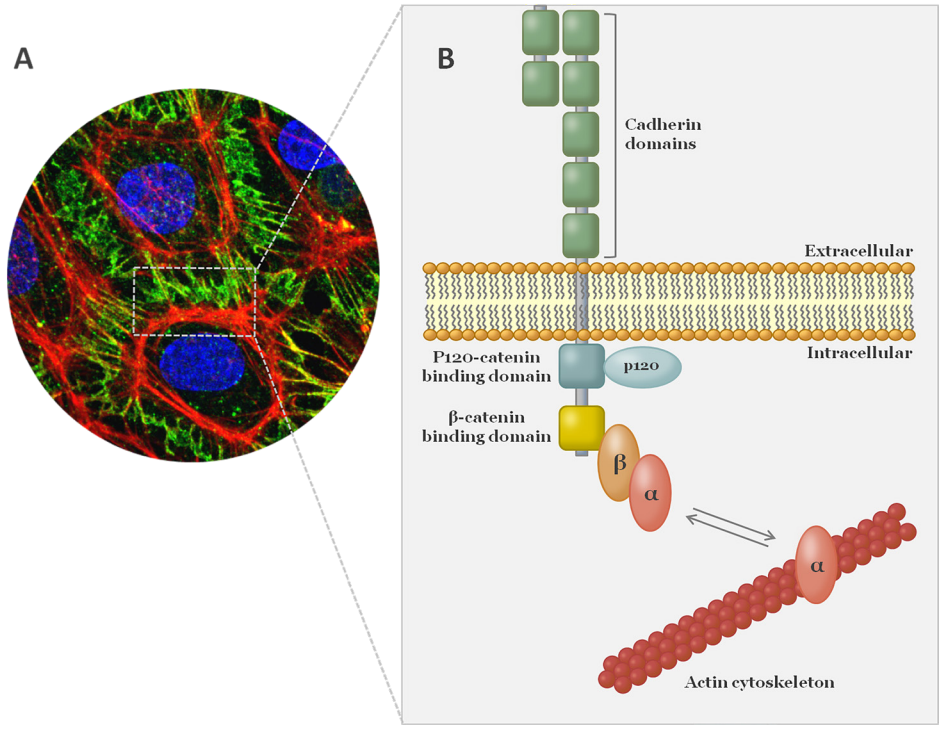

Figure 3. Schematic illustration of the classical cadherin-catenin complex. (A) Endothelial cells establish a dynamic permeability barrier containing VE-cadherin (green) and the actin cytoskeleton (red). (B) Cadherin receptors interact with other cadherins on neighboring cells via their extracellular cadherin domains. Through their intracellular domains, cadherins interact with both p120-catenin and β-actinin. p120 binds to the juxtamembrane domain of the cadherin tail, preventing cadherin internalization. β-catenin binds to the cadherin C-terminal domain, mediating the connection with α-catenin. In turn, α-catenin mediates the association of the cadherin complex with the actin cytoskeleton.

Many events during embryonic development are associated with changes in cell-cell adhesion strength, predominantly during vascular development. Here, endothelial AJs must provide stable connections that prevent leakage, while also allowing dynamic cellular rearrangements during the formation of new blood vessels[77].

The role of adherens junctions in angiogenesis

Angiogenesis is the process through which new blood vessels are formed from pre-existing vessels by sprouting new branches that connect and remodel into a functional network. It is stimulated in hypoxic tissues by high levels of permeability-increasing agents, such as VEGF. The importance of VEGF for angiogenesis is

highlighted by the phenotypic defects seen in VEGF knockout mice, as embryonic lethality occurs even in the heterozygous state due to impaired vascular development[78,79]. VEGF is secreted into the extracellular space to initiate sprouting of neighboring vessels towards the hypoxic cells. In more detail, VEGF binding to VEGF receptor 2 (VEGFR2) on quiescent cells activates the small GTPase Rac, which in turn induces phosphorylation of the VE-cadherin cytoplasmic tail and associated catenins, leading to loosening of the VE-cadherin/catenin binding. This results in the recruitment of β-arrestin to VE-cadherin, thereby promoting its internalization and decreasing the junctional adhesive strength[80]. VE-cadherin internalization is required for the disruption of AJs in order to allow EC migration and morphological adaptation into tip and stalk cells.

The ability of an individual EC to become a tip cell is dependent on the bioavailability of VEGFR2 on its plasma membrane compared to neighboring cells. These chosen tips cells lead the growing sprout towards the VEGF signal by developing filopodia on the cell edge containing activated VEGFR2. Simultaneously, VEGF stimulation upregulates Delta-like 4 (DLL4) expression in the chosen tip cells. After secretion, this ligand for the Notch receptor activates Notch signaling in the neighboring cells of the growing sprout, consequently suppressing the tip cell phenotype in these cells by reducing VEGFR2 expression and upregulating the decoy receptor VEGFR1. Instead, these cells acquire a stalk cell phenotype, allowing them to follow the tips cells in their migration along the VEGF gradient and to support sprout elongation by proliferation. In addition, low Notch signaling in the tip cells maintains the high expression of VEGFR2, further enhancing differential Notch activity between tip and stalk cells[81].

Thus, sprout extension upon VEGF stimulation requires migration of the tip cells and elongation of the stalk cells. This requests a coordinating role by AJs in both polarizing the tip cells and maintaining sprout cohesion at the stalk. To allow effective sprouting, VEGF signaling increases the junctional permeability and loosens AJs by internalization of VE-cadherin. During this process, the amount of VE-cadherin at AJs and associated actin polymerization must be tightly controlled, as too little contractility of the actin cytoskeleton leads to unstable AJs, whereas too much will not allow enough plasticity for sprouting[77]. Indeed, blocking VE-cadherin *in vitro* by the use of antibodies increases vascular permeability, whereas stimulating VE-cadherin-dependent cell-cell adhesion enhances EC barrier function[82,83]. In

concordance, VE-cadherin-deficient mice suffer from impaired vascular sprouting, resulting in death at mid-gestation[84,85].

Along their path, migrating tips cells project multiple filopodia containing VE-cadherin. Upon encounter with another sprout, excessive filopodia are retracted and the migrating sprouts will fuse by anastomosis. During this process, a single spot of VE-cadherin is deposited at the contact site to facilitate the initial adhesion. Zebrafish carrying a VE-cadherin null mutation are not able to retract the excessive filopodia upon contact formation during vascular sprouting, resulting in the formation of several contact sites[86]. Thus, VE-cadherin is necessary to halt the sprouting activity. This VE-cadherin spot is expanded into a junctional ring by increased actin polymerization and specifies the apical site[87]. Shortly before lumenization, F-actin becomes enriched at AJs, enabling cell rearrangements and shape changes[88]. This additional remodeling converts the sprout into a multicellular tube and hemodynamic forces drive lumen expansion[89]. During this process, AJs play an important role in the reinforcement of polarity, as knockdown of VE-cadherin is known to disrupt the formation of the apical membrane[90]. Additional signals from the ECM aid in the polarization process. Maintaining an open lumen requires active organization of the actin cytoskeleton into a cortical actin belt for stabilization[77].

Nascent vascular networks undergo extensive remodeling through the pruning of unnecessary branches and by stabilizing the remaining connections. Vessel pruning is mediated by hemodynamic forces, as irregular flow will initiate vessel regression and dissolvement of junctions. Cells from such a low-flow-branch migrate back towards high-flow-regions, converting the branch back into a unicellular tube with a single junctional ring[77,91]. In the end, this last junction dissolves and the cells from the disappearing branch incorporate into the neighboring vessels, creating new junctions in the process. AJs are essential for stabilizing the nascent network to prevent unwanted dissociation[77]. These stable AJs are characterized by a linear morphology and VE-cadherin linked to the cortical actin belt. This provides the mechanical strength and tightness needed to establish a permeability barrier. Additional stabilization and maturation comes from the recruitment of mural cells and deposition of ECM. Once the metabolic demand of the surrounding tissue is met, the new vessels will become quiescent[81]. This phenotype is characterized by reduced EC motility and proliferation, loss of the tip-stalk phenotype and

solid apical-basal polarity. VE-cadherin signaling at AJ is needed to maintain this quiescent phenotype, as VE-cadherin depletion causes increased EC apoptosis. Consequently, VE-cadherin-deficient mice suffer from vessel regression and limited organization of ECs into quiescent vessels[84,85].

Thus, the amount of VE-cadherin at the plasma membrane is linked to the degree of cell-cell adhesion and endothelial barrier function. This bioavailability is regulated by endocytosis in a tightly controlled manner.

Regulation of VE-cadherin function by endocytosis

Membrane-bound VE-cadherin is taken up into the cytosol in specialized regions called clathrin-coated pits that bud from the membrane to form clathrin-coated vesicles[80]. These vesicles then fuse with early endosomes in which VE-cadherin is further sorted for recycling, lysosomal, or other trafficking routes. Members of the Rab family of small GTPases regulate distinct steps along the endocytic pathway. Rab5 is required for the delivery of VE-cadherin to early endosomes[92]. In more detail, Rab5 is essential for the binding of early endosomal antigen 1 (EEA1) to the endosomal membrane. This docking protein brings endosomes physically closer to allow fusion[93]. From the early endosomes, VE-cadherin can be recycled back to the plasma membrane through two distinct recycling pathways: the Rab4-mediated rapid recycling pathway and the Rab11-mediated slow endosome pathway[94]. Rapid recycling occurs directly from the early endosomes, whereas slow recycling involves additional trafficking through pericentriolar recycling endosomes, before returning to the cell surface[95,96]. Instead of recycling back to the plasma membrane, VE-cadherin can also be targeted to the lysosomal trafficking route for degradation. Rab7 is involved in the regulation of late endosomal trafficking to lysosomes[97]. Thus, each distinct trafficking step is controlled by a unique subset of Rab GTPases, making these proteins ideal markers to monitor the transport route of endocytosed proteins (Figure 4). In chapters 5 and 6 of this thesis, these markers have been used to follow the trafficking route of VE-cadherin.

Whereas endocytosis plays a vital role in modulating vascular permeability by controlling the adhesive strength in AJs, little is known about the exact contribution of endocytic regulators to the angiogenic process. Increasing our understanding of these regulators could aid in the search for novel therapeutic treatments of various diseases characterized by abnormal angiogenesis. A family of endocytic

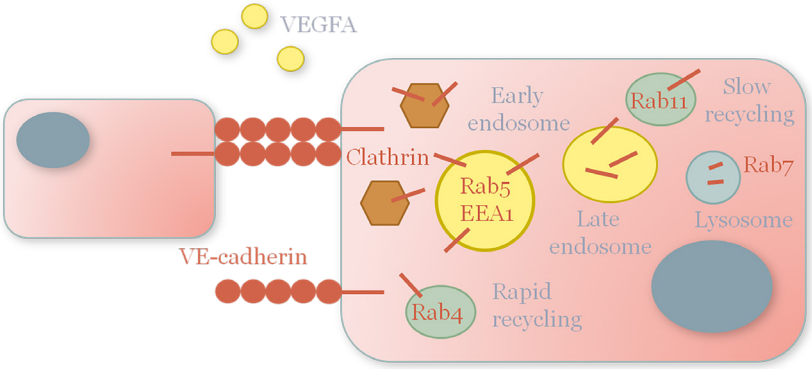

Figure 4. Simplified overview of VE-cadherin endocytosis. VEGFA stimulates rapid endocytosis of VE-cadherin and the subsequent disassembly of adherens junctions. VE-cadherin is taken up in clathrin-coated vesicles that fuse with early endosomes, which are marked by Rab5 and EEA1. From these vesicles, VE-cadherin is sorted for recycling, following either the Rab11-mediated slow recycling route or the Rab4-mediated rapid recycling route, or for degradation via the lysosomal trafficking route marked by Rab7.

regulators recently discovered to be involved in angiogenesis are epsins, which can modulate VEGF signaling by regulating the bioavailability of VEGFR2 on the plasma membrane. VEGFR2 undergoes ubiquitination as result of VEGF binding and this process triggers the binding of epsins through a ubiquitin-interacting motif, initiating receptor internalization for degradation. Loss of epsins impairs the endocytosis of VEGFR2, resulting in excessive VEGF signaling and subsequent destabilization of AJs[98,99]. This makes targeting endothelial epsins a promising therapeutic option for VEGF-driven tumor growth, as inactivation of epsins should lead to non-productive and leaky vessels and therefore impeding tumor progression[100]. The involvement of other regulators in early endocytosis and subsequent trafficking routes in ECs remains to be further elucidated. **Chapters 5 and 6** of this thesis report two novel proteins involved in regulating endocytosis during angiogenesis: CMTM3 and CMTM4. These proteins are members of the CKLF-like MARVEL transmembrane domain-containing (CMTM) family and were only known for their potential to act as tumor suppressor genes[101,102]. However, the chemical structure of CMTM family members links them to vesicle trafficking. This thesis describes a novel function for both CMTM3 and CMTM4 in endothelial cell-cell adhesion by regulating the bioavailability of VE-cadherin on the plasma membrane.

Gene alterations in angiogenesis

Angiogenesis is a normal process during embryonic development and is re-activated during wound healing and inflammation. However, when dysregulated, represented by either excessive or insufficient growth, angiogenesis contributes to a wide range of disorders, including cancer, psoriasis, arthritis, blindness, stroke, atherosclerosis, hypertension, pre-eclampsia, cardiovascular disease and nephropathy[103]. Genetic alterations have been linked to angiogenesis in general and to many of these disorders in particular. For example, the VEGF gene is highly polymorphic and some variants can subtly alter VEGF production. These VEGF polymorphisms have been linked with susceptibility to and severity of several cancer types and many other angiogenic diseases[104]. In addition to effects on disease, they have also been linked to the outcome of several treatments. In the case of organ rejection, specific VEGF polymorphisms are associated to increased kidney graft survival[104].

A common method for discovery of gene-disease relationships in such complex disorders is a genome-wide association study (GWAS). This tool is aimed at determining the statistical relationship between an observable disease trait and common DNA variants, mostly single nucleotide polymorphisms (SNPs). GWASs have been highly successful in unraveling the genetic architecture of coronary artery disease (CAD). Next to confirming classic CAD risk factors, such as LDL cholesterol, hypertension and coagulation, GWASs have helped in revealing hundreds of novel genetic variants demonstrating significant associations with CAD. In this manner, causal roles for cell proliferation and adhesion, the ECM and inflammation have been emphasized[105,106]. For chronic kidney disease (CKD), recent GWASs identified over a hundred SNPs associated with CKD traits, such as estimated glomerular filtration rate (eGFR), blood urea nitrogen, urinary albumin excretion and serum creatinine levels[107-109]. Unfortunately, ±90% of these SNPs lie within the non-coding genome, which, in contrast to SNPs in coding regions, do not act through alterations in the associated mRNA and protein sequence[110]. Instead, they most likely exert their effect through alterations in gene expression level, timing or location.

The causal contribution of non-coding SNPs to disease etiology is far less straightforward than for coding SNPs. Non-coding SNPs associated with CKD traits could be located within DNA regulatory regions (DREs), such as enhancers

and silencers[108,110]. These DREs activate or repress transcription of genes over large genomic distances (up to a million base pairs). Spatial localization of DREs with their target promoter is achieved by looping out the intervening chromosomal region[111]. Thus, common DNA variants in DREs could lead to dysregulation of target gene expression and thereby contribute to disease. In **Chapter 7** of this thesis, circular chromosome conformation capture-sequencing (4C-seq) was used to examine the 3D interactions between DREs harboring a CKD-associated SNP and their target genes. Since DREs regulate gene expression in a cell-specific manner and CKD is associated with both tubulointerstitial damage and loss of peritubular and glomerular capillaries[112-114], 4C-seq was conducted in both human renal proximal tubular epithelial cells and glomerular endothelial cells. The resulting overview of CKD candidate genes that are potentially dysregulated by DREs harboring CKD-associated SNPs aids in the understanding of the complex genetics of CKD.

THESIS SCOPE AND OUTLINE

The aim of this thesis is to unravel molecular mechanisms underlying cardiovascular health and disease, focusing on two different research topics where anchoring junctions have a prominent role: (1) extracellular matrix and (2) angiogenesis.

Extracellular matrix

The first part of this thesis describes novel insights in tissue-specific ECM composition and cell-matrix adhesion. The focus of chapter 2 and 3 lies on the difference between the fetal and mature ECM of both kidney and renal arteries. A critical difference is the abundance of Elastin Microfibril Interfacer 1 (EMILIN1) in the fetal ECM of both tissues. The role of this glycoprotein in focal adhesion assembly and migration of renal and vascular cells is described in these two chapters. Chapter 4 describes the tissue-specific ECM changes in the context of DCM. Next to a summary of the existing literature on this topic, a catalogue of ECM genes associated with DCM is created using published transcriptome-based datasets and their potential involvement in disease onset and progression is discussed.

Angiogenesis

The second part of this thesis describes novel insights in cell-cell adhesion and associated pathways underlying angiogenesis. In chapter 5 and 6, the role of CKLF like MARVEL transmembrane domain containing (CMTM) family members CMTM3 and CMTM4 in angiogenesis is described, with focus on their role in AJs as regulators of VE-cadherin internalization and recycling. Chapter 7 describes the results of a 4C-sequencing project using both renal epithelial and endothelial cells to identify target genes linked to regulatory elements with CKD-associated variation. The role of the identified target genes in maintaining kidney homeostasis is further discussed.

Summarizing discussion

Lastly, a general summary and discussion on the studies performed in this thesis is described in chapter 8.

References

1. Lock JG, Wehrle-Haller B, Stromblad S. Cell-matrix adhesion complexes: master control machinery of cell migration. Semin Cancer Biol. 2008;18(1):65-76.
2. Humphries JD, Chastney MR, Askari JA, et al. Signal transduction via integrin adhesion complexes. Curr Opin Cell Biol. 2019;56:14-21.
3. Pieters T, van Roy F. Role of cell-cell adhesion complexes in embryonic stem cell biology. J Cell Sci. 2014;127(Pt 12):2603-2613.
4. Wei Q, Huang H. Insights into the role of cell-cell junctions in physiology and disease. Int Rev Cell Mol Biol. 2013;306:187-221.
5. Winograd-Katz SE, Fassler R, Geiger B, et al. The integrin adhesome: from genes and proteins to human disease. Nat Rev Mol Cell Biol. 2014;15(4):273-288.
6. Jansen S, Gosens R, Wieland T, et al. Paving the Rho in cancer metastasis: Rho GTPases and beyond. Pharmacol Ther. 2018;183:1-21.
7. Gloushankova NA, Rubtsova SN, Zhitnyak IY. Cadherin-mediated cell-cell interactions in normal and cancer cells. Tissue Barriers. 2017;5(3):e1356900.
8. Lambiase PD, Tinker A. Connexins in the heart. Cell Tissue Res. 2015;360(3):675-684.
9. Bauer H, Traweger A. Tight Junctions of the Blood-Brain Barrier - A Molecular Gatekeeper. CNS Neurol Disord Drug Targets. 2016;15(9):1016-1029.
10. Capaldo CT, Powell DN, Kalman D. Layered defense: how mucus and tight junctions seal the intestinal barrier. J Mol Med (Berl). 2017;95(9):927-934.
11. Gumbiner BM. Cell adhesion: the molecular basis of tissue architecture and morphogenesis. Cell. 1996;84(3):345-357.
12. Jansen KA, Atherton P, Ballestrem C. Mechanotransduction at the cell-matrix interface. Semin Cell Dev Biol. 2017;71:75-83.
13. Trepat X, Chen Z, Jacobson K. Cell migration. Compr Physiol. 2012;2(4):2369-2392.
14. Takada Y, Ye X, Simon S. The integrins. Genome Biol. 2007;8(5):215.
15. Humphries JD, Byron A, Humphries MJ. Integrin ligands at a glance. J Cell Sci. 2006;119(Pt 19):3901-3903.
16. Berrier AL, Yamada KM. Cell-matrix adhesion. J Cell Physiol. 2007;213(3):565-573.
17. Barczyk M, Carracedo S, Gullberg D. Integrins. Cell Tissue Res. 2010;339(1):269-280.
18. Kreidberg JA, Donovan MJ, Goldstein SL, et al. Alpha 3 beta 1 integrin has a crucial role in kidney and lung organogenesis. Development. 1996;122(11):3537-3547.
19. Muller U, Wang D, Denda S, et al. Integrin alpha8beta1 is critically important for epithelial-mesenchymal interactions during kidney morphogenesis. Cell. 1997;88(5):603-613.
20. Yang JT, Rayburn H, Hynes RO. Cell adhesion events mediated by alpha 4 integrins are essential in placental and cardiac development. Development. 1995;121(2):549-560.
21. Zhu J, Motejlek K, Wang D, et al. beta8 integrins are required for vascular morphogenesis in mouse embryos. Development. 2002;129(12):2891-2903.
22. Huang XZ, Wu JF, Ferrando R, et al. Fatal bilateral chylothorax in mice lacking the integrin alpha9beta1. Mol Cell Biol. 2000;20(14):5208-5215.
23. Stephens LE, Sutherland AE, Klimanskaya IV, et al. Deletion of beta 1 integrins in mice results in inner cell mass failure and peri-implantation lethality. Genes Dev. 1995;9(15):1883-1895.
24. Gardner H, Kreidberg J, Koteliansky V, et al. Deletion of integrin alpha 1 by homologous recombination permits normal murine development but gives rise to a specific deficit in cell adhesion. Dev Biol. 1996;175(2):301-313.
25. Mayer U, Saher G, Fassler R, et al. Absence of integrin alpha 7 causes a novel form of muscular dystrophy. Nat Genet. 1997;17(3):318-323.
26. Hodivala-Dilke KM, McHugh KP, Tsakiris DA, et al. Beta3-integrin-deficient mice are a model for Glanzmann thrombasthenia showing placental defects and reduced survival. J Clin Invest.

1999;103(2):229-238.
27. Gabriel HM, Oliveira EI. Role of abciximab in the treatment of coronary artery disease. Expert Opin Biol Ther. 2006;6(9):935-942.
28. Monkley SJ, Zhou XH, Kinston SJ, et al. Disruption of the talin gene arrests mouse development at the gastrulation stage. Dev Dyn. 2000;219(4):560-574.
29. Xu W, Baribault H, Adamson ED. Vinculin knockout results in heart and brain defects during embryonic development. Development. 1998;125(2):327-337.
30. Hagel M, George EL, Kim A, et al. The adaptor protein paxillin is essential for normal development in the mouse and is a critical transducer of fibronectin signaling. Mol Cell Biol. 2002;22(3):901-915.
31. Furuta Y, Ilic D, Kanazawa S, et al. Mesodermal defect in late phase of gastrulation by a targeted mutation of focal adhesion kinase, FAK. Oncogene. 1995;11(10):1989-1995.
32. Hynes RO, Naba A. Overview of the matrisome--an inventory of extracellular matrix constituents and functions. Cold Spring Harb Perspect Biol. 2012;4(1):a004903.
33. Zamir E, Geiger B. Molecular complexity and dynamics of cell-matrix adhesions. J Cell Sci. 2001;114(Pt 20):3583-3590.
34. Burridge K, Guilluy C. Focal adhesions, stress fibers and mechanical tension. Exp Cell Res. 2016;343(1):14-20.
35. Nobes CD, Hall A. Rho GTPases control polarity, protrusion, and adhesion during cell movement. J Cell Biol. 1999;144(6):1235-1244.
36. Hynes RO. The evolution of metazoan extracellular matrix. J Cell Biol. 2012;196(6):671-679.
37. Leivo I, Vaheri A, Timpl R, et al. Appearance and distribution of collagens and laminin in the early mouse embryo. Dev Biol. 1980;76(1):100-114.
38. van der Rest M, Garrone R. Collagen family of proteins. Faseb j. 1991;5(13):2814-2823.
39. Ricard-Blum S. The collagen family. Cold Spring Harb Perspect Biol. 2011;3(1):a004978.
40. Gelse K, Poschl E, Aigner T. Collagens--structure, function, and biosynthesis. Adv Drug Deliv Rev. 2003;55(12):1531-1546.
41. Frantz C, Stewart KM, Weaver VM. The extracellular matrix at a glance. J Cell Sci. 2010;123(Pt 24):4195-4200.
42. Morita H, Yoshimura A, Inui K, et al. Heparan sulfate of perlecan is involved in glomerular filtration. J Am Soc Nephrol. 2005;16(6):1703-1710.
43. Ruoslahti E, Yamaguchi Y. Proteoglycans as modulators of growth factor activities. Cell. 1991;64(5):867-869.
44. Wijelath ES, Rahman S, Namekata M, et al. Heparin-II domain of fibronectin is a vascular endothelial growth factor-binding domain: enhancement of VEGF biological activity by a singular growth factor/matrix protein synergism. Circ Res. 2006;99(8):853-860.
45. Bonnans C, Chou J, Werb Z. Remodelling the extracellular matrix in development and disease. Nat Rev Mol Cell Biol. 2014;15(12):786-801.
46. Rozario T, DeSimone DW. The extracellular matrix in development and morphogenesis: a dynamic view. Dev Biol. 2010;341(1):126-140.
47. Flaim CJ, Chien S, Bhatia SN. An extracellular matrix microarray for probing cellular differentiation. Nat Methods. 2005;2(2):119-125.
48. Plotnikov SV, Pasapera AM, Sabass B, et al. Force fluctuations within focal adhesions mediate ECM-rigidity sensing to guide directed cell migration. Cell. 2012;151(7):1513-1527.
49. Vorotnikova E, McIntosh D, Dewilde A, et al. Extracellular matrix-derived products modulate endothelial and progenitor cell migration and proliferation in vitro and stimulate regenerative healing in vivo. Matrix Biol. 2010;29(8):690-700.
50. Homan KA, Kolesky DB, Skylar-Scott MA, et al. Bioprinting of 3D Convoluted Renal Proximal Tubules on Perfusable Chips. Sci Rep. 2016;6:34845.
51. Joraku A, Stern KA, Atala A, et al. In vitro generation of three-dimensional renal structures.

Methods. 2009;47(2):129-133.
52. Schutgens F, Rookmaaker MB, Margaritis T, et al. Tubuloids derived from human adult kidney and urine for personalized disease modeling. Nat Biotechnol. 2019;37(3):303-313.
53. Hobeika L, Barati MT, Caster DJ, et al. Characterization of glomerular extracellular matrix by proteomic analysis of laser-captured microdissected glomeruli. Kidney Int. 2017;91(2):501-511.
54. Lennon R, Byron A, Humphries JD, et al. Global analysis reveals the complexity of the human glomerular extracellular matrix. J Am Soc Nephrol. 2014;25(5):939-951.
55. Yoshida Y, Miyazaki K, Kamiie J, et al. Two-dimensional electrophoretic profiling of normal human kidney glomerulus proteome and construction of an extensible markup language (XML)-based database. Proteomics. 2005;5(4):1083-1096.
56. Cui Z, Yoshida Y, Xu B, et al. Profiling and annotation of human kidney glomerulus proteome. Proteome Sci. 2013;11(1):13.
57. Byron A, Randles MJ, Humphries JD, et al. Glomerular cell cross-talk influences composition and assembly of extracellular matrix. J Am Soc Nephrol. 2014;25(5):953-966.
58. Kanwar YS, Wada J, Lin S, et al. Update of extracellular matrix, its receptors, and cell adhesion molecules in mammalian nephrogenesis. Am J Physiol Renal Physiol. 2004;286(2):F202-215.
59. Bressan GM, Daga-Gordini D, Colombatti A, et al. Emilin, a component of elastic fibers preferentially located at the elastin-microfibrils interface. J Cell Biol. 1993;121(1):201-212.
60. Braghetta P, Ferrari A, de Gemmis P, et al. Expression of the EMILIN-1 gene during mouse development. Matrix Biol. 2002;21(7):603-609.
61. Colombatti A, Spessotto P, Doliana R, et al. The EMILIN/Multimerin family. Front Immunol. 2011;2:93.
62. Verdone G, Corazza A, Colebrooke SA, et al. NMR-based homology model for the solution structure of the C-terminal globular domain of EMILIN1. J Biomol NMR. 2009;43(2):79-96.
63. Kim HE, Dalal SS, Young E, et al. Disruption of the myocardial extracellular matrix leads to cardiac dysfunction. J Clin Invest. 2000;106(7):857-866.
64. Bergers G, Brekken R, McMahon G, et al. Matrix metalloproteinase-9 triggers the angiogenic switch during carcinogenesis. Nat Cell Biol. 2000;2(10):737-744.
65. Verrecchia F, Chu ML, Mauviel A. Identification of novel TGF-beta /Smad gene targets in dermal fibroblasts using a combined cDNA microarray/promoter transactivation approach. J Biol Chem. 2001;276(20):17058-17062.
66. Parker MW, Rossi D, Peterson M, et al. Fibrotic extracellular matrix activates a profibrotic positive feedback loop. J Clin Invest. 2014;124(4):1622-1635.
67. Bhattacharyya S, Tamaki Z, Wang W, et al. FibronectinEDA promotes chronic cutaneous fibrosis through Toll-like receptor signaling. Sci Transl Med. 2014;6(232):232ra250.
68. Elliott P, Andersson B, Arbustini E, et al. Classification of the cardiomyopathies: a position statement from the European Society Of Cardiology Working Group on Myocardial and Pericardial Diseases. Eur Heart J. 2008;29(2):270-276.
69. Rubis P. The diagnostic work up of genetic and inflammatory dilated cardiomyopathy. E-journal of Cardiology Practice. 2015;13(19).
70. Brooks A, Schinde V, Bateman AC, et al. Interstitial fibrosis in the dilated non-ischaemic myocardium. Heart. 2003;89(10):1255-1256.
71. Heneghan MA, Malone D, Dervan PA. Myocardial collagen network in dilated cardiomyopathy. Morphometry and scanning electron microscopy study. Ir J Med Sci. 1991;160(12):399-401.
72. Unverferth DV, Baker PB, Swift SE, et al. Extent of myocardial fibrosis and cellular hypertrophy in dilated cardiomyopathy. Am J Cardiol. 1986;57(10):816-820.
73. Saito M, Tucker DK, Kohlhorst D, et al. Classical and desmosomal cadherins at a glance. J Cell Sci. 2012;125(Pt 11):2547-2552.
74. Shapiro L, Weis WI. Structure and biochemistry of cadherins and catenins. Cold Spring Harb

Perspect Biol. 2009;1(3):a003053.
75. Millan J, Cain RJ, Reglero-Real N, et al. Adherens junctions connect stress fibres between adjacent endothelial cells. BMC Biol. 2010;8:11.
76. Ayollo DV, Zhitnyak IY, Vasiliev JM, et al. Rearrangements of the actin cytoskeleton and E-cadherin-based adherens junctions caused by neoplasic transformation change cell-cell interactions. PLoS One. 2009;4(11):e8027.
77. Szymborska A, Gerhardt H. Hold Me, but Not Too Tight-Endothelial Cell-Cell Junctions in Angiogenesis. Cold Spring Harb Perspect Biol. 2018;10(8).
78. Ferrara N, Carver-Moore K, Chen H, et al. Heterozygous embryonic lethality induced by targeted inactivation of the VEGF gene. Nature. 1996;380(6573):439-442.
79. Carmeliet P, Ferreira V, Breier G, et al. Abnormal blood vessel development and lethality in embryos lacking a single VEGF allele. Nature. 1996;380(6573):435-439.
80. Gavard J, Gutkind JS. VEGF controls endothelial-cell permeability by promoting the beta-arrestin-dependent endocytosis of VE-cadherin. Nat Cell Biol. 2006;8(11):1223-1234.
81. Blanco R, Gerhardt H. VEGF and Notch in tip and stalk cell selection. Cold Spring Harb Perspect Med. 2013;3(1):a006569.
82. Corada M, Liao F, Lindgren M, et al. Monoclonal antibodies directed to different regions of vascular endothelial cadherin extracellular domain affect adhesion and clustering of the protein and modulate endothelial permeability. Blood. 2001;97(6):1679-1684.
83. Fukuhara S, Sakurai A, Sano H, et al. Cyclic AMP potentiates vascular endothelial cadherin-mediated cell-cell contact to enhance endothelial barrier function through an Epac-Rap1 signaling pathway. Mol Cell Biol. 2005;25(1):136-146.
84. Carmeliet P, Lampugnani MG, Moons L, et al. Targeted deficiency or cytosolic truncation of the VE-cadherin gene in mice impairs VEGF-mediated endothelial survival and angiogenesis. Cell. 1999;98(2):147-157.
85. Gory-Faure S, Prandini MH, Pointu H, et al. Role of vascular endothelial-cadherin in vascular morphogenesis. Development. 1999;126(10):2093-2102.
86. Lenard A, Ellertsdottir E, Herwig L, et al. In vivo analysis reveals a highly stereotypic morphogenetic pathway of vascular anastomosis. Dev Cell. 2013;25(5):492-506.
87. Blum Y, Belting HG, Ellertsdottir E, et al. Complex cell rearrangements during intersegmental vessel sprouting and vessel fusion in the zebrafish embryo. Dev Biol. 2008;316(2):312-322.
88. Phng LK, Gebala V, Bentley K, et al. Formin-mediated actin polymerization at endothelial junctions is required for vessel lumen formation and stabilization. Dev Cell. 2015;32(1):123-132.
89. Gebala V, Collins R, Geudens I, et al. Blood flow drives lumen formation by inverse membrane blebbing during angiogenesis in vivo. Nat Cell Biol. 2016;18(4):443-450.
90. Wang Y, Kaiser MS, Larson JD, et al. Moesin1 and Ve-cadherin are required in endothelial cells during in vivo tubulogenesis. Development. 2010;137(18):3119-3128.
91. Chen Q, Jiang L, Li C, et al. Haemodynamics-driven developmental pruning of brain vasculature in zebrafish. PLoS Biol. 2012;10(8):e1001374.
92. Bucci C, Parton RG, Mather IH, et al. The small GTPase rab5 functions as a regulatory factor in the early endocytic pathway. Cell. 1992;70(5):715-728.
93. Mills IG, Jones AT, Clague MJ. Involvement of the endosomal autoantigen EEA1 in homotypic fusion of early endosomes. Curr Biol. 1998;8(15):881-884.
94. Sonnichsen B, De Renzis S, Nielsen E, et al. Distinct membrane domains on endosomes in the recycling pathway visualized by multicolor imaging of Rab4, Rab5, and Rab11. J Cell Biol. 2000;149(4):901-914.
95. Van Der Sluijs P, Hull M, Zahraoui A, et al. The small GTP-binding protein rab4 is associated with early endosomes. Proc Natl Acad Sci U S A. 1991;88(14):6313-6317.
96. Ullrich O, Reinsch S, Urbe S, et al. Rab11 regulates recycling through the pericentriolar

recycling endosome. J Cell Biol. 1996;135(4):913-924.
97. Bucci C, Thomsen P, Nicoziani P, et al. Rab7: a key to lysosome biogenesis. Mol Biol Cell. 2000;11(2):467-480.
98. Klauber-Demore N. Are epsins a therapeutic target for tumor angiogenesis? J Clin Invest. 2012;122(12):4341-4343.
99. Pasula S, Cai X, Dong Y, et al. Endothelial epsin deficiency decreases tumor growth by enhancing VEGF signaling. J Clin Invest. 2012;122(12):4424-4438.
100. Song K, Wu H, Rahman HN, et al. Endothelial epsins as regulators and potential therapeutic targets of tumor angiogenesis. Cell Mol Life Sci. 2017;74(3):393-398.
101. Xie J, Yuan Y, Liu Z, et al. CMTM3 is frequently reduced in clear cell renal cell carcinoma and exhibits tumor suppressor activities. Clin Transl Oncol. 2014;16(4):402-409.
102. Li T, Cheng Y, Wang P, et al. CMTM4 is frequently downregulated and functions as a tumour suppressor in clear cell renal cell carcinoma. J Exp Clin Cancer Res. 2015;34:122.
103. Carmeliet P. Angiogenesis in health and disease. Nat Med. 2003;9(6):653-660.
104. Rogers MS, D'Amato RJ. The effect of genetic diversity on angiogenesis. Exp Cell Res. 2006;312(5):561-574.
105. Shu L, Blencowe M, Yang X. Translating GWAS Findings to Novel Therapeutic Targets for Coronary Artery Disease. Front Cardiovasc Med. 2018;5:56.
106. Erdmann J, Kessler T, Munoz Venegas L, et al. A decade of genome-wide association studies for coronary artery disease: the challenges ahead. Cardiovasc Res. 2018;114(9):1241-1257.
107. Wuttke M, Kottgen A. Insights into kidney diseases from genome-wide association studies. Nat Rev Nephrol. 2016;12(9):549-562.
108. Pattaro C, Teumer A, Gorski M, et al. Genetic associations at 53 loci highlight cell types and biological pathways relevant for kidney function. Nat Commun. 2016;7:10023.
109. Gorski M, van der Most PJ, Teumer A, et al. 1000 Genomes-based meta-analysis identifies 10 novel loci for kidney function. Sci Rep. 2017;7:45040.
110. Xu X, Eales JM, Akbarov A, et al. Molecular insights into genome-wide association studies of chronic kidney disease-defining traits. Nat Commun. 2018;9(1):4800.
111. Williamson I, Hill RE, Bickmore WA. Enhancers: from developmental genetics to the genetics of common human disease. Dev Cell. 2011;21(1):17-19.
112. Bohle A, Grund KE, Mackensen S, et al. Correlations between renal interstitium and level of serum creatinine. Morphometric investigations of biopsies in perimembranous glomerulonephritis. Virchows Arch A Pathol Anat Histol. 1977;373(1):15-22.
113. Nangaku M. Chronic hypoxia and tubulointerstitial injury: a final common pathway to end-stage renal failure. J Am Soc Nephrol. 2006;17(1):17-25.
114. Kozakowski N, Herkner H, Bohmig GA, et al. The diffuse extent of peritubular capillaritis in renal allograft rejection is an independent risk factor for graft loss. Kidney Int. 2015;88(2):332-340.

Extracellular matrix – **Chapter 2**

A proteome comparison between human fetal and mature renal extracellular matrix identifies EMILIN1 as a regulator of renal cell adhesion

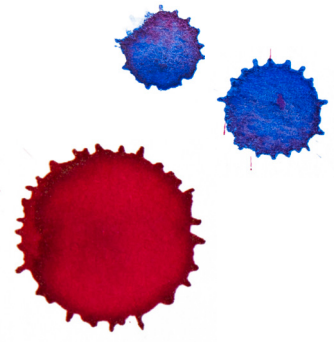

L. Louzao Martinez, C.G.M van Dijk, Y.J. Xu, A. Korn, N. Bekker, R. Brouwhuis, M.N. Nicese, J.A.A. Demmers, M.T.H. Goumans, R. Masereeuw, D.J. Duncker, M.C. Verhaar, C. Cheng.

(2019) Matrix Biology Plus [Epub ahead of print]

Abstract

Cell-based approaches using tissue engineering and regenerative medicine to replace damaged renal tissue with 3D constructs is a promising emerging therapy for kidney disease. Besides living cells, a template provided by a scaffold based on biomaterials and bioactive factors is needed for successful kidney engineering. Nature's own template for a scaffolding system is the extracellular matrix (ECM). Research has focused on mapping the mature renal ECM; however, the developing fetal ECM matches more the active environment required in 3D renal constructs. Here, we characterized the differences between the human fetal and mature renal ECM using spectrometry-based proteomics of decellularized tissue. We identified 99 different renal ECM proteins of which the majority forms an overlapping core, but also includes proteins enriched in either the fetal or mature ECM. Relative protein quantification showed a significant dominance of Elastin Microfibril Interfacer 1 (EMILIN1) in the fetal ECM. We functionally tested the role of EMILIN1 in the ECM using a novel methodology that permits the reliable anchorage of native cell-secreted ECM to glass coverslips. Depletion of EMILIN1 from the ECM layer using siRNA mediated knock-down technologies does not affect renal epithelial cell growth, but does promote migration. Lack of EMILIN1 in the ECM layer reduces the adhesion strength of renal epithelial cells, shown by a decrease in focal adhesion points and associated stress fibers. We showed in this study the importance of a human renal fetal and mature ECM catalogue for identifying promising ECM components that have high implementation potential in scaffolds for 3D renal constructs.

Introduction

In search of a potential treatment for kidney disease, current investigations focus on cell-based approaches using tissue engineering and regenerative medicine (TERM) to replace damaged renal tissue with engineered 3D structures. One promising TERM-based approach is the use of organoids. Renal organoids derived from induced pluripotent stem cells that model the morphology and segmentation of human fetal nephrons have been developed[1,2]. Human primary renal cells can also grow into 3D kidney-like constructs with tubular structures. When implanted into mice, these constructs survived and maintained their renal phenotypes for up to 6 weeks[3]. However, these techniques cannot fully recapitulate the complex organization of the kidney and cannot be grown on a large scale yet.

Besides cells, another basic component for kidney engineering is a template provided by a scaffolding system based on biomaterials and bioactive factors that create a microenvironment which facilitates cell-specific behavior. Nature's own template for a scaffolding system is the extracellular matrix (ECM), which is a collection of molecules deposited by surrounding cells, making it a tissue-specific 3D structure in which cells are embedded. The ECM not only gives structural support, it also contains biochemical cues that influence many biological processes, including cell migration, adhesion, proliferation and differentiation[4-7]. The matrices used to embed stem or primary renal cells are mostly collagen-based hydrogels or matrigel, which do not reflect the tissue-specific ECM of the kidney. Matrices containing renal-specific ECM cues could greatly advance TERM by promoting renal tissue formation. In order to create such a scaffolding system, the components of the human renal ECM first need to be fully characterized.

Proteomic techniques have been used to characterize the ECM composition in various tissues[8,9]. For the renal ECM, studies have focused on the human glomerular ECM and identified a highly connected network comprised of almost 200 different structural and regulatory ECM proteins[10-13]. Despite previous work, ECM proteome research until now only focused on mapping the mature renal ECM. In the fetal microenvironment, the ECM balance is shifted towards an active environment[14-17], which matches the need for tissue generation in 3D tissue constructs.

In this study, we characterized the differences between the developing fetal and the more static mature human renal ECM proteome. The resulting catalogue gives important insights into renal ECM structure and function and enables a detailed investigation of promising renal ECM molecules and their potential use

for implementation in scaffolds.

Based on our proteome analysis, we identified Elastin Microfibril Interfacer 1 (EMILIN1) as an important component enriched in the fetal ECM. EMILIN1 is located in elastic fibers at the interface between elastin and the surrounding microfibrils[18]. The distinctive C-terminus gC1q structure of EMILIN1 interacts with integrins, thereby connecting cells to elastic fibers[19,20]. Many cell types depend on this gC1q-integrin interaction for cell adhesion, migration and proliferation[21-24]. EMILIN1 is particularly abundant in the walls of blood and lymphatic vessels, where it is necessary for the formation of elastic fibers and anchoring filaments[25,26]. Despite studies implying that EMILIN1 is an important factor in maintaining cardiovascular health[26-29], the role of EMILIN1 in the kidney is unknown. Here, we have shown for the first time that EMILIN1 is an important regulator of renal cell migration and adhesion. These findings validate the importance of our human renal fetal and mature ECM catalogue for identifying promising ECM components with high potential for implementation in scaffolds for 3D kidney constructs.

Results

Enrichment of extracellular matrix proteins

We analyzed healthy kidney samples from adult and fetal human donors. The ECM was enriched in these samples by decellularization (Figure 1A). Cellular components were removed without disrupting the structure and morphology of the ECM (Figure 1B). The obtained ECM extracts were separated by SDS-PAGE and liquid chromatography-tandem mass spectrometry (LC-MS/MS) was used to characterize the differences between the fetal and mature renal ECM proteome (Figure 1A, Supplemental Figure 1A).

Comparison of the renal proteome: fetal versus mature

The obtained proteomic data were used to generate a catalogue of fetal and mature renal ECM proteins. Proteins that were identified in at least two replicates were included (Supplementary Figure 2A). By crossreferencing with the Human Matrisome Project[8,9], we categorized our data proteins into core ECM proteins, including collagens, glycoproteins and proteoglycans, and ECM-associated proteins, including ECM-affiliated proteins, regulators and secreted factors. Relative protein quantification showed a dominance of collagens and glycoproteins in both the fetal and mature ECM: 62% of the fetal and 64% of the mature signal consisted of collagens, whereas 33% of the fetal and 28% of the mature selection consisted of

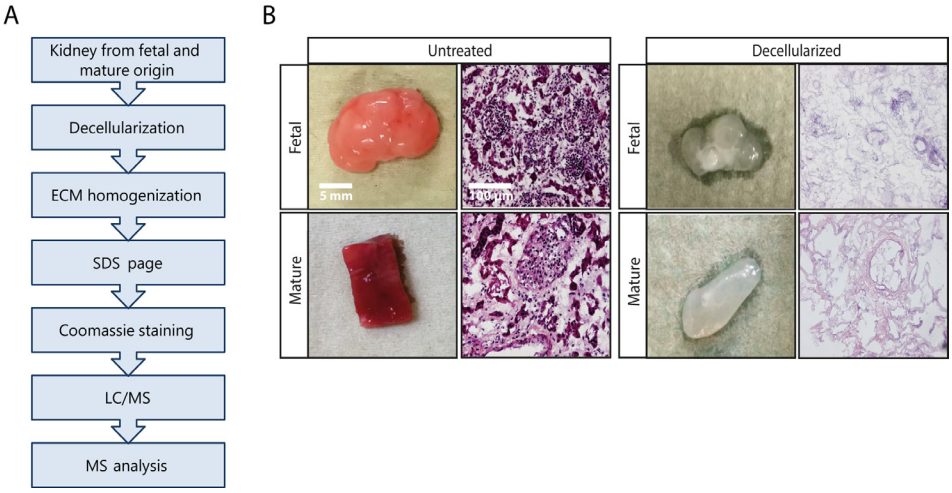

Figure 1. Isolation of human renal fetal and mature extracellular matrix proteins. (A) Workflow for the isolation of the extracellular matrix (ECM) from healthy human fetal and mature renal tissue. (B) Macroscopic appearance of representative human fetal and mature renal samples before and after decellularization (left panels). Scale bar represents 5 mm. Hematoxylin and eosin staining (200x magnification) of human fetal and mature renal tissue before and after decellularization demonstrates the successful removal of cellular components (right panels). Scale bar represents 100 µm.

glycoproteins (Figure 2A).

We identified 94 fetal and 76 mature renal ECM proteins, from which the majority could be classified as core ECM proteins (60 and 51, respectively). The most abundant signal came from core ECM proteins as well, with many collagens comprising ≥2% of the total ECM signal (Figure 2B, Supplemental Table 1). Four glycoproteins (EMILIN1, FGG, FBN1 and FBN2) and one proteoglycan (HSPG2) showed abundant signal, each comprising ≥2% of the total ECM signal (Figure 2B, Supplemental Table 1). We identified 23 proteins that were significantly enriched in the fetal renal ECM compared to the mature ECM. Only 6 ECM proteins were significantly enriched in the mature renal ECM. Among the 23 proteins significantly enriched in the fetal selection were the abundant glycoproteins EMILIN1, fibrillin1 (FBN1) and fibrillin2 (FBN2) (Figure 2C, Supplemental Table 1).

Lennon and colleagues published the composition of the human glomerular ECM[10]. By crossreferencing their dataset with the Human Matrisome Project[8,9] and subsequently with our dataset, we further classified our list in either glomerular or tubulointerstitial ECM proteins (Supplemental Figure 3). By this means, we identified 55 glomerular ECM proteins, including 8 proteins detected exclusively

in either the mature or fetal renal ECM. 29 glomerular ECM proteins were not detected by our MS analysis and were only found by Lennon *et al* due to their extra glomeruli enrichment step prior to MS analysis[10]. Our remaining 54 ECM proteins could then be classified as mainly tubulointerstitial, including 19 proteins

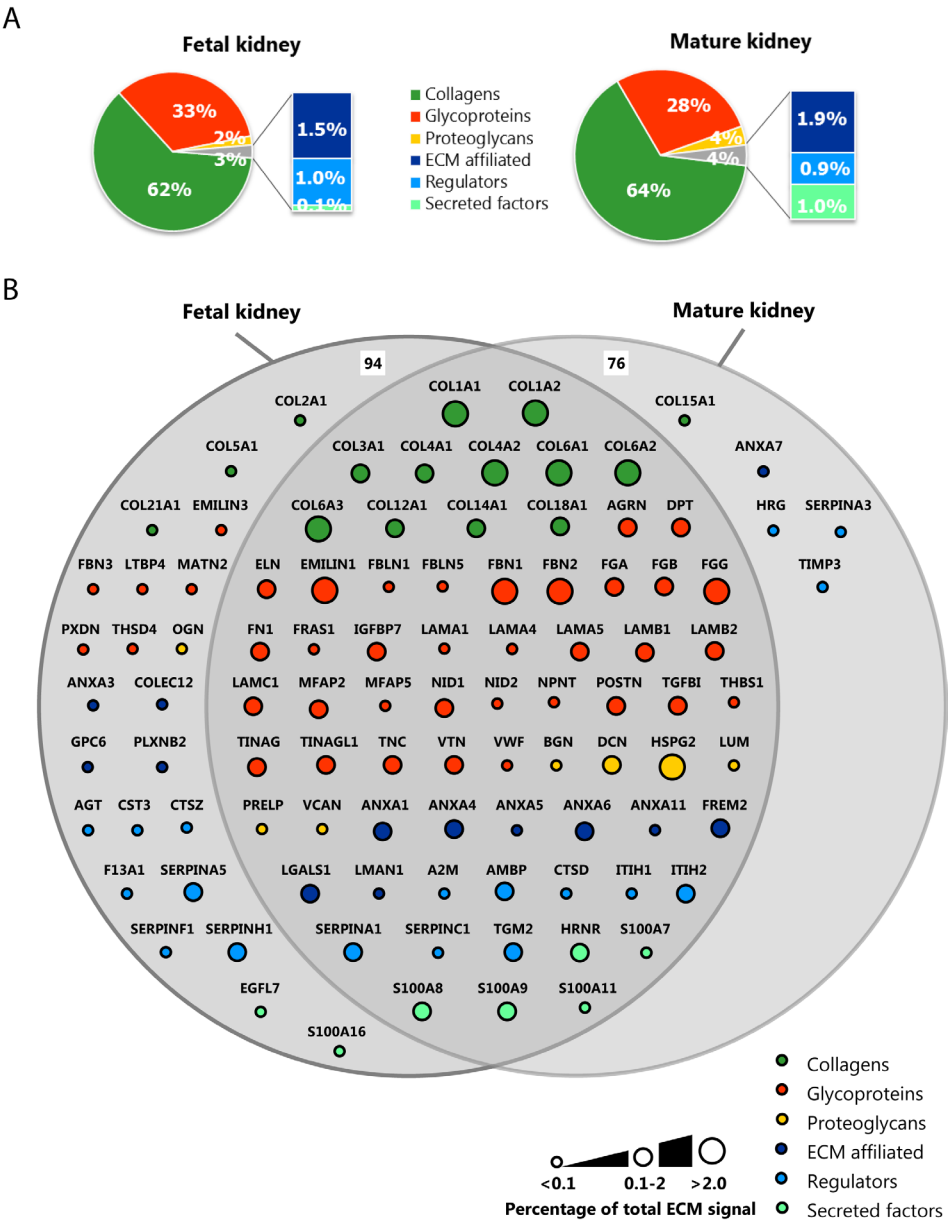

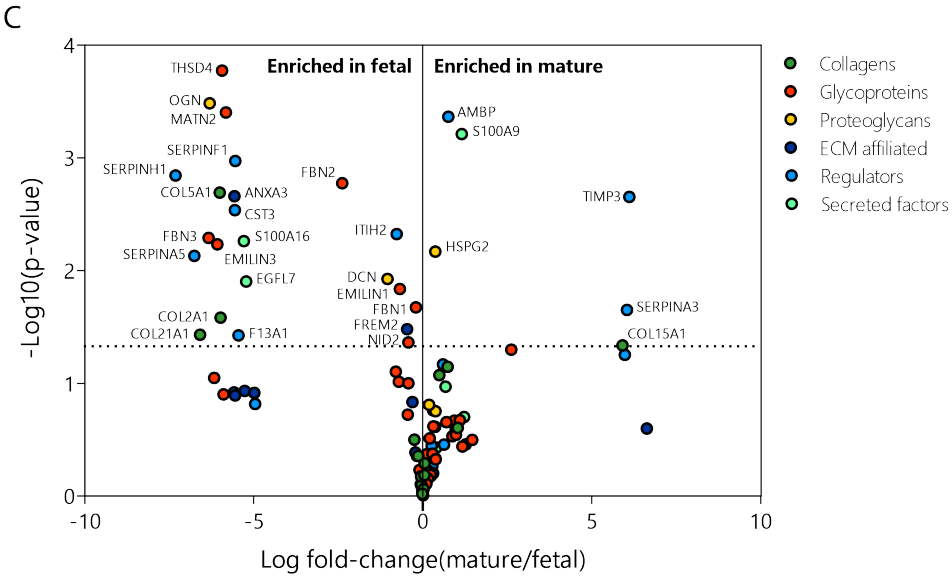

Figure 2. Defining the human renal fetal and mature extracellular matrix proteome. Extracellular matrix (ECM) proteins identified by mass-spectrometry were classified as collagens, glycoproteins, proteoglycans, ECM affiliated, regulators or secreted factors and they were colored and arranged accordingly. (A) Pie charts summarizing the relative protein quantification for both the fetal (left) and mature (right) human renal ECM proteome. (B) Euler-diagram visualizing the overlap and differences between the human fetal and mature renal ECM proteome. Each node represents a single protein and is labeled with the gene name. Node size is proportional to the abundance of the protein within the renal ECM proteome (≤0.1%, between 0.1 and 2% or ≥2% of the total ECM signal in at least one dataset (fetal or mature)). (C) A volcano plot representation of the human fetal and mature ECM proteome showing the protein distribution between fetal and mature (log fold-change(mature/fetal), x-axis) and significance (P-value, y-axis) of all detected ECM proteins. Each circle represents a single protein. The horizontal dashed line indicates the threshold of statistical significance (P<0.05).

unique for the fetal renal ECM. One tubulointerstitial ECM protein was found to be unique for the mature renal ECM. These findings show that the fetal and mature renal ECM are complex and share a central overlap, but are also characterized by unique ECM proteins.

Validation of selected proteins within the renal extracellular matrix

EMILIN1 was found to be one of the glycoproteins with the most abundant signal in the renal ECM and significantly enriched in the fetal selection, making it an interesting ECM protein for further investigation. EMILIN1 is a component of elastic fibers and previous studies have implied that its main function is to bind integrins,

thereby connecting cells to the ECM[23,24]. In the fetal renal ECM, the EMILIN1 signal comprises 6.8% of the total ECM signal, compared to only 1.5% of the mature ECM (Figure 3A, Supplemental Table 1). Protein verification was conducted using immunohistochemistry on non-decellularized renal tissue. Immunolocalization of EMILIN1 in mature and fetal human kidney showed localization mainly to the tubulointerstitial space (Figure 3B). In concordance with the proteomic analysis, EMILIN1 was significantly enriched in the fetal kidney compared to the mature kidney (Figure 3C).

Another significantly abundant glycoprotein in the fetal renal ECM is FBN1, which is a major component of microfibrils that, together with elastins, form the elastic fibers[30]. The FBN1 signal comprises 11.1% of the fetal ECM signal, compared to 7.3% of the mature ECM (Supplemental Figure 4A, Supplemental Table 1). Immunolocalization of FBN1 showed localization to both the glomerular and tubulointerstitial space, leading to no differences in fluorescent signal between the fetal and mature kidney (Supplemental Figure 4B,C). MRNA levels on the other hand showed a significant increase of *FBN1* in the fetal kidney compared to the mature kidney (Supplemental Figure 4D). Elastic fiber components in general seemed to be increased in the fetal kidney (Supplemental Table 1). Verification by gene expression analysis indeed showed that *MFAP2* was significantly increased in the fetal kidney compared to the adult kidney and the same trend was visible for *ELN* (Supplemental Figure 4E, F). Based on these results, EMILIN1 likely plays a fundamental role within the fetal renal ECM.

Anchored cell-derived extracellular matrix can be modified by depleting specific proteins

EMILIN1 was further investigated by using a method to reliably anchor native ECM through copolymer thin-film chemistry[31-33]. Poly(octadecene-*alt*-maleic anhydride) (POMA) was covalently coupled to aminosilanized glass coverslips[32]. Next, fibronectin (FN) was covalently attached via its lysine sidechain to the reactive anhydride moieties[33] (Figure 4A). Immobilized FN allows the stable anchorage of the ECM via its binding domains to collagen, fibrin and heparin sulfate proteoglycans[31].

We cultured smooth muscle cells (SMCs) to confluency on POMA-FN coverslips to capture their secreted ECM (Figure 4B). SMCs were chosen as ECM production cells, since they expressed the highest amount of *EMILIN1* and *FBN1* compared to other cell types (Supplemental Figure 5A). A culture period of 6 days and a cell density of 150,000 was found to be the ideal combination

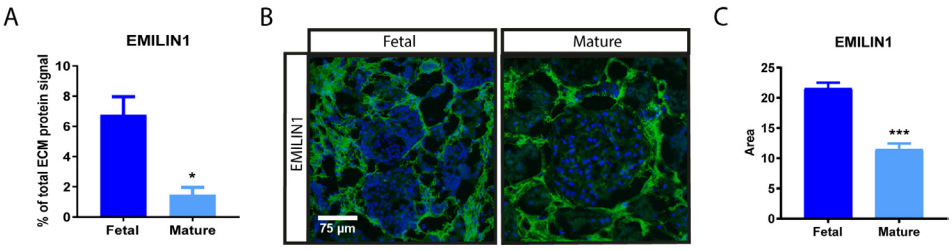

Figure 3. Validation of selected extracellular matrix protein. (A) EMILIN1 signal identified with mass-spectrometry (MS) within fetal and mature renal extracellular matrix (ECM) extracts. N=3 MS analyses, each containing 3-5 human kidney samples per group (fetal or mature). Shown is mean ± SEM; *P<0.05. (B) Representative fluorescence immunohistochemistry images (200x magnification) demonstrate the localization and amount of EMILIN1 (green) in human fetal and mature renal tissue. Scale bar represents 75 µm. (C) Quantification of normalized EMILIN1 area in both fetal and mature human renal samples. N≥25 fluorescent images derived from N=3 samples. Shown is mean ± SEM; ***P<0.001.

between ECM deposition and time (Figure 4C,D). We verified the capacity of the POMA-FN coverslips to reliably anchor the SMC-secreted ECM by collagen type IV staining. When compared to a collagen or gelatin coating, solely a POMA layer, or no coating, the POMA-FN coverslips captured a significantly higher amount of homogeneously distributed ECM, with the rest exhibiting drastic delamination. With regards to a sole FN coating, almost double the amount of ECM was captured on POMA-FN coverslips (Figure 4E-F). SMCs did not grow to confluency on solely POMA or uncoated coverslips after 6 days of culture, as indicated by a significant decrease in F-actin area (Supplemental Figure 5B,D). However, no differences were found in collagen type IV production between SMCs grown on all coatings, as identified by intracellular staining (Supplemental Figure 5C,D). Thus, although production level of collagen type IV by SMCs remained unaffected by the type of coating, the POMA-FN coverslips captured the most intact and highest amount of ECM.

The next step was to deplete EMILIN1 from the anchored cell-secreted ECM. This was accomplished by using short interference RNA (siRNA) mediated silencing in the production cells. FBN1 was used as a second target to deplete from the ECM. QPCR analysis after 3, 6 and 9 days of culture showed efficient silencing of *EMILIN1* or *FBN1* expression in SMCs treated with a siRNA pool specific for *EMILIN1* (siEMILIN1) or *FBN1* (siFBN1), when compared to cells transfected with a pool of non-targeting siRNA sequences (siSHAM) (Figure 5A,B). The mRNA levels of other EMILIN/multimerin and fibrillin family members were not affected

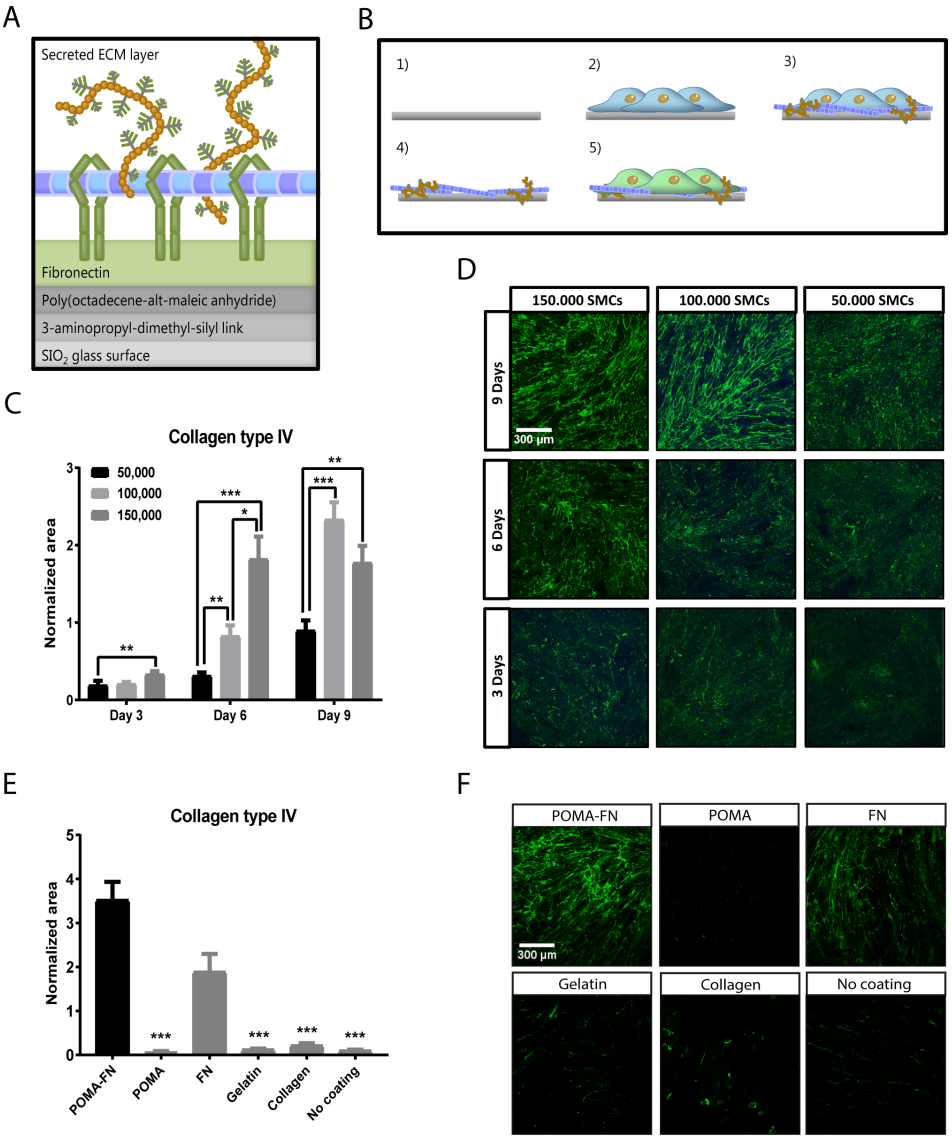

Figure 4. Reliable anchorage of native cell-secreted extracellular matrix to a glass surface. (A) Schematic overview of the chemical layers needed to reliably anchor cell-secreted extracellular matrix (ECM) to a glass coverslip. Fibronectin (FN) is immobilized by a covalent linkage with poly(octadecene-*alt*-maleic anhydride (POMA) on an aminosilanized glass coverslip. Immobilized FN allows stable binding of cell-secreted ECM proteins. (B) Workflow for anchoring smooth muscle cell (SMC) ECM to glass coverslips: 1) FN is covalently immobilized on a POMA coverslip. 2) SMCs are grown to confluency. 3) During this culture time, the SMCs will deposit their own ECM. 4) The SMCs are removed by a decellularization process with NH_4OH, leaving the secreted ECM attached to the POMA-FN coverslip. 5) Evaluation of renal cell function on captured ECM. (C) Quantification of collagen type

(Figure 4 continued) IV area deposited by 50,000, 100,000 or 150,000 SMCs cultured for 3, 6 or 9 days on POMA-FN coverslips. N≥23 fluorescent Z-stacks derived from N=3 samples. Shown is mean ± SEM; **P<0.01, ***P<0.001. (D) Representative immunofluorescence Z-stacks (100x magnification) of anchored collagen type IV on POMA-FN coverslips, deposited by 50,000, 100,000 or 150,000 SMCs cultured for 3, 6 or 9 days. Scale bar represents 300 µm. (E) Quantification of collagen type IV area deposited by 150,000 SMCs cultured for 6 days on coverslips coated with POMA-FN, POMA, FN, gelatin or collagen or no coating. N≥19 fluorescent Z-stacks derived from N=4 samples. Shown is mean ± SEM; ***P<0.001. (F) Representative immunofluorescence Z-stacks (100x magnification) of anchored collagen type IV deposited by 150,000 SMCs cultured for 6 days on coverslips coated with POMA-FN, POMA, FN, gelatin or collagen or no coating. Scale bar represents 300 µm.

by either siEMILIN1 or siFBN1 when compared to siSHAM, indicating that the siRNA-mediated silencing was specific for *EMILIN1* and *FBN1* (Supplemental Figure 6A-H). Importantly, genes encoding for major ECM components, such as *COL1A1*, *COL4A1*, *ELN* and *LAMA5* were not affected by *EMILIN1* knockdown, implying that the absence of EMILIN1 did not greatly alter ECM composition (Supplemental Figure 7A-D). Immunofluorescence confirmed a significant loss of EMILIN1 or FBN1 expression in siEMILIN1 or siFBN1 transfected SMCs when compared to siSHAM cells, with no variance in cellular F-actin area (Figure 5C-H). Western blot analysis for EMILIN1 verified the loss of protein expression (Supplemental Figure 8A,B). Additionally, SMC secreted ECM was significantly depleted of EMILIN1 or FBN1 and successfully anchored to the POMA-FN coverslips, with no difference in extracellular collagen type IV deposition (Figure 5I-N).

Depletion of EMILIN1 from the extracellular matrix promotes renal epithelial cell migration, but does not affect cell growth

Previous studies have shown that EMILIN1 is important for migration and growth of various cell types through the interaction of its gC1q domain with integrins[21-24]. Therefore, we studied the migration and growth of renal epithelial cells cultured on an ECM layer depleted of EMILIN1. Depletion of either EMILIN1 or FBN1 from the ECM did not affect proliferation, viability and DNA abundance of renal epithelial cells, when compared to cells cultured on siSHAM ECM (Figure 6A-C). Next, the migration capacity was assessed using live-cell tracking. A significant increase in velocity and distance covered by renal epithelial cells cultured on siEMILIN1 ECM was observed when compared to cells cultured on siSHAM ECM (Figure 6D-F, J-K). This positive effect was absent in renal epithelial cells cultured on siFBN1 ECM (Figure 6G-J, L), hinting towards a link between enhanced renal cell migration and disruption of gC1q-intergrin interaction.

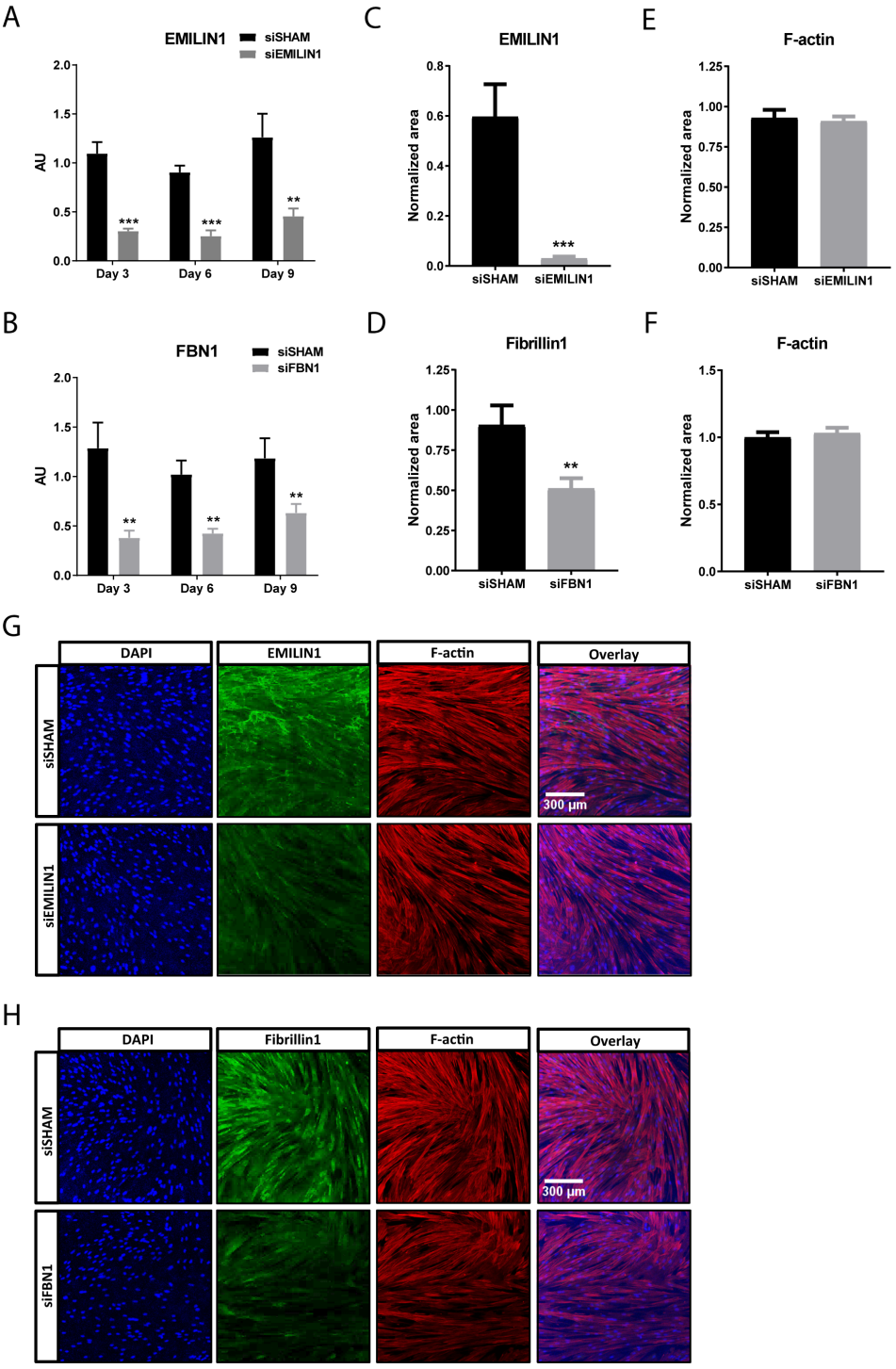
A
EMILIN1
siSHAM
siEMILIN1
AU
2.0
1.5
1.0
0.5
0.0
***
***
**
Day 3
Day 6
Day 9
C
EMILIN1
Normalized area
0.8
0.6
0.4
0.2
0.0
***
siSHAM
siEMILIN1
E
F-actin
Normalized area
1.25
1.00
0.75
0.50
0.25
0.00
siSHAM
siEMILIN1
B
FBN1
siSHAM
siFBN1
AU
2.0
1.5
1.0
0.5
0.0
**
**
**
Day 3
Day 6
Day 9
D
Fibrillin1
Normalized area
1.25
1.00
0.75
0.50
0.25
0.00
**
siSHAM
siFBN1
F
F-actin
Normalized area
1.5
1.0
0.5
0.0
siSHAM
siFBN1
G
DAPI
EMILIN1
F-actin
Overlay
siSHAM
siEMILIN1
300 µm
H
DAPI
Fibrillin1
F-actin
Overlay
siSHAM
siFBN1
300 µm

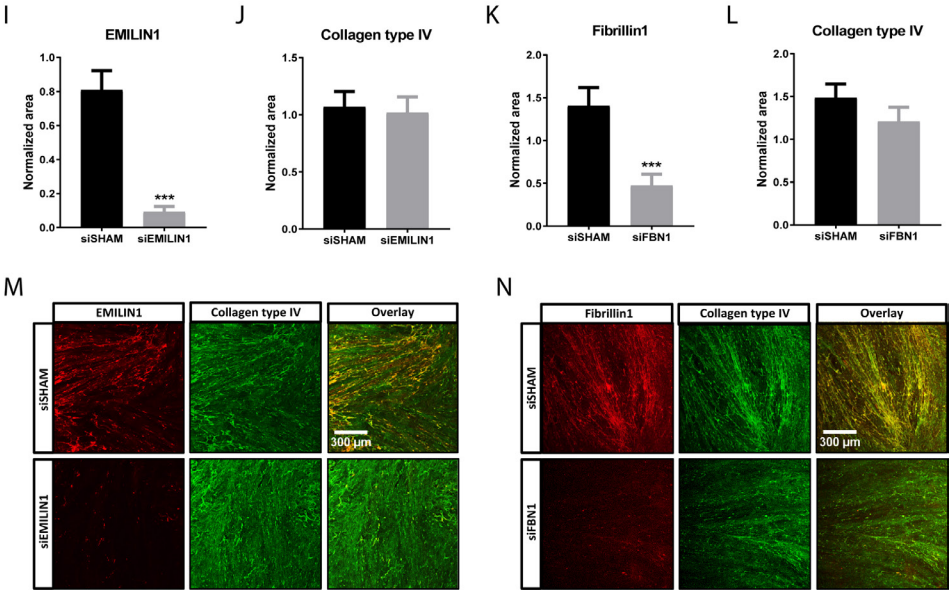

Figure 5. *EMILIN1* and *FBN1* targeting siRNAs induce significant silencing intracellular and on secreted extracellular matrix level. Quantitative polymerase chain reaction (qPCR) of *EMILIN1* (A) and *FBN1* (B) in smooth muscle cells (SMCs) transfected with *EMILIN1*-targeting siRNA (siEMILIN1), *FBN1*-targeting siRNA (siFBN1) or non-targeting siRNA (siSHAM), cultured for 3, 6 or 9 days on POMA-FN coverslips. Shown are target gene/housekeeping gene (*β-actin*) ratios (AU). Control (non-transfected SMCs) values are set to 1 (not shown). N≥5 qPCRs. Shown is mean ± SEM. **P<0.01, ***P<0.001. Quantification of intracellular EMILIN1 (C), Fibrillin1 (D) or F-actin (E, F) area in confluent SMCs transfected with siSHAM, siEMILIN1 or siFBN1 cultured for 6 days on POMA-FN coverslips. Control (non-transfected SMCs) values are set to 1 (not shown). N≥29 fluorescent Z-stacks derived from N=3 samples. Shown is mean ± SEM; **P<0.01, ***P<0.001. Representative immunofluorescence Z-stacks (100x magnification) of SMCs transfected with siSHAM, siEMILIN1 (G) or siFBN1 (H) cultured for 6 days on POMA-FN coverslips and stained for F-actin (red), EMILIN1 or Fibrillin1 (green) and DAPI (blue). Scale bar represents 300 µm. Quantification of EMILIN1 (I), Fibrillin1 (J) or collagen type IV (K, L) area in the extracellular matrix (ECM) deposited by SMCs transfected with siSHAM, siEMILIN1 or siFBN1 cultured for 6 days on POMA-FN coverslips. Control (non-transfected SMCs) values are set to 1 (not shown). N≥29 fluorescent Z-stacks derived from N=3 samples. Shown is mean ± SEM; ***P<0.001. Representative immunofluorescence Z-stacks (100x magnification) of the ECM deposited by SMCs transfected with siSHAM, siEMILIN1 (M) or siFBN1 (N) cultured for 6 days on POMA-FN coverslips and stained for collagen type IV (green) and EMILIN1 or Fibrillin1 (red). Scale bar represents 300 µm.

EMILIN1 is important for binding of renal epithelial cells to the extracellular matrix and for focal adhesion assembly

Integrins form part of large dynamic protein complexes that connect the cell cytoskeleton to the ECM, called focal adhesion complexes. We assessed whether EMILIN1 in the ECM is required for assembly of focal adhesion complexes during

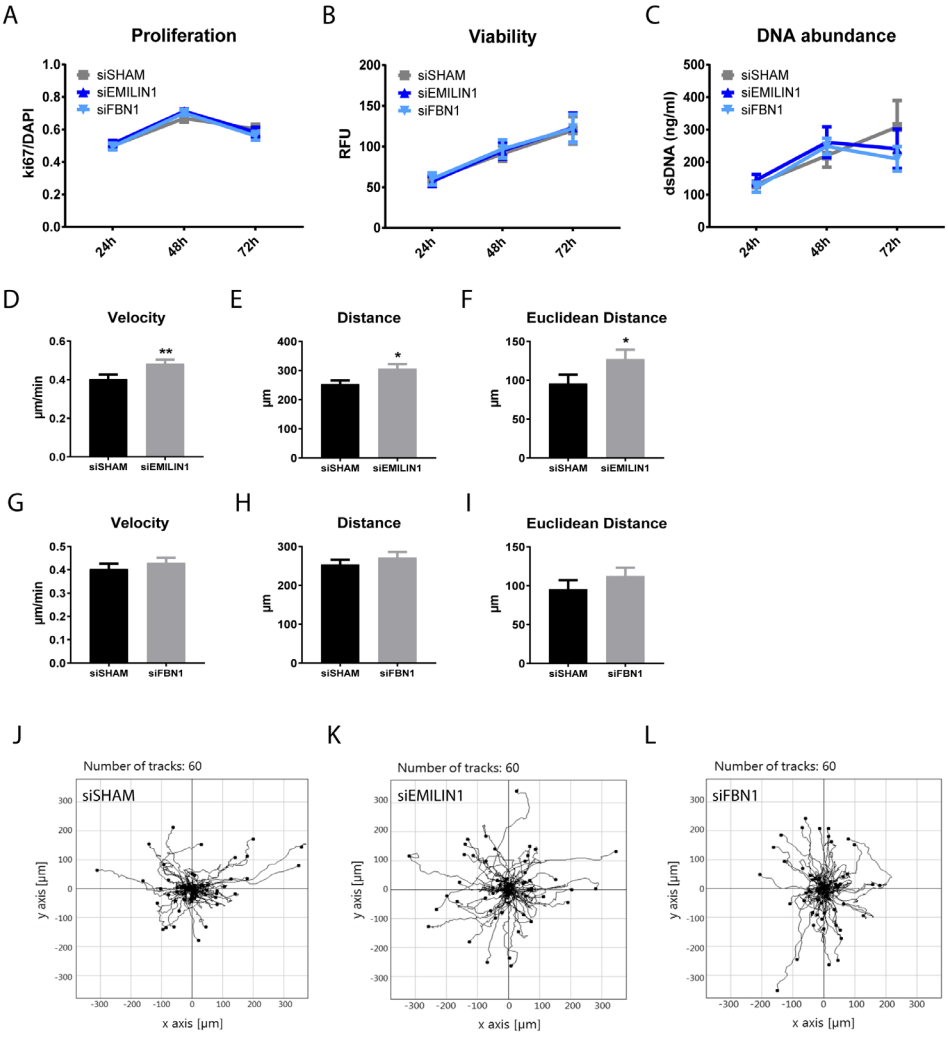

Figure 6. Effect of EMILIN1 or Fibrillin1 depletion from the extracellular matrix on renal epithelial cell growth and migration. (A) ki67/DAPI ratio as measure for cell proliferation at 24, 48 or 72 hours post seeding of HRPTECs cultured on siSHAM, siEMILIN1 and siFBN1 extracellular matrix (ECM). N≥26 fluorescent images derived from N=3 samples. Shown is mean ± SEM. (B) Viability measurements using the PrestoBlue assay after 24, 48 or 72 hours post seeding of HRPTECs on siSHAM, siEMILIN1 and siFBN1 ECM. N=6 assays. Shown is mean ± SEM. (C) DNA abundance measurements using the PicoGreen assay after 24, 48 or 72 hours post seeding of HRPTECs on siSHAM, siEMILIN1 and siFBN1 ECM. N=5 assays. Shown is mean ± SEM. Quantified live cell migration assay results showing velocity and covered and Euclidean distance of HK2 cells on either siEMILIN1 (D-F) and siFBN1 (G-I) ECM compared to cells on siSHAM ECM. The cell migration on the ECM layer was tracked overnight with a confocal microscope. N=60 individual cells tracked derived from N=4 assays. Shown is mean ± SEM; *P<0.05, **P<0.01. Migration plots showing multiple tracks of individual HK2 cells on siSHAM (J), siEMILIN1 (K) and siFBN1 ECM (L).

the initial binding of renal epithelial cells to the ECM. Depletion of EMILIN1 from the ECM caused defects in the initial assembly of the focal adhesion-structural protein paxillin. Renal cells cultured for only 2 hours on siEMILIN1 ECM exhibited a significant decrease of paxillin area when compared to cells cultured on siSHAM ECM, indicating a reduced spreading ability (Figure 7A-B). Cells cultured on siFBN1 ECM for 2 hours did not show a decrease in paxillin area (Supplemental Figure 9A-B), verifying that the putative effect is specific for EMILIN1 depletion. Next, we assessed the capacity of renal epithelial cells to form a tight monolayer when cultured on siEMILIN1 ECM. The tight junction protein ZO-1 was used to measure barrier formation. Intracellular staining revealed no changes in ZO-1 protein expression in renal cell cultured for 48 hours on siEMILIN1 ECM compared to siSHAM ECM, indicating that these cells are capable of creating a connected monolayer (Figure 7C). However, silencing of EMILIN1 in the ECM appeared to alter the junctional pattern of ZO-1 into a linear instead of zigzagged configuration (Figure 7E). A significant decrease in F-actin area was also observed in cells grown on siEMILIN1 ECM compared to siSHAM ECM (Figure 7D). Immunofluorescence visualization of F-actin revealed that formation of stress fibers was affected (Figure 7E). The assembly of focal adhesion complexes in confluent renal epithelial monolayers was impaired as well. Intracellular staining revealed that EMILIN1-depleted ECM significantly inhibited formation of paxillin points and stress fibers in confluent renal epithelial monolayers, since less paxillin colocalized with F-actin (Figure 7F-G). Cells cultured to confluency on FBN1-depleted ECM did not exhibit a significant reduction in colocalization of paxillin with F-actin (Supplemental Figure 9C-D), further verifying that the impairment of focal adhesion assembly is specific for EMILIN1 depletion. Actin cytoskeleton remodeling upon integrin mediated focal adhesion formation is regulated by RhoA signaling. Thus, we assessed the RhoA activity in renal epithelial cells grown on siEMILIN1 ECM for 48 hours when compared to cells grown on siSHAM ECM. In concordance with our previous results, EMILIN1 silencing in the ECM significantly reduced RhoA activation in renal cells (Figure 7H). All together, these findings indicate that EMILIN1 in the ECM is important for assembly of focal adhesion complexes and subsequent actin-cytoskeleton adaptation in renal epithelial cells.

Discussion

This study presents to date the first catalogue that compares the human fetal and mature renal ECM. A total of 99 different ECM proteins was detected by

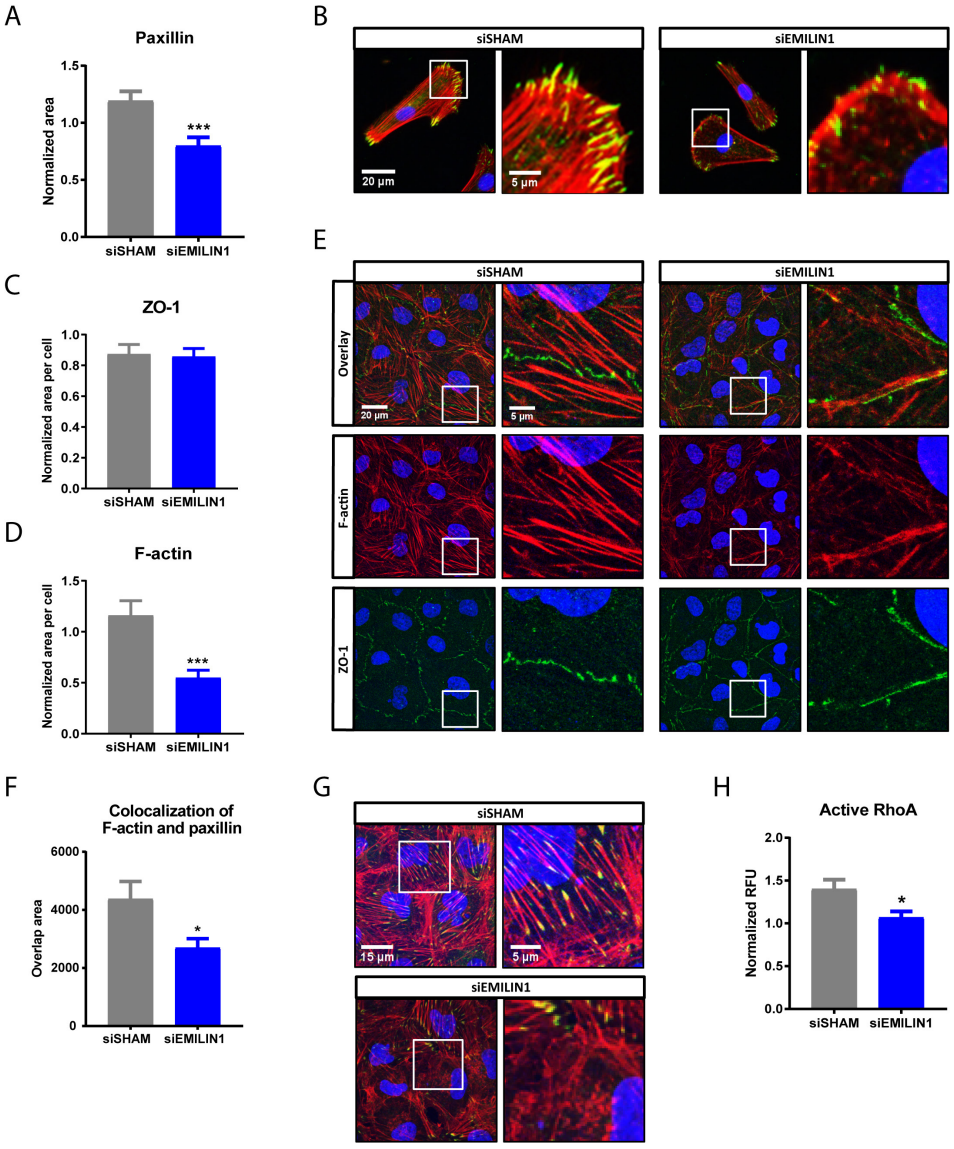

Figure 7. Depletion of EMILIN1 from the extracellular matrix layer reduces paxillin area and stress fibers in renal epithelial cells. (A) Quantified results showing the paxillin area in HRPTECs on siSHAM or siEMILIN1 extracellular matrix (ECM) during initial binding to the ECM (cultured for 2 hours). N=30 fluorescent images derived from N=3 samples. Shown is mean ± SEM; ***P<0.001. (B) Representative immunofluorescence images (400x magnification) of HRPTECs after 2 hours of binding on siSHAM or siEMILIN1 ECM and stained for paxillin (green), F-actin (red) and DAPI (blue). Scale bar represents 20 µm (overview image, left) and 5 µm (zoomed-in image, right). Quantified results showing the ZO-1 (C) and F-actin area (D) in HK2 cells cultured to confluency on siSHAM or siEMILIN1 ECM. N=20 fluorescent Z-stacks derived from N=4 samples.

(Figure 7 continued) Shown is mean ± SEM; ***P<0.001. (E) Representative immunofluorescence Z-stacks (630x magnification) of HK2 cells cultured to confluency (cultured for 48 hours) on siSHAM or siEMILIN1 ECM and stained for ZO-1 (green), F-actin (red) and DAPI (blue). Scale bar represents 20 µm (overview image, left) and 5 µm (zoomed-in image, right). (F) Colocalization of paxillin and F-actin in HK2 cells cultured to confluency on siSHAM or siEMILIN1 ECM. N≥25 fluorescent Z-stacks, from N≥5 samples. Shown is mean ± SEM; *P<0.05. (G) Representative immunofluorescence Z-stacks (630x magnification) of HK2 cells cultured to confluency on siSHAM or siEMILIN1 ECM and stained for paxillin (green), F-actin (red) and DAPI (blue). Colocalization is displayed as yellow. Scale bar represents 15 µm (overview image, left) and 5 µm (zoomed-in image, right). (H) RhoA activation levels in HK2 cells cultured for 48 hours on siSHAM or siEMILIN1 ECM. N=5 assays. Shown is mean ± SEM; *P<0.05.

proteomic analysis of which the majority form an overlapping core, but also includes many renal ECM proteins that are enriched in either the fetal or mature condition.

Using immunohistochemistry, we confirmed the identification of EMILIN1 and FBN1 as key proteins in the renal ECM. EMILIN1 mainly localizes to the tubulointerstitial space, but is also classified as a structural glomerular protein by Lennon *et al*[10]. However, they solely focused on identifying glomerular proteins and did not analyze the remainder from their glomerular enrichment strategy. Immunolocalization of FBN1 showed its presence in both glomeruli and tubulointerstitial space, which is in concordance with Lennon *et al*, who classified it as a glomerular basement membrane protein.

Our proteome comparison between the fetal and mature renal ECM has the potential to mark novel molecular players by which the renal ECM can influence cellular behavior. Percentile ranking by LFQ intensity proved effective at finding proteins enriched in the fetal ECM. One striking difference between the fetal and mature renal ECM proteome is the enrichment of elastic fiber components in the fetal ECM, including fibrillin1, MFAP2 and elastin. Particularly the glycoprotein EMILIN1 was abundant in the fetal ECM. Many other ECM proteins differ significantly between fetal and mature tissue, however most of them are present in low quantities in the renal ECM (<2%) and are therefore less likely to play a fundamental role (for example EMILIN3).

The importance of EMILIN1 has been previously studied using EMILIN$^{-/-}$ mice, which display several vascular defects, including impaired lymph drainage, increased leakage and elevated blood pressure associated with narrower vessels[26-29]. The latter is due to an increased presence of transforming growth factor β (TGF-β), since EMILIN1 prevents TGF-β processing[27-29]. In aortic valves, increased

TGF-β signaling due to EMILIN1 deficiency causes elastic fiber fragmentation and subsequent aortic valve disease[34]. Both these mutant mice and aged mice exhibit ECM stiffness, fibrosis, increased collagen expression and cell adhesion and fibronectin alterations[35]. This suggests that loss of EMILIN1 and associated phenotype is linked to a mature state, which is in concordance with our proteomic data. Despite several studies described the function of EMILIN1, a possible renal function remains unclear.

Lack of EMILIN1 is associated with altered vascular and lymphatic cell anchorage, patterning and morphology[25,26]. Previous studies have reported that the gC1q domain of EMILIN1 is responsible for promoting cell adhesion[23,24,36]. Our study showed that renal epithelial cells exhibit a weaker adhesion pattern on EMILIN1-depleted ECM, indicated by fewer focal adhesion points. Focal adhesions provide linkage points between the cell cytoskeleton and the ECM, playing a central role in adhesion[37]. Renal epithelial cells grown on EMILIN1-depleted ECM exhibit a low number of actin stress fibers and less paxillin, a focal adhesion adaptor protein that localizes to large focal contacts at the tips of these fibers. More evidence for the role of EMILIN1 in renal cell adhesion comes from the activation of signaling molecule RhoA, that is recruited and activated upon integrin-ECM binding and leads to maturation of focal adhesions[37]. Less RhoA was activated in renal epithelial cells grown on EMILIN1-depleted ECM, indicating reduced stabilization of focal structures. Furthermore, the junctional pattern of ZO-1 in these renal cells appeared linear instead of zigzagged. High bioavailability of ZO-1 at tight junctions induces zigzag patterning and increases the overall permeability of epithelia[38]. Actin filaments terminate at tight junctions, thereby linking them with focal adhesions[39]. This suggests that defects in focal adhesion assembly by EMILIN1 depletion in the ECM can result in F-actin stress fibre dysregulation and subsequent reduction of functional tight junctions, affecting renal epithelial barrier function. Indeed, previous studies showed that ZO-1 interaction with F-actin at tight junctions is important for epithelial polarization and formation of single lumens[40]. Altogether, our study indicates that EMILIN1 could be a promising candidate for implementation in renal scaffolds for the enhancement of cell attachment and barrier formation.

Our findings are not in line with previous studies, in which actin organization in cells attached to EMILIN1 was described to be organized along the cell periphery without any apparent focal contacts[24,36]. More in depth experiments have shown that in these cells, the gC1q domain of EMILIN1 promotes cell adhesion by

interacting with α4/α9/β1 integrins[23,24,36]. The reported synovial sarcoma cells and T lymphocytes use α4β1 integrins for gC1q-mediated cell attachment, whereas lymphatic endothelial cells (LECs) and microvascular ECs attachment to EMILIN1 is mediated by α9β1 integrins[23,24]. These reports suggest that different cell types express a specific selection of integrins to react to environmental stimuli.

β1 is the most widely expressed renal integrin subunit and is responsible for interactions with the cell cytoskeleton via binding with several focal adhesion complex proteins[41,42]. Different α subunits have been demonstrated to be expressed by renal tissue, which all can form heterodimers with β1: α1, α2, α3, α5, α6, α8 and αv[41,42]. The renal cells used in our migration and confluent adhesion assays showed high expression of the integrin subunits α3, α5, αv, and β1, modest levels of α2, α4, α6 and non-detectable expression of α9 (data not shown). EMILIN1 may exerts its effect in renal cells through another αβ1 integrin heterodimer than the α4/α9/β1-gC1q interaction described, which might explain the distinct effect we found of EMILIN1 on renal epithelial cell adhesion strength.

The dynamic assembly and disassembly of focal adhesions play a central role in cell migration and proliferation. EMILIN1 also plays an important role in these processes: fibroblasts, keratinocytes and LECs obtained from EMILIN1$^{-/-}$ mice retain a high proliferation rate compared to wildtype cells[22,23]. This reduction in proliferation is associated with the gC1q–α9 integrin interaction, which also stimulates LEC migration[23]. Furthermore, the gC1q–α4 integrin interaction promotes haptotactic directional migration of trophoblasts[36], indicating that EMILIN1 can promote cell proliferation and migration by interacting with α4/α9/β1 integrins.

In contrast, the present study shows that EMILIN1-deficient ECM does not influence proliferation of renal epithelial cells and absence of EMILIN1 stimulates renal epithelial cell migration. Hence, the effect of EMILIN1 seems to be cell type specific. Indeed, Colombatti and colleagues indicated that the effect of EMILIN1 on cell adhesion and migration can be either enhancing or reducing depending on the cell type investigated[43], which might be linked to different integrin expression profiles.

Strong adhesion through focal adhesion formation stabilized by stress fibers is considered to be unfavorable for cell detachment needed for migration[44]. In 1979, Couchman and Rees already made the observation that fibroblasts displayed little to no focal adhesions during the initial period of rapid migration. Focal adhesions and associated ventral stress fibers only developed when migration slowed

down[45]. This observation implies that focal adhesion disassembly facilitates rapid migration. Indeed, we observed that renal epithelial cells migrate faster and cover more distance when less EMILIN1 is present in the ECM. Therefore, this rapid migration pattern is most likely stimulated by the reduction of focal adhesions and stress fibers seen in these renal cells as well.

The motility phenotype of cells also depends on which integrins are available on the cell membrane. For example, previous research has observed that the α4/α9/β1-gC1q interaction encourages a cellular phenotype that lacks stress fibers and promotes lamellipodia formation, thereby facilitating cell spreading[23,24,36]. The α4/α9 subfamily is a specific subset of α subunits based on evolutionary relationships, that share a high sequence similarity and ligand specificities[46]. In contrast, the present study showed that lack of EMILIN1 interaction stimulates cell migration. Renal cells express other α subunits in high quantities[41,42]; suggesting that they likely express subunits that stabilize focal adhesions. For example, the renal cells used in our migration assay highly express integrin subunits α5 and β1, which as a heterodimer is known to mediate stabilization of mature focal adhesions[47].

Apparent differences between the renal epithelial cell behavior seen in response to EMILIN1 in this study and the results of earlier studies may also be due to differences in study design. We cultured our renal cells on a complex ECM network depleted from a protein of interest from the beginning, rather than culturing on a coating of one specific ECM protein. It is inevitable that this rich ECM background from the start will have an influence on focal adhesion composition, mostly the integrin expression profile, and subsequent cell behavior. This environment mimics more the *in vivo* ECM complexity, even though it lacks a 3D configuration. Nevertheless, this 2D ECM model is a valuable resource for additional investigation and thereby aids in the search for promising ECM components to implement in 3D culture.

In conclusion, based on our proteome analysis we provide evidence for EMILIN1 as a promising candidate for implementation in renal scaffolds as a bioactive factor. Here, it would most likely stimulate an adhesive phenotype of the embedded renal cells. Matrices containing organ specific ECM cues to direct cell adhesion may ultimately allow the generation of whole 3D kidney constructs for implantation.

Acknowledgements

We would like to thank the Proteomics Center of the Erasmus University Medical

Center for excellent technical support.

This work was supported by the Ministry of Education, Culture and Science (Gravitation Program 024.003.013), the Netherlands Foundation for Cardiovascular Excellence [to C.C.], NWO VIDI grant [no. 91714302 to C.C.], the RM fellowship grant of the UMC Utrecht [to C.C.] and the Netherlands Cardiovascular Research Initiative: An initiative with support of the Dutch Heart Foundation [CVON2014-11 RECONNECT to C.C., M.V. and D.D.].

Experimental procedures

Antibodies

Polyclonal antibodies used were against EMILIN1 (HPA002822; Sigma-Aldrich), fibrillin1 (HPA021057; Sigma-Aldrich) and collagen type IV (AB769; Merck Millipore). Monoclonal antibodies used were against ki-67 (RM-9106-R7, ThermoFisher), paxillin (ab32084, Abcam), ZO-1 (610967; BD Biosciences) and β-actin (ab8226, Abcam). Rhodamine phalloidin conjugate was used for staining F-actin (R415; ThermoFischer). Secondary antibodies used for immunohistochemistry were goat-anti-rabbit Alexa Fluor 488 (A11034; ThermoFisher), donkey-anti-rabbit Alexa Fluor 568 (A10042; ThermoFisher), donkey-anti-goat Alexa Fluor 488 (A11055; ThermoFisher) and goat-anti-mouse Alexa Fluor 488 (A11029; ThermoFisher). Secondary antibodies used for Western blot were goat-anti-rabbit IRDye 800CW (926-32211; Li-cor Biosciences) and goat-anti-mouse IRDye 680RD (926-68070; Li-cor Biosciences).

Human samples

Normal human renal tissue from healthy adult donors was obtained from the Erasmus MC Tissue Bank (n=13; gender: 8 male, 5 female; age [mean ± SD]: 55 ± 24 years). Normal human kidneys from healthy fetal donors were received from the department of Molecular Cell Biology from the Leiden UMC (n=13; age range: 18-24 weeks of pregnancy).

Cell culture

Primary aortic smooth muscle cells (aSMCs) were purchased from Lonza (CC-2571) and maintained in Smooth Muscle Growth Medium (CC-3182; Lonza). Primary Human Renal Proximal Tubular Epithelial Cells (HRPTECs) were purchased from ScienCell (#4100) and maintained in Epithelial Cell Medium (#4101; ScienCell). Immortalized Human Kidney[48] (HK2) cells were maintained in RPMI-1640 medium with glutamine (61870010; ThermoFisher), supplemented with 10% (vol/vol) FCS (Biowest) and 100 UmL^{-1} PS (Gibco).

All cells were cultured at 37°C in a humidified atmosphere containing 5% CO2. Primary cell lines were used between passages 3 and 8.

Tissue decellularization and ECM homogenization

Tissue decellularization was used to reduce the complexity of samples by removing cellular components and thereby enriching for ECM proteins. Renal tissue was cut into 4 pieces of uniform thickness and one piece was fixed and saved for hematoxylin and eosin (H&E) staining to asses tissue morphology. The other pieces were decellularized overnight in 1% SDS under constant rotation. Next, a shorter decellularization step was performed for one hour with 1% Triton X-100 under constant rotation. Tissue was washed thoroughly in PBS for 2 hours under constant rotation to remove as much residual detergent as possible before proceeding with tissue lysis. One decellularized piece was fixed and saved for H&E staining to validate the removal of all cellular content and assess preservation of the ECM architecture. Tissue was homogenized in lysis buffer (10mM Tris [pH 7.4], 100mM NaCl, 0.1% SDS, 0.5% Na deoxycholate, 1% Triton X-100, 1mM EGTA, 1mM EDTA, 10% glycerol, 1mM NaF, 1mM Na orthovanadate, supplemented with a protein inhibitor cocktail (cOmplete, Mini Protease Inhibitor Tablets)) using an Ultra-Turrax (IKA) and lysed for an hour at 4°C under rotation. After homogenizing a second time, tissue lysates were centrifuged [10 min, 1000xg, 4°C] and supernatant was saved at -80°C until further processing.

MS data acquisition and analyses

ECM extracts were separated by SDS-PAGE. Three gels were loaded with a fetal and mature ECM extract of the same protein concentration, each containing 3-5 pooled kidney samples that were randomly selected (mixed age and gender). The separated samples were prepared for LC-MS/MS by the Proteomics Centre of the Erasmus MC as follows. 1D SDS-PAGE gel was visualized with a Coomassie staining and lanes were cut into 2-mm slices using an automatic gel slicer and subjected to in-gel reduction with dithiothreitol, alkylation with iodoacetamide and digestion with trypsin (Promega, sequencing grade), essentially as described previously[49]. Supernatants were stored in glass vials at -20°C until LC-MS. Nanoflow liquid chromatography-tandem mass spectrometry (LC-MS/MS) was performed on an 1100 series capillary LC system (Agilent Technologies) coupled to an LTQ-Orbitrap XL mass spectrometer (Thermo) operating in positive mode and equipped with a nanospray source, essentially as previously described[50]. Peptide mixtures were trapped on a ReproSil C18 reversed phase column (Dr Maisch GmbH; column dimensions 1.5 cm × 100 µm, packed in-house) at a flow rate of 8 µl/min. Peptide separation was performed

on ReproSil C18 reversed phase column (Dr Maisch GmbH; column dimensions 15 cm × 50 µm, packed in-house) using a linear gradient from 0 to 80% B (A = 0.1 % formic acid; B = 80% (v/v) acetonitrile, 0.1 % formic acid) in 70 min and at a constant flow rate of 200 nl/min using a splitter. The column eluent was directly sprayed into the ESI source of the mass spectrometer. Mass spectra were acquired in continuum mode; fragmentation of the peptides was performed in data-dependent mode.

Raw data files were analyzed using the MaxQuant software as described by Cox *et al*[51]. Proteins that were identified in at least two of the three fetal or mature replicates were used for further analysis. By crossreferencing with the Human Matrisome Project[8,9], we categorized the obtained proteins into ECM core and associated proteins. The label free quantification (LFQ) module was used to quantify the relative abundances of fetal and mature renal ECM proteins.

POMA-fibronectin coverslips preparation

Circular glass coverslips were cleaned to remove organic residues with a quick rinse in acetone and sonication in 50% methanol for 20 min and in chloroform for another 20 min. Coverslips were oxidized with piranha solution [70% sulphuric acid (99% w/v) and 30% hydrogen peroxide (35% w/v)] for 20 min and sonicated in chloroform for 10 min. To ensure complete removal of the piranha solution, coverslips were washed by sonication with ultrapure water for 5 min and with chloroform for another 5 min in an alternating fashion and repeated for at least 5 times[32]. Freshly oxidized coverslips were aminosilanized with a 2% (3-Aminopropyl)triethoxysilane (APTES, Sigma-Aldrich) solution in 95% ethanol for 10 min. Excess APTES was removed by 4 washings with 95% ethanol for 5 min. The APTES layer was cured at 120°C for 30 min[31,33]. In order to covalently bind fibronectin (FN), the coverslips were coated with a thin layer of 0.16% (w/v) poly(octadecene-*alt*-maleic anhydride (POMA; Sigma-Aldrich) solution in tetrahydrofuran (Sigma-Aldrich) using a spin-coater (Brewer Science) [1500 rpm s^{-1}, 30 sec, 4000 rpm]. The polymer coating was cured at 120°C for 2 hours[31,33]. The POMA-coated coverslips were stored in the dark for up to 3 months. Heat activation of the anhydride moieties needed to be repeated if coverslips were stored for longer than 2 weeks. Prior to use in cell culture, the POMA-coated coverslips were sterilized under UV-light for 30 min. Lastly, the coverslips were coated with sterile 50 µg/mL fibronectin (FN; Roche) in PBS for 1 hour at 37°C to allow stable anchorage of cell secreted ECM. POMA-FN coverslips were rinsed twice with sterile PBS to remove excess FN and to achieve a homogeneous coating before seeding with cells[33].

Anchored cell-secreted ECM layer preparation

To create cell derived ECM layers anchored to POMA-FN coverslips, SMCs were seeded at 40,000 cells per cm^2. The cultures were decellularized at day 6 using warm 20mM NH_4OH by gentle agitation for 15 min, which disrupts lipid interactions but preserves protein interactions. The resulting ECM layers were treated with 10% DNase I (Qiagen) for 10 min to remove DNA traces. Cell remnants were removed by washing thrice with ultrapure water and twice with PBS. The decellularized ECM layer was immediately re-seeded with renal cells or fixated for immunofluorescence analysis. The presence of nucleic acids was assessed with DAPI staining. After the decellularization procedure, cellular components such as DNA remnants were barely detected.

Immunofluorescence

Sucrose cryoprotected renal tissue was embedded in an OCT compound (TissueTek) and stored at -80°C. Frozen samples were cut into 7-µm-thick sections, fixated with acetone and stained with H&E or used for immunofluorescence stainings. Cells or ECM attached to coverslips were washed with PBS and fixed with 4% paraformaldehyde for 30 min. Blocking of tissue, cells or ECM occurred with 1% BSA/PBS for 30 min before incubation with primary and secondary antibodies for 1 hour at room temperature. Cells and tissue were also permeabilized with 0.5% Triton X-100/PBS for 30 min before antibody incubation. DAPI was used as a nuclear counterstaining. Images of fluorescent-labeled markers were obtained with a Leica SP8X confocal microscope. For quantification of the total area, 3D images were obtained by scanning multiple XY planes in the Z direction. Serial pictures along the Z-axis were combined to create a stacked XY image that was further analyzed using ImageJ 1.47v. Single XY pictures were taken with the Olympos BX51 upright microscope.

Quantitative PCR

Total RNA was isolated from SMCs using the ISOLATE II RNA mini kit (Bioline) according to manufacturer's instructions and from human renal tissue using TRIzol. Briefly, tissue was homogenized in 1mL TRIzol using an Ultra-Turrax (IKA) on ice. 200µl chloroform was added per 1mL TRIzol, mixed and incubated for 3 minutes at room temperature. The aqueous phase was separated from the phenol by centrifugation [15 min, 12,000xg, 4°C] and transferred to a new tube. RNA was precipitated by mixing the aqueous phase with 600µl isopropanol and 1µl of glycogen (20mg/mL). After incubation for 10 minutes at room temperature, the precipitate was pelleted by centrifugation [10 min, 12,000xg, 4°C]. The pellet was washed with 600µl ice-cold 75% ethanol and pelleted again [5 min, 7,500xg,

4°C]. The pellet was dried at room temperature and the RNA was precipitated over night at -20°C to increase yield by mixing the pellet with 200µl Nuclease-free water (Qiagen), 20µl 3M Sodium acetate and 600µl 75% ice-cold ethanol. The precipitate was pelleted by centrifugation [30 min, 15,000xg, 4°C]. The pellet was washed with 200µl ice-cold 75% ethanol and pelleted again [5 min, 15,000xg, 4°C]. The RNA pellet was dried at room temperature and dissolved in 50µl Nuclease-free water (Qiagen). RNA concentrations were assessed with a nanodrop spectrophotometer. Total RNA was reverse-transcribed using the SensiFAST cDNA synthesis kit (Bioline) according to manufacturer's instructions. Gene expression was determined using quantitative real-time PCR (qPCR) by loading samples in duplicate on a CFX96 Real-Time PCR Detection System (Biorad). The primer sequences used are listed in Supplemental Table 2. Data was normalized for the expression of housekeeping gene *β-actin*.

Short interference RNA

EMILIN1 or *FBN1* knockdown in SMCs was achieved by using a mix of 4 complementary siRNA sequences directed against the mRNA of either *EMILIN1* or *FBN1* (ThermoScientific). As a negative control, cells were either untreated or transfected with a mix of 4 non-targeting siRNA sequences (ThermoScientific). The siRNA sequences used are listed in Supplemental Table 3.

Western blot

SMCs received a PBS wash twice and were harvested in lysis buffer (50mM Tris [pH 8.0], 1% NP-40, 150mM NaCl, 0.1% SDS, 0.5% Na deoxycholate, supplemented with a protein inhibitor cocktail (cOmplete, Mini Protease Inhibitor Tablets)). The lysates were incubated on ice for 20 minutes, centrifuged [12 min, 13,000xg 4°C] and the supernatant was stored at -80°C until further processing. Total protein concentration was determined by using the Pierce® BCA Protein Assay Kit (Thermo Scientific). Lysates were denaturated in Laemmli buffer (60mM Tris [pH 6.8], 2% SDS, 10% glycerol, 5% β-mercaptoethanol, 0.01% bromophenol blue) at 90 °C for 5 minutes. Equal amounts of sample were separated by electrophoresis on a 10% SDS-PAGE gel and transferred onto a nitrocellulose membrane (Pierce) at 4°C overnight. Membranes were blocked and probed with primary antibodies. Protein bands were visualized with Li-Cor secondary antibodies and detection system (Westburg) according to manufacturer`s instructions.

Live-cell tracking

POMA-FN coverslips were placed into a 6-wells plate containing a No. 0 coverslip

glass bottom (P06G-0-20-F, MatTek) to allow live-cell tracking. SMCs were transfected with siRNA after 24 hours and coverslips were decellularized 6 days post-transfection. Before reseeding with 3,700 HK2 cells per cm^2, HK2 cells were visualized for fluorescent tracking by incubating the cells for 15 min at 37°C in basal RMPI medium containing 4 µM CellTracker Blue CMAC dye (ThermoFisher). 24 hours post-seeding, single cell migration was tracked overnight at 37°C in a humidified atmosphere containing 5% CO2 using a Leica SP8X confocal microscope. Per condition, three positions were selected and imaged every 15 min for 12 hours. Obtained videos were analyzed with ImageJ (v1.47) Manual Tracking and Chemotaxis Tool.

In vitro assays

Prior to all *in vitro* assays, SMCs were seeded on POMA-FN coverslips and transfected with siRNA after 24 hours. The coverslips were decellularized 6 days post-transfection and reseeded with renal cells.

Cell adhesion assay. Captured ECM was reseeded with 6,500 HRPTECs per cm^2 for testing initial binding to the ECM or 25,000 HK2 per cm^2 for measuring cell-ECM adhesion of a confluent monolayer. For testing initial binding, HRPTECs were left to adhere for 2 hours. HK2 were cultured to confluence (48 hours) on the captured ECM. Fixated cells were stained for either paxillin, a focal adhesion complex protein, or for ZO-1, a tight junction protein, and for F-actin.

PrestoBlue assay. Captured ECM was reseeded with 6,500 HRPTECs per cm^2. Cell viability was measured 24, 48 and 72 hours post-seeding using PrestoBlue Cell Viability Reagent (ThermoScientific) according to manufacturer's protocol.

Ki67 nuclear staining. Captured ECM was reseeded with 6,500 HRPTECs per cm^2. Cell proliferation was visualized 24, 48 and 72 hours post-seeding by immunofluorescence labelling with the proliferation marker ki67. The images were analyzed with ImageJ (v 1.47) to obtain the percentage of proliferating cells by dividing the amount of $ki67^+$ cells by the $DAPI^+$ count.

PicoGreen assay. Captured ECM was reseeded with 6,500 HRPTECs per cm^2. To quantify the amount of double stranded DNA, a Quant-iT™ PicoGreen™ dsDNA Assay (ThermoFisher) was performed 24, 48 and 72 hours post-seeding according to manufacturer's protocol.

RhoA activation assay. Captured ECM was reseeded with 25,000 HK2 per cm^2. The activation of the small G-protein RhoA was determined 48 hours post-seeding using the G-LISA RhoA Activation Assay Biochem Kit (Cytoskeleton, BK124) according to manufacturer's instructions. HK2 cells were serum starved overnight (in RPMI containing 0.2% FCS) and

stimulated with full RPMI medium (containing the standard 10% FCS) for 1 min before starting the RhoA activation assay to modulate GTP-RhoA levels.

Statistical analyses

Graphpad Prism (version 7.02) was used to perform the statistical analyses. To test if values came from a Gaussian distribution, either the D'Agostino-Pearson omnibus or Shapiro-Wilk normality test was used. The ordinary one-way ANOVA or unpaired t-test was used if the values were normally distributed. In case the values did not pass the normality test, either Kruskal-Wallis or the Mann-Whitney test was used as non-parametric tests. P-values <0.05 were considered significant. All measurements are shown as mean ± SEM.

References

1. Takasato M, Er PX, Becroft M, et al. Directing human embryonic stem cell differentiation towards a renal lineage generates a self-organizing kidney. Nat Cell Biol. 2014;16(1):118-126.
2. Takasato M, Er PX, Chiu HS, et al. Kidney organoids from human iPS cells contain multiple lineages and model human nephrogenesis. Nature. 2015;526(7574):564-568.
3. Guimaraes-Souza NK, Yamaleyeva LM, AbouShwareb T, et al. In vitro reconstitution of human kidney structures for renal cell therapy. Nephrol Dial Transplant. 2012;27(8):3082-3090.
4. Flaim CJ, Chien S, Bhatia SN. An extracellular matrix microarray for probing cellular differentiation. Nat Methods. 2005;2(2):119-125.
5. Plotnikov SV, Pasapera AM, Sabass B, et al. Force fluctuations within focal adhesions mediate ECM-rigidity sensing to guide directed cell migration. Cell. 2012;151(7):1513-1527.
6. Vorotnikova E, McIntosh D, Dewilde A, et al. Extracellular matrix-derived products modulate endothelial and progenitor cell migration and proliferation in vitro and stimulate regenerative healing in vivo. Matrix Biol. 2010;29(8):690-700.
7. van Genderen AM, Jansen J, Cheng C, et al. Renal Tubular- and Vascular Basement Membranes and their Mimicry in Engineering Vascularized Kidney Tubules. Adv Healthc Mater. 2018;7(19):e1800529.
8. Naba A, Clauser KR, Ding H, et al. The extracellular matrix: Tools and insights for the "omics" era. Matrix Biol. 2016;49:10-24.
9. Naba A, Clauser KR, Hoersch S, et al. The matrisome: in silico definition and in vivo characterization by proteomics of normal and tumor extracellular matrices. Mol Cell Proteomics. 2012;11(4):M111.014647.
10. Lennon R, Byron A, Humphries JD, et al. Global analysis reveals the complexity of the human glomerular extracellular matrix. J Am Soc Nephrol. 2014;25(5):939-951.
11. Yoshida Y, Miyazaki K, Kamiie J, et al. Two-dimensional electrophoretic profiling of normal human kidney glomerulus proteome and construction of an extensible markup language (XML)-based database. Proteomics. 2005;5(4):1083-1096.
12. Cui Z, Yoshida Y, Xu B, et al. Profiling and annotation of human kidney glomerulus proteome. Proteome Sci. 2013;11(1):13.
13. Byron A, Randles MJ, Humphries JD, et al. Glomerular cell cross-talk influences composition and assembly of extracellular matrix. J Am Soc Nephrol. 2014;25(5):953-966.
14. Virtanen I, Laitinen L, Korhonen M. Differential expression of laminin polypeptides in developing and adult human kidney. J Histochem Cytochem. 1995;43(6):621-628.
15. Guinobert I, Viltard M, Piquemal D, et al. Identification of differentially expressed genes between fetal and adult mouse kidney: candidate gene in kidney development. Nephron Physiol. 2006;102(3-4):p81-91.
16. Upadhyay KK, Silverstein DM. Renal development: a complex process dependent on inductive interaction. Curr Pediatr Rev. 2014;10(2):107-114.
17. Wang P, Chen Y, Yong J, et al. Dissecting the Global Dynamic Molecular Profiles of Human Fetal Kidney Development by Single-Cell RNA Sequencing. Cell Rep. 2018;24(13):3554-3567. e3553.
18. Bressan GM, Daga-Gordini D, Colombatti A, et al. Emilin, a component of elastic fibers preferentially located at the elastin-microfibrils interface. J Cell Biol. 1993;121(1):201-212.
19. Colombatti A, Spessotto P, Doliana R, et al. The EMILIN/Multimerin family. Front Immunol. 2011;2:93.
20. Verdone G, Corazza A, Colebrooke SA, et al. NMR-based homology model for the solution structure of the C-terminal globular domain of EMILIN1. J Biomol NMR. 2009;43(2):79-96.
21. Verdone G, Doliana R, Corazza A, et al. The solution structure of EMILIN1 globular C1q domain reveals a disordered insertion necessary for interaction with the alpha4beta1 integrin.

J Biol Chem. 2008;283(27):18947-18956.
22. Danussi C, Petrucco A, Wassermann B, et al. EMILIN1-alpha4/alpha9 integrin interaction inhibits dermal fibroblast and keratinocyte proliferation. J Cell Biol. 2011;195(1):131-145.
23. Danussi C, Del Bel Belluz L, Pivetta E, et al. EMILIN1/alpha9beta1 integrin interaction is crucial in lymphatic valve formation and maintenance. Mol Cell Biol. 2013;33(22):4381-4394.
24. Spessotto P, Cervi M, Mucignat MT, et al. beta 1 Integrin-dependent cell adhesion to EMILIN-1 is mediated by the gC1q domain. J Biol Chem. 2003;278(8):6160-6167.
25. Zanetti M, Braghetta P, Sabatelli P, et al. EMILIN-1 deficiency induces elastogenesis and vascular cell defects. Mol Cell Biol. 2004;24(2):638-650.
26. Danussi C, Spessotto P, Petrucco A, et al. Emilin1 deficiency causes structural and functional defects of lymphatic vasculature. Mol Cell Biol. 2008;28(12):4026-4039.
27. Raman M, Cobb MH. TGF-beta regulation by Emilin1: new links in the etiology of hypertension. Cell. 2006;124(5):893-895.
28. Zacchigna L, Vecchione C, Notte A, et al. Emilin1 links TGF-beta maturation to blood pressure homeostasis. Cell. 2006;124(5):929-942.
29. Litteri G, Carnevale D, D'Urso A, et al. Vascular smooth muscle Emilin-1 is a regulator of arteriolar myogenic response and blood pressure. Arterioscler Thromb Vasc Biol. 2012;32(9):2178-2184.
30. Kielty CM, Sherratt MJ, Shuttleworth CA. Elastic fibres. J Cell Sci. 2002;115(Pt 14):2817-2828.
31. Prewitz MC, Seib FP, von Bonin M, et al. Tightly anchored tissue-mimetic matrices as instructive stem cell microenvironments. Nat Methods. 2013;10(8):788-794.
32. Labit H, Goldar A, Guilbaud G, et al. A simple and optimized method of producing silanized surfaces for FISH and replication mapping on combed DNA fibers. Biotechniques. 2008;45(6):649-652, 654, 656-648.
33. Pompe T, Salchert K, Alberti K, et al. Immobilization of growth factors on solid supports for the modulation of stem cell fate. Nat Protoc. 2010;5(6):1042-1050.
34. Munjal C, Opoka AM, Osinska H, et al. TGF-beta mediates early angiogenesis and latent fibrosis in an Emilin1-deficient mouse model of aortic valve disease. Dis Model Mech. 2014;7(8):987-996.
35. Angel PM, Narmoneva DA, Sewell-Loftin MK, et al. Proteomic Alterations Associated with Biomechanical Dysfunction are Early Processes in the Emilin1 Deficient Mouse Model of Aortic Valve Disease. Ann Biomed Eng. 2017;45(11):2548-2562.
36. Spessotto P, Bulla R, Danussi C, et al. EMILIN1 represents a major stromal element determining human trophoblast invasion of the uterine wall. J Cell Sci. 2006;119(Pt 21):4574-4584.
37. Parsons JT, Horwitz AR, Schwartz MA. Cell adhesion: integrating cytoskeletal dynamics and cellular tension. Nat Rev Mol Cell Biol. 2010;11(9):633-643.
38. Tokuda S, Higashi T, Furuse M. ZO-1 knockout by TALEN-mediated gene targeting in MDCK cells: involvement of ZO-1 in the regulation of cytoskeleton and cell shape. PLoS One. 2014;9(8):e104994.
39. Itoh M, Nagafuchi A, Moroi S, et al. Involvement of ZO-1 in cadherin-based cell adhesion through its direct binding to alpha catenin and actin filaments. J Cell Biol. 1997;138(1):181-192.
40. Odenwald MA, Choi W, Buckley A, et al. ZO-1 interactions with F-actin and occludin direct epithelial polarization and single lumen specification in 3D culture. J Cell Sci. 2017;130(1):243-259.
41. Kreidberg JA, Symons JM. Integrins in kidney development, function, and disease. Am J Physiol Renal Physiol. 2000;279(2):F233-242.
42. Mathew S, Chen X, Pozzi A, et al. Integrins in renal development. Pediatr Nephrol. 2012;27(6):891-900.
43. Colombatti A, Doliana R, Bot S, et al. The EMILIN protein family. Matrix Biol. 2000;19(4):289-301.

44. Palecek SP, Loftus JC, Ginsberg MH, et al. Integrin-ligand binding properties govern cell migration speed through cell-substratum adhesiveness. Nature. 1997;385(6616):537-540.
45. Couchman JR, Rees DA. The behaviour of fibroblasts migrating from chick heart explants: changes in adhesion, locomotion and growth, and in the distribution of actomyosin and fibronectin. J Cell Sci. 1979;39:149-165.
46. Hynes RO. Integrins: bidirectional, allosteric signaling machines. Cell. 2002;110(6):673-687.
47. Laukaitis CM, Webb DJ, Donais K, et al. Differential dynamics of alpha 5 integrin, paxillin, and alpha-actinin during formation and disassembly of adhesions in migrating cells. J Cell Biol. 2001;153(7):1427-1440.
48. Ryan MJ, Johnson G, Kirk J, et al. HK-2: an immortalized proximal tubule epithelial cell line from normal adult human kidney. Kidney Int. 1994;45(1):48-57.
49. Wilm M, Shevchenko A, Houthaeve T, et al. Femtomole sequencing of proteins from polyacrylamide gels by nano-electrospray mass spectrometry. Nature. 1996;379(6564):466-469.
50. Sap KA, Bezstarosti K, Dekkers DHW, et al. Quantitative Proteomics Reveals Extensive Changes in the Ubiquitinome after Perturbation of the Proteasome by Targeted dsRNA-Mediated Subunit Knockdown in Drosophila. J Proteome Res. 2017;16(8):2848-2862.
51. Cox J, Mann M. MaxQuant enables high peptide identification rates, individualized p.p.b.-range mass accuracies and proteome-wide protein quantification. Nat Biotechnol. 2008;26(12):1367-1372.

Supplemental figures

A

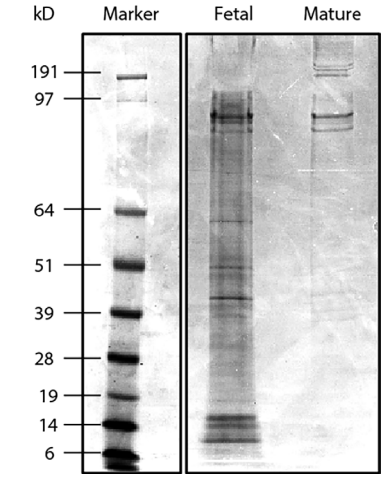

Supplemental Figure 1. (A) Extracellular matrix (ECM) extracts from human fetal and mature renal samples were separated by SDS-PAGE and visualized with a Coomassie staining, before further processing for mass-spectrometry analysis. Shown is a representative blot of 3 separate experiments, each containing 3-5 human renal samples per group (fetal or mature).

A

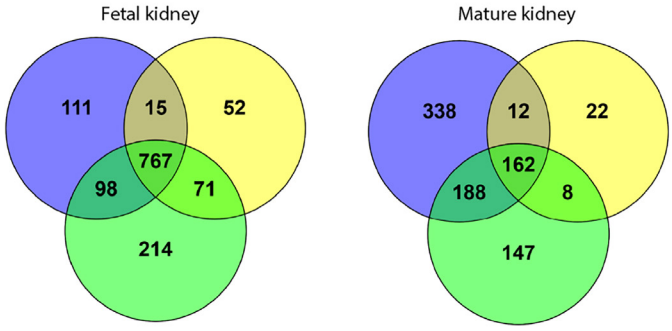

Supplemental Figure 2. (A) The Venn diagrams show the total amount and overlap of proteins identified in three separate mass-spectrometry analyses. Each analysis contained 3-5 renal samples per group (fetal or mature).

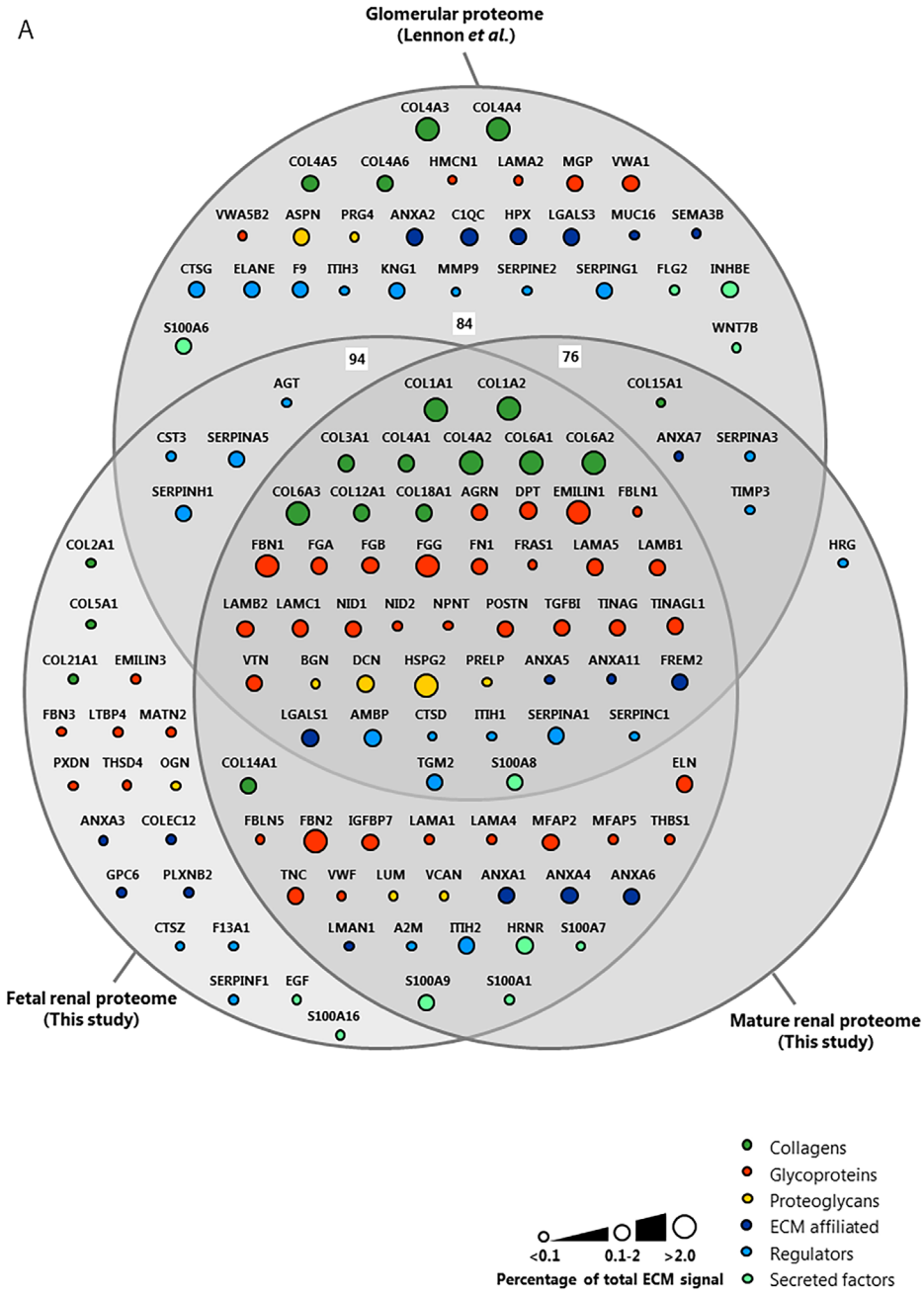
A
Glomerular proteome
(Lennon et al.)
COL4A3 COL4A4
COL4A5 COL4A6 HMCN1 LAMA2 MGP VWA1
VWA5B2 ASPN PRG4 ANXA2 C1QC HPX LGALS3 MUC16 SEMA3B
CTSG ELANE F9 ITIH3 KNG1 MMP9 SERPINE2 SERPING1 FLG2 INHBE
S100A6
84
WNT7B
94
76
AGT
COL1A1 COL1A2
COL15A1
CST3 SERPINA5
COL3A1 COL4A1 COL4A2 COL6A1 COL6A2
ANXA7 SERPINA3
SERPINH1
COL6A3 COL12A1 COL18A1 AGRN DPT EMILIN1 FBLN1
TIMP3
COL2A1
FBN1 FGA FGB FGG FN1 FRAS1 LAMA5 LAMB1
HRG
COL5A1
LAMB2 LAMC1 NID1 NID2 NPNT POSTN TGFBI TINAG TINAGL1
COL21A1 EMILIN3
VTN BGN DCN HSPG2 PRELP ANXA5 ANXA11 FREM2
FBN3 LTBP4 MATN2
LGALS1 AMBP CTSD ITIH1 SERPINA1 SERPINC1
PXDN THSD4 OGN
COL14A1
TGM2 S100A8
ELN
ANXA3 COLEC12
FBLN5 FBN2 IGFBP7 LAMA1 LAMA4 MFAP2 MFAP5 THBS1
GPC6 PLXNB2
TNC VWF LUM VCAN ANXA1 ANXA4 ANXA6
CTSZ F13A1
LMAN1 A2M ITIH2 HRNR S100A7
SERPINF1 EGF
S100A9 S100A1
S100A16
Fetal renal proteome
(This study)
Mature renal proteome
(This study)
Collagens
Glycoproteins
Proteoglycans
ECM affiliated
Regulators
Secreted factors
<0.1 0.1-2 >2.0
Percentage of total ECM signal

◀ **Supplemental Figure 3.** (A) Euler-diagram visualizing the overlap and differences between the human fetal and mature renal extracellular matrix (ECM) proteome found in this study and the glomerular proteome identified by Lennon *et al*[10]. Each node represents a single protein and is labeled with the gene name. Node size is proportional to the abundance of the protein within the renal ECM proteome (less than 0.1%, between 0.1 and 2% or more than 2% of the total ECM signal in at least one dataset (fetal or mature)).

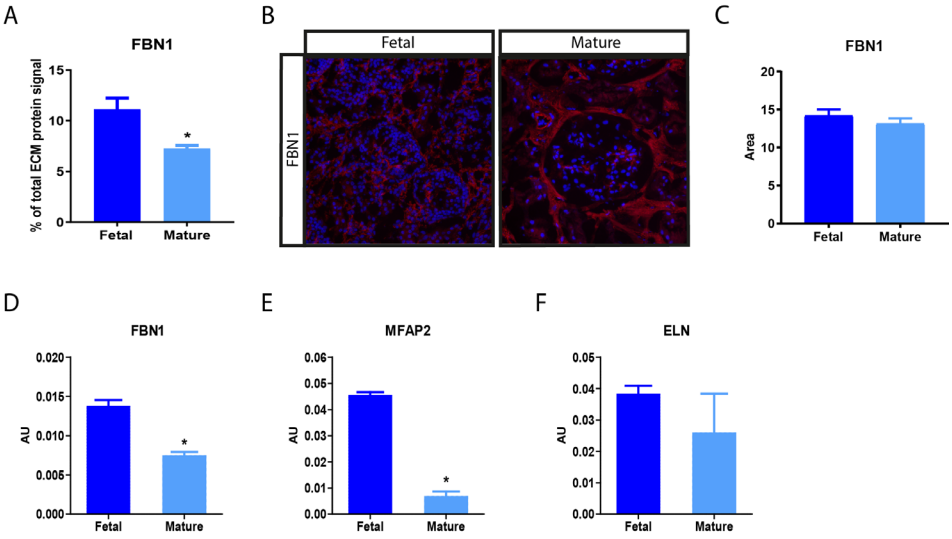

Supplemental Figure 4. (A) Bar graph showing FBN1 signal identified with mass-spectrometry (MS) within fetal and mature renal extracellular matrix (ECM) extracts. N=3 MS analyses, each containing 3-5 kidney samples per group (fetal or mature). Shown is mean ± SEM; *P<0.05. (B) Representative fluorescence immunohistochemistry images (200x magnification) demonstrate the localization and amount of FBN1 (red) in fetal and mature renal tissue. (C) Quantification of normalized FBN1 area in both fetal and mature renal samples. N≥15 fluorescent images derived from N=3 samples. Shown is mean ± SEM. Quantitative polymerase chain reaction (qPCR) of *FBN1* (D), *MFAP2* (E) and *ELN* (F) in human renal fetal and mature tissue. Shown is target gene/housekeeping gene (*β-actin*) ratio (AU). N≥4 qPCRs. Shown is mean ± SEM; *P<0.05.

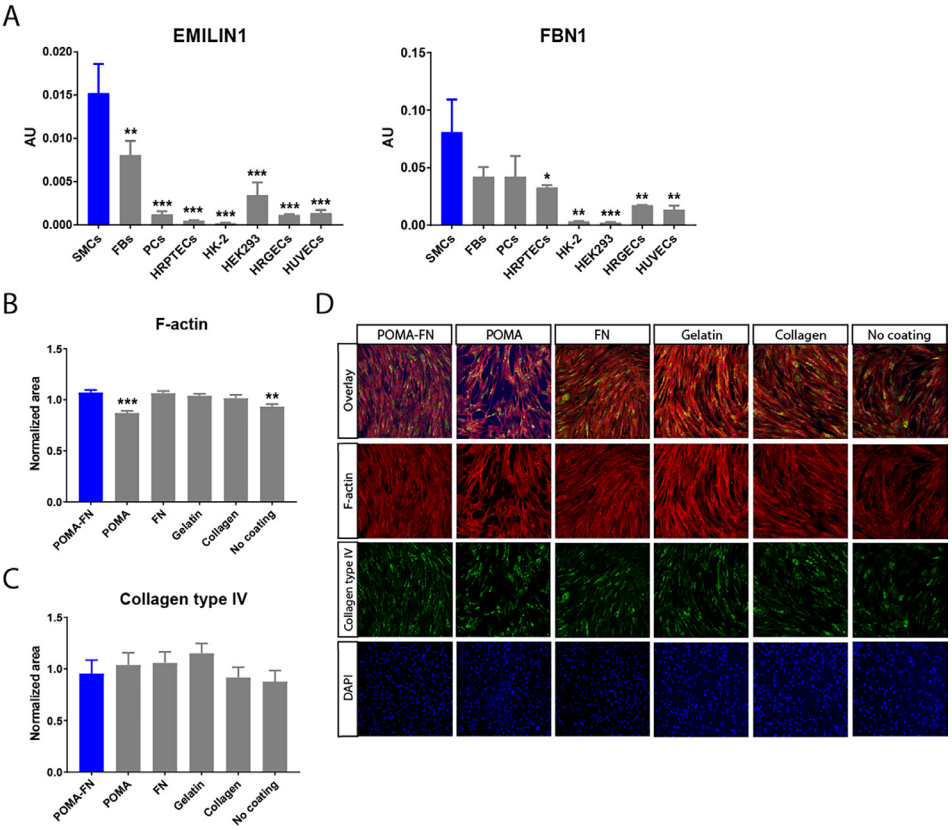

Supplemental Figure 5. (A) Quantitative polymerase chain reaction (qPCR) of *EMILIN1* (left) or *FBN1* (right) expression in the following cell types: HRPTECs, HK-2 cells, HK293 cells, HRGECs, HUVECs, PCs, SMCs and FBs. Shown are target gene/housekeeping gene (*β-actin*) ratios (AU). N≥5 qPCRs. Shown is mean ± SEM; *P<0.05, **P<0.01, ***P<0.001. Quantification of F-actin area (B) or collagen type IV area (C) of 150,000 SMCs cultured for 6 days on coverslips coated with POMA-FN, POMA, FN, gelatin or collagen or no coating. N=15 fluorescent images derived from N=3 samples. Shown is mean ± SEM; **P<0.01, ***P<0.001. (D) Representative immunofluorescence images (100x magnification) of 150,000 SMCs cultured for 6 days and stained for F-actin (red), collagen type IV (green) and DAPI (blue).

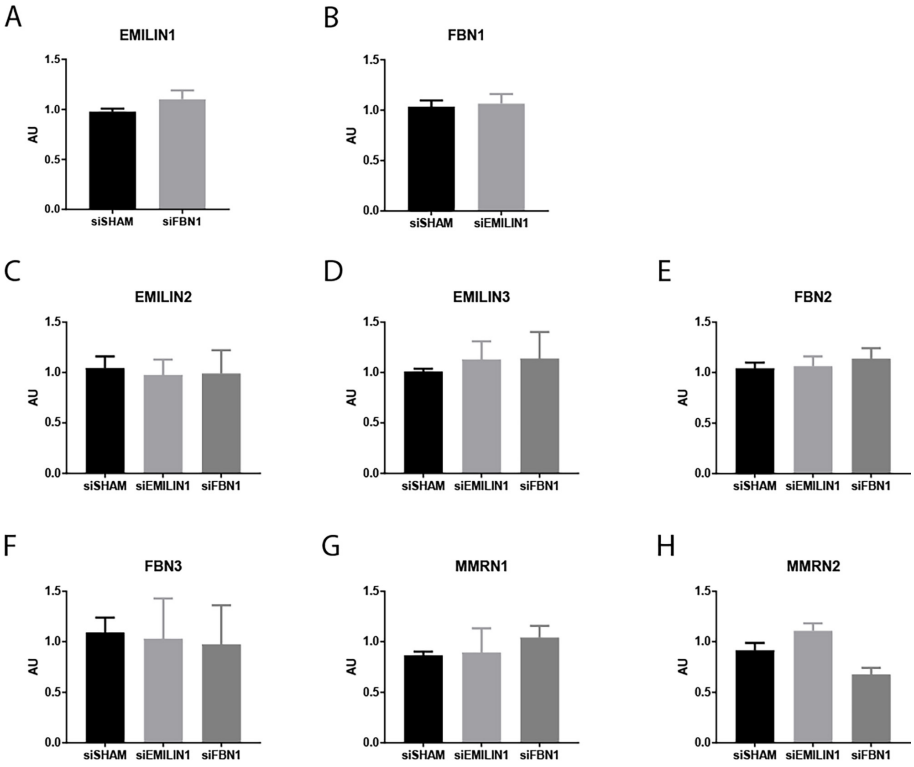

Supplemental Figure 6. Quantitative polymerase chain reaction (qPCR) of *EMILIN1* (A), *FBN1* (B), *EMILIN2* (C), *EMILIN3* (D), *FBN2* (E), *FBN3* (F), *MMRN1* (G) and *MMRN2* (H) expression in smooth muscle cells (SMCs) transfected with *EMILIN1*-targeting siRNA (siEMILIN1), *FBN1*-targeting siRNA (siFBN1) or non-targeting siRNA (siSHAM). Shown are target gene/housekeeping gene (*β-actin*) ratios (AU). Control values are set to 1 (not shown). N=3 qPCRs. Shown is mean ± SEM.

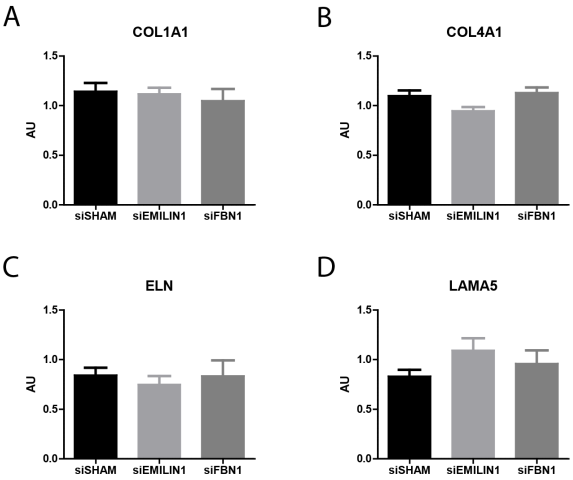

Supplemental Figure 7. Quantitative polymerase chain reaction (qPCR) of *COL1A1* (A), *COL4A1* (B), *ELN* (C) and *LAMA5* (D) expression in smooth muscle cells (SMCs) transfected with *EMILIN1*-targeting siRNA (siEMILIN1), *FBN1*-targeting siRNA (siFBN1) or non-targeting siRNA (siSHAM). Shown are target gene/housekeeping gene (*β-actin*) ratios (AU). Control values are set to 1 (not shown). N=5 qPCRs. Shown is mean ± SEM.

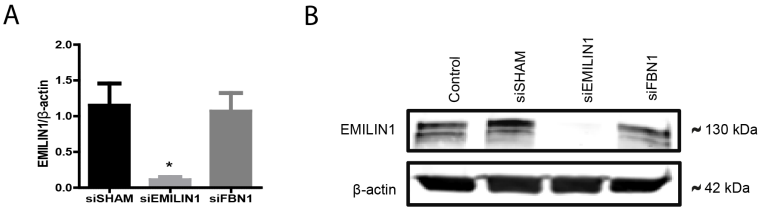

Supplemental Figure 8. (A) Western blot analysis of EMILIN1 expression in smooth muscle cells (SMCs) transfected with *EMILIN1*-targeting siRNA (siEMILIN1), *FBN1*-targeting siRNA (siFBN1) or non-targeting siRNA (siSHAM). Shown is EMILIN1/β-actin ratio. Control values are set to 1 (not shown). N=4 Western blots. Shown is mean ± SEM. *P<0.05 compared to siSHAM. (B) Representative Western blot of EMILIN1 and β-actin protein levels in siSHAM, siEMILIN1, siFBN1 and control SMCs.

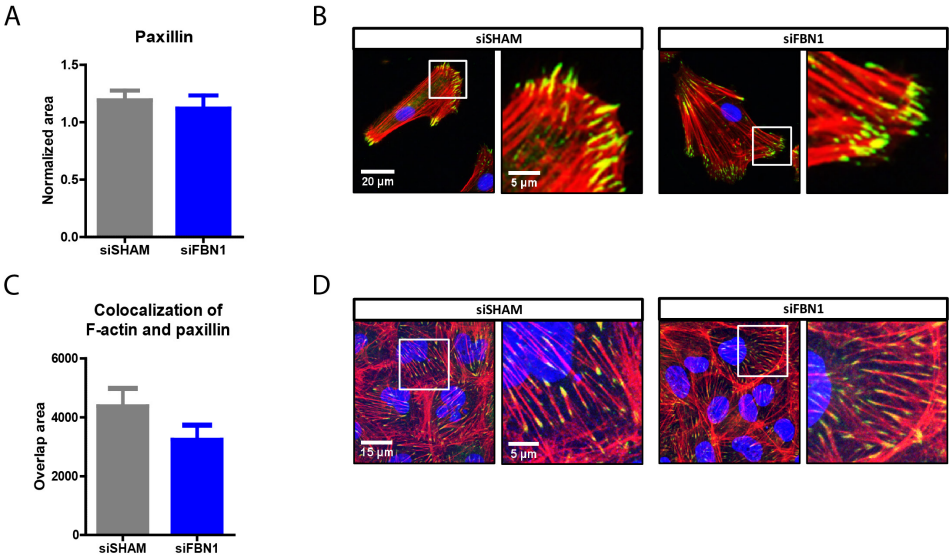

Supplemental Figure 9. (A) Quantified results showing the paxillin area in HRPTECs on siSHAM or siFBN1 extracellular matrix (ECM) during initial binding to the ECM (cultured for 2 hours). N=30 fluorescent images derived from N=3 samples. Shown is mean ± SEM. (B) Representative immunofluorescence images (400x magnification) of HRPTECs after 2 hours of binding on siSHAM or siFBN1 ECM and stained for paxillin (green), F-actin (red) and DAPI (blue). Scale bar represents 20 µm (overview image, left) and 5 µm (zoomed-in image, right). (C) Colocalization of paxillin and F-actin in HK2 cells cultured to confluency on siSHAM or siFBN1 ECM. N≥15 fluorescent Z-stacks, from N≥3 samples. Shown is mean ± SEM. (D) Representative immunofluorescence Z-stacks (630x magnification) of HK2 cells cultured to confluency on siSHAM or sFBN1 ECM and stained for paxillin (green), F-actin (red) and DAPI (blue). Colocalization is displayed as yellow. Scale bar represents 15 µm (overview image, left) and 5 µm (zoomed-in image, right).

Supplemental Tables

Supplemental tables can be downloaded from: http://bit.ly/2LM2cK9

Extracellular matrix analysis of human renal arteries in both quiescent and active vascular state

C.G.M. van Dijk, L. Louzao Martinez, E. van Mulligen, B. Boermans, J.A.A Demmers, T.P.P. van den Bosch, M.T.H. Goumans, D.J. Duncker, M.C. Verhaar, C. Cheng.

[In preparation]

Abstract

The two main components for engineering a functional vascular tissue construct are living cells and a scaffolding system. Addition of vascular-specific extracellular matrix (ECM) components to the scaffold would better mimic the *in vivo* microenvironment and potentially enhance cell-matrix interactions and subsequent tissue growth. In order to create such a scaffold, the components of the human vascular ECM first need to be fully characterized. Research has focused on characterizing ECM components in healthy, mature vascular tissue in comparison with diseased tissue; however, the developing fetal ECM matches more the active environment required in vascular tissue constructs. Here, we characterized the ECM protein composition present in active (fetal) and quiescent (mature) renal arteries using spectrometry-based proteomics after enriching for ECM proteins by decellularization. The ECM protein composition differs significantly between fetal and mature vascular tissue. Elastic ECM proteins EMILIN1 and FBN1 are significantly enriched in fetal renal arteries and are mainly produced by cells of mesenchymal origin. We functionally tested the role of EMILIN1 and FBN1 by anchoring the ECM secreted by vascular smooth muscle cells (SMCs) to glass coverslips. This ECM layer was depleted form either EMILIN1 or FBN1 by using targeted siRNAs in the SMCs. Growing HUVECs on this modified ECM layer provoked alterations on transcriptome level associated with multiple pathways, especially Rho GTPase controlled pathways. However, no significant alterations in HUVEC adhesion, migration or proliferation was seen when grown on EMILIN1 or FBN1 deficient ECM. Nevertheless, the obtained human renal artery ECM proteome during active and quiescent vascular state contains many more promising ECM proteins involved in vascular development that are interesting candidates for further research on implementation in scaffolds of vascular tissue constructs.

Introduction

The human vasculature consists of mainly two different cell types that have their own specific function. Along with the endothelial cells (ECs) that line blood vessels, mural cells play an important role in maintaining vascular homeostasis. Where pericytes associate with capillaries to maintain barrier function, vascular smooth muscle cells (SMCs) are found predominantly on larger arteries to provide strength and elasticity. These cells create their own dynamic microenvironment for protection and stability by synthesizing and secreting extracellular matrix (ECM) components, including constituents of the basement membrane[1,2]. This matrix microenvironment consists of many components, such as collagens, proteoglycans and glycoproteins and forms a reservoir for bound growth factors[3,4]. Thus, ECM proteins do not only provide structural and organizational stability for the surrounding cells, they are also responsible for a wide variety of biochemical cues.

ECM remodeling is a critical aspect during vascular development. At the onset of angiogenesis, the basement membrane matrix is degraded to allow endothelial sprouting. As angiogenesis proceeds, the ECM is known to provide signals controlling EC migration, proliferation, survival, differentiation, shape and invasion. Ultimately, through specific integrin-signaling pathways, the ECM controls the EC cytoskeleton to guide vascular morphogenesis into a mature vascular network with functional lumens[5]. During this vascular response, different ECM cues are active. For example, ECs cultured on a collagen type 1 coating are stimulated to rearrange their cytoskeleton and cell junctions, inducing capillary morphogenesis. In contrast, culturing ECs on a laminin-1 coating inhibits this rearrangement[6]. This is in concordance with the laminin-rich basement membrane characteristic for mature vessels in a quiescent state. Thus, there is a marked difference in ECM composition during vessel development compared with mature stable vessels.

Applied technologies, such as vascular tissue engineering and regenerative medicine, could benefit from mimicking the vascular specific ECM active during development. This research area uses cells embedded in a scaffolding system (synthetic or biological) to recreate tissues. For example, polymer scaffolds are being used to mimic blood vessels and heart valves[7,8]. For *in situ* tissue engineering, achieving a balance between the biodegradability of the scaffold and how fast cells are recruited remains a significant challenge. The addition of vascular-specific ECM components to these scaffolds might better mimic the *in vivo* microenvironment and enhance cell-matrix interactions and subsequent tissue growth. In order to create such a scaffold, the components of the human vascular ECM first need to

be fully characterized.

Mass spectrometry-based approaches have been used to characterize ECM compositions of various tissues[3,9]. To unravel the vascular ECM, previous work mainly focused on characterizing ECM components in healthy, mature tissue in comparison with diseased tissue, rather than changes during vascular development[10,11]. The fetal microenvironment is more dynamic and active compared to the matured ECM in order to cope with tissue morphogenesis and growth, which matches the environment needed in tissue scaffolds.

The aim of this study was to define the ECM proteome in vascular tissue during development compared to matured tissue. By using proteomics, we created a catalogue of ECM proteins present in human fetal renal arteries (active state) and human mature renal arteries (quiescent state). Based on this vascular ECM proteome, we selected two elastic components, Elastin Microfibril Interfacer 1 (EMILIN1) and fibrillin-1 (FBN1), based on their abundance in the fetal renal artery to evaluate their contribution to vascular ECM guided cell function. Both EMILIN1 and FBN1 are glycoproteins located at elastic fibers and microfibrils[12,13]. Next to structural roles, EMILIN1 is known to be a receptor for integrins, connecting cells with the surrounding ECM[14,15]. Many cell types need this interaction for adhesion, migration and proliferation[16-19]. Deficiency of either EMILIN1 or FBN1 in mice leads to aortic valve disease and vascular abnormalities, respectively[20,21]. Furthermore, mutations in the *FBN1* gene cause Marfan syndrome, a genetic connective tissue disorder characterized by aortic aneurysms and dissections[22]. Both EMILIN1 and FBN1 seem to play an important role in maintaining vascular homeostasis. These findings validate the importance of our human renal artery ECM proteome during active and quiescent vascular state in indentifying interesting candidates that can contribute to the field of vascular tissue engineering and regenerative medicine.

Results

Enrichment of extracellular matrix proteins in vascular tissue

Healthy human fetal and mature renal arteries were decellularized to enrich for ECM components (Figure 1A). The white appearance of the tissue after decellularization indicates loss of cells (Figure 1B). HE staining confirms complete decellularization, visualized by the absence of nuclei while maintaining the ECM architecture (Figure 1C,D). Proteins detected by LC-MS/MS in at least 2 pooled groups were used for further analysis (Supplemental Figure 1A,B). Detected fetal and mature proteins were categorized by crossreferencing with the Human

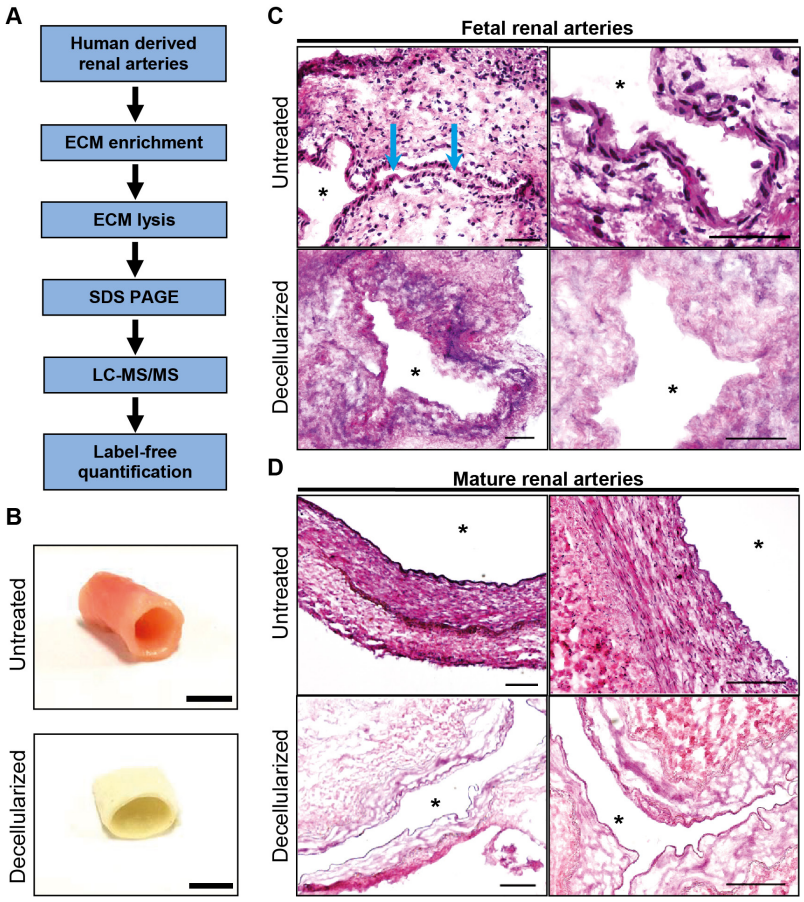

Figure 1. Proteomic workflow for extracellular matrix enriched vascular samples. (A) After decellularization of the human renal artery tissue, extracellular matrix (ECM) enriched samples were lysed and separated with SDS-PAGE prior to LC-MS/MS with label-free quantification. (B) Mature human renal arteries, before and after decellularization. Scale bars represent 1 cm. Hematoxylin and eosin staining for validation of the decellularization procedure in fetal human renal arteries (C) and mature human renal arteries (D). Arrows indicate lumen. Open lumen is indicated with an asterisk. Representative images of 3 experiments. Scale bars represent 200 μm.

Matrisome Project[3,9].

Of all proteins detected, 39% of the fetal and 35% of the mature samples represent matrisome components. The majority form part of the matrisome core proteins, subdivided by glycoproteins, collagens and proteoglycans. A quarter of the matrisome proteins detected are allocated to matrisome associated proteins, such as ECM affiliated proteins, ECM regulators and growth factors. There is only a subtle difference between the number of detected proteins of fetal and mature

human origin (Table 1).

Matrisome protein expression differs between human fetal and mature renal arteries

Although there is almost no difference in the number and types of ECM proteins detected, relative protein quantification revealed a difference in protein abundance between fetal and mature samples. Mature renal arteries contain more proteoglycan signal compared to fetal tissue: 11.8% of the mature signal consists of proteoglycans, compared to only 1.8% in de fetal selection (Supplemental Figure 1C).

97 fetal and 90 mature renal artery ECM proteins were detected in the human samples, from which the majority overlaps between the two groups. From this overlap, the most abundant signal comes from collagens and glycoproteins, with many comprising ≥1% of the total signal (Supplemental Figure 2). 15 proteins were significantly enriched in the fetal renal artery ECM compared to the mature ECM (Figure 2A), including collagen type I (Figure 2B). 16 proteins were significantly enriched in the mature renal artery ECM compared to the fetal ECM (Figure 2A), including collagen type IV (Figure 2B). Different subtypes of laminins are also significantly more abundant in the mature renal arteries compared to fetal renal arteries (Figure 2B). The proteoglycans HSPG2 and BGN are more abundant in the mature renal arteries as well. Growth factor TGF-β1, which is part of an important signaling pathway in vascular cells, is present in both fetal

Table 1. Proteomic hits detected in the human fetal and mature renal artery after enrichment for extracellular matrix (ECM) proteins.

	Fetal renal artery	Mature renal artery
Total no. proteins detected	206	246
Matrisome proteins	79 (38.3% of total)	87 (35% of total)
Non-matrisome proteins	127 (61.7% of total)	159 (65% of total)
Matrisome core proteins	58 (73.4% of matrisome)	63 (73.3% of matrisome)
Glycoproteins	38 (65.6% of core)	39 (61.9% of core)
Collagens	14 (24.1% of core)	15 (23.8% of core)
Proteoglycans	6 (10.3% of core)	9 (14.3% of core)
Matrisome associated proteins	21 (26.6% of matrisome)	23 (26.7% of matrisome)
ECM affiliated	9 (42.9% of associated)	9 (39.1% of associated)
ECM regulators	7 (33.3% of associated)	10 (43.5% of associated)
Secreted factors	5 (23.8% of associated)	4 (17.4% of associated)

and mature renal arteries and composes ±1% of the total signal. The detection of proteoglycans and growth factors verifies that the used decellularization protocol is gentle enough to preserve the more delicate ECM proteins in the tissue. The full list of all fetal renal artery ECM proteins detected and their abundance compared

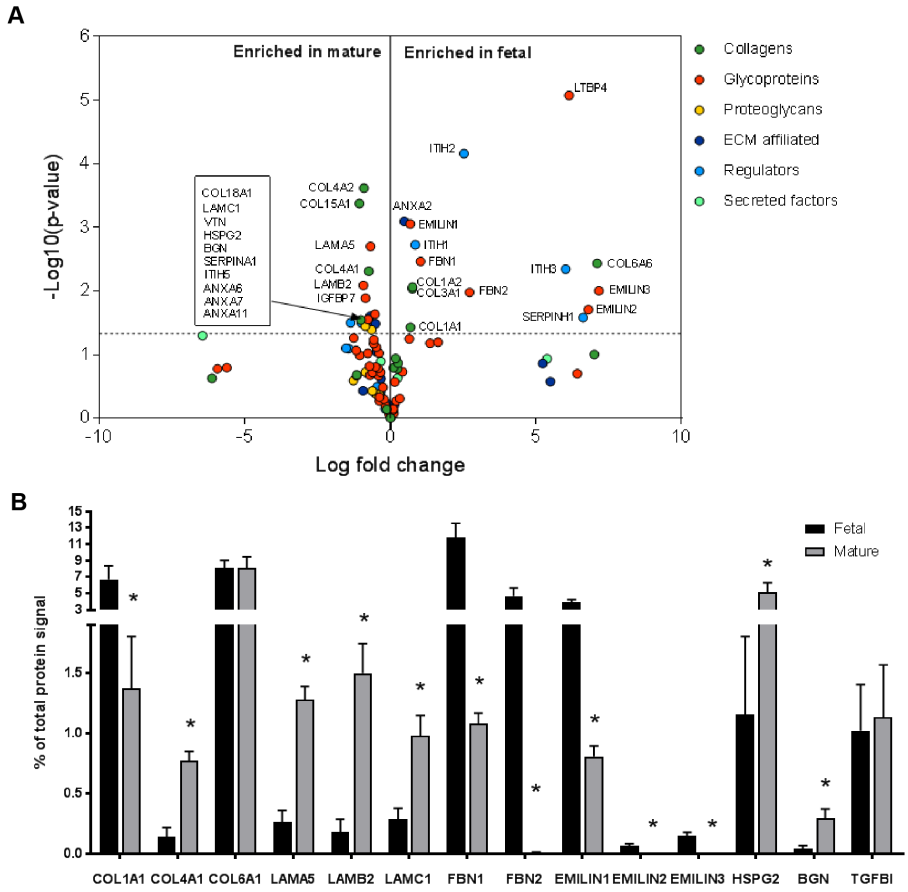

Figure 2. Defining the renal artery fetal and mature extracellular matrix proteome. (A) A volcano plot showing the extracellular matrix (ECM) protein distribution in the fetal and mature renal artery by fold changes (x-axis, log fold change) and significance (y-axis, -log P-value). Each circle represents a single ECM protein and each color a specific matrisome subset (collagens, glycoproteins, proteoglycans, ECM affiliated, regulators, secreted factors). The horizontal line indicates P<0.05. Box summarizes the names of the clustered mature ECM proteins marked by an arrow. (B) Bar graph showing examples of ECM proteins in the fetal and mature renal artery. Each bar represents the percentage of the total protein signal identified with LC-MS/MS. N=3. Shown is mean ± SEM; *P<0.05 when comparing the fetal (black bar) with the mature (grey bar) signal of each ECM protein (Student's t-test).

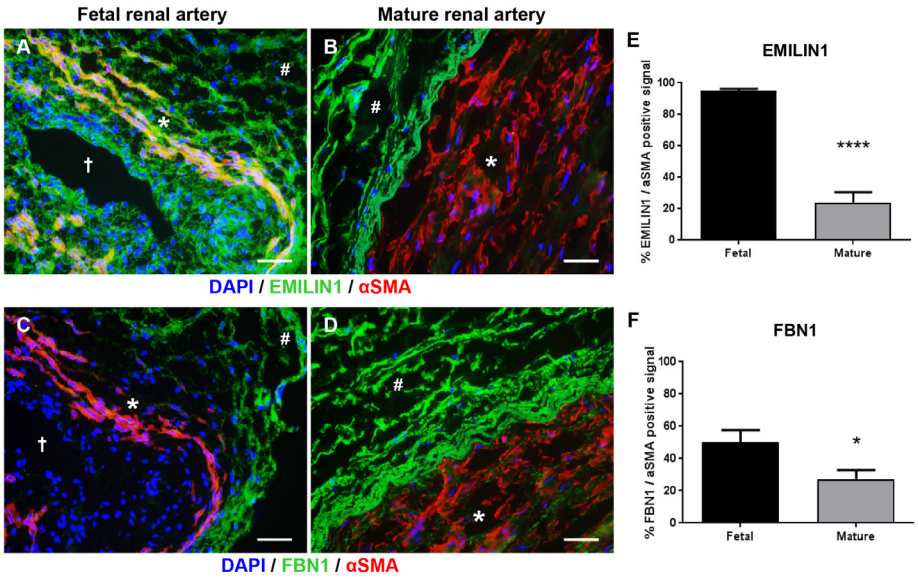

Figure 3. Validation of selected extracellular matrix proteins EMILIN1 and FBN1. Representative images demonstrating the distribution of EMILIN1 co-stained with smooth muscle actin (αSMA) in fetal (A) and mature (B) human renal arteries. Representative images demonstrating the distribution of FBN1 co-stained with αSMA in fetal (C) and mature (D) human renal arteries. Scale bars represent 50 μm. Open lumen is indicated with a cross, tunica media layer is indicated with an asterisk and the tunica adventitia layer is indicated with a hashtag. (E) Percentage of EMILIN1 per αSMA positive signal in fetal and mature renal arteries. (F) Percentage of FBN1 per αSMA positive signal in fetal and mature renal arteries. N=4-5 fluorescent images in fetal samples, N=15-11 fluorescent images in mature samples. Shown is mean ± SEM; *P<0.05, ****P<0.0001.

to the mature tissue is available in Supplemental Table 1.

Glycoproteins EMILIN1 and FBN1 are enriched in fetal renal arteries and are produced by cells of the mesenchymal lineage

Elastic components EMILIN1 and FBN1 are significantly more abundant in the fetal renal arteries: 5% and 12% of the total signal consist of EMILIN1 and FBN1, respectively, compared to only 1% in the mature tissue (Figure 2A,B). The high levels of EMILIN1 and FBN1 in fetal renal arteries hint towards an important role for both ECM proteins in vascular development. Verification of EMILIN1 and FBN1 expression in fetal and mature renal arteries by immunohistochemistry showed indeed enrichment of these proteins in the fetal versus mature samples (Figure 3A-D). EMILIN1 is present in all layers of the fetal renal artery, while in the mature renal artery it is almost exclusively present in the adventitia. FBN1 is exclusively present

in the adventitia of both fetal and mature renal arteries. EMILIN1 and FBN1 co-stained with alpha smooth muscle actin (αSMA) showed more overlap between this mesenchymal marker and both proteins in the fetal renal artery (Figure 3A-F). MRNA expression analysis confirmed a higher expression of EMILIN1 and FBN1 in SMCs and pericytes compared to ECs (Figure 4A). This suggests that cells from the mesenchymal lineage produce more EMILIN1 and FBN1 compared to ECs and thereby contribute to the ECM composition of the renal arteries.

Smooth muscle cell secreted extracellular matrix can be altered by depleting specific components

Elastic proteins EMILIN1 and FBN1 are abundantly present in fetal renal arteries, suggesting a pivotal role in the development of the vasculature. To study the effect of EMILIN1 and FBN1 on ECs, a specific loss of function assay on matrix level was conducted. SMCs treated with siRNA against EMILIN1 or FBN1 were used and their secreted ECM was anchored to glass coverslips. After 6 days, the SMCs were removed, leaving behind a coating of SMC-secreted ECM depleted from either EMILIN1 or FBN1. Coverslips coated with POMA-FN significantly improved anchorage of the secreted ECM at 6 days compared with a standard gelatin coating or no coating (Supplemental Figure 3A-C). This approach provides a unique way to study and modify the composition of cell-secreted ECM. QPCR and immunocytochemistry analyses confirmed the knockdown of EMILIN1 in SMCs after 6 days of culturing (Figure 4B-D). After decellularization, the EMILIN1 amount in the anchored ECM was significantly lower compared to ECM derived from SMCs treated with non-targeting siRNA (siSham) and untreated control ECM (Figure 4C,E). Secreted collagen type IV was stained as a reference control in the decellularized conditions and showed no difference in the deposited amount of ECM anchored between control and siRNA conditions (Supplemental Figure 3D). Knockdown of FBN1 in SMCs showed similar results (Figure 4B, Supplemental Figure 4A-C). Thus, the expression and secretion of EMILIN1 and FBN1 by SMCs can be altered, creating a modified ECM layer with significant lower EMILIN1 and FBN1 content that can be used in functional assays to study EC behavior.

Loss of EMILIN1 and FBN1 in the extracellular matrix does not influence endothelial cell fate

Twenty-four hours post seeding, HUVECs cultured on EMILIN1 or FBN1 deficient ECM were lysed for RNA isolation and processed for RNA-sequencing (RNA-

seq). In total, 481 and 474 genes were found to be differentially expressed (P<0.05; Supplemental Figure 5A, Supplemental Table 2 and 3,) for EMILIN1 and FBN1, respectively, compared to HUVECs cultured on siSham ECM. Subsequent pathway analysis demonstrated that multiple pathways were altered in HUVECs

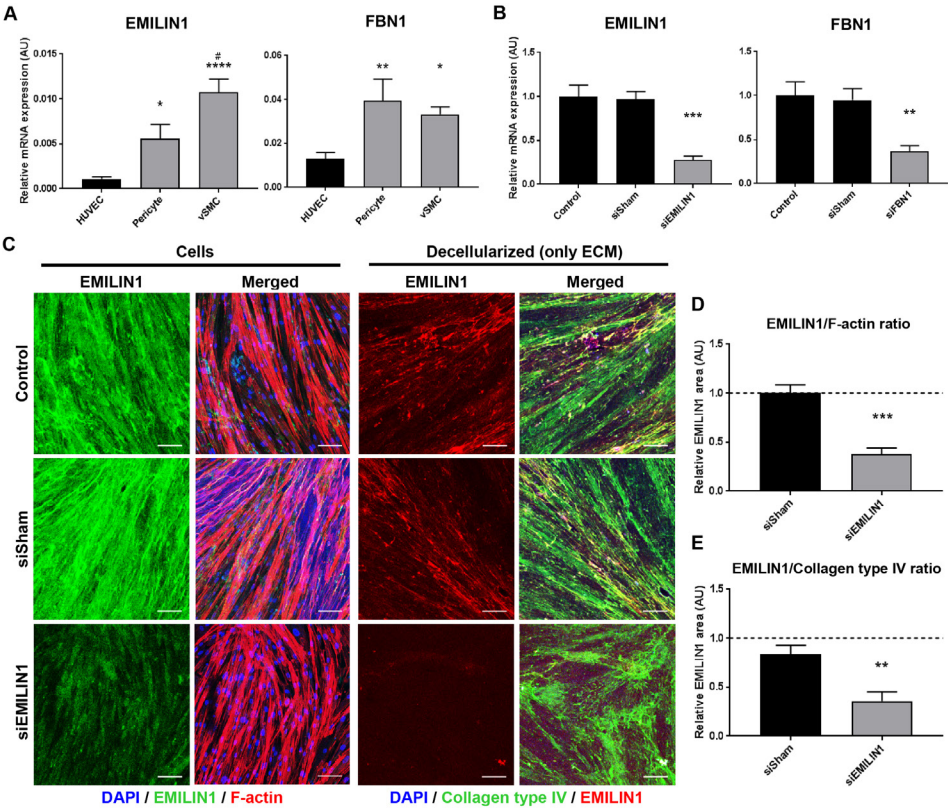

Figure 4. siRNA induces silencing of EMILIN1 and FBN1 intracellular and on secreted extracellular matrix level. (A) Quantitative polymerase chain reaction (qPCR) analysis of *EMILIN1* and *FBN1* in different vascular cell types: HUVECs (as endothelium source) and both SMCs and pericytes (as mural cell source). Shown are target gene/housekeeping gene (*β-actin*) ratios (AU). N≤10 qPCRs. Shown is mean ± SEM; *P<0.05, **P<0.01, ****P<0.0001 compared to HUVECs, #P<0.05 compared to pericytes. (B) qPCR validation of *EMILIN1* and *FBN1* knockdown in SMCs 6 days after siRNA transfection. Shown are target gene/housekeeping gene (*β-actin*) ratios (AU). N=9-7 qPCRs. Shown is mean ± SEM; **P<0.01, ***P<0.001 compared to siSham. (C) Representative Z-stacks of EMILIN1 in SMCs cultured for 6 days after siRNA transfection and after decellularization. Scale bars represent 100 µm. (D) Quantification of EMILIN1 signal corrected for the amount of F-actin in siRNA treated SMCs. N=5. Shown is mean ± SEM. (E) Quantification of EMILIN1 signal corrected for the amount of collagen type IV present in SMCs-derived extracellular matrix (ECM). N=7. Shown is mean ± SEM; **P<0.01, ***P<0.0001. Non-treated SMCs are set to 1 (dotted lines).

cultured on EMILIN1 or FBN1 deficient ECM (Supplemental Table 4 and 5). A cut off for the z-score (>2 or <-2) was used to highlight the most prominent mechanisms with increased or decreased transcriptional activity. This conical approach revealed "regulation of actin-based motility by Rho" and "signaling by Rho family GTPases" pathways as the overlapping mechanism upregulated at mRNA level in ECs cultured on EMILIN1 or FBN1 deficient ECM, respectively.

In line with the RNA-seq data, previous studies have shown that both EMILIN1 and FBN1 can promote cell movement[16,18,23,24]. Therefore, we performed a live cell migration assay to validate these altered pathways in EC cultured on EMILIN1 or FBN1 deficient ECM. In contrast with previous studies, overnight tracking did not reveal a difference in the migratory capabilities of HUVECs cultured on either EMILIN1 or FBN1 deficient ECM when compared to ECs cultured on siSham ECM (Figure 5A, Supplemental Figure 5B). Next, we assessed the activity of RhoA, a Rho GTPase that is primarily associated with cytoskeleton regulation, in HUVECs grown on EMILIN1 or FBN1 deficient ECM. There was no difference in RhoA activation in these HUVECs compared to ECs cultured on siSham ECM (Figure 5B).

Rho GTPase signaling also coordinates cell proliferation by regulating cytoskeleton adaptations[25]. Previous studies have shown that both EMILIN1 and FBN1 regulate cell proliferation through integrin-mediated signaling[17,18,24]. Therefore, *in vitro* functional assays on cell proliferation and viability were performed with HUVECs cultured on EMILIN1 or FBN1 deficient ECM. Depletion of either EMILIN1 or FBN1 from the ECM did not affect proliferation, DNA content and viability of ECs when compared to EC cultured on siSham ECM (Figure 5C-E).

Paxillin is a focal adhesion adaptor protein known to be critical for cytoskeleton rearrangements coordinated by Rho GTPases, especially for cell adhesion during migration[26]. According to the pathway analysis, "paxillin signaling" was decreased in HUVECs cultured on EMILIN1 deficient ECM. To further validate this, an adhesion assay was performed followed by immunostaining for paxillin in HUVECs after 2 and 24 hours of culturing. There was no difference observed in the paxillin^{+} area in ECs cultured on EMILIN1 or FBN1 depleted ECM when compared to ECs cultured on siSham ECM (Figure 5F-G, Supplemental Figure 5C). Furthermore, these ECs did not show any difference on the actin cytoskeleton arrangement (Figure 5F-G, Supplemental Figure 5D), although according to the RNA-seq data, the pathway "regulation of actin-based motility by Rho" was increased in ECs cultured on EMILIN1 or FBN1 depleted ECM.

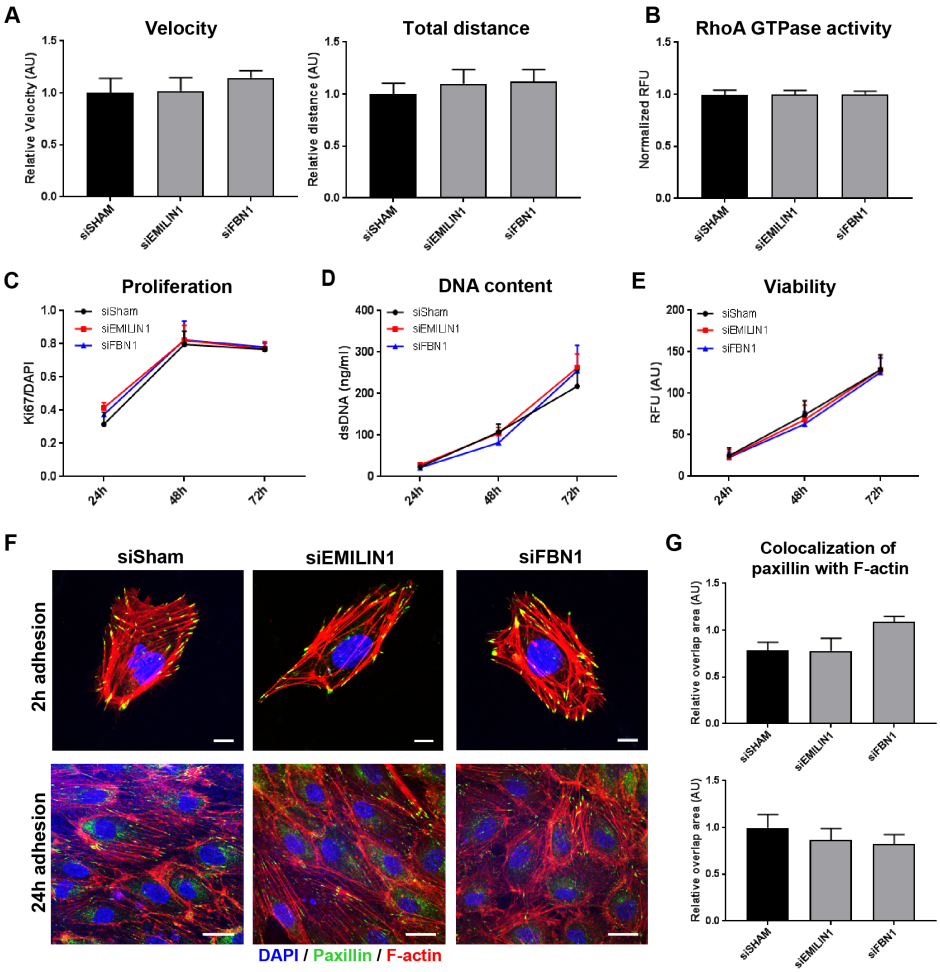

Figure 5. Depletion of EMILIN1 or FBN1 from the extracellular matrix layer has no effect on endothelial cells. (A) Live cell migration assay results showing the velocity and total distance of HUVECs cultured on siSham, siEMILIN1 or siFBN1 extracellular matrix (ECM). N=6 assays with 10 images per assay and 10 HUVECs per image. Shown is mean ± SEM. (B) RhoA activation measurements using the G-LISA RhoA GTPase activity assay in HUVECs cultured 24 hours on siSham, siEMILIN1 or siFBN1 ECM. N=4. Shown is mean ± SEM. (C) Ki67/DAPI ratio was used as a measure for HUVEC proliferation after 24, 48 and 72 hours of culturing on siSham, siEMILIN1 or siFBN1 ECM. N=3 assays with 20 fluorescent images per assay. Shown is mean ± SEM. (D) DNA content measurements with the PicoGreen assay was used as a measure for HUVEC proliferation after 24, 48 and 72 hours of culturing on siSham, siEMILIN1 or siFBN1 ECM. N=3 assays. Shown is mean ± SEM. (E) HUVEC viability was measured with the PrestoBlue assay after 24, 48 and 72 hours of culturing on siSham, siEMILIN1 or siFBN1 ECM. N=3 assays. Shown is mean ± SEM. (F) Representative Z-stacks of HUVECs cultured on siSham, siEMILIN1 or siFBN1 ECM for 2 hours (not confluent) or 24 hours (confluent) to show paxillin and F-actin changes after the initial binding to the ECM and after strong adhesion, respectively. Scale bars represent 20 µm.

(Figure 5 continued) (G) Colocalization of paxillin and F-actin in HUVECs cultured on siSham, siEMILIN1 or siFBN1 ECM for 2 hours (not confluent) or 24 hours (confluent). N=4 assays with 10 fluorescent images per assay. Shown is mean ± SEM.

All together, these findings indicate that depletion of EMILIN1 or FBN1 from the ECM has a significant effect on transcriptome level of ECs, but functional adaptation associated with the distinct mRNA profile was not detected.

Discussion

In this study, we characterized the ECM protein composition present in fetal and mature renal arteries and focused on the impact of two elastic proteins on ECs: EMILIN1 and FBN1. Enriched ECM was successfully obtained from human vascular tissue by decellularization and aided in the detection of ECM specific proteins using LC-MS/MS. Our main findings are as follows: (1) The ECM protein composition differs significantly between active (fetal) and quiescent (mature) vascular tissue. (2) Elastic ECM proteins EMILIN1 and FBN1 are significantly enriched in fetal renal arteries and are mainly produced by cells of mesenchymal origin. (3) SMCs-secreted ECM can be altered and tightly anchored to POMA-FN coverslips, creating a platform to study EC-matrix interactions. (4) EMILIN1 and FBN1 deficient ECM provokes alterations in HUVECs on transcriptome level that are associated with multiple pathways, especially Rho GTPase controlled pathways. (5) However, alterations in these pathways on transcriptome level does not provoke significant behavioral changes in HUVECs.

Our proteomic approach to unravel the differences between the fetal and mature vascular ECM has the potential to find interesting proteins that can influence EC behavior. Decellularization assured enrichment of ECM proteins before proteomic analysis. Not all cellular components were removed, as proteins associated with the actin cytoskeleton or with intermediate filaments were still detected, but it guaranteed an enriched ECM fraction of 38% and 35% in fetal and mature conditions, respectively. The complete matrisome accounts for ±4% of the human proteome[3], confirming the necessity to enrich for ECM proteins. Detergents for decellularization can be very stringent, however fragile components of the ECM (proteoglycans, secreted factors) were still detected in our samples.

ECM proteins were identified by crossreferencing with the Human Matrisome Project[3,9] and differences in protein abundance were observed between active (fetal) and quiescent (mature) vascular ECM. Overall, elastic proteins, such as

members from the EMILIN/multimerin and fibrillin families, are more abundant in the fetal ECM compared to the mature, while the contrary is observed for the laminin family and collagen type IV. Although it was already known that the mature basement membrane is rich in laminin and collagen type IV[5,27], the distribution of multiple subunits of laminin and collagen type IV in the active and quiescent vascular ECM is now further elucidated. Furthermore, this result is in line with the observation that a quiescent and more mature phenotype arises in ECs when cultured on a laminin coating when compared to a collagen coating[6].

Multiple members of the EMILIN/multimerin and fibrillin families are significantly more abundant in the fetal renal artery ECM compared to the mature, namely: EMILIN1, -2 and -3 and fibrillin-1 and -2. Fibrillin-2 is needed for the initial assembly of the aortic matrix during development and overlaps with fibrillin-1 expression[28]. This indicates an important role in embryonic development for fibrillin-2. Our vascular ECM catalogue provides a number of interesting targets for further research, especially ECM interaction proteins such as members from the MAGP and LTBP families. Mutations in Microfibril Associated Protein 5 (MFAP5), a member of the MGAP family, are linked to aortic aneurysms and dissections[29]. In concordance, double knockout of both MFAP2 and -5 in mice results in aortic dilation[30]. These studies indicate that MFAPs contribute to large vessel integrity. Latent Transforming Growth Factor Beta Binding Proteins (LTBPs) attach to both fibrillins and latency-associated protein of TGF-β (LAP), thereby forming a TGF-β reservoir within the ECM[31,32]. LTBP(1-4) null mice exhibit severe phenotypes, including defects in bone, lung and cardiovascular development[32]. These are examples of promising ECM proteins detected in this study known to be important during vascular development and might therefore be interesting candidates for improving the bioactivity of scaffolds for vascular tissue constructs.

Due to their abundant presence in our vascular ECM catalogue compared to other family members, elastic proteins EMILIN1 and FBN1 were selected in this study to further elucidate their impact on EC fate. The role of EMILIN1 is extensively studied in EMILIN1-deficient mice, which display aortic valve malformations and hypertension[20,33]. EMILIN1 plays a pivotal role in mice blood vessel development and elastogenesis[34,35]. Most of the diseases accompanied by EMILIN1 deficiency are driven by TGF-β. In the vasculature, EMILIN1 functions as an antagonist in the processing steps of TGF-β and thereby regulates vascular tone and blood pressure[36-38]. EMILIN1 has multiple domains which exhibit different functions in

the vasculature. The EMI domain is linked to hypertension and TGF-β processing[36], while adhesive functions of EMILIN1 are related to its gC1q domain. The gCq1 domain regulates cell migration and proliferation via a specific interaction with α4/α9/β1 integrins[17-19,23]. Similarly, FBN1 can mediate the adhesion, migration and proliferation of several cell types, including ECs[24]. Endothelium dysfunction is an important contributor to Marfan syndrome, caused by mutations in the *FBN1* gene. A heterozygous FBN1 mutation in mice accelerates vascular aging and eventually leads to aortic manifestations resembling those of Marfan syndrome[21].

RNA-sequencing data presented in this study hinted towards a regulatory role of EMILIN1 and FBN1 in Rho-mediated cytoskeleton rearrangements required for migration. Indeed, it has been shown that EMILIN1 acts as a guiding molecule in the migration of lymphatic ECs (LECs) and trophoblasts[16,18,23] and that FBN1 has the potential to enhance migration of HUVECs[24]. However, functional assays performed in this study revealed that HUVECs are not altered in their capacity to migrate when either EMILIN1 or FBN1 is depleted from the ECM. Rho-mediated adaptations of the actin cytoskeleton are also needed for proliferation. Studies have shown that EMILIN1 inhibits fibroblast, keratinocyte and LEC proliferation[17,18] and that FBN1 enhances HUVEC proliferation[24]. However, functional assays performed this study did not find any alterations in HUVEC proliferation when either EMILIN1 or FBN1 is depleted from the ECM. RNA-sequencing data also hinted towards decreased paxillin signaling in HUVECs cultured on EMILIN1 deficient ECM, but not on FBN1 deficient ECM. Paxillin is a focal adhesion adaptor protein known to be critical for cytoskeletal rearrangements during the formation and turnover of focal adhesions. Spesotto and colleagues revealed that EMILIN1 promotes a distinct cell adhesive phenotype with wide ruffles, actin filaments along the cell periphery and paxillin distribution evenly in the cell cytoplasm without any apparent focal adhesion formation[19]. We on the other hand, found no differences in paxillin or actin filament rearrangements in HUVECs grown on EMILIN1-deficient ECM.

This discrepancy with the existing literature may be attributed to differences in study design. We cultured our cells on a complex ECM network depleted from either EMILIN1 or FBN1 from the beginning, rather than using a pure EMILIN1 or FBN1 coating. Although this microenvironment resembles more the complex ECM *in vivo*, it might not be ideal to pick up small behavioral changes. On the other hand, our recently published study shows that renal epithelial cells cultured on

the exact same 2D ECM coating approach do respond to depletion of EMILIN1 by reducing their adhesive strength and subsequently adopting a more migratory phenotype[39].

Another explanation why we did not see an EC response to depletion of either EMILIN1 or FBN1 from the ECM is that we used HUVECs, which might actively express an integrin profile that is not sensitive to these small ECM changes. HUVECs have been used as the golden standard in vascular research since the late 1970s[40] and are considered to be a robust cell model with a high proliferation rate. Using a different and more ECM sensitive type of EC instead, for example HMVECs, could have resulted in a different outcome. In line with this hypothesis, EMLIN1 can regulate the proliferation of HMVECs and acts as a guiding molecule during their migration by interacting with α9 integrins actively expressed by these cells[18].

In conclusion, the addition of EMILIN1 or FBN1 to scaffolds holding HUVECs most likely will not have an effect on their adhesive and migratory behavior. EMILIN1 and FBN1 might still be interesting candidates for implementing in scaffolds holding other cell types, as previous studies have shown that these elastic proteins can act as regulators of cell adhesion and migration. Nevertheless, our human renal artery ECM proteome during active and quiescent vascular state contains many more promising ECM proteins involved in vascular development that are interesting candidates for further research on implementation in scaffolds of vascular tissue constructs.

Acknowledgements

We would like to thank Dr. O. G. de Jong for donating lentiviral GFP constructs and Dr. J. Y. Xu for performing immunohistochemical stainings of the human tissue.

This work was supported by Netherlands Foundation for Cardiovascular Excellence [C.C.], Netherlands Organization for Scientific Research Vidi grant [no. 91714302 to C.C.], the Erasmus MC fellowship grant [C.C.], the Regenerative Medicine Fellowship grant of the University Medical Center Utrecht [C.C.], the Netherlands Cardiovascular Research Initiative: An initiative with support of the Dutch Heart Foundation [CVON2014-11 RECONNECT to C.C., D.D., and M.V.] and the Ministry of Education, Culture and Science [Gravitation Program 024.003.013].

Materials and Methods

Human tissue

Healthy human fetal and mature renal artery tissue was used for ECM analysis by liquid chromatography tandem mass spectrometry (LC-MS/MS). Fetal renal arteries were obtained from the department of Molecular Cell Biology at the Leiden UMC. Samples from mature renal arteries were obtained from the department of Pathology at the Erasmus MC. All samples were fresh-frozen and stored at -80°C prior to use.

Sample preparation

To enrich the ECM protein content, renal arteries were decellularized by several detergents. First, 1% SDS was used to decellularize the tissue for 12 hours. Next, 1% Triton X-100 was used for 1 hour. The samples were washed for 2 hours with PBS to remove the detergents. All steps were performed at room temperature and under constant rotation. Frozen sections of decellularized and non-decellularized tissue were used for hematoxylin and eosin (HE) staining to confirm complete decellularization of the renal arteries while preserving the ECM architecture. Decellularized renal arteries were homogenized in lysis buffer (10 mM Tris (pH 7.4), 100 mM NaCl, 0.1% SDS, 0.5% sodium deoxycholate, 1% Triton X-100, 1 mM EGTA, 1 mM EDTA, 10% Glycerol, 1 mM NaF, 1 mM sodium orthovanadate and a protease inhibitor cocktail (Roche)) using an Ultra-Turrax (IKA). Lysates were placed on ice for 30 minutes and cell debris was pelleted via centrifugation (10 min, 1000xg, 4°C). A pool of either 2 mature or 3 fetal renal arteries was considered as 1 sample for sufficient protein yield (Supplemental Table 6). Tissue lysates were separated by SDS-PAGE on an equally loaded pre-cast 4-12% linear gradient gel (NuPAGE Bis-Tris Mini gels, Life Technologies) and visualized with Coomassie Blue (Supplemental Figure 1A). LC-MS/MS analysis was performed in triplicate.

LC-MS/MS analysis

SDS-PAGE separated samples were prepared according previously used protocols for LC-MS/MS analysis by the Proteomics Centre of the Erasmus MC[39]. In short, protein lanes were cut out of the gel, reduced with dithiothreitol, alkylated with iodoacetamide and digested with trypsin as described previously[41]. Supernatants were stored in glass vials at -20°C until further measurements. An 1100 series capillary LC system (Agilent Technologies) was used for nanoflow LC-MS/MS coupled to an LTQ-Orbitrap XL mass spectrometer (Thermo) operating in positive mode and equipped with a nanospray source as previously described[42]. Samples were trapped on a 1.5 cm x 100 µm in-house packed ReproSil C18 reversed phase column (Dr Maisch GmbH) at a flow rate of 8 µl/min. Sequentially, samples

were separated on a 15 cm x 50 µm in-house packed ReproSil C18 reversed phase column (Dr Maisch GmbH) by adding a linear gradient from 0-80% solvent B in solvent A, where A consisted of 0.1 % formic acid and B of 80% (v/v) acetonitrile and 0.1 % formic acid. Flow rate was set at 200 nl/min, and elution took place in 70 minutes. The eluent was sprayed by a nanospray device directly into the ESI source of the LTQ ion trap mass spectrometer. Mass spectra were acquired in continuum mode; peptide fragmentation was performed in data-dependent mode. MS/MS spectra were extracted out of raw data files and were analysed by using MaxQuant software as previously described[43].

MS data analysis

Analysis was conducted with proteins present in at least 2 fetal or 2 mature sample groups. Data from the Human Matrisome project[3,9] was used to filter ECM core and associated proteins from the generated datasets. Label free quantification (LFQ) intensity was used to further specify the abundance of ECM components in the fetal and mature renal artery. Differences in the abundance of ECM components between fetal and mature tissue was showed as percentage of the total ECM protein signal.

Immunohistochemistry

Protein validation was performed by immunohistochemistry on 7 µm thick frozen sections of non-decellularized tissue. Frozen sections were used for a standard hematoxylin and eosin stainings and for protein specific stainings. Aceton fixed sections were blocked with 1% BSA in PBS for 1 hour. Polyclonal primary antibodies against EMILIN1 and FBN1 were diluted in 1% BSA/PBS (1:100 and 1:200, respectively; both Sigma) and incubated for 1 hour at room temperature. Sections were washed 3 times in PBS/T solution and incubated with Alexa Fluor 488 donkey anti-goat IgG (1:100; Life Technologies) and αSMA-Cy3 (1:500; Sigma) diluted in 1% BSA/PBS for 1 hour at room temperature. After 3 times washing with PBS/T solution, sections were incubated with DAPI for 5 minutes, washed with PBS and mounted. Stained sections were imaged using fluorescent microscope (Olympus) and ImageJ (version 1.47) to analyze EMILIN1, FBN1 and αSMA area.

Cell culture

Human umbilical vein endothelial cells (HUVECs; Lonza) and HUVECs transfected with lentiviral green fluorescent protein (GFP) were cultured on gelatin coated plates in endothelial growth medium (EBM-2 basal medium supplemented with EGM-2 bullit kit; Lonza) in 5% CO_2 at 37°C. Human smooth muscle cells (SMCs) were cultured on gelatin coated plates in smooth muscle growth medium (SMBM basal medium supplemented

with SMGM bullet kit; Lonza) in 5% CO_2 at 37°C. Experiments were performed with cells between passage 3 and 6. Knockdown of the ECM components FBN1 and EMILIN1 were performed using their specific ON-TARGETplus SMARTpool siRNAs (Dharmacon) and DharmaFECT-1 (Dharmacon) with a final concentration of 200nM. ON-TARGETplus Non-targeting pool (siSham; Dharmacon) was used as a negative control (Supplemental Table 7)

POMA slides for tight anchoring of ECM

To anchor secreted ECM proteins, coverslips were treated following the protocol as described by Labit *et al*[44]. Briefly, contaminants on coverslips (ø18mm; VWR) were removed by serially washing with acetone, methanol/water and chloroform in combination with sonication. Coverslips were oxidized using piranha solution consisting of sulphuric acid (99,99%; Sigma) and hydrogen peroxide (35% wt. in H2O, Merck) in a ratio of 7:3, followed by silanization with a 2% (3-Aminopropyl)triethoxysilane (APTES, 99%; Sigma) solution in 95% ethanol. A poly(maleic anhydride-*alt*-1-octadecene) (POMA; Sigma) layer was applied by spin coating at 4000 rpm for 30 seconds, using a 0.16% solution of POMA in tetrahydrofuran (Sigma). Polymerized coverslips were sterilized with UV-light and used immediately or stored in the dark at room temperature. Prior to cell culture, POMA treated coverslips were coated with 50 µg/ml fibronectin (Roche) in PBS for 1 hour at 37°C, creating POMA-FN coverslips.

SMCs were harvested and seeded onto POMA-FN coverslips at 150.000 cells per well. After transfection with siRNA, cells were cultured for six days in order to produce sufficient ECM. Decellularization was achieved by mild agitation in combination with warm 20 mM ammonium hydroxide. Light microscopy was used to confirm whether decellularization was complete. Coverslips were incubated with DNase (Qiagen) for 15 minutes at room temperature to remove DNA traces. Finally, decellularized ECM layers were washed in ultrapure water and PBS to remove cellular residues.

Immunocytochemistry

Prior to fixation, both control and decellularized ECM layers were washed in PBS twice. Samples were fixated with 4% paraformaldehyde (PFA), permeabilized with 0.1% Triton X-100 and blocked with 1% BSA in PBS. Samples were incubated for 1 hour with collagen IV antibody (1:50, Millipore), EMILIN1 antibody (1:100; Sigma) or FBN1 antibody (1:200; Sigma). Samples were incubated with Alexa Fluor 488 donkey anti-goat IgG (1:100, Life Technologies) or Alexa Fluor 488 goat anti-rabbit IgG (1:100, Life Technologies) and Alexa Fluor 594 donkey anti-goat IgG (1:100; Life Technologies) or rhodamine-phalloidin

(1:40; Life Technologies) in the dark for 1 hour. Nuclei were counterstained with DAPI (1:5000) for 15 minutes. Washing with 0.05% Tween in PBS occurred after every antibody incubation. Samples were mounted on object slides using Mowiol. Imaging was performed using a Leica SP8X confocal microscope and LAS X software. Z-stacks were made to capture all fluorescent signal (5 a 6 Z-stacks/coverslip). Projections of the Z-stack images were analyzed with ImageJ to calculate the area of EMILIN1, FBN1, collagen IV and F-actin.

Quantitative PCR

RNA was isolated at indicated time points using ISOLATE II RNA kit (Bioline) and cDNA was made using SensiFAST cDNA synthesis kit (Bioline) according to the manufacturer's protocol. qPCR was performed using FastStart Universal SYBR Green Master (Roche) according the following qPCR program: 8.5' 95 °C, 38 cycles (15" 95 °C; 45" 60 °C) 1' 95 °C, 1' 65 °C, 62 cycles (10" 65 °C + 0.5 °C). Expression levels are relative to housekeeping gene *β-actin*. Primer sequences are listed in Supplemental Table 8.

Endothelial cell assays

HUVECs were cultured on siSham, EMILIN1 and FBN1 deficient ECM for various assays:
RNA sequencing: RNA was isolated from HUVECs using the ISOLATE II RNA kit after 24 hours culturing. RNA sequencing was done as previously described[45]. Briefly, sequencing libraries were made from poly-adenylated RNA using the Rapid Directional RNA-Seq Kit (NEXTflex) and sequenced on Illumina NextSeq500 to produce single-end 75 base long reads (Utrecht Sequencing Facility). Reads were aligned to the human reference genome GRCh37 using STAR version2.4.2a. Read groups were added to the BAM files with Picard's AddOrReplaceReadGroups (v1.98). The BAM files were sorted with Sambamba v0.4.5, and transcript abundances were quantified with HTSeq-count version 0.6.1p117 using the union mode. Subsequently, reads per kilobase of transcript per million reads sequenced were calculated with edgeR's rpkm() function. RNA-seq results were analyzed using Qiagen's Ingenuity Pathway Analysis (IPA). IPA was used to identify pathways that were altered by differentially expressed genes. P-values were calculated by IPA based on a right-tailed Fisher Exact Test.
Proliferation assay: HUVECs were fixed with 4% PFA after 24, 48 and 72 hours of culturing. Proliferation was assessed by staining with a Ki67 antibody (1:200; ThermoScientific). Coverslips were imaged using a Leica DM 5500B microscope and images were quantified for $Ki67^+$ and $DAPI^+$ cells using ImageJ.
PicoGreen assay: HUVECs were isolated from the ECM coverslips after 24, 48 and 72 hours culturing for dsDNA measurements using PicoGreen according to the manufacturer's

protocol (ThermoFisher).

PrestoBlue assay: Viability was measured using PrestoBlue Cell Viability Reagent (ThermoScientific) in the medium of HUVECs cultured on siRNA treated ECM for 24, 48 and 72 hours according to the manufacturer's protocol.

Adhesion assay: After 2 and 24 hours, HUVECs were fixed with 4% PFA. Adhesion was assessed by staining with a paxillin antibody (1:100; Abcam). Projection of the Z-stack images were analyzed using ImageJ to calculate the area of paxillin, F-actin (phalloidin) and their colocalization.

Migration assay: HUVECs-GFP (to visualize the cells) were live imaged overnight using a Leica SP8X confocal microscope at 37°C and humid atmosphere containing 5% CO_2. Single cell migration was imaged every 15 minutes at 10 positions in each condition. Obtained videos were analyzed using ImageJ Manual Tracking and Chemotaxis Tool.

RhoA GTPase activity assay: HUVECs were starved overnight in bare EBM-2 medium and stimulated to activate RhoA for 5 minutes in full EGM-2 medium 24 hours after seeding. Cells were lysed for GTPase activity using the G-Lisa RhoA Activation Assay Colorimetric Kit (Cytoskeleton) according to the manufacturer's protocol.

Statistical analysis

All results were analyzed and presented using GraphPad Prism 6. All statistical comparisons were made by performing a Student's t-test or a one-way ANOVA. Error bars were visualized as standard error of the mean. P-values < 0.05 were considered statistically significant.

References

1. Stratman AN, Malotte KM, Mahan RD, et al. Pericyte recruitment during vasculogenic tube assembly stimulates endothelial basement membrane matrix formation. Blood. 2009;114(24):5091-5101.
2. Stratman AN, Davis GE. Endothelial cell-pericyte interactions stimulate basement membrane matrix assembly: influence on vascular tube remodeling, maturation, and stabilization. Microsc Microanal. 2012;18(1):68-80.
3. Naba A, Clauser KR, Hoersch S, et al. The matrisome: in silico definition and in vivo characterization by proteomics of normal and tumor extracellular matrices. Mol Cell Proteomics. 2012;11(4):M111.014647.
4. Hynes RO, Naba A. Overview of the matrisome--an inventory of extracellular matrix constituents and functions. Cold Spring Harb Perspect Biol. 2012;4(1):a004903.
5. Davis GE, Senger DR. Endothelial extracellular matrix: biosynthesis, remodeling, and functions during vascular morphogenesis and neovessel stabilization. Circ Res. 2005;97(11):1093-1107.
6. Liu Y, Senger DR. Matrix-specific activation of Src and Rho initiates capillary morphogenesis of endothelial cells. Faseb j. 2004;18(3):457-468.
7. Thottappillil N, Nair PD. Scaffolds in vascular regeneration: current status. Vasc Health Risk Manag. 2015;11:79-91.
8. Bouten CVC, Smits A, Baaijens FPT. Can We Grow Valves Inside the Heart? Perspective on Material-based In Situ Heart Valve Tissue Engineering. Front Cardiovasc Med. 2018;5:54.
9. Naba A, Clauser KR, Ding H, et al. The extracellular matrix: Tools and insights for the "omics" era. Matrix Biol. 2016;49:10-24.
10. Barallobre-Barreiro J, Oklu R, Lynch M, et al. Extracellular matrix remodelling in response to venous hypertension: proteomics of human varicose veins. Cardiovasc Res. 2016;110(3):419-430.
11. Mustafa DA, Dekker LJ, Stingl C, et al. A proteome comparison between physiological angiogenesis and angiogenesis in glioblastoma. Mol Cell Proteomics. 2012;11(6):M111.008466.
12. Bressan GM, Daga-Gordini D, Colombatti A, et al. Emilin, a component of elastic fibers preferentially located at the elastin-microfibrils interface. J Cell Biol. 1993;121(1):201-212.
13. Kielty CM, Sherratt MJ, Shuttleworth CA. Elastic fibres. J Cell Sci. 2002;115(Pt 14):2817-2828.
14. Colombatti A, Spessotto P, Doliana R, et al. The EMILIN/Multimerin family. Front Immunol. 2011;2:93.
15. Verdone G, Corazza A, Colebrooke SA, et al. NMR-based homology model for the solution structure of the C-terminal globular domain of EMILIN1. J Biomol NMR. 2009;43(2):79-96.
16. Verdone G, Doliana R, Corazza A, et al. The solution structure of EMILIN1 globular C1q domain reveals a disordered insertion necessary for interaction with the alpha4beta1 integrin. J Biol Chem. 2008;283(27):18947-18956.
17. Danussi C, Petrucco A, Wassermann B, et al. EMILIN1-alpha4/alpha9 integrin interaction inhibits dermal fibroblast and keratinocyte proliferation. J Cell Biol. 2011;195(1):131-145.
18. Danussi C, Del Bel Belluz L, Pivetta E, et al. EMILIN1/alpha9beta1 integrin interaction is crucial in lymphatic valve formation and maintenance. Mol Cell Biol. 2013;33(22):4381-4394.
19. Spessotto P, Cervi M, Mucignat MT, et al. beta 1 Integrin-dependent cell adhesion to EMILIN-1 is mediated by the gC1q domain. J Biol Chem. 2003;278(8):6160-6167.
20. Angel PM, Narmoneva DA, Sewell-Loftin MK, et al. Proteomic Alterations Associated with Biomechanical Dysfunction are Early Processes in the Emilin1 Deficient Mouse Model of Aortic Valve Disease. Ann Biomed Eng. 2017;45(11):2548-2562.
21. Mariko B, Pezet M, Escoubet B, et al. Fibrillin-1 genetic deficiency leads to pathological ageing of arteries in mice. J Pathol. 2011;224(1):33-44.
22. Sakai LY, Keene DR, Renard M, et al. FBN1: The disease-causing gene for Marfan syndrome and

other genetic disorders. Gene. 2016;591(1):279-291.
23. Spessotto P, Bulla R, Danussi C, et al. EMILIN1 represents a major stromal element determining human trophoblast invasion of the uterine wall. J Cell Sci. 2006;119(Pt 21):4574-4584.
24. Mariko B, Ghandour Z, Raveaud S, et al. Microfibrils and fibrillin-1 induce integrin-mediated signaling, proliferation and migration in human endothelial cells. Am J Physiol Cell Physiol. 2010;299(5):C977-987.
25. Provenzano PP, Keely PJ. Mechanical signaling through the cytoskeleton regulates cell proliferation by coordinated focal adhesion and Rho GTPase signaling. J Cell Sci. 2011;124(Pt 8):1195-1205.
26. Hu YL, Lu S, Szeto KW, et al. FAK and paxillin dynamics at focal adhesions in the protrusions of migrating cells. Sci Rep. 2014;4:6024.
27. Marchand M, Monnot C, Muller L, et al. Extracellular matrix scaffolding in angiogenesis and capillary homeostasis. Semin Cell Dev Biol. 2019;89:147-156.
28. Carta L, Pereira L, Arteaga-Solis E, et al. Fibrillins 1 and 2 perform partially overlapping functions during aortic development. J Biol Chem. 2006;281(12):8016-8023.
29. Barbier M, Gross MS, Aubart M, et al. MFAP5 loss-of-function mutations underscore the involvement of matrix alteration in the pathogenesis of familial thoracic aortic aneurysms and dissections. Am J Hum Genet. 2014;95(6):736-743.
30. Combs MD, Knutsen RH, Broekelmann TJ, et al. Microfibril-associated glycoprotein 2 (MAGP2) loss of function has pleiotropic effects in vivo. J Biol Chem. 2013;288(40):28869-28880.
31. Nakajima Y, Miyazono K, Kato M, et al. Extracellular fibrillar structure of latent TGF beta binding protein-1: role in TGF beta-dependent endothelial-mesenchymal transformation during endocardial cushion tissue formation in mouse embryonic heart. J Cell Biol. 1997;136(1):193-204.
32. Rifkin DB, Rifkin WJ, Zilberberg L. LTBPs in biology and medicine: LTBP diseases. Matrix Biol. 2018;71-72:90-99.
33. Litteri G, Carnevale D, D'Urso A, et al. Vascular smooth muscle Emilin-1 is a regulator of arteriolar myogenic response and blood pressure. Arterioscler Thromb Vasc Biol. 2012;32(9):2178-2184.
34. Braghetta P, Ferrari A, de Gemmis P, et al. Expression of the EMILIN-1 gene during mouse development. Matrix Biol. 2002;21(7):603-609.
35. Zanetti M, Braghetta P, Sabatelli P, et al. EMILIN-1 deficiency induces elastogenesis and vascular cell defects. Mol Cell Biol. 2004;24(2):638-650.
36. Zacchigna L, Vecchione C, Notte A, et al. Emilin1 links TGF-beta maturation to blood pressure homeostasis. Cell. 2006;124(5):929-942.
37. Raman M, Cobb MH. TGF-beta regulation by Emilin1: new links in the etiology of hypertension. Cell. 2006;124(5):893-895.
38. Carnevale D, Facchinello N, Iodice D, et al. Loss of EMILIN-1 Enhances Arteriolar Myogenic Tone Through TGF-beta (Transforming Growth Factor-beta)-Dependent Transactivation of EGFR (Epidermal Growth Factor Receptor) and Is Relevant for Hypertension in Mice and Humans. Arterioscler Thromb Vasc Biol. 2018;38(10):2484-2497.
39. Louzao-Martinez L, van Dijk CGM, Xu YJ, et al. A proteome comparison between human fetal and mature renal extracellular matrix identifies EMILIN1 as a regulator of renal epithelial cell adhesion. Matrix Biology Plus. 2019.
40. Sacks T, Moldow CF, Craddock PR, et al. Oxygen radicals mediate endothelial cell damage by complement-stimulated granulocytes. An in vitro model of immune vascular damage. J Clin Invest. 1978;61(5):1161-1167.
41. Wilm M, Shevchenko A, Houthaeve T, et al. Femtomole sequencing of proteins from polyacrylamide gels by nano-electrospray mass spectrometry. Nature. 1996;379(6564):466-469.

42. Sap KA, Bezstarosti K, Dekkers DHW, et al. Quantitative Proteomics Reveals Extensive Changes in the Ubiquitinome after Perturbation of the Proteasome by Targeted dsRNA-Mediated Subunit Knockdown in Drosophila. J Proteome Res. 2017;16(8):2848-2862.
43. Cox J, Mann M. MaxQuant enables high peptide identification rates, individualized p.p.b.-range mass accuracies and proteome-wide protein quantification. Nat Biotechnol. 2008;26(12):1367-1372.
44. Labit H, Goldar A, Guilbaud G, et al. A simple and optimized method of producing silanized surfaces for FISH and replication mapping on combed DNA fibers. Biotechniques. 2008;45(6):649-652, 654, 656-648.
45. Brandt MM, Meddens CA, Louzao-Martinez L, et al. Chromatin Conformation Links Distal Target Genes to CKD Loci. J Am Soc Nephrol. 2018;29(2):462-476.

Supplemental Figures

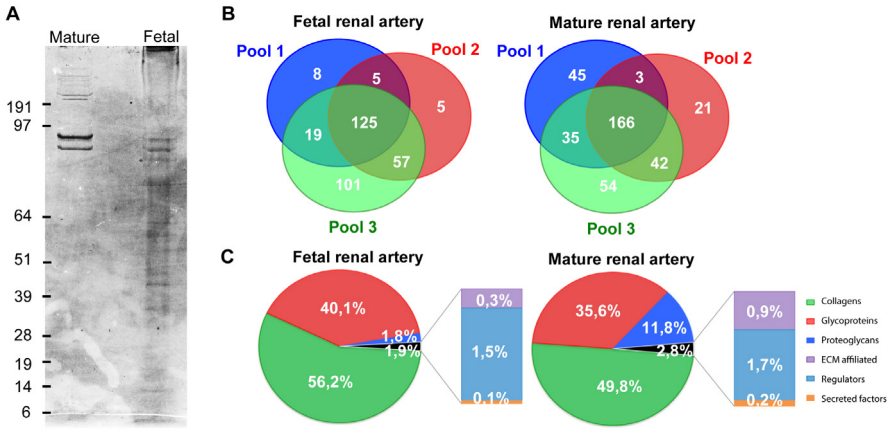

Supplemental Figure 1. (A) Extracellular matrix (ECM) lysates from human fetal and mature renal arteries were separated by SDS-PAGE and stained with Coomassie Blue prior to LC-MS/MS analysis. Shown is a representative blot of 3 experiments containing pooled renal arteries samples (fetal or mature). (B) Venn diagrams showing the total amount and overlap of proteins identified in the three pools of either fetal and mature samples by LC-MS/MS. Proteins identified in at least 2 pools were used for further analysis. (C) Pie charts showing the distribution of the six matrisome classes in percentages of the LFQ intensity compared to the LFQ intensity of the total matrisome present in fetal and mature human renal arteries.

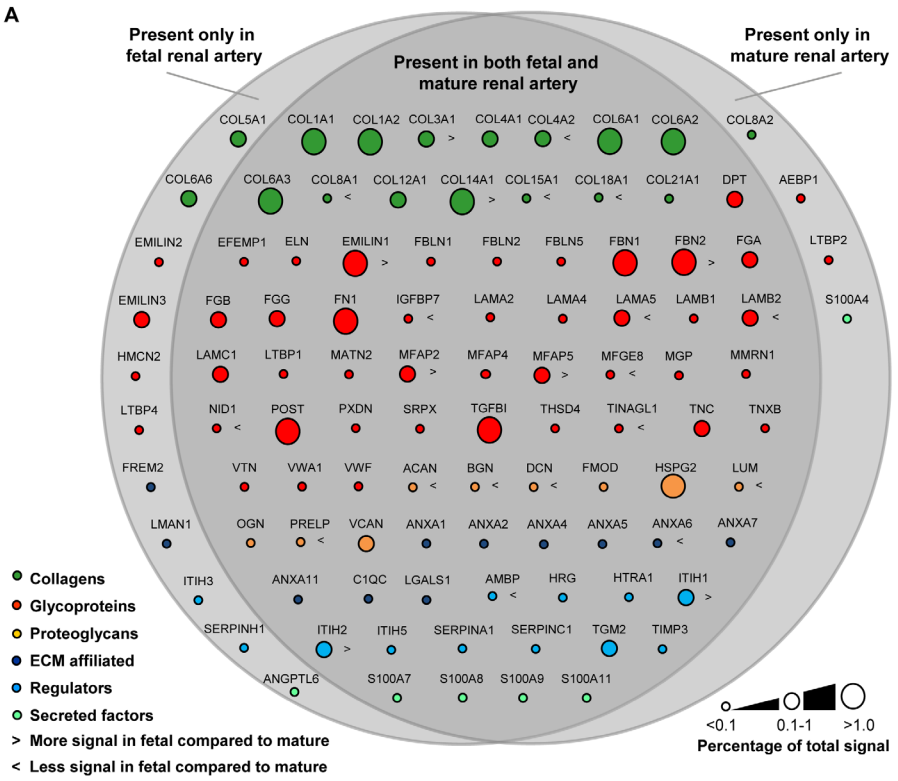

Supplemental Figure 2. (A) Euler-diagram visualizing the overlap and differences between the human fetal and mature renal artery proteome. Each node represents an extracellular matrix (ECM) protein labeled with the gene name. Node size represents protein abundance in percentages of the total protein signal. Shown is the mean of all pooled samples (N=3).

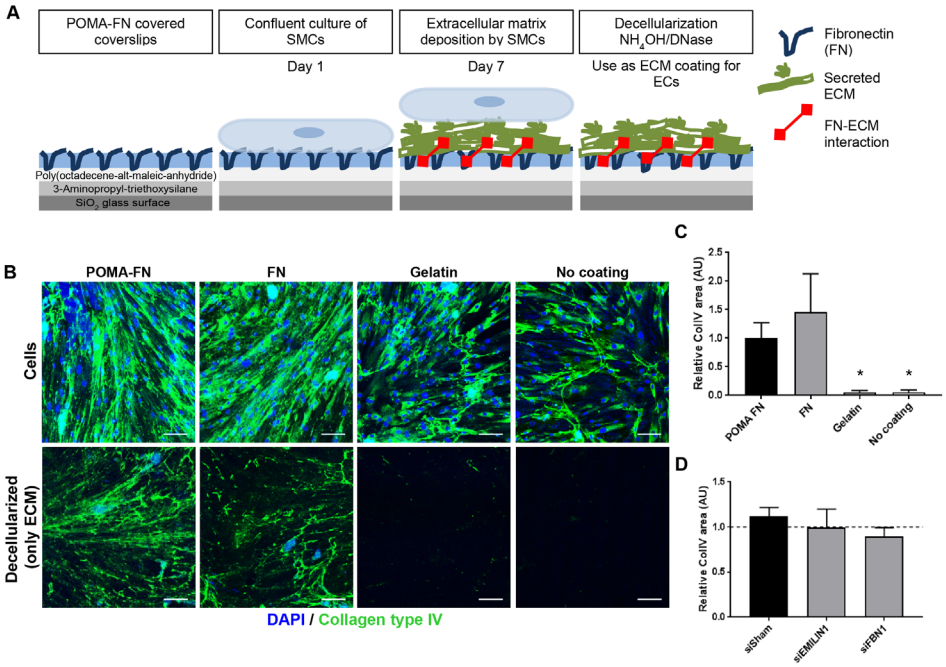

Supplemental Figure 3. (A) Timeline for the production of smooth muscle cell (SMC) derived extracellular matrix (ECM) on poly(octadecene-*alt*-maleic) anhydride-fibronectin (POMA-FN) treated coverslips. First, coverslips are oxidized using piranha solution to link a silane group to the aminosilane (APTES) group. Next, APTES binds POMA, which on its turn can covalently bind fibronectin (FN). Over time, SMCs deposit ECM, which covalently binds to the FN layer, thereby anchoring the secreted ECM. Ammoniumhydroxide (NH_4OH) and DNase treatments remove all traces of the SMCs, leaving only a cell-derived ECM coating attached to a glass coverslip behind that can be used for functional assays. (B) Representative immunofluorescence images of SMCs cultured for 6 days on coverslips with a coating of either POMA-FN, FN or gelatin or without a coating. All cells are positively stained for collagen type IV. After decellularization, deposited collagen type IV remained anchored to only POMA-FN and FN treated coverslips. Scale bars represent 100 µm. (C) Quantification of collagen type IV area deposited by SMC on coverslips with different coatings (POMA-FN, FN or gelatin or no coating). N=4-5. Shown is mean ± SEM; *P<0.05 when compared to POMA-FN (One-way ANOVA). (D) Quantification of collagen type IV area deposited by SMC treated by different siRNAs (siSham, siEMILIN1 or siFBN1). N=5-7. Shown is mean ± SEM. Non-treated SMCs are set to 1 (dotted line).

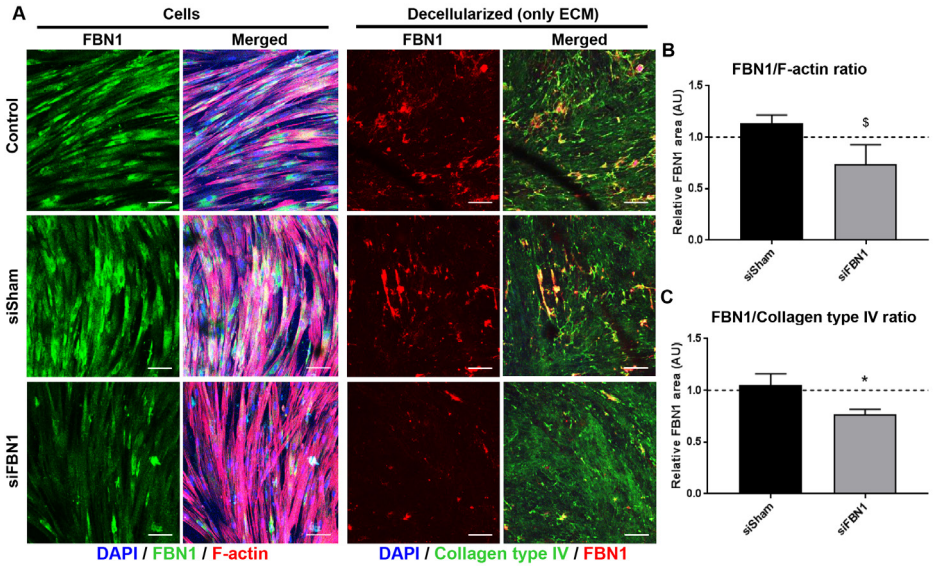

Supplemental Figure 4. (A) Representative Z-stacks of SMCs cultured for 6 days after siRNA transfection and after decellularization. Stained for FBN1 and either F-actin (cells) or collagen type IV (Extracellular matrix (ECM)). Scale bars represent 100 µm. (B) Quantification of FBN1 signal corrected for the amount of F-actin in siRNA treated SMCs. N=4. Shown is mean ± SEM; $P<0.10. (C) Quantification of FBN1 signal corrected for the amount of collagen type IV present in SMC-derived ECM. N=5. Shown is mean ± SEM; *P<0.05. Non-treated SMCs are set to 1 (dotted lines).

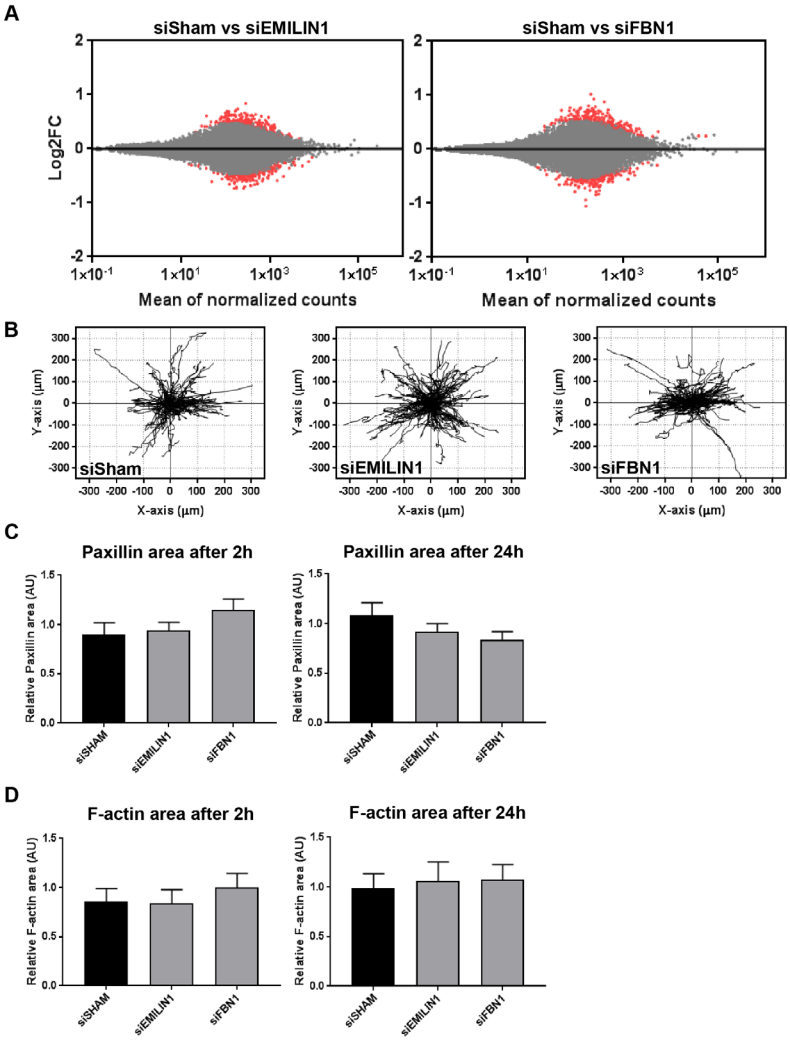

Supplemental Figure 5. (A) Visualization of differential gene expression in which Log2 fold change (FC) is plotted against the mean of normalized counts (MA-plot) in HUVECs cultured on siSham extracellular matrix (ECM) vs. either EMILIN1-deficient or FBN1-deficient ECM. Gray dots represent non-differentially expressed genes, red dots represent differentially expressed genes (P<0.05, 481 and 474 genes for siEMILIN1 and siFBN1, respectively). RNA sequencing was performed on 3 samples per condition. (B) Representative migration plots showing tracks of individual HUVEC on siRNA treated ECM (siSham, siEMILIN1 or siFBN1). Migration of HUVECs was traced overnight with a confocal microscope. N=4 assays with ±90 individual tracks per assay. Paxillin area (C) and F-actin area (D) in HUVECs after 2 hours (not confluent) or after 24 hours (confluent) of culture on siRNA-treated ECM (siSham, siEMILIN1 or siFBN1). N=4. Shown is mean ± SEM.

Supplemental Tables

Supplemental tables can be downloaded from: http://bit.ly/2MhVPyI

Extracellular matrix – **Chapter 4**

Characteristic adaptations of the extracellular matrix in dilated cardiomyopathy

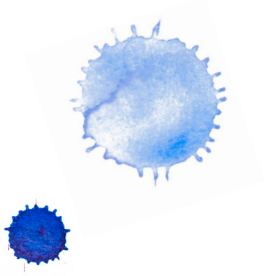

L. Louzao Martinez, A. Vink, M. Harakalova, F.W. Asselbergs, M.C. Verhaar, C. Cheng.

(2016) International Journal of Cardiology, 1(220):634-646

Abstract

Dilated cardiomyopathy (DCM) is a relatively common heart muscle disease characterized by the dilation and thinning of the left ventricle accompanied with left ventricular systolic dysfunction. Myocardial fibrosis is a major feature in DCM and therefore it is inevitable that corresponding extracellular matrix (ECM) changes are involved in DCM onset and progression. Increasing our understanding of how ECM adaptations are involved in DCM could be important for the development of future interventions. This review article discusses the molecular adaptations in ECM composition and structure that have been reported in both animal and human studies of DCM. Furthermore, we provide a transcriptome-based catalogue of ECM genes that are associated with DCM, generated by using NCBI Gene Expression Omnibus database sets for DCM. Based on this *in silico* analysis, many novel ECM components involved in DCM are identified and discussed in this review. With the information gathered, we propose putative pathways of ECM adaptations in onset and progression of DCM.

Dilated cardiomyopathy

In the developed world, 1-2% of the population suffers from heart failure, from which approximately half of the patients have systolic heart failure with a reduction in ejection fraction of at least 40%. The underlying cause for systolic heart failure is predominantly ischemic heart disease and dilated cardiomyopathy (DCM). DCM is a relatively common heart muscle disease with a prevalence that increases with age: it is rare in the pediatric population (1-2:100,000), however in adults it has an estimated prevalence of 1:2500[1,2]. The disease is characterized by the dilation and thinning of the left ventricle accompanied with left ventricular systolic dysfunction[3,4]. The diagnosis is primarily based on evidence of dilation and impaired contraction of the left ventricle (left ventricular ejection fraction (LVEF) <45%)[3-5]. DCM has a poor prognosis with a five-year survival rate of approximately 50% after diagnosis[6].

The etiology of DCM can be divided into ischemic (50-70%) and non-ischemic (30-50%), with the latter phenotype including genetic and acquired causes[7]. In Western countries, 20-50% of DCM patients have evidence for familial disease. Autosomal dominant is the primary mode of inheritance, although X-linked, recessive and mitochondrial inheritance occur as well. It is important to consider that sporadic DCM cases can also be due to genetic mutations[4,8]. Genetic forms of DCM are caused by mutations in cytoskeletal, sacromeric protein, Z-band, nuclear membrane, intercalated disc protein genes etc.[3,8]. Recently, up to 110 nuclear genes and 24 mitochondrial DNA genes have been linked to DCM[9]. Regarding the acquired causes of DCM; chronic myocardial inflammation (myocarditis) can lead to DCM at a later stage and is most commonly evoked by infectious triggers. The majority of non-ischemic DCM cases (≥70%) are considered idiopathic: they remain unexplained after a thorough search for primary or secondary causes[7].

Myocardial fibrosis is a major feature in DCM[10-12]. In cardiac tissue, fibrosis has often been described to develop in the setting of an ischemic scar as a result of a myocardial infarction (MI). This reparative response is referred to as replacement fibrosis: dead cardiomyocytes are replaced mainly by collagen. Myocardial fibrosis has also been increasingly recognized in diffuse form in the absence of an ischemic trigger as reported in cardiomyopathies, including DCM[10,11]. Here, the cardiac interstitial space expands without cell loss, leaving a patchy fibrotic pattern in the myocardium or large collagen strands in between cardiomyocytes. This type of fibrosis is called reactive or interstitial fibrosis. Myocardial fibrosis is a pathogenic form of extracellular matrix (ECM) remodeling and therefore it is inevitable that corresponding ECM changes are involved in DCM development and progression.

Various animal and human studies have been performed in the last decades trying to elucidate the role of ECM components in DCM and the clinical manifestation of DCM, systolic heart failure (SHF). Studies based on non-ischemic and non-genetic DCM and SHF are summarized and briefly discussed in the following two paragraphs. The third paragraph will discuss the new information gathered from the online NCBI Gene Expression Omnibus (GEO) database sets for DCM. Based on this, we propose putative pathways of ECM adaptations in onset and progression of DCM.

Extracellular matrix adaptation in myocardial fibrosis associated with systolic heart failure and dilated cardiomyopathy

Animal studies

Collagen and type I/III collagen ratio

In relation to SHF and DCM, various animal models demonstrated that these diseases are causally associated with changes in ECM composition, structure and function (Table 1). Already in 1990, Weber and colleagues[13] performed a histopathological study with dilated LVs of dogs that underwent rapid ventricular pacing. In these tissue samples, disruption by degradation and disappearance of collagen fibers together with interstitial fibrosis in the midwall and epimyocardium was observed. The collagen network in the heart consist mostly of type I and III collagen, that self-organize into fibrils with a diameter ranging from 0.01 to 3 μm[14]. These fibrillar collagens aggregate into fibers that are connected through cross-links and form a strong tensile network that tethers cardiomyocytes in support of their alignment. Supported by this typical ECM configuration, the myocyte-generated force can be transduced in all directions. Pro-collagen molecules in their long and rigid triple helix forms are synthesized mostly by fibroblasts and secreted into the interstitial space. Here they will undergo cleavage of their end-terminal pro-peptide sequences to enable collagen fiber formation, since the resultant collagen molecule will be less soluble. This process is crucial in collagen network formation as it initiates self-assembly into collagen fibrils. Quantification of these cleaved terminal peptides can serve as a measure for the activity of the fibrotic process[15].

The ratio of type III to type I collagen can be considered as an index of myocardial distensibility, since type I is stiffer and provides more tensile strength when compared to type III, that is more elastic. The collagen type I/type III ratio is

relatively stable in the healthy myocardium. However, in cardiomyopathies, studies imply that this ratio will shift. Subsequent studies performed by various research groups have analyzed in more detail the role of specific ECM components in DCM development and progression (Table 1). A study of ECM changes in a popular experimental model of DCM, hereditary dilated cardiomyopathy in hamsters (BIO 53.58 hamsters), demonstrated that type III collagen increases significantly at 10 weeks of age, whereas the total collagen content remains stable in control hamsters[16]. In addition, Masutomo and colleagues[17] found a significant increase in the collagen type III:I ratio in the hearts of BIO 53.38 hamsters at 20 and 40 weeks of age, when compared with age-matched control hamsters, further suggesting that the ECM of the affected hamsters was decreased in myocardial stiffness. Collagen crosslinks increased as cardiomyopathy progressed in BIO 53.58 hamsters, suggesting that the formation of crosslinks is activated at the stage of cardiac dilation. The solubility of collagen depends on the amount of crosslinks formed. Therefore, this advanced cross-linking in BIO 53.58 hamsters may indicate a progressive decrease in acid solubility of collagen[16]. In contrast, Woodiwiss and colleagues[18] reported a decrease in the ratio of myocardial insoluble to soluble collagen in two different rat models of systolic chamber dysfunction with LV dilation. In one of these models, an increase in the myocardial collagen type I to type III ratio was observed due to an increase in type I collagen, that is again not in line with the findings in the BIO 53.58 hamsters. Adaptation of collagen composition during cardiac LV dilation appears to be either model or species specific and caution should be taken to extrapolate these findings to the human condition.

Balance in extracellular matrix degradation by matrix metalloproteinases and their inhibitors

The ECM architecture of the cardiac wall is maintained by balanced protein synthesis and degradation. Collagens are synthesized by cardiac fibroblasts, which are in turn activated by different factors in the microenvironment. Potent stimulators of collagen-production by cardiac fibroblasts include growth factors such as transforming growth factor-β (TGF-β), nitric oxide and components of the renin-angiotensin-aldosterone system (RAAS)[19]. At the other end of the spectrum, ECM degradation is mediated by a family of enzymes called matrix metalloproteinases (MMPs), that are most commonly secreted by fibroblasts among other cells including endothelial cells (ECs), cardiomyocytes and inflammatory cells. The main

MMPs present within the cardiovascular tissue are MMP-1, -2 and -9. MMP-1 is the key enzyme in collagen degradation and facilitates breakdown of the collagen molecule into two fragments. Further degradation steps are carried out by two different enzymes, MMP-2 and -9. In general, MMPs are kept in their latent form by specific inhibitors called tissue inhibitors of MMPs (TIMPs), that colocalize with MMPs throughout the myocardium[20]. Four different TIMPs are known, with TIMP-1 being expressed at low levels in the healthy heart. A fine balance between MMPs and their inhibitors is required to reach equilibrium, and disturbances in their ratios will affect the collagen content and consequently the mechanical properties of the cardiac wall.

MMPs have been demonstrated to play an important role in ECM remodeling in a number of pathological processes associated with cardiac diseases, including DCM (Table 1). Spinale and colleagues[21-24] used the pacing-induced cardiomyopathy pig model to test if LV dilation and remodeling during the progression of congestive heart failure is associated with early changes in MMPs activity and expression. These pigs experience systolic dysfunction and reduced collagen support between adjacent myocytes. Pacing-induced CM is associated with a reduction in the collagen concentration and cross-linking and with an increase the ECM component chondroitin sulfate proteoglycan within the extracellular space. However, a 4-week recovery period results in an increase in the collagen concentration, increased LV stiffness and normal proteoglycan distribution[25,26]. In subsequent studies, a time-dependent increase was observed in overall MMP activity and protein abundance of MMP-1, 2 and 3 in the pacing group that was accompanied by a decrease in LV myocardial collagen content. These changes co-occurred with the initiation and progression of LV dilation[21,24]. More research revealed that chronic inhibition of multiple MMPs in the pacing group attenuated the degree of LV dilation and improved LV ejection performance in comparison with untreated rapid pacing pigs[21-23]. Additional studies used the same MMP inhibition therapy in rat and mice models for heart failure: in general, all animals receiving a broad-spectrum inhibitor of MMPs showed diminished ventricular dilation and preservation of systolic function[27-29]. In line with these findings, mice with a *Timp-3* deficiency developed spontaneous left-ventricular dilation and contractile dysfunction, coincided with increased MMP-9 activity[30].

Activation of MMPs was also causally related to LV dilation in animal models of SHF. Nishikawa *et al*[31] demonstrated that both MMP-2 and -9 activation and protein expression is increased in SHF rats throughout the heart wall. The

gene expression of type I collagen, *Timp-1* and *-2* is significantly enhanced in the SHF model as well when compared with control rats. More evidence for the involvement of MMPs in LV dilation comes from a study that used transgenic mice with cardiac restricted overexpression of TNFα. These mice develop progressive LV dilation and structural remodeling from 4 to 12 weeks of age. Sivasubramanian and colleagues[32] showed that during the early phases of LV dilation, the total MMP activity increases significantly and corresponds to a decrease in total myocardial fibrillary collagen content in these mice. However, as the mice age, the total MMP activity significantly decreases and is accompanied by an increase in the total amount of fibrillary collagen. These changes were related to a progressive increase in TIMP-1 levels from 4 to 12 weeks of age. In conclusion, MMPs might be an early event in the development of DCM that co-occurs with LV dilation. This process can be counteracted by mechanisms that activate TIMPs regulation at later stages.

MMPs and TIMPs in inflammatory DCM

Myocarditis and subsequent heart damage can ultimately lead to DCM. It is assumed that during the inflammatory phase, ECM remodeling might be triggered causing DCM at a later stage. Three different studies investigated this notion by infecting mice with cardiovirulent coxsackie virus B3 (CVB3), a major cause of myocarditis in humans, and assessing the expression of several MMPs and TIMPs as a measure of ECM remodeling (Table 1). Li and colleagues[33] demonstrated that viral infection causes a significant upregulation of MMP-3 and -9 mRNA and protein along with a downregulation of TIMP-1 and -4 mRNA and TIMP-4 protein. Furthermore, an increase of the degraded soluble fraction of type I collagen was found in these animals. Cheung and co-workers[34] found that already at 9 days post infection (pi), mRNA and protein abundances of MMP-2, -9 and -12 are upregulated, whereas the protein expression of TIMP-3 and -4 are down regulated. During the inflammatory phase (day 9 pi), the activity of both MMP-2 and -9 is increased as well. Moreover, the murine hearts showed an increase in the total amount of collagen during the acute phase of infection (day 9 pi). In line with the previous studies, Heymans *et al*[35] showed an increase in transcript levels of several MMPs, including MMP-2, -3, -8, -9 and -13 in mice 7 days after CVB3 infection. Furthermore, the activity and protein level of MMP-9 is significantly enhanced. Interestingly, loss of MMP activity through overexpression of TIMP-1 decreases cardiac inflammation and prevents cardiac dilation at 7 days pi. Besides MMPs, the activity and transcript level of another proteolytic enzyme was found

to be enhanced in this study: urokinase-type plasminogen activator (uPA). This enzyme converts plasminogen into its active form plasmin, which is responsible for the induction of MMP-9. Absence of uPA reduces the presence of active plasmin in CVB3-infected hearts and correspondingly, a reduction in MMP-9 activity was seen. Furthermore, absence of uPA reduces the inflammation and fibrosis 7 days pi and subsequently protects against cardiac dilation[35]. These findings demonstrate that ECM remodeling is triggered during the inflammatory phase prior to DCM and an early reduction of this process may protect against the dilation.

Connective tissue growth factor

Connective tissue growth factor (CTGF) is a glycoprotein that binds the ECM. Szabó and colleagues[36] recently investigated the role of CTGF in regulating the development of cardiac fibrosis during heart failure. Mice were subjected to pressure overload by thoracic aortic constriction (TAC) and received CTGF monoclonal antibodies (mAb) to antagonize CTGF. Animals treated with the target mAb showed improved LV systolic function and reduced LV dilation when compared to untreated mice. Furthermore, CTGF mAb treatment reduces the type I collagen production induced by TAC. In addition, the gene expressions of ECM components *Serpin-E1* and *Mmp-2* were decreased in CTGF mAb-treated mice.

Studying the effect of preventing LV dilation and preserving normal LVEF during the advancement of heart failure on ECM composition can give useful insights in the involvement of these components in the development of DCM. Aortocaval fistula (ACF) induced LV volume overload leads to progressive LV chamber dilation and systolic dysfunction. Hutchinson and colleagues[37] demonstrated that ACF-induced rats, which underwent a load-reversal procedure, exhibited improved LV chamber dimensions and function. Total collagen content was significantly decreased following ACF, but returns to normal levels after 15 weeks. ACF significantly increases the gene expressions of type I and III collagen and elastin but these were blunted at the reversal stage. Moreover, protein levels of MMP-13 and -14 were increased in ACF-induced rats, but returned to normal values after reversal. In contrast, MMP-7 remained increased after reversal. The reversal procedure caused a decrease of MMP-9 and TIMP-2 protein expression below normal values. These results show that reversal of LV dilation promotes a shift in ECM expression pattern that is associated with heart function normalization.

A summary of the expression profile of ECM components in the different cardiac animal models with LV dilation and systolic dysfunction is provided in Table 1. Only significant and direct changes in ECM components are included.

Human studies

Collagen and type I/III collagen ratio

Several human studies have elucidated the role of ECM turnover in the development and progression of SHF and DCM (Table 2). Most of the observations were supportive of the findings in the animal studies. For example, Gunja-Smith and colleagues were one of the first to provide evidence that DCM is characterized by more matrix deposition due to an increase in the collagen content. The newly produced collagen is deficient in forming stable cross-links and may therefore contribute to the dilation of the ventricular wall[38,39]. Numerous human studies reported a similar increase in total collagen content, that mainly consists of collagen type I and III with an increase in the collagen type I/type III ratio. In general, collagen type I provides more tensile strength and stiffness compared to collagen type III[40-47]. Besides type I and III collagen, other collagens, such as type IV and VI are present in minor quantities in the healthy myocardium. However, in DCM hearts the enlargement of the extracellular space is associated with abundant collagen VI[47,48]. In concordance with the results obtained from animal studies, DCM is characterized by an increase in both collagen type I and III. In addition, all human studies reported a clear increase in the collagen type I to type III ratio, that may contribute to the DCM phenotype due to an increase in stiffness and decrease in elasticity of the cardiac wall. Furthermore, Sivakumar *et al*[46] found that both transcriptional and translational levels of lysyl oxidase (LOX), a key ECM enzyme catalyzing crosslinks in collagen and elastin, were significantly upregulated in DCM hearts.

Balance in extracellular matrix turnover mediated by MMPs and TIMPs

DCM is also characterized by enhanced matrix turnover (Table 2). Gunja-Smith and colleagues[38,39] were one of the first to demonstrate that this shift is caused by an increase in MMP activity. In more detail, both active and latent MMP-1 and -8 levels were found to be higher in DCM hearts, whereas the expression of their inhibitor, TIMP-1, felt to negligible levels. Several additional studies have been performed on the role of MMPs in DCM, in which an overall increase in total MMP activity was observed[49]. Tyagi *et al*[50,51] demonstrated that MMPs are present in the

Table 1. Summary of the extracellular matrix response in myocardial fibrosis associated with dilated cardiomyopathy and systolic heart failure in animal studies.

Name		Expression	Study model	References
Core matrisome				
Glycoprotein				
ELN	Elastin	mRNA ↑	ACF-induced rat	Hutchinson *et al* 2011
Collagen				
COL1	Collagen, type I	mRNA ↑	SHF rat	Nishikawa *et al* 2003
			ACF-induced rat	Hutchinson *et al* 2011
		Protein ↑	SHF rat	Woodiwiss *et al* 2001
COL3	Collagen, type III	mRNA ↑	ACF-induced rat	Hutchinson *et al* 2011
		Protein ↑	BIO 53.58 hamster	Okada *et al* 1996
Matrisome-associated				
ECM-affiliated				
GSPG	Chondroitin sulfate proteoglycan	Protein ↑	Pacing-induced CM pig	Spinale *et al* 1996
ECM regulator				
PLAU	Plasminogen activator, urokinase	mRNA ↑	CVB3-infected mouse	Heymans *et al* 2006
		Activity ↑	CVB3-infected mouse	Heymans *et al* 2006
MMP-1	Matrix metallopeptidase 1	Protein ↑	Pacing-induced CM pig	Spinale *et al* 1998
				Coker *et al* 1998
MMP-2	Matrix metallopeptidase 2	mRNA ↑	CVB3-infected mouse	Cheung *et al* 2006
				Heymans *et al* 2006
		Protein ↑	Pacing-induced CM pig	Spinale *et al* 1998
				Coker *et al* 1998
		Activity ↑	SHF rat	Nishikawa *et al* 2003
			CVB3-infected mouse	Cheung *et al* 2006
MMP-3	Matrix metallopeptidase 3	mRNA ↑	CVB3-infected mouse	Li *et al* 2002
				Heymans *et al* 2006
		Protein ↑	Pacing-induced CM pig	Spinale *et al* 1998
				Coker *et al* 1998
			CVB3-infected mouse	Li *et al* 2002
MMP-7	Matrix metallopeptidase 7	mRNA ↑	ACF-induced rat	Hutchinson *et al* 2011
MMP-8	Matrix metallopeptidase 8	mRNA ↑	CVB3-infected mouse	Heymans *et al* 2006
MMP-9	Matrix metallopeptidase 9	mRNA ↑	CVB3-infected mouse	Li *et al* 2002
				Cheung *et al* 2006
				Heymans *et al* 2006
		Protein ↑	CVB3-infected mouse	Li *et al* 2002
				Heymans *et al* 2006
		Activity ↑	SHF rat	Nishikawa *et al* 2003
			CVB3-infected mouse	Cheung *et al* 2006
				Heymans *et al* 2006

MMP-12	Matrix metallopeptidase 12	mRNA ↑	CVB3-infected mouse	Cheung *et al* 2006
MMP-13	Matrix metallopeptidase 13	mRNA ↑	CVB3-infected mouse	Heymans *et al* 2006
MMP-14	Matrix metallopeptidase 14	mRNA ↓	CVB3-infected mouse	Li *et al* 2002
TIMP-1	Tissue inhibitor of metallopeptidase 1	mRNA ↑	SHF rat	Nishikawa *et al* 2003
		mRNA ↓	CVB3-infected mouse	Li *et al* 2002
TIMP-2	Tissue inhibitor of metallopeptidase 2	mRNA ↑	SHF rat	Nishikawa *et al* 2003
		mRNA ↑	ACF-induced rat	Hutchinson *et al* 2011
TIMP-3	Tissue inhibitor of metallopeptidase 3	Protein ↓	CVB3-infected mouse	Cheung *et al* 2006
TIMP-4	Tissue inhibitor of metallopeptidase 4	Protein ↓	CVB3-infected mouse	Li *et al* 2002 Cheung *et al* 2006

Abbreviations: ACF, aortocaval fistula; SHF, systolic heart failure; ECM, extracellular matrix; CM, cardiomyopathy; CVB3, coxsackievirus B3

latent form in the normal myocardium, but are activated in DCM. In more detail, MMP-1 expression was found to be induced in the DCM heart on both mRNA, protein and activity level when compared to normal tissue. Furthermore, TIMP-1 is repressed in DCM. Rouet-Benzineb *et al*[52] found that besides *TIMP-1*; *TIMP-2*, *-3* and *-4* were downregulated in ventricle samples from DCM patients when compared to healthy controls. However, the activity of MMP-2 and -9 remains unchanged. In contrast, two studies reported that MMP-1 levels were decreased in DCM[53,54]. Several studies found MMP-2, -3 and -9 levels to be increased in DCM myocardial tissue when compared to non-failing hearts. However, in contrast with previous results, a rise in TIMP-1, -2 and -3 levels was also detected[46,53,54]. In addition, MMP-14 was found to be also increased in DCM hearts[53]. An increase in MMP-1 and -9 protein expression, with an increase in the MMP-1 to TIMP-1 ratio was observed in DCM patients by Klotz and colleagues[42]. These mixed findings suggest that a complex interplay between MMPs and their inhibitors TIMPs exists in the DCM heart.

Evidence provided by serological markers

More evidence for an enhanced matrix turnover in DCM comes from studies performed on serological markers of collagen metabolism (Table 2). It has to be noted that evidence based on serological markers should be considered with

caution, since the difference in serum concentration can also be the result of secondary effects due to forward failure that decreases the blood flow to various organs. Klappacher and colleagues[55] demonstrated that patients with DCM have higher serum concentrations of two collagen cleavage products: procollagen type III aminoterminal peptide (PIIINP) and type I collagen carboxyterminal telopeptide (ICTP) compared to healthy controls. In addition, the authors reported that serum PIIINP and ICTP positively correlates with their tissue analogues, myocardial collagen type III and I, making these results more reliable. Schwartzkopff and colleagues[56] showed an increase in serum ICTP, a marker for collagen type I degradation, but no increase was reported for procollagen type I carboxyterminal propeptide (PICP), a marker for collagen type I synthesis. They also demonstrated an elevation in serum MMP-1 and TIMP-1 concentrations in DCM patients and a higher MMP-1/TIMP-1 ratio than in control subjects. Other studies have investigated the serum concentrations of MMPs and their inhibitors in patients with SHF. According to Yan and colleagues[57], patients with chronic SHF (LVEF <40%) have higher plasma levels of MMP-2 compared to baseline at 43 weeks of follow-up. MMP-9 and TIMP-1 plasma levels did not change significantly in the overall study population. However, elevated MMP-9 levels correlates with lower LVEF and deterioration of LV function. Results obtained by Jordán *et al*[58] demonstrated that patients with systolic dysfunction (LVEF <50%) have lower levels of MMP-1 and higher levels of TIMP-1 in their serum. This results in a higher TIMP-1/MMP-1 ratio than in healthy controls. In yet another study population of patients with SHF (LVEF <45%), serum MMP-1 and -2 levels were found to be significantly upregulated in SHF patients on admission when compared to healthy subjects. Only MMP-1 levels remained high at discharge[59].

In addition to collagen and MMPs, other extracellular matrix components are differentially expressed in DCM. Klappacher and colleagues[55] demonstrated that patients with DCM have higher serum concentrations of basement membrane laminin when compared to healthy controls, that positively correlates with myocardial laminin content. Serum tenascin C (TNC), a glycoprotein that is specifically expressed at high levels during embryogenesis, but not in the adult heart, was found to be increased in DCM patients compared to healthy controls. Moreover, a significantly negative correlation was found between TNC levels and LVEF[60]. TNC is mostly deposited along the margin of the replacement fibrotic lesions found in DCM hearts, implying that the fibrotic change is a continuous process[61].

Besides differences between healthy and DCM hearts, ECM components also differ in distribution within the diseased myocardium. The volume densities of fibronectin, collagen type I and IV were reported to be higher in the left ventricle than in the right ventricle of DCM hearts[62]. Another group observed fibronectin in both the endomysium and perimysium of DCM heart biopsy specimens, co-existent with collagen type I and III. Laminin was also observed in the endomysium and was localized together with collagen type IV. In addition, fibronectin and collagen type I, III and IV are non-homogenously distributed in the replacement fibrotic lesions[63]. Furthermore, pediatric DCM is characterized by a specific profile compared with adult DCM: MMP-8, MMP-9, TMP-1 and TMP-2 levels are increased in pediatric DCM, whereas MMP-3, MMP-7 and TIMP-3 levels are decreased[64].

A summary of the expression profile of ECM components in the human DCM and SHF populations is provided in Table 2. Only significant changes in ECM components are included and indirect but significant serum changes are also mentioned.

It has to be noted that there is a discrepancy in the findings between animal and human studies, in particular differences in MMP expression. An almost unanimous enhanced MMP expression is seen in the animal studies, with the exception of MMP-14, whereas in the human studies the overall expression pattern found is contradicting. Animal models provide the opportunity to study ECM changes in a more controlled environment and allow for the assessment of more subtle changes. Even though the findings obtained from animal models are more consistent, the question remains if animals are reliable enough in predicting the humane response. Only one animal model mentioned in this review, the BIO 53.58 hamsters, resembles the human situation in terms of developing DCM over time without intervention. In all the other models, the DCM phenotype had to be induced experimentally. The reason for the opposing findings in MMP expression within the human studies could be explained by the fact that these studies cannot be controlled on the same level as animal studies. Factors such as timing, heterogeneity of the patient population, sample size, biopsy location and the fact that various studies investigate only mRNA or protein levels of relevant factors among other issues contribute to the rise of contradicting results. It is also important to point out that the majority of studies investigate mRNA and/or protein levels of the MMP/TIMP system, whereas the overall net enzymatic

Table 2. Summary of the extracellular matrix response in myocardial fibrosis associated with dilated cardiomyopathy and systolic heart failure in human studies.

Name	Function	Expression	Study model		References
Core matrisome					
Glycoprotein					
LAM	Laminin	Protein ↑	DCM	(serum)	Klappacher *et al* 1995
TNC	Tenascin C	Protein ↑	DCM	(serum)	Terasaki *et al* 2007
Collagen					
COL1	Collagen, type I	mRNA ↑	DCM		Pauschinger *et al* 1999 Khan *et al* 2014
		Protein ↑	DCM		Bishop *et al* 1990 Klotz *et al* 2005 Sivakumar *et al* 2008
COL3	Collagen, type III	mRNA ↑	DCM		Pauschinger *et al* 1999 Khan *et al* 2014
		Protein ↑	DCM		Bishop *et al* 1990 Klotz *et al* 2005 Sivakumar *et al* 2008
Matrisome-associated					
ECM regulator					
LOX	Lysyl oxidase	mRNA ↑	DCM		Sivakumar *et al* 2008
		Protein ↑	DCM		Sivakumar *et al* 2008
MMP-1	Matrix metallopeptidase 1	mRNA ↑	DCM		Tyagi *et al* 1996b
		Protein ↑	SHF	(serum)	Naito *et al* 2009
			DCM		Klotz *et al* 2005 Tyagi *et al* 1996b
				(serum)	Swartzkopff *et al* 2002
		Protein ↓	SHF	(serum)	Jordán *et al* 2007
			DCM		Spinale *et al* 2000 Thomas *et al* 1998
MMP-2	Matrix metallopeptidase 2	Protein ↑	SHF	(serum)	Yan *et al* 2006
				(serum)	Naito *et al* 2009
			DCM		Sivakumar *et al* 2008 Spinale *et al* 2000
MMP-3	Matrix metallopeptidase 3	Protein ↑	DCM		Spinale *et al* 2000 Thomas *et al* 1998
		Protein ↓	pDCM		Hsia *et al* 2011
MMP-7	Matrix metallopeptidase 7	Protein ↓	pDCM		Hsia *et al* 2011
MMP-8	Matrix metallopeptidase 8	Protein ↑	pDCM		Hsia *et al* 2011
MMP-9	Matrix metallopeptidase 9	Protein ↑	DCM		Klotz *et al* 2005 Sivakumar *et al* 2008 Spinale *et al* 2000

					Thomas *et al* 1998
			pDCM		Hsia *et al* 2011
MMP-14	Matrix metallopeptidase 14	Protein ↑	DCM		Spinale *et al* 2000
TIMP-1	Tissue inhibitor of metalloproteinases 1	mRNA ↑	DCM		Sivakumar *et al* 2008
		mRNA ↓	DCM		Rouet-Benzineb *et al* 1999
		Protein ↑	SHF	(serum)	Jordán *et al* 2007
			DCM		Thomas *et al* 1998
				(serum)	Swartzkopff *et al* 2002
			pDCM		Hsia *et al* 2011
		Protein ↓	DCM		Tyagi *et al* 1996b
					Rouet-Benzineb *et al* 1999
TIMP-2	Tissue inhibitor of metalloproteinases 2	mRNA ↑	DCM		Sivakumar *et al* 2008
		mRNA ↓	DCM		Rouet-Benzineb *et al* 1999
		Protein ↑	DCM		Thomas *et al* 1998
			pDCM		Hsia *et al* 2011
TIMP-3	Tissue inhibitor of metalloproteinases 3	mRNA ↑	DCM		Sivakumar *et al* 2008
		mRNA ↓	DCM		Rouet-Benzineb *et al* 1999
		Protein ↓	pDCM		Hsia *et al* 2011
TIMP-4	Tissue inhibitor of metalloproteinases 4	mRNA ↓	DCM		Rouet-Benzineb *et al* 1999

Abbreviations: DCM, dilated cardiomyopathy; ECM, extracellular matrix; SHF, systolic heart failure; pDCM, pediatric DCM

activity is the determining factor in terms of ECM remodeling. The amount of contradictory data in the field highlights the need for additional studies.

Novel extracellular matrix changes identified in dilated cardiomyopathy by GEO datasets analysis

The human matrisome is composed of an ensemble of ECM and ECM-associated proteins, of which some have been suggested to play a role in DCM onset and progression, as discussed in previous paragraphs. We analyzed specific gene expression datasets that are publicly available on the NCBI's GEO database (http://www.ncbi.nlm.nih.gov/sites/GDSbrowser) to find novel ECM components that are altered in their cardiac expression by DCM and might be involved in disease development. We selected three datasets from studies that included human DCM and non-failing heart samples in their study design, see supplemental Figure 1 for an overview of the pipeline used for dataset selection. Two of the

three selected studies obtained their tissue biopsies from the left ventricle and the third used septal myocardial tissue. Other characteristics of the patient subset used in each study are summarized in Table 3. NCBI's GEO2R tool (www.ncbi.nlm.nih.gov/geo/geo2r/) was used in order to identify genes that are significantly differentially expressed between the DCM and healthy control groups. Datasets matching the earlier described criteria were downloaded (Supplementary Figure 1). Each raw dataset was sorted by an R script provided by the GEO2R program. Gene expression was analyzed as follows: (1) P-value below 0.05 was used to filter genes that reached significance; (2) Selected genes with a logFC value above 0 represented increased expressions, and those with a logFC value below 0 represented decreased expressions. (3) Genes with significantly increased and/or decreased expression were mapped among all matrisome subgroups. The list of ECM genes associated with DCM were obtained from the resulting expression data after filtering with an *in silico* matrisome dataset (http://matrisomeproject.mit.edu/). This dataset contains all the components of the human matrisome based on characterization and bioinformatic prediction, subdivided into two main categories: the core matrisome and ECM-associated components[65,66]. The core matrisome consist of glycoproteins, collagens and proteoglycans, whereas

Table 3. Characteristics of the patient groups used in three dilated cardiomyopathy GEO datasets.

	GSE42955	GSE3586	GSE3585
Tissue	Left ventricular; Transmural near the apex	Cardiac septum	Left ventricular; subendocardial
Sample size	17	28	12
DCM	12	13	7
Control	5	15	5
Gender			
DCM	12	13	7
Male	12	8	4
Female	0	5	3
Control	5	15	5
Male	5	11	0
Female	0	4	5
Ethnicity	N/A	Caucasian	Caucasian
Age (yrs.)			
DCM	48 ± 9	44 ± 18	37 ± 14
Control	N/A	54 ± 4	49 ± 9
EF DCM (%)	20 ± 6	21 ± 9	25 ± 6

Abbreviations: DCM, dilated cardiomyopathy; EJ, ejection fraction

the categories ECM-affiliated, ECM regulators and secreted factors represent the ECM-associated group. The resulting expression datasets are summarized in Table 4 and 5 and Figure 1.

Many genes are differentially expressed between the DCM and healthy control groups in all three datasets (Table 4 and 5). From these, ±5% can be assigned to the human matrisome. From the genes that are increased in DCM hearts, half is represented by core matrisome components. Further classification reveals that most of these genes can be assigned to the glycoprotein family. Collagens and proteoglycans are present as well, but in lower quantities. The remaining genes increased in DCM based on the GEO analysis are represented by matrisome associated components, with approximately equal distribution between the three subgroups. A different pattern is observed within the group of down regulated matrisome genes. Less genes are represented by core matrisome components, ranging from 8-31% between the different datasets. Nevertheless, as with the upregulated genes, most of the core genes are classified as glycoproteins. In contrast with the other two sets, in dataset GSE42955, none of the downregulated genes are either collagens or proteoglycans. The majority of downregulated genes can be classified as matrisome associated, with the secreted factors being the most represented subgroup. All the genes that are differentially expressed in the three datasets are listed in the supplemental data (Supplementary Tables 1-4 and Supplementary Figure 2).

To look in more detail at the differential gene expression data obtained from the GEO analysis, a heat map was constructed (Figure 1). Only genes are included that are significantly up- or downregulated in at least two datasets. Conform the literature for both animal and human studies summarized in the previous sections, collagen type I and III are upregulated in DCM hearts based on our GEO analysis. In addition, the glycoproteins elastin and laminin are upregulated as well, the latter for the subtypes α2 and β1. On the other hand, uPA is found to be upregulated in CVB3-infected hearts, however in our analysis the expression is found to be reduced in DCM hearts. In addition, tenascin C, lysyl oxidase and chondroitin sulfate proteoglycan are mentioned in the literature as ECM components with increased expression in DCM, but are not significantly upregulated in our analysis. Strikingly, neither MMPs nor TIMPs are found as differentially expressed, even though many studies have provided evidence for their involvement in DCM pathology. An explanation for missing these important ECM regulators in the GEO analysis could be that ECM degradation through MMP activity is a cyclic and

Table 4. Number of extracellular matrix (ECM) genes identified as upregulated in three dilated cardiomyopathy GEO datasets and classified in matrisome subgroups.

	GSE42955	GSE3586	GSE3585
Total no. of genes	972	3877	927
Matrisome	49 (5%)	154 (4%)	84 (9%)
Non-matrisome	923 (95%)	3723 (96%)	843 (91%)
Core matrisome	24 (49%)	60 (39%)	52 (62%)
Glycoproteins	15 (62%)	38 (63%)	32 (62%)
Collagens	6 (25%)	12 (20%)	12 (23%)
Proteoglycans	3 (13%)	10 (17%)	8 (15%)
Matrisome associated	25 (51%)	94 (61%)	32 (38%)
ECM-affiliated genes	4 (16%)	25 (27%)	6 (19%)
ECM regulators	8 (32%)	30 (32%)	14 (44%)
Secreted factors	13 (52%)	39 (41%)	12 (37%)
Retired	0 (0%)	0 (0%)	0 (0%)

transient process. When sampling at specific (later) time points, lower levels of MMPs and TIMPs may present within the biopsies.

ECM regulators

Within the ECM regulators group, we find ECM components that play a role in ECM turn-over and stabilization that are differentially expressed (Figure 1 and 2). For example, HTRA1 is a highly conserved serine protease that degrades numerous extracellular matrix proteins, including collagen and fibronectin. An upregulation in *HTRA1* is observed in our analysis, hinting at more matrix degradation in DCM. Subsequent fibronectin cleavage products can promote transcriptional activation of MMPs, that will additionally contribute to matrix degradation. Furthermore, HTRA1 has also the ability to sequester or proteolyse TGF-β. Since TGF-β induces fibroblasts to synthesize ECM components, degradation of TGF-β will result in more matrix remodeling[67]. In addition, two members of the proprotein convertase family, *PCSK5* and *PCSK6*, show a higher expression in DCM. These serine proteinases activate other proteins, thereby regulating their functional activity. The processing of proMMP-14 as well as its proteolytic activity has been shown to be catalyzed by PCSK5, thereby indirectly inducing more breakdown of the extracellular matrix[68].

However, many more ECM regulators found in our analysis contribute to ECM

Table 5. Number of extracellular matrix (ECM) genes identified as downregulated in three dilated cardiomyopathy GEO datasets and classified in matrisome subgroups.

	GSE42955	GSE3586	GSE3585
Total no. of genes	1223	3508	546
Matrisome	49 (4%)	160 (5%)	31 (6%)
Non-matrisome	1174 (96%)	3348 (95%)	515 (94%)
Core matrisome	4 (8%)	50 (31%)	5 (16%)
Glycoproteins	4 (100%)	38 (76%)	2 (40%)
Collagens	0 (0%)	8 (16%)	1 (20%)
Proteoglycans	0 (0%)	4 (8%)	2 (40%)
Matrisome associated	45 (92%)	109 (68%)	26 (84%)
ECM-affiliated genes	10 (22%)	20 (18%)	5 (19%)
ECM regulators	11 (25%)	43 (40%)	8 (31%)
Secreted factors	24 (53%)	46 (42%)	13 (50%)
Retired	0 (0%)	1 (1%)	0 (0%)

synthesis and stabilization (Figure 1 and 2). For instance, *P4HA2* expression is upregulated in our analysis that encodes a component of prolyl 4-hydroxylase. This is a key enzyme in collagen synthesis and is composed of two α and two β subunits. The α2 subunit composes a major part of the catalytic site of the active enzyme. In collagen and related proteins, prolyl 4-hydroxylase catalyzes the formation of 4-hydroxyproline residues that are essential for stabilization and proper three-dimensional folding of newly synthesized collagen[69]. The expression of *PLOD1*, an enzyme that catalyzes the hydroxylation of lysine in collagens and related proteins, is also upregulated. The resultant hydroxylysine groups serve as attachment sites and are therefore critical for the formation and stability of intermolecular collagen cross-links. In addition, *ADAMTSL5* and *ITIH5* are induced during DCM and can contribute to ECM strengthening. ADAMTSL5 can bind to both fibrillin-1 and -2 and is thought to promote fibrillin microfibril formation[70,71]. The *ITIH5* gene encodes a heavy chain component of one of the inter-α-trypsin inhibitor family members, that are thought to be involved in extracellular matrix stabilization[72]. Additional contribution to preserve the ECM may come from the downregulation of the genes *A2M*, *ADAMTS9*, *CD109* and *PLAU*, as seen in our analysis. The *A2M* gene encodes a protease inhibitor that inhibits many proteases, including collagenases (e.g. MMP-2 and -9)[73]. ADAMTS9 is a member of the ADAMTS protein family, that is associated with the cleavage of two large aggregating proteoglycans, aggrecan

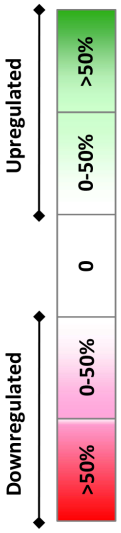

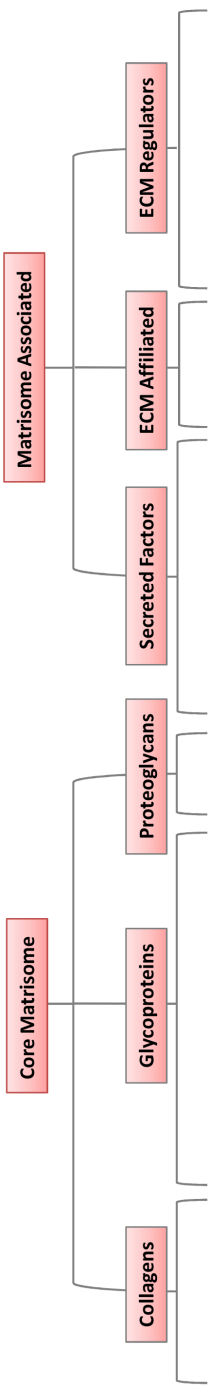

	logFC GSE42955	logFC GSE3586	logFC GSE3585	P-value
ADAMTSL5	0.38	0.28	0.00	1.93E-03
CTSF	0.00	0.14	0.22	3.21E-02
EGLN3	0.64	0.15	0.55	1.71E-02
HTRA1	0.00	0.95	0.62	5.25E-04
ITIH5	0.54	0.25	0.00	2.43E-03
P4HA2	0.45	0.11	0.43	1.37E-02
PCSK5	0.45	0.00	0.45	8.94E-03
PCSK6	0.00	0.17	0.43	2.63E-02
PLOD1	0.39	0.00	0.20	1.45E-02
A2M	-0.46	-0.21	-0.31	8.79E-03
ADAMTS9	0.00	-0.31	-0.53	5.71E-04
CD109	-0.70	-0.12	0.00	2.34E-03
F13A1	0.00	-0.65	-0.92	7.77E-03
PLAU	-0.28	0.00	-0.63	2.50E-02
SERPINA3	-1.84	0.00	-0.81	3.51E-03
ANXA7	0.00	0.14	0.19	2.28E-02
SDC2	0.00	0.34	0.40	2.38E-02
CD209	0.00	-0.14	-0.61	7.01E-03
COLEC10	-0.43	-0.31	0.00	1.32E-03
FCN3	-0.98	0.00	-1.24	1.33E-02
SEMA3D	-0.41	-0.26	0.00	2.89E-03
SEMA4B	-0.53	-0.15	0.00	8.57E-03
CRLF1	0.00	0.10	0.78	1.50E-02
FGF1	0.00	0.51	0.43	1.25E-02
FRZB	0.95	0.00	1.64	2.40E-03
FSTL3	0.71	0.00	0.61	8.98E-04
IL16	0.20	0.15	0.00	2.04E-02
PTN	0.58	0.36	0.00	1.03E-02
SFRP4	0.90	0.00	1.27	5.97E-03
CCL11	0.00	-0.23	-0.78	5.27E-04
CCL2	-1.86	-1.08	-1.46	9.05E-04
CCL8	-0.77	0.00	-0.68	3.50E-02
EGF	0.00	-0.12	-0.26	2.81E-02
FGF7	-0.39	0.00	-0.41	4.53E-02
FIGF	-1.01	0.00	-0.68	3.61E-02
IL6	-0.67	-0.14	-0.26	2.59E-02
S100A12	-0.31	0.00	-0.29	2.72E-02
ASPN	0.00	0.88	1.31	2.73E-04
BGN	0.00	0.23	0.73	2.50E-02
LUM	0.64	0.81	0.00	1.74E-02
OGN	0.82	0.00	1.19	1.01E-02
SPOCK1	0.00	0.34	1.35	1.09E-02
CTGF	0.00	0.52	1.92	2.20E-03
DPT	0.60	0.00	0.74	2.75E-02
ECM2	0.64	0.28	0.79	1.34E-03
ELN	0.25	0.00	1.23	1.16E-02
FN1	0.00	0.12	0.73	1.97E-02
IGFBP3	0.46	0.00	0.83	1.98E-03
LAMA2	0.39	0.00	0.55	1.68E-02
LAMB1	0.37	0.40	0.65	2.33E-03
LTBP1	0.00	0.27	0.80	3.53E-03
LTBP2	0.00	0.71	1.29	5.66E-04
NDNF	0.51	0.24	0.00	1.53E-02
PCOLCE2	0.00	0.58	0.91	1.01E-03
SPON1	0.65	0.00	0.70	1.97E-02
SRPX2	0.53	0.00	0.33	2.96E-02
SVEP1	0.00	0.21	0.45	3.07E-03
TSP2	0.00	0.14	1.03	1.55E-03
CRIM1	-0.42	-0.12	0.00	1.71E-02
IGFBP4	0.00	-0.20	-0.50	1.55E-02
MMRN2	-0.40	-0.15	0.00	3.73E-04
COL14A1	0.00	0.14	0.90	1.35E-02
COL1A1	0.51	0.00	1.15	3.09E-02
COL1A2	0.49	0.00	1.16	2.45E-02
COL21A1	0.00	0.58	0.41	1.29E-02
COL3A1	0.00	0.70	2.75	2.92E-02
COL4A1	0.33	0.00	0.39	9.47E-03
COL4A2	0.22	0.00	0.29	3.22E-02
COL5A1	0.00	0.33	0.64	2.03E-03
COL5A2	0.45	0.00	0.78	8.11E-03
COL8A1	0.37	0.32	0.35	8.41E-03

◀ **Figure 1.** Heatmap composed of genes found to be significantly up-or downregulated in dilated cardiomyopathy based on three GEO datasets. Only genes differentially expressed in two or more datasets were included. Expression levels are displayed in $\log^2$ fold change.

and versican, resulting in less ECM degradation[74]. CD109 has been identified as a negative regulator of TGF-β signaling. It increases binding of TGF-β to its receptors, enhances their internalization and facilitates their degradation[75]. Thus, downregulation of CD109 will result in more TGF-β signaling. *PLAU* encodes for the enzyme uPA that is part of the extracellular protease system. It converts plasminogen into plasmin, that is an important fibrinolytic protease with a wide range of substrates. Plasmin can directly degrade ECM components, such as fibronectin, that binds to cell surfaces and various compounds including collagen and fibrin[76]. In addition, plasmin is needed to activate a wide number of MMPs, including MMP-3, -9 -12 and -13[77]. Therefore, downregulation of *PLAU* will result in less active plasmin and subsequent less degradation of ECM components and fewer active MMPs available to degrade collagens. This is in line with the result mentioned in the animal data section that loss of uPA protects against cardiac dilation during CVB3-induced myocarditis[35].

To conclude, in the DCM group, more ECM regulators are involved in ECM synthesis and stabilization compared to ECM degradation, therefore the balance in DCM may be shifted towards a stiffer and denser ECM (Figure 2).

Secreted factors

Besides ECM regulators, the secreted factors compose another major group within the heat map (Figure 1). Within this group, two members of the fibroblast

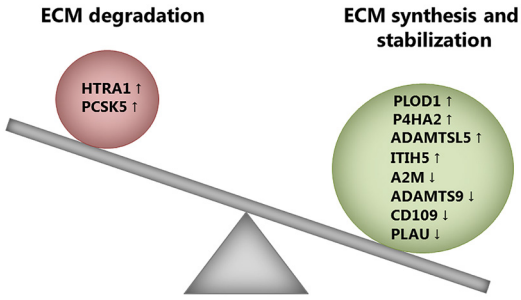

Figure 2. Hypothetical schematic representation of the involvement of extracellular matrix (ECM) regulators in dilated cardiomyopathy.

growth factor family are present. These components are essential regulators of the proliferation, chemotaxis and survival of numerous structural cells, including fibroblasts. During normal tissue repair, fibroblasts proliferate and are recruited into the lesion, where they remodel the ECM by producing, adhering to and contracting the ECM. Eventually the fibroblasts disappear due to apoptosis and normal tissue function is restored. Excessive fibrosis is the result of fibroblasts persisting in the wounded area, resulting in scarring[78]. Myocardial fibrosis is a major feature in DCM and excessive fibroblast activation and survival due to the upregulation of fibrogenic components might contribute to the formation of scar tissue in the DCM heart (Figure 1 and 3). *FGF1* is upregulated in our GEO analysis and it was already known in 1974 that FGF1 stimulates fibroblasts proliferation[79]. Intracellular FGF1 has the ability to inhibit both p53-dependent apoptosis and cell growth arrest in rat embryonic fibroblasts by decreasing the stability of p53 and through modification of the transactivation properties of p53[80]. *FGF7* expression is reduced in DCM, however, this protein is only mitogenic for epithelial cells and not for fibroblasts[81]. More secreted factors with a high gene expression in our analysis are found to be positively linked to fibroblast activity. For example, PTN is another growth factor that is recognized as a mitogen towards fibroblast[82]. In addition, PTN can inhibit apoptosis of NIH3T3 fibroblasts through activation of the MAPK pathway[83]. We also see an induction of *FSTL3* expression in our GEO analysis, which is is a potent inhibitor of activin signaling and angiogenesis. It has been shown that production of FSTL3 by cardiomyocytes contributes to

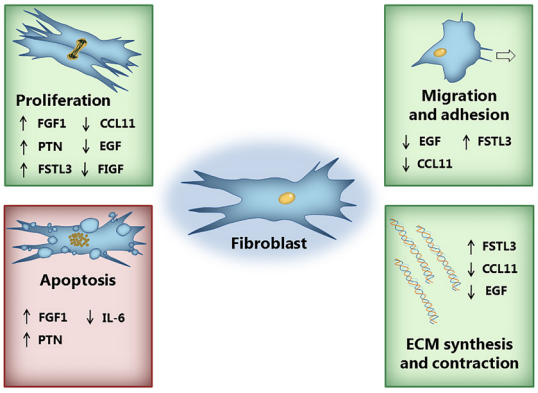

Figure 3. Hypothetical schematic representation of the effects of secreted factors within the extracellular matrix on fibroblast activity in dilated cardiomyopathy. Green framing represents stimulation of the process mentioned, red framing represents inhibition.

the paracrine activation of cardiac fibroblasts. An increased gene expression will promote proliferation, increase collagen production and induce changes in cell adhesion[84]. Also, cultured human fibroblasts express constitutive *IL-16* and *CRLF1* mRNA. Both these molecules are found to be upregulated in DCM, giving an indirect indication of induced fibroblast activity[85,86].

On the contrary, other factors found in our GEO analysis that are associated with fibroblast activity are downregulated, which could contribute to an antifibrogenic effect (Figure 1 and 3). Two of these components are *CCL2* and *IL-6*. CCL2 can induce IL-6, that in turn can mediate fibroblast survival by inhibiting apoptosis via the ERK1/2 signaling pathway[87]. The expression of *CCL11*, a small cytokine that can modulate fibroblast activity by increasing their proliferation, chemotaxis, collagen synthesis and MMP-2 activity, and *FIGF*, a growth factor that is able to stimulate mitogenic activity and induce morphological alterations in fibroblasts, are both reduced[88,89]. Besides FGFs, EGF has also been implicated as a potent mitogenic factor for numerous cell types, including fibroblast. It has been found by several studies using fibroblast in culture that EGF can stimulate fibroblast migration and proliferation and can also promote fibroblast contractility and motility via a protein kinase C delta-dependent pathway[90-93]. Furthermore, the EGF receptor is required for MMP expression and collagen contraction in fibroblasts through the MAPK and AP-1 pathways[94]. EGF is also part of the fibroblast growth factor receptor signaling pathway, for it can upregulate TGF-β receptor II in human fibroblasts via the p38 mitogen-activated protein kinase pathway[95]. TGF-β induces fibroblasts to contract and synthesize ECM and is considered to be a key player in the fibrotic response[96]. Altogether, a downregulation of *EGF* as found in our analysis will most likely have a negative impact on fibroblast activity. Lastly, CCL8 and FGF7, a small cytokine and growth factor respectively, can be produced by fibroblasts itself. Since the gene expression of both is reduced in our analysis, it might indirectly indicate fibroblast suppression[81,97].

In summary, there is no clear pattern found within the secreted factors in relation with fibroblasts. Instead, it seems that a balance between fibroblast activation and suppression is present in the DCM samples (Figure 3). Different stadia of fibrosis are intermixed in tissue biopsies taken from the DCM heart. This could explain the diverse signals seen within this group. In addition, the suppression of some fibrogenic factors might also be the result of a negative feedback mechanism to prevent excessive fibroblast growth and activation. More research is needed to fully understand the involvement of these factors in fibroblast regulation during

DCM onset and progression.

Collagens

We identified highly interesting targets within the matrisome associated group, however, many additional interesting targets were found among the core components, such as various collagen subtypes (Figure 1). Collagens are the most abundant core component in the extracellular matrix that typically contain a characteristic triple helical conformation. The vertebrate collagen family includes more than 40 genes that code for collagen α chains, which can form at least 28 different collagen subtypes[98]. Fibrillar collagens are the main subgroup in vertebrates, where they fulfill a structural role by contributing to the molecular organization, mechanical properties and shape of tissues. In concordance with the extensive literature on fibrillar collagen involvement in DCM, collagen type I and III are significantly upregulated in DCM according to our GEO dataset analysis. These two collagen subtypes are found throughout the body and are known to be synthesized in response to injury. Additionally, we find a novel fibrillar collagen enhanced in DCM, namely collagen type V. Only two combinations of α chains can produce this low abundance fibrillar collagen and both genes, *COL5A1* and *COL5A2*, are upregulated. Collagen type V is found in tissues containing collagen type I and it appears to have an essential role in initiating collagen fibril assembly[99]. Therefore, the enhanced synthesis and deposition of collagen I seen in the DCM heart might be directly associated with excessive collagen V production. Furthermore, mutations in these two genes are associated with the Ehlers-Danlos syndrome (EDS). This disorder includes a vascular type characterized by a fragile vasculature with a high risk of lethal vascular events, such as arterial rupture[100], indicating that collagen type V might be important for vascular stability.

In addition to a novel fibrillar collagen, we find four additional collagen subtypes enhanced in DCM. Two of them, collagen type XIV and XXI, belong to a subgroup of fibril-associated collagens with interrupted triple helices (FACITs) that do not form fibrils by themselves. Instead, these collagens are considered regulators of fibrillogenesis, since they have specific regions designed for the adhesion and interaction with fibrils[101]. Collagen XIV interacts with collagen type I and is found to be highly expressed in areas of high mechanical stress, such as the cardiac muscle[102]. Similarly, collagen type XXI is present in tissues expressing a muscle phenotype enriched with collagen type I. In more detail, high expression of *COL21A1* is found within the heart, with the left ventricle expressing lower

levels compared to the right ventricle, apex and septum[103]. FACITs are required for the assembly of a tightly regulated collagen network in the heart. In line with this statement, *Col14a1*-/- mice experience diminished cardiac function, including dilation of the heart and reduced ejection fraction, indicating the importance of collagen type XIV for the structural integrity of the myocardium[104]. In contrast to these results obtained using a murine model, our data indicates that during the progression of DCM in humans, *COL14A1* is enhanced. An explanation might be that during the later phases of the disease, a surplus of adhesive collagens is produced as an attempt to strengthen the dilated left ventricle, mostly subtypes that interact with collagen type I.

Besides collagens involved in fibril formation and interactions, additional subgroups of non-fibrillar collagens have been described. Among these are collagens involved in the formation of two-dimensional sheets that give structure to protein membranes surrounding tissues. An example of such a membrane is the basement membrane and one of its major constituents is collagen type IV. Two of the six human genes associated with it are upregulated in DCM according to our analysis; *COL4A1* and *COL4A2*. Mice with a *Col4a1* missense mutation experience defects in vascular function, including focal detachment of the endothelium, and low blood pressure[105], showing the importance of collagen type IV for the stability of vascular structures during mechanical demand. Furthermore, mutations in both genes have been linked to small-vessel disease and hemorrhagic stroke[106,107]. Collagen type VIII is another example of a collagen that forms two-dimensional sheets. It is an important component of the subendothelium and it is expressed by ECs and vascular smooth muscle cells (vSMCs) as a heterotrimer composed of α1 and α2 chains. In our GEO dataset analysis, *COL8A1* is found to be upregulated in DCM. Collagen type VIII is necessary for the migration and growth of vSMCs[108], hinting towards a potential role of this collagen in the maintenance of vessel wall structure and integrity.

In conclusion, besides the well-described collagen I and III, the expression of several other collagen family members is found to be enhanced in DCM, including both fibrillar and non-fibrillar collagens. It is interesting to speculate that this unanimous enhancement of collagen expression is most likely a joined protective response towards the ventricular dilation in other to maintain proper mechanical stability and functionality of the myocardium.

Glycoproteins

Besides collagens, other proteins within the extracellular matrix are considered fibrous proteins, including elastins, fibronectin and laminins. These proteins belong to the family of glycoproteins that composes a major part of the core matrisome and our heatmap as well (Figure 1). Tissues that undergo substantial stretching and bending contain a high amount of the structural glycoprotein elastin, which arranges in bundles called elastic fibers. Particularly the walls of large arteries are rich in elastic fibers allowing them to stretch in response to each pulse and resume their shape afterwards. In addition to structural glycoproteins, specialized glycoproteins are present in the ECM that have an important adhesive role, such as fibronectin and laminin. Both are fibrous glycoproteins that attach cells to the ECM. In more detail, fibronectin exist as a protein dimer that binds both cell-surface receptors called integrins and a broad variety of matrix components, except collagen type IV. Instead, type IV matrices contain laminins as adhesive proteins. All isoforms of fibronectin arise by alternative RNA splicing of the pre-mRNA encoded by a single gene, *FN1*[109]. This gene is upregulated in DCM hearts based on our GEO dataset analysis. Conform the literature summarized in the previous sections, the genes encoding elastin and laminin (*ELN* and *LAM*, respectively) are upregulated as well, the latter for the subtypes α2 and β1. Loss of functionality caused by the dilation and increased stiffness through enhanced collagen deposition might be compensated by an increase in these structural and adhesive glycoproteins.

Fibrous ECM components such as fibronectin are necessary for the incorporation of the latent TGF-β1 complex into the matrix. The healthy myocardium contains an inactive TGF-β1 pool awaiting for activation upon injury or overload. The major effects of TGF-β pathway activation include inhibition of proliferation and enhancement of ECM production[110]. Storage of latent TGF-β1 requires the presence of latent transforming growth factor-beta-binding proteins (LTBPs) that covalently bind the complex to the matrix. Fibronectin provides a scaffold for LTBP1 in particular, which is an LTPB known to be involved in vascular remodeling[111-113]. *LTBP1* is upregulated in our GEO dataset analysis together with *FN1*. We find *LTBP2*, the largest member of the LTPB family, to be highly expressed in DCM as well. TGF-β is a potent regulator of ECM formation and its deposition seems to be enhanced in DCM hearts.

Evidence for fibronectin accumulation in the damaged heart is found in the early phase post infarction, where it is expected to stimulate adhesion and proliferation of progenitor cells[114,115]. Furthermore, regulators of fibronectin

are also upregulated according to our analysis, hinting towards promoted cell adhesion in DCM (Figure 1 and 4). *CTGF* encodes a fibrogenic protein, which expression is induced by TGF-β in various cell types including cardiac fibroblasts and myocytes. By mediating downstream events of the TGF-β signaling pathway, CTGF induces the secretion of fibronectin and mediates its matrix deposition by controlling integrin expression[116,117]. Another regulator, *DPT*, encodes a protein that interacts with fibronectin and enhances its fibril formation. It is suggested that DPT has an important role in wound healing by inducing cardiac fibroblast adhesion and migration via integrins[118,119]. More evidence comes from the upregulation of *SRPX2* and *NDNF*. It is demonstrated *in vitro* that SRPX2 enhances cellular migration and adhesion by increasing the phosphorylation of focal adhesion kinase (FAK), a cytoplasmic protein needed for the activation of integrin related signaling pathways[120]. *NDNF* encodes a secretory protein that has fibronectin type III domains. This allows for the speculation that NDNF can modulate integrin-dependent signals. In line with this, Ohasi *et al*[121] revealed that NDNF promotes EC function and survival by activating the integrin α5β3-associated pathway.

On the contrary, several components found in our GEO analysis are associated with negative regulation of cell adhesion (Figure 1 and 4). *TSP2* has not been extensively studied, however because of its similarity to family-member TSP1; it

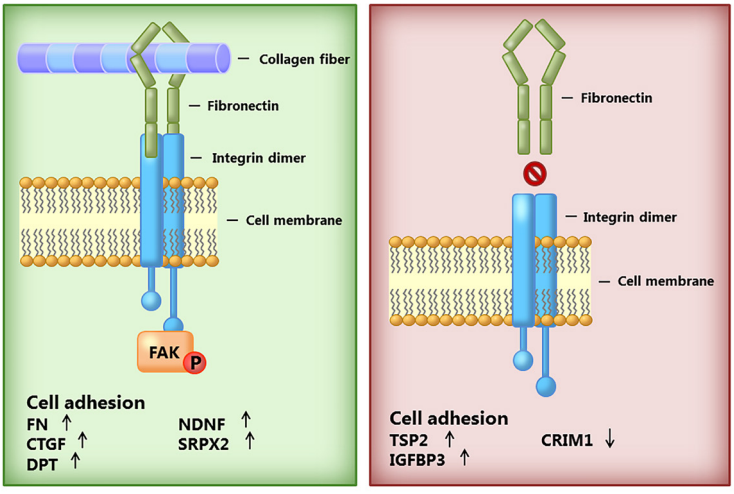

Figure 4. Hypothetical schematic representation of the effects of glycoproteins within the extracellular matrix on cell adhesion in dilated cardiomyopathy. Green framing represents stimulation of the process mentioned, red framing represents inhibition.

is believed that it can interact with the same targets including fibronectin[122]. TSP2 inhibits the formation of focal adhesions in ECs *in vitro*[123] and TSP2-null fibroblasts showed a marked defect in attachment to fibronectin and a reduction in cell spreading[124]. Therefore, the upregulation of *TSP2* seen in our analysis will probably have a negative effect on cell adhesion. Furthermore, *IGFBP3* encodes a protein that associates with the cell binding domain of fibronectin. This allows for the speculation that an upregulation of *IGFBP3* as seen in our analysis has the potential to displace cells from the matrix[125]. Downregulation of *CRIM1* as seen within our analysis most likely has a negative impact on cell adhesion, since it is demonstrated that silencing CRIM1 expression decreases cell migration and adhesion *in vitro*[126].

To conclude, the increase of the adhesive glycoproteins fibronectin and laminin in DCM indicates that the response towards the dilation might include enhanced cell adhesion activities and increased deposition of latent TGF-β1 into the matrix. Further evidence for enhanced cell adhesion comes from the upregulation of several glycoproteins regulating fibronectin deposition and integrin signaling. The expression pattern of other factors indicate that cell displacement activities are present in de DCM heart as well, possibly functioning as a negative feedback mechanism to prevent excessive cell adhesion (Figure 4). More research is needed to fully understand the involvement of these factors during DCM onset and progression.

Conclusion

It is inevitable that ECM changes are involved in the development and progression of DCM, since myocardial fibrosis is a major feature of this disease. In this review, we have provided literature sources for the involvement of diverse ECM components in non-ischemic and non-genetic DCM and SHF. In both animal and human studies, a consistent increase in collagen type I and III synthesis and deposition has been described, with an increase in the collagen type I/type III ratio. Collagen type I provides more tensile strength, resulting in a stiffer matrix. This excessive production of collagen is most likely an effort to strengthen the heart wall during the progression of DCM. Besides collagen, more core matrix components are abundant within the DCM heart, including elastin, laminin and tenascin C. Furthermore, a complex interplay between various MMPs and TIMPs arises in the DCM heart that includes the main MMPs present within the cardiovascular tissue (MMP-1, 2 and 9) and all four known TIMPs. Based on the results from the animal studies, the enhanced MMP activity and protein abundance might be an early

event in DCM that co-occurs with the initiation of LV dilation. Progression of the disease is characterized by a fall in MMPs, due to an increase in TIMPs.

Increasing our understanding of the involvement of the ECM in the onset and progression of DCM is important for the development of future interventions. Here, the focus should not merely lie on the core matrisome components, but on the ECM associated factors as well, that provide biochemical support to the surrounding cells and thus can regulate many biological processes. Our GEO dataset analysis provides a catalogue of ECM genes that might be involved in the development and progression of DCM. These components have the potential in becoming future candidates for therapeutic targets or prognostic markers. Within the matrisome associated components, a considerable part is represented by ECM regulators and secreted factors. Excessive ECM synthesis and stabilization is most likely the joint outcome from the ECM regulators, either by stimulating fibril construction with the formation of extra protein residues and cross-links or by inhibiting proteases and increasing TGF-β signaling. Together with the increase in collagen I and III already described in the literature and the enhanced expression of additional fibrillar and non-fibrillar collagens found with our GEO datasets analysis, these results indicate that strengthening the heart wall through ECM remodeling is a major feature of DCM. Furthermore, a wide array of secreted factors is found and their combined effect will likely lead to altered fibroblast activity. Many of these molecules are involved in fibroblast proliferation, apoptosis, migration and the production of ECM components among others. More research is needed to fully understand the involvement of these factors in fibroblast regulation. Finally, within the core components, the increase of the adhesive glycoprotein fibronectin and several regulators of its deposition and associated signaling pathway indicate that the response towards the dilation might include enhanced cell adhesion activities.

This transcriptome-based catalogue of novel ECM components expands the fundamental knowledge about the involvement of ECM remodeling in DCM. However, more research is required before any of these components can be considered as a prognostic marker or as a target for treatment. The function of these potential targets needs to be validated by using *in vitro* assays and assessing the causality with animal models is recommended to further elucidate the added value of these newly identified ECM components.

Acknowledgements

The work was supported by Netherlands Foundation for Cardiovascular Excellence

[to C.C], two NWO VIDI grants [no. 91714302 to C.C., and no. 016096359 to M.V.], the Erasmus MC fellowship grant [to C.C.], the RM fellowship grant of the UMC Utrecht [to C.C.] and the Netherlands Cardiovascular Research Initiative: An initiative with support of the Dutch Heart Foundation [CVON2014-11 RECONNECT; to C.C., M.V.].

References

1. Maron BJ, Towbin JA, Thiene G, et al. Contemporary definitions and classification of the cardiomyopathies: an American Heart Association Scientific Statement from the Council on Clinical Cardiology, Heart Failure and Transplantation Committee; Quality of Care and Outcomes Research and Functional Genomics and Translational Biology Interdisciplinary Working Groups; and Council on Epidemiology and Prevention. Circulation. 2006;113(14):1807-1816.
2. Wilkinson JD, Landy DC, Colan SD, et al. The pediatric cardiomyopathy registry and heart failure: key results from the first 15 years. Heart Fail Clin. 2010;6(4):401-413.
3. Elliott P, Andersson B, Arbustini E, et al. Classification of the cardiomyopathies: a position statement from the European Society Of Cardiology Working Group on Myocardial and Pericardial Diseases. Eur Heart J. 2008;29(2):270-276.
4. Rubis P. The diagnostic work up of genetic and inflammatory dilated cardiomyopathy. E-journal of Cardiology Practice. 2015;13(19).
5. Gopal DM, Sam F. New and emerging biomarkers in left ventricular systolic dysfunction--insight into dilated cardiomyopathy. J Cardiovasc Transl Res. 2013;6(4):516-527.
6. Michels VV, Driscoll DJ, Miller FA, et al. Progression of familial and non-familial dilated cardiomyopathy: long term follow up. Heart. 2003;89(7):757-761.
7. Hershberger RE, Hedges DJ, Morales A. Dilated cardiomyopathy: the complexity of a diverse genetic architecture. Nat Rev Cardiol. 2013;10(9):531-547.
8. McNally EM, Golbus JR, Puckelwartz MJ. Genetic mutations and mechanisms in dilated cardiomyopathy. J Clin Invest. 2013;123(1):19-26.
9. Harakalova M, Kummeling G, Sammani A, et al. A systematic analysis of genetic dilated cardiomyopathy reveals numerous ubiquitously expressed and muscle-specific genes. Eur J Heart Fail. 2015;17(5):484-493.
10. Brooks A, Schinde V, Bateman AC, et al. Interstitial fibrosis in the dilated non-ischaemic myocardium. Heart. 2003;89(10):1255-1256.
11. Heneghan MA, Malone D, Dervan PA. Myocardial collagen network in dilated cardiomyopathy. Morphometry and scanning electron microscopy study. Ir J Med Sci. 1991;160(12):399-401.
12. Unverferth DV, Baker PB, Swift SE, et al. Extent of myocardial fibrosis and cellular hypertrophy in dilated cardiomyopathy. Am J Cardiol. 1986;57(10):816-820.
13. Weber KT, Pick R, Silver MA, et al. Fibrillar collagen and remodeling of dilated canine left ventricle. Circulation. 1990;82(4):1387-1401.
14. Caulfield JB, Wolkowicz PE. Myocardial connective tissue alterations. Toxicol Pathol. 1990;18(4 Pt 1):488-496.
15. Jellis C, Martin J, Narula J, et al. Assessment of nonischemic myocardial fibrosis. J Am Coll Cardiol. 2010;56(2):89-97.
16. Okada H, Kawaguchi H, Kudo T, et al. Alteration of extracellular matrix in dilated cardiomyopathic hamster heart. Mol Cell Biochem. 1996;156(1):9-15.
17. Masutomo K, Makino N, Maruyama T, et al. Effects of enalapril on the collagen matrix in cardiomyopathic Syrian hamsters (Bio 14.6 and 53.58). Jpn Circ J. 1996;60(1):50-61.
18. Woodiwiss AJ, Tsotetsi OJ, Sprott S, et al. Reduction in myocardial collagen cross-linking parallels left ventricular dilatation in rat models of systolic chamber dysfunction. Circulation. 2001;103(1):155-160.
19. Kapelko VI. Extracellular matrix alterations in cardiomyopathy: The possible crucial role in the dilative form. Exp Clin Cardiol. 2001;6(1):41-49.
20. Tyagi SC, Kumar SG, Banks J, et al. Co-expression of tissue inhibitor and matrix metalloproteinase in myocardium. J Mol Cell Cardiol. 1995;27(10):2177-2189.
21. Coker ML, Thomas CV, Clair MJ, et al. Myocardial matrix metalloproteinase activity and

abundance with congestive heart failure. Am J Physiol. 1998;274(5 Pt 2):H1516-1523.
22. McElmurray JH, 3rd, Mukherjee R, New RB, et al. Angiotensin-converting enzyme and matrix metalloproteinase inhibition with developing heart failure: comparative effects on left ventricular function and geometry. J Pharmacol Exp Ther. 1999;291(2):799-811.
23. Spinale FG, Coker ML, Krombach SR, et al. Matrix metalloproteinase inhibition during the development of congestive heart failure : effects on left ventricular dimensions and function. Circ Res. 1999;85(4):364-376.
24. Spinale FG, Coker ML, Thomas CV, et al. Time-dependent changes in matrix metalloproteinase activity and expression during the progression of congestive heart failure: relation to ventricular and myocyte function. Circ Res. 1998;82(4):482-495.
25. Spinale FG, Tomita M, Zellner JL, et al. Collagen remodeling and changes in LV function during development and recovery from supraventricular tachycardia. Am J Physiol. 1991;261(2 Pt 2):H308-318.
26. Spinale FG, Zellner JL, Johnson WS, et al. Cellular and extracellular remodeling with the development and recovery from tachycardia-induced cardiomyopathy: changes in fibrillar collagen, myocyte adhesion capacity and proteoglycans. J Mol Cell Cardiol. 1996;28(8):1591-1608.
27. Chancey AL, Brower GL, Peterson JT, et al. Effects of matrix metalloproteinase inhibition on ventricular remodeling due to volume overload. Circulation. 2002;105(16):1983-1988.
28. Peterson JT, Hallak H, Johnson L, et al. Matrix metalloproteinase inhibition attenuates left ventricular remodeling and dysfunction in a rat model of progressive heart failure. Circulation. 2001;103(18):2303-2309.
29. Rohde LE, Ducharme A, Arroyo LH, et al. Matrix metalloproteinase inhibition attenuates early left ventricular enlargement after experimental myocardial infarction in mice. Circulation. 1999;99(23):3063-3070.
30. Fedak PW, Smookler DS, Kassiri Z, et al. TIMP-3 deficiency leads to dilated cardiomyopathy. Circulation. 2004;110(16):2401-2409.
31. Nishikawa N, Yamamoto K, Sakata Y, et al. Differential activation of matrix metalloproteinases in heart failure with and without ventricular dilatation. Cardiovasc Res. 2003;57(3):766-774.
32. Sivasubramanian N, Coker ML, Kurrelmeyer KM, et al. Left ventricular remodeling in transgenic mice with cardiac restricted overexpression of tumor necrosis factor. Circulation. 2001;104(7):826-831.
33. Li J, Schwimmbeck PL, Tschope C, et al. Collagen degradation in a murine myocarditis model: relevance of matrix metalloproteinase in association with inflammatory induction. Cardiovasc Res. 2002;56(2):235-247.
34. Cheung C, Luo H, Yanagawa B, et al. Matrix metalloproteinases and tissue inhibitors of metalloproteinases in coxsackievirus-induced myocarditis. Cardiovasc Pathol. 2006;15(2):63-74.
35. Heymans S, Pauschinger M, De Palma A, et al. Inhibition of urokinase-type plasminogen activator or matrix metalloproteinases prevents cardiac injury and dysfunction during viral myocarditis. Circulation. 2006;114(6):565-573.
36. Szabo Z, Magga J, Alakoski T, et al. Connective tissue growth factor inhibition attenuates left ventricular remodeling and dysfunction in pressure overload-induced heart failure. Hypertension. 2014;63(6):1235-1240.
37. Hutchinson KR, Guggilam A, Cismowski MJ, et al. Temporal pattern of left ventricular structural and functional remodeling following reversal of volume overload heart failure. J Appl Physiol (1985). 2011;111(6):1778-1788.
38. Gunja-Smith Z, Morales AR, Romanelli R, et al. Remodeling of human myocardial collagen in idiopathic dilated cardiomyopathy. Role of metalloproteinases and pyridinoline cross-links. Am J Pathol. 1996;148(5):1639-1648.

39. Stetler-Stevenson WG. Dynamics of matrix turnover during pathologic remodeling of the extracellular matrix. Am J Pathol. 1996;148(5):1345-1350.
40. Bishop JE, Greenbaum R, Gibson DG, et al. Enhanced deposition of predominantly type I collagen in myocardial disease. J Mol Cell Cardiol. 1990;22(10):1157-1165.
41. Khan S, Joyce J, Margulies KB, et al. Enhanced bioactive myocardial transforming growth factor-beta in advanced human heart failure. Circ J. 2014;78(11):2711-2718.
42. Klotz S, Foronjy RF, Dickstein ML, et al. Mechanical unloading during left ventricular assist device support increases left ventricular collagen cross-linking and myocardial stiffness. Circulation. 2005;112(3):364-374.
43. Marijianowski MM, Teeling P, Mann J, et al. Dilated cardiomyopathy is associated with an increase in the type I/type III collagen ratio: a quantitative assessment. J Am Coll Cardiol. 1995;25(6):1263-1272.
44. Pauschinger M, Doerner A, Remppis A, et al. Differential myocardial abundance of collagen type I and type III mRNA in dilated cardiomyopathy: effects of myocardial inflammation. Cardiovasc Res. 1998;37(1):123-129.
45. Pauschinger M, Knopf D, Petschauer S, et al. Dilated cardiomyopathy is associated with significant changes in collagen type I/III ratio. Circulation. 1999;99(21):2750-2756.
46. Sivakumar P, Gupta S, Sarkar S, et al. Upregulation of lysyl oxidase and MMPs during cardiac remodeling in human dilated cardiomyopathy. Mol Cell Biochem. 2008;307(1-2):159-167.
47. Yoshikane H, Honda M, Goto Y, et al. Collagen in dilated cardiomyopathy--scanning electron microscopic and immunohistochemical observations. Jpn Circ J. 1992;56(9):899-910.
48. Mollnau H, Munkel B, Schaper J. Collagen VI in the extracellular matrix of normal and failing human myocardium. Herz. 1995;20(2):89-94.
49. Reddy HK, Tjahja IE, Campbell SE, et al. Expression of matrix metalloproteinase activity in idiopathic dilated cardiomyopathy: a marker of cardiac dilatation. Mol Cell Biochem. 2004;264(1-2):183-191.
50. Tyagi SC, Campbell SE, Reddy HK, et al. Matrix metalloproteinase activity expression in infarcted, noninfarcted and dilated cardiomyopathic human hearts. Mol Cell Biochem. 1996;155(1):13-21.
51. Tyagi SC, Kumar S, Voelker DJ, et al. Differential gene expression of extracellular matrix components in dilated cardiomyopathy. J Cell Biochem. 1996;63(2):185-198.
52. Rouet-Benzineb P, Buhler JM, Dreyfus P, et al. Altered balance between matrix gelatinases (MMP-2 and MMP-9) and their tissue inhibitors in human dilated cardiomyopathy: potential role of MMP-9 in myosin-heavy chain degradation. Eur J Heart Fail. 1999;1(4):337-352.
53. Spinale FG, Coker ML, Heung LJ, et al. A matrix metalloproteinase induction/activation system exists in the human left ventricular myocardium and is upregulated in heart failure. Circulation. 2000;102(16):1944-1949.
54. Thomas CV, Coker ML, Zellner JL, et al. Increased matrix metalloproteinase activity and selective upregulation in LV myocardium from patients with end-stage dilated cardiomyopathy. Circulation. 1998;97(17):1708-1715.
55. Klappacher G, Franzen P, Haab D, et al. Measuring extracellular matrix turnover in the serum of patients with idiopathic or ischemic dilated cardiomyopathy and impact on diagnosis and prognosis. Am J Cardiol. 1995;75(14):913-918.
56. Schwartzkopff B, Fassbach M, Pelzer B, et al. Elevated serum markers of collagen degradation in patients with mild to moderate dilated cardiomyopathy. Eur J Heart Fail. 2002;4(4):439-434.
57. Yan AT, Yan RT, Spinale FG, et al. Plasma matrix metalloproteinase-9 level is correlated with left ventricular volumes and ejection fraction in patients with heart failure. J Card Fail. 2006;12(7):514-519.
58. Jordan A, Roldan V, Garcia M, et al. Matrix metalloproteinase-1 and its inhibitor, TIMP-1, in systolic heart failure: relation to functional data and prognosis. J Intern Med. 2007;262(3):385-

392.
59. Naito Y, Tsujino T, Lee-Kawabata M, et al. Matrix metalloproteinase-1 and -2 levels are differently regulated in acute exacerbation of heart failure in patients with and without left ventricular systolic dysfunction. Heart Vessels. 2009;24(3):181-186.
60. Terasaki F, Okamoto H, Onishi K, et al. Higher serum tenascin-C levels reflect the severity of heart failure, left ventricular dysfunction and remodeling in patients with dilated cardiomyopathy. Circ J. 2007;71(3):327-330.
61. Tamura A, Kusachi S, Nogami K, et al. Tenascin expression in endomyocardial biopsy specimens in patients with dilated cardiomyopathy: distribution along margin of fibrotic lesions. Heart. 1996;75(3):291-294.
62. Herpel E, Singer S, Flechtenmacher C, et al. Extracellular matrix proteins and matrix metalloproteinases differ between various right and left ventricular sites in end-stage cardiomyopathies. Virchows Arch. 2005;446(4):369-378.
63. Nogami K, Kusachi S, Nunoyama H, et al. Extracellular matrix components in dilated cardiomyopathy. Immunohistochemical study of endomyocardial biopsy specimens. Jpn Heart J. 1996;37(4):483-494.
64. Hsia TY, Ringewald JM, Stroud RE, et al. Determinants of extracellular matrix remodelling are differentially expressed in paediatric and adult dilated cardiomyopathy. Eur J Heart Fail. 2011;13(3):271-277.
65. Naba A, Clauser KR, Hoersch S, et al. The matrisome: in silico definition and in vivo characterization by proteomics of normal and tumor extracellular matrices. Mol Cell Proteomics. 2012;11(4):9.
66. Naba A, Clauser KR, Ding H, et al. The extracellular matrix: Tools and insights for the "omics" era. Matrix Biol. 2015;8(15):00121-00123.
67. Clausen T, Kaiser M, Huber R, et al. HTRA proteases: regulated proteolysis in protein quality control. Nat Rev Mol Cell Biol. 2011;12(3):152-162.
68. Yana I, Weiss SJ. Regulation of membrane type-1 matrix metalloproteinase activation by proprotein convertases. Mol Biol Cell. 2000;11(7):2387-2401.
69. Pihlajaniemi T, Myllyla R, Kivirikko KI. Prolyl 4-hydroxylase and its role in collagen synthesis. J Hepatol. 1991;13(3):S2-7.
70. Bader HL, Wang LW, Ho JC, et al. A disintegrin-like and metalloprotease domain containing thrombospondin type 1 motif-like 5 (ADAMTSL5) is a novel fibrillin-1-, fibrillin-2-, and heparin-binding member of the ADAMTS superfamily containing a netrin-like module. Matrix Biol. 2012;31(7-8):398-411.
71. Tsutsui K, Manabe R, Yamada T, et al. ADAMTSL-6 is a novel extracellular matrix protein that binds to fibrillin-1 and promotes fibrillin-1 fibril formation. J Biol Chem. 2010;285(7):4870-4882.
72. Bost F, Diarra-Mehrpour M, Martin JP. Inter-alpha-trypsin inhibitor proteoglycan family--a group of proteins binding and stabilizing the extracellular matrix. Eur J Biochem. 1998;252(3):339-346.
73. Bergqvist D, Nilsson IM. Hereditary alpha 2-macroglobulin deficiency. Scand J Haematol. 1979;23(5):433-436.
74. Somerville RP, Longpre JM, Jungers KA, et al. Characterization of ADAMTS-9 and ADAMTS-20 as a distinct ADAMTS subfamily related to Caenorhabditis elegans GON-1. J Biol Chem. 2003;278(11):9503-9513.
75. Bizet AA, Liu K, Tran-Khanh N, et al. The TGF-beta co-receptor, CD109, promotes internalization and degradation of TGF-beta receptors. Biochim Biophys Acta. 2011;5:742-753.
76. Bonnefoy A, Legrand C. Proteolysis of subendothelial adhesive glycoproteins (fibronectin, thrombospondin, and von Willebrand factor) by plasmin, leukocyte cathepsin G, and elastase.

Thromb Res. 2000;98(4):323-332.
77. Carmeliet P, Moons L, Lijnen R, et al. Urokinase-generated plasmin activates matrix metalloproteinases during aneurysm formation. Nat Genet. 1997;17(4):439-444.
78. Leask A. TGFbeta, cardiac fibroblasts, and the fibrotic response. Cardiovasc Res. 2007;74(2):207-212.
79. Gospodarowicz D. Localisation of a fibroblast growth factor and its effect alone and with hydrocortisone on 3T3 cell growth. Nature. 1974;249(453):123-127.
80. Bouleau S, Grimal H, Rincheval V, et al. FGF1 inhibits p53-dependent apoptosis and cell cycle arrest via an intracrine pathway. Oncogene. 2005;24(53):7839-7849.
81. Powers CJ, McLeskey SW, Wellstein A. Fibroblast growth factors, their receptors and signaling. Endocr Relat Cancer. 2000;7(3):165-197.
82. Li YS, Milner PG, Chauhan AK, et al. Cloning and expression of a developmentally regulated protein that induces mitogenic and neurite outgrowth activity. Science. 1990;250(4988):1690-1694.
83. Bowden ET, Stoica GE, Wellstein A. Anti-apoptotic signaling of pleiotrophin through its receptor, anaplastic lymphoma kinase. J Biol Chem. 2002;277(39):35862-35868.
84. Panse KD, Felkin LE, Lopez-Olaneta MM, et al. Follistatin-like 3 mediates paracrine fibroblast activation by cardiomyocytes. J Cardiovasc Transl Res. 2012;5(6):814-826.
85. Elson GC, Graber P, Losberger C, et al. Cytokine-like factor-1, a novel soluble protein, shares homology with members of the cytokine type I receptor family. J Immunol. 1998;161(3):1371-1379.
86. Sciaky D, Brazer W, Center DM, et al. Cultured human fibroblasts express constitutive IL-16 mRNA: cytokine induction of active IL-16 protein synthesis through a caspase-3-dependent mechanism. J Immunol. 2000;164(7):3806-3814.
87. Liu X, Das AM, Seideman J, et al. The CC chemokine ligand 2 (CCL2) mediates fibroblast survival through IL-6. Am J Respir Cell Mol Biol. 2007;37(1):121-128.
88. Orlandini M, Marconcini L, Ferruzzi R, et al. Identification of a c-fos-induced gene that is related to the platelet-derived growth factor/vascular endothelial growth factor family. Proc Natl Acad Sci U S A. 1996;93(21):11675-11680.
89. Puxeddu I, Bader R, Piliponsky AM, et al. The CC chemokine eotaxin/CCL11 has a selective profibrogenic effect on human lung fibroblasts. J Allergy Clin Immunol. 2006;117(1):103-110.
90. Iwabu A, Smith K, Allen FD, et al. Epidermal growth factor induces fibroblast contractility and motility via a protein kinase C delta-dependent pathway. J Biol Chem. 2004;279(15):14551-14560.
91. Lembach KJ. Induction of human fibroblast proliferation by epidermal growth factor (EGF): enhancement by an EGF-binding arginine esterase and by ascorbate. Proc Natl Acad Sci U S A. 1976;73(1):183-187.
92. Westermark B, Blomquist E. Stimulation of fibroblast migration by epidermal growth factor. Cell Biol Int Rep. 1980;4(7):649-654.
93. You DH, Nam MJ. Effects of human epidermal growth factor gene-transfected mesenchymal stem cells on fibroblast migration and proliferation. Cell Prolif. 2013;46(4):408-415.
94. Kajanne R, Miettinen P, Mehlem A, et al. EGF-R regulates MMP function in fibroblasts through MAPK and AP-1 pathways. J Cell Physiol. 2007;212(2):489-497.
95. Yamane K, Asano Y, Tamaki K, et al. Epidermal growth factor up-regulates transforming growth factor-beta receptor type II in human dermal fibroblasts via p38 mitogen-activated protein kinase pathway. Biochem Biophys Res Commun. 2007;352(1):69-77.
96. LeRoy EC, Trojanowska MI, Smith EA. Cytokines and human fibrosis. Eur Cytokine Netw. 1990;1(4):215-219.
97. Struyf S, Proost P, Vandercappellen J, et al. Synergistic up-regulation of MCP-2/CCL8 activity is counteracted by chemokine cleavage, limiting its inflammatory and anti-tumoral effects. Eur

J Immunol. 2009;39(3):843-857.
98. Heino J. The collagen family members as cell adhesion proteins. Bioessays. 2007;29(10):1001-1010.
99. Wenstrup RJ, Florer JB, Brunskill EW, et al. Type V collagen controls the initiation of collagen fibril assembly. J Biol Chem. 2004;279(51):53331-53337.
100. Monroe GR, Harakalova M, van der Crabben SN, et al. Familial Ehlers-Danlos syndrome with lethal arterial events caused by a mutation in COL5A1. Am J Med Genet A. 2015;167(6):1196-1203.
101. van der Rest M, Garrone R. Collagen family of proteins. Faseb j. 1991;5(13):2814-2823.
102. Walchli C, Koch M, Chiquet M, et al. Tissue-specific expression of the fibril-associated collagens XII and XIV. J Cell Sci. 1994;107 (Pt 2):669-681.
103. Fitzgerald J, Bateman JF. A new FACIT of the collagen family: COL21A1. FEBS Lett. 2001;505(2):275-280.
104. Tao G, Levay AK, Peacock JD, et al. Collagen XIV is important for growth and structural integrity of the myocardium. J Mol Cell Cardiol. 2012;53(5):626-638.
105. Van Agtmael T, Bailey MA, Schlotzer-Schrehardt U, et al. Col4a1 mutation in mice causes defects in vascular function and low blood pressure associated with reduced red blood cell volume. Hum Mol Genet. 2010;19(6):1119-1128.
106. Gould DB, Phalan FC, van Mil SE, et al. Role of COL4A1 in small-vessel disease and hemorrhagic stroke. N Engl J Med. 2006;354(14):1489-1496.
107. Verbeek E, Meuwissen ME, Verheijen FW, et al. COL4A2 mutation associated with familial porencephaly and small-vessel disease. Eur J Hum Genet. 2012;20(8):844-851.
108. Adiguzel E, Hou G, Mulholland D, et al. Migration and growth are attenuated in vascular smooth muscle cells with type VIII collagen-null alleles. Arterioscler Thromb Vasc Biol. 2006;26(1):56-61.
109. Pankov R, Yamada KM. Fibronectin at a glance. J Cell Sci. 2002;115(Pt 20):3861-3863.
110. Hyytiainen M, Penttinen C, Keski-Oja J. Latent TGF-beta binding proteins: extracellular matrix association and roles in TGF-beta activation. Crit Rev Clin Lab Sci. 2004;41(3):233-264.
111. Dallas SL, Sivakumar P, Jones CJ, et al. Fibronectin regulates latent transforming growth factor-beta (TGF beta) by controlling matrix assembly of latent TGF beta-binding protein-1. J Biol Chem. 2005;280(19):18871-18880.
112. Kanzaki T, Shiina R, Saito Y, et al. Role of latent TGF-beta 1 binding protein in vascular remodeling. Biochem Biophys Res Commun. 1998;246(1):26-30.
113. Zilberberg L, Todorovic V, Dabovic B, et al. Specificity of latent TGF-beta binding protein (LTBP) incorporation into matrix: role of fibrillins and fibronectin. J Cell Physiol. 2012;227(12):3828-3836.
114. Konstandin MH, Toko H, Gastelum GM, et al. Fibronectin is essential for reparative cardiac progenitor cell response after myocardial infarction. Circ Res. 2013;113(2):115-125.
115. van Dijk A, Niessen HW, Ursem W, et al. Accumulation of fibronectin in the heart after myocardial infarction: a putative stimulator of adhesion and proliferation of adipose-derived stem cells. Cell Tissue Res. 2008;332(2):289-298.
116. Chen MM, Lam A, Abraham JA, et al. CTGF expression is induced by TGF- beta in cardiac fibroblasts and cardiac myocytes: a potential role in heart fibrosis. J Mol Cell Cardiol. 2000;32(10):1805-1819.
117. Frazier K, Williams S, Kothapalli D, et al. Stimulation of fibroblast cell growth, matrix production, and granulation tissue formation by connective tissue growth factor. J Invest Dermatol. 1996;107(3):404-411.
118. Kato A, Okamoto O, Ishikawa K, et al. Dermatopontin interacts with fibronectin, promotes fibronectin fibril formation, and enhances cell adhesion. J Biol Chem. 2011;286(17):14861-14869.

119. Liu X, Meng L, Shi Q, et al. Dermatopontin promotes adhesion, spreading and migration of cardiac fibroblasts in vitro. Matrix Biol. 2013;32(1):23-31.
120. Tanaka K, Arao T, Maegawa M, et al. SRPX2 is overexpressed in gastric cancer and promotes cellular migration and adhesion. Int J Cancer. 2009;124(5):1072-1080.
121. Ohashi K, Enomoto T, Joki Y, et al. Neuron-derived neurotrophic factor functions as a novel modulator that enhances endothelial cell function and revascularization processes. J Biol Chem. 2014;289(20):14132-14144.
122. Bornstein P, Devarayalu S, Li P, et al. A second thrombospondin gene in the mouse is similar in organization to thrombospondin 1 but does not respond to serum. Proc Natl Acad Sci U S A. 1991;88(19):8636-8640.
123. Murphy-Ullrich JE, Gurusiddappa S, Frazier WA, et al. Heparin-binding peptides from thrombospondins 1 and 2 contain focal adhesion-labilizing activity. J Biol Chem. 1993;268(35):26784-26789.
124. Yang Z, Kyriakides TR, Bornstein P. Matricellular proteins as modulators of cell-matrix interactions: adhesive defect in thrombospondin 2-null fibroblasts is a consequence of increased levels of matrix metalloproteinase-2. Mol Biol Cell. 2000;11(10):3353-3364.
125. Beattie J, Kreiner M, Allan GJ, et al. IGFBP-3 and IGFBP-5 associate with the cell binding domain (CBD) of fibronectin. Biochem Biophys Res Commun. 2009;381(4):572-576.
126. Zeng H, Zhang Y, Yi Q, et al. CRIM1, a newfound cancer-related player, regulates the adhesion and migration of lung cancer cells. Growth Factors. 2015;33(5-6):384-392.

Supplemental Figures

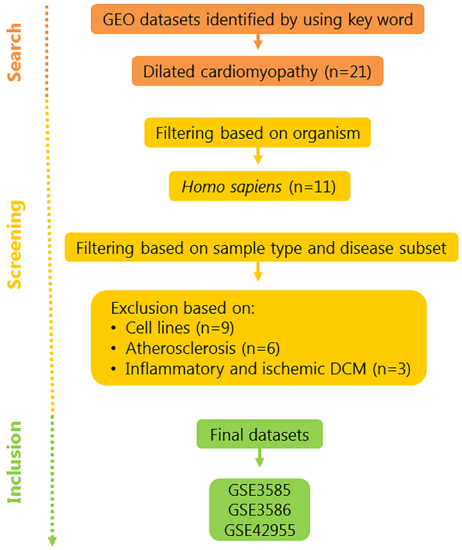

Supplementary Figure 1. Overview of the pipeline used for dataset selection. Workflow consisted of searching for the key word "dilated cardiomyopathy" on NCBI's GEO database, followed by filtering based on organism, sample type and disease subset. The final three selected datasets included human DCM and non-failing heart samples in their study design. DCM; dilated cardiomyopathy.

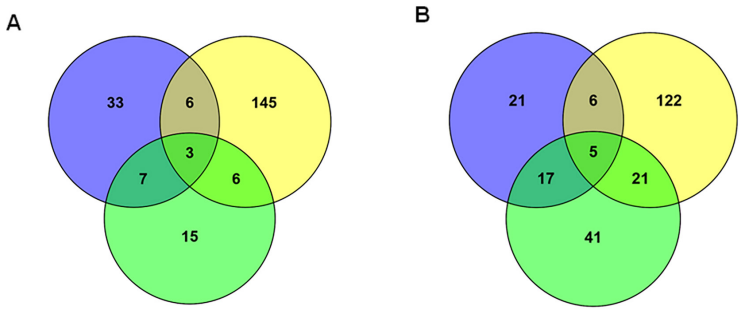

Supplementary Figure 2. Venn diagram of up-regulated (A) and down-regulated (B) matrisome genes in three dilated cardiomyopathy GEO datasets: GSE 42955 (blue), GSE 3586 (yellow) and GSE 3585 (green).

Supplemental Tables

Supplemental tables can be downloaded from: http://bit.ly/35d1woJ

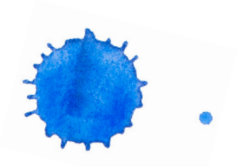

Angiogenesis – **Chapter 5**

CMTM3 mediates angiogenesis by regulating cell surface availability of VE-cadherin in endothelial adherens junctions

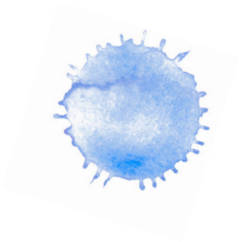

I. Chrifi, L. Louzao Martinez, M.M. Brandt, C.G.M. van Dijk, P.E. Bürgisser, C. Zhu, J.M. Kros, D.J. Duncker, C. Cheng.

(2017) Arteriosclerosis Thrombosis and Vascular Biology, 37(6):1098-1114

Abstract

Decrease of vascular endothelial (VE) cadherin in adherens junctions (AJs) reduces vascular stability, whereas disruption of AJs is a requirement for neovessel sprouting during angiogenesis. Endocytosis plays a key role in regulating junctional strength by altering bio-availability of cell surface proteins, including VE-cadherin. Identification of new mediators of endothelial endocytosis could enhance our understanding of angiogenesis. Here we assessed the function of CKLF-like MARVEL Transmembrane domain 3 (CMTM3), which we have previously identified as highly expressed in Flk1+ endothelial progenitor cells during embryonic development. Using a 3D co-culture of HUVECs-GFP and pericytes-RFP, we demonstrated that siRNA-mediated CMTM3 silencing in HUVECs impairs angiogenesis. *In vivo* CMTM3 inhibition by morpholino injection in developing zebrafish larvae confirmed that CMTM3 expression is required for vascular sprouting. CMTM3 knockdown in HUVECs does not affect proliferation or migration. Intracellular staining demonstrated that CMTM3 co-localizes with early endosome markers endosomal antigen-1 positive (EEA1) and Clathrin+ vesicles, and with cytosolic VE-cadherin in HUVECs. Adenovirus-mediated CMTM3 overexpression enhances endothelial endocytosis, shown by an increase in Clathrin+, EEA1+, Rab11+, Rab5+, and Rab7+ vesicles. CMTM3 overexpression enhances, whereas CMTM3 knockdown decreases internalization of cell surface VE-cadherin *in vitro*. CMTM3 promotes loss of endothelial barrier function in thrombin-induced responses, shown by trans-endothelial electrical resistance (TEER) measurements *in vitro*. In this study we have identified a new regulatory function for CMTM3 in angiogenesis. CMTM3 is involved in VE-cadherin turnover and is a regulator of the cell surface pool of VE-cadherin. Therefore, CMTM3 mediates cell-cell adhesion at AJs and contributes to the control of vascular sprouting.

Introduction

Angiogenesis is a hypoxia-driven process that produces the vascular network during embryogenesis, mature wound healing and disease progression in adult life[1]. Intercellular adhesion and signaling mediated by homophilic interaction of VE-cadherin proteins in endothelial adherens junctions (AJs) play key roles in maintaining endothelial barrier function and vascular homeostasis during and after angiogenesis[2-5]. Gene ablation studies of VE-cadherin and associated proteins have revealed that junction strength dictates endothelial function and microvascular morphology and integrity[6,7]. An important aspect in angiogenesis is the ability of endothelial cells (ECs) to dynamically modulate cell-cell adhesive state by regulating VE-cadherin availability at the cell membranes. Although reduced VE-cadherin mediated cell-cell adhesion reduces microvascular stability, decrease in adhesive strength and disruption of endothelial AJs is required to allow ECs migration and neovessel sprouting during vascular expansion.

Endocytosis is a cellular process that is commonly used to alter bio-availability of cell surface proteins to modulate their functions. Endocytosis involves uptake of cell surface proteins in transport vesicles and sorting of vesicle cargo to either recycling or degradation compartments. By using Rab family GTPases as markers for intracellular vesicular compartments, the transport route of the membrane proteins can be actively monitored[8]. Previous studies have indicated that p120-catenin regulates VE-cadherin lysosomal degradation by inhibiting endocytosis of the cell surface pool via interaction with the cytoplasmic tail of VE-cadherin proteins[9]. Further analysis revealed that p102-catenin acts as a key protein in the plasma membrane retention mechanism of VE-cadherin by preventing recruitment of VE-cadherin into membrane domains enriched with endocytic machinery proteins, including Clathrin[10]. Other studies also indicate that cell surface availability of VE-cadherin is regulated by vascular enodhtelial growth factor A (VEGFA) and is mediated by ß-arrestin and Clathrin-dependent endocytosis[4].

Although endothelial endocytosis plays such a critical role in VE-cadherin and AJ regulation during and after angiogenesis, our overview of important regulators involved in these early endocytotic and subsequent intracellular transport processes is still far from complete. To identify new key regulators in angiogenesis and vascular homeostasis we conducted a micro-array screen on the transcriptome of murine embryos, comparing Flk+ endothelial progenitor cells with the Flk1- cell population. We identified CKLF-like MARVEL Transmembrane domain 3 (CMTM3)

as a putative candidate gene enriched in the Flk1+ endothelial progenitor cell population. CMTM3 is a member of the ChemoKine-Like Factor Super Family (CKLFSF/CMTM) located on chromosome 16q22.1[11]. CMTM is a family of proteins linking chemokines and the Transmembrane 4 Super Family (TM4SF), encoded by 9 genes in humans, CKLF and CKLFSF1-8[11]. Previous reports have indicated that CMTM members play important roles in cancer development[9,12,13]. Furthermore, some members of the CMTM family are highly expressed in immune cells[11,14]. For CMTM3, more recent reports indicate involvement of the protein in preventing growth and invasion of different types of cancer[15-17]. However, the putative function of CMTM3 in angiogenic regulation in ECs remains to be elucidated.

Here we studied the angiogenic potential of CMTM3 and investigated the molecular pathways that are mediated by CMTM3 in ECs. Our findings indicate that CMTM3 promotes neovessel formation *in vitro* in a 3D collagen matrix based co-culture of primary vascular cells. Loss-of function studies *in vivo* by morpholino-silencing of the orthologue of CMTM3 in developing zebrafish larvae validate CMTM3 pro-angiogenic capacities. *In vitro* studies demonstrate that CMTM3 co-localizes with the early endosomes markers (early endosome marker 1 (EEA1) and Clathrin) and internalized VE-cadherin. CMTM3 overexpression in HUVECs promotes endocytosis and intracellular vesicular trafficking, and augments basal and VEGFA-induced internalization of VE-cadherin. In contrast, knockdown of CMTM3 in human umbilical vein endothelial cells (HUVECs) significantly reduces VE-cadherin internalization. On the basis of these findings, we propose a model in which CMTM3 contributes to early endocytosis of VE-cadherin, a crucial step for reducing cell-cell adhesive strength in AJs to facilitate neovascular sprouting in the initial steps of angiogenesis. Our study provides new insights into the regulatory mechanisms by which endocytosis controls bio-availability of VE-cadherin in endothelial AJs and presents the first evidence of CMTM3-mediated control of early endocytosis of cell membrane surface proteins in vascular cells during angiogenesis.

Results

CMTM3 silencing in endothelial cells impairs vascular growth in a 3D collagen matrix vascular co-culture system in vitro.

CMTM3 function in angiogenesis was assessed in loss-of-function studies, conducted by transfection of *CMTM3* targeting siRNA in HUVECs with GFP marker expression. QPCR analysis validated efficient silencing of *CMTM3* in cells

treated with *CMTM3* targeting siRNA (siCMTM3) versus non-transfected controls (control) or cells transfected with a pool of non-targeting siRNA sequences (sisham) (Figure 1A). Expression levels of the other CMTM-family members did not differ between groups, indicating that the siRNA mediated silencing of *CMTM3* was specific (Figure 1B). Next, the angiogenic capacities of these *CMTM3*-silenced ECs were evaluated in an *in vitro* 3D angiogenesis assay that was previously developed for studying the formation of lumenized micro-capillary structures (Figure 1C)[18,19]. In this assay, GFP labeled HUVECs and RFP labeled pericytes were co-cultured in a collagen matrix, which enabled direct interaction between the two cell types. EC sprouting and onset of tubule formation can be observed after 1 day of co-culture. At the same time, stabilization of neovascular structures is triggered by perivascular recruitment of pericytes. Both processes proceed untill 5 days post-seeding, eventually forming micro-capillaries with pericyte coverage and clear distinction of open luminal areas (Figure 1C). Imaging and quantification of the vascular structures were conducted at days 2 and 5.

Data obtained at days 2 and 5 showed that CMTM3 silencing in GFP-HUVECs severely impaired formation of neovascular structures in the 3D vascular assay, compared with non-treated and sisham controls (Figure 1D and E). CMTM3 silencing reduced total tubule length (by 4.6- and 3.9-fold at day 2 and by 2.7- and 2.6-fold at day 5), number of tubules (by 3.6- and 3.1-fold at day 2 and by 2.2- and 2.1-fold at day 5), number of junctions (by 10.2- and 7.5-fold at day 2 and by 4.8- and 4.7-fold at day 5), and mean tubule length (by 1.3- and 1.2-fold at day 2 and by 1.4- and 1.3-fold at day 5), compared with control and sisham, respectively. In contrast CMTM3 silencing in RFP-pericytes did not affect neovascular growth, demonstrated by lack of differences between groups in vascular parameters at both time points (Figure 1F). Similarly, CMTM3 silencing in GFP-HUVECs using a second siRNA sequence significantly decreased total tubule length, and the number of junctions and tubules in the 3D vascular assay (Supplemental Figure 1).

Mural cell interaction induces expression of CMTM3 and CMTM-family members CKLF1, CMTM2, CMTM4 and CMTM8 in endothelial cells.

To investigate the CMTM3 expression in vascular cells, qPCR analysis was conducted on single cultured vascular cells and compared with co-cultured human vascular cells that mimicked the *in vivo* physiological condition in which pericytes and ECs are in direct contact during angiogenesis and vascular homeostasis. *CMTM3* was significantly upregulated in HUVECs in response to co-culture with pericytes and

vascular smooth muscle cells (VSMCs) (Figure 2A,B). Further evaluation of the other CMTM family members showed upregulation of *CMTM4* and *CMTM8* in response to co-culture with VSMCs or pericytes, whereas *CMTM2* and *CLKF1* were only upregulated in the VSMCs co-culture condition (Figure 2B). *CMTM3*

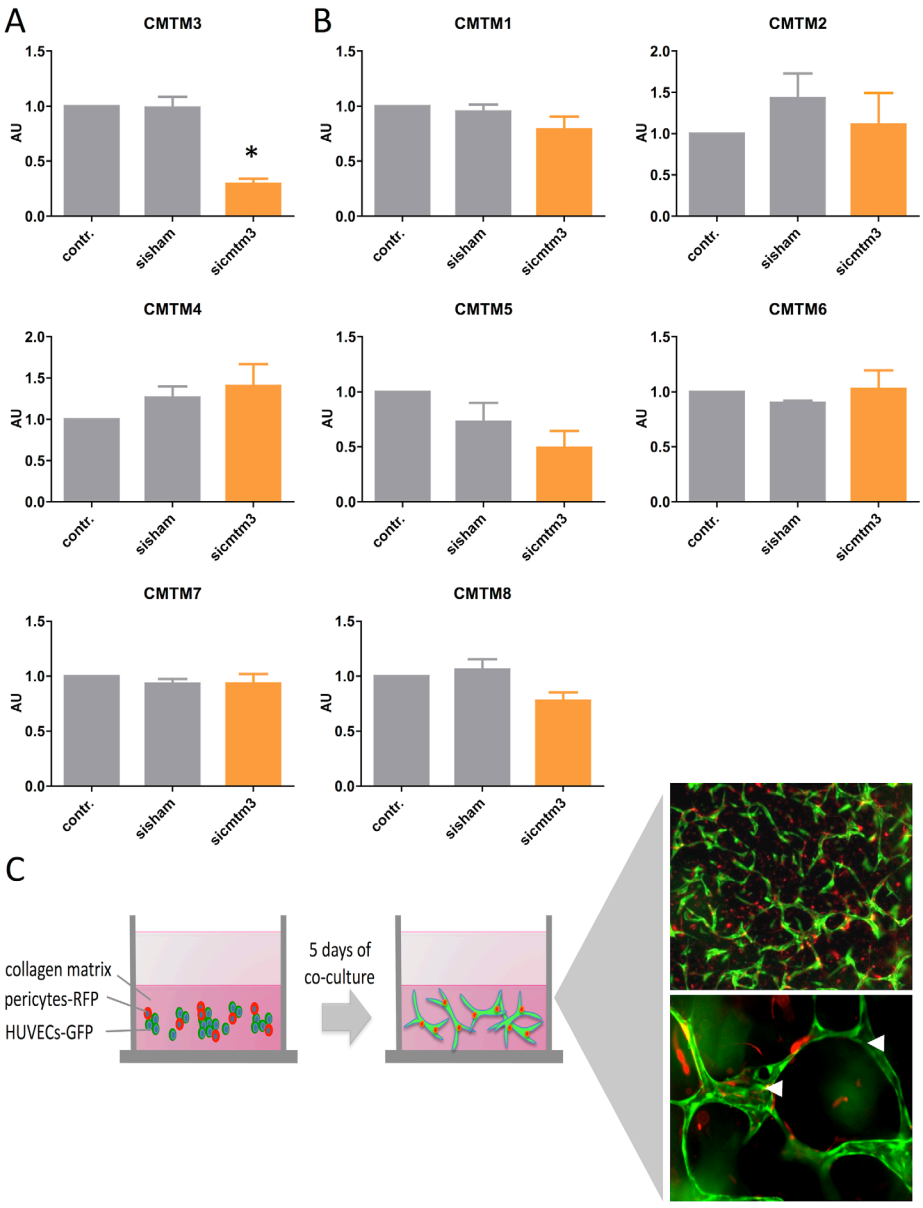

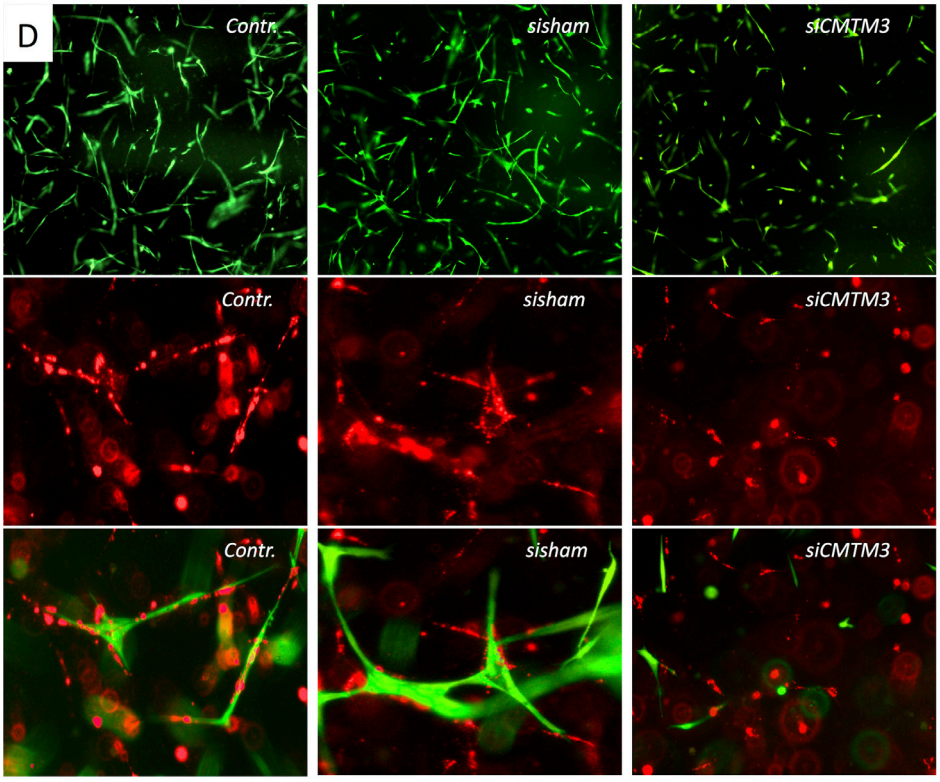
D
Contr.
sisham
siCMTM3
Contr.
sisham
siCMTM3
Contr.
sisham
siCMTM3

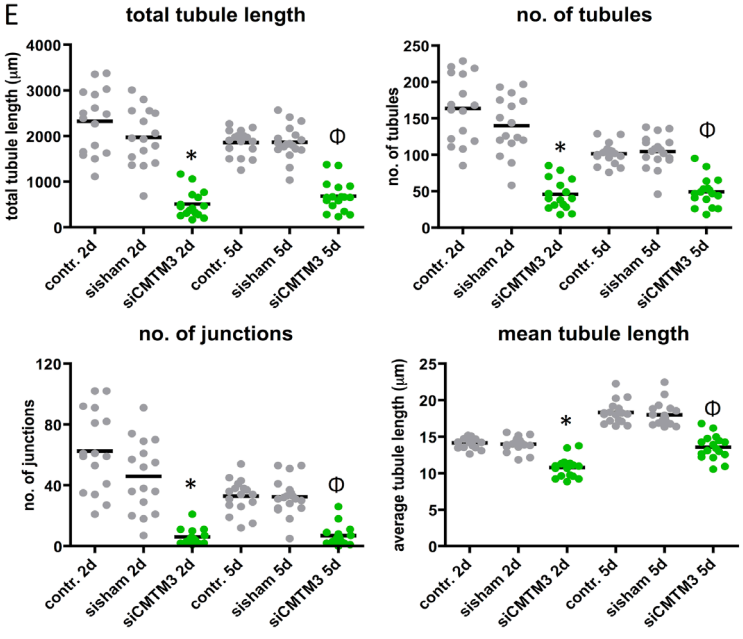
E
total tubule length
total tubule length (µm)
4000
3000
2000
1000
0
no. of tubules
no. of tubules
250
200
150
100
50
0
no. of junctions
no. of junctions
120
80
40
0
mean tubule length
average tubule length (µm)
25
20
15
10
5
0
*
Φ
contr. 2d
sisham 2d
siCMTM3 2d
contr. 5d
sisham 5d
siCMTM3 5d

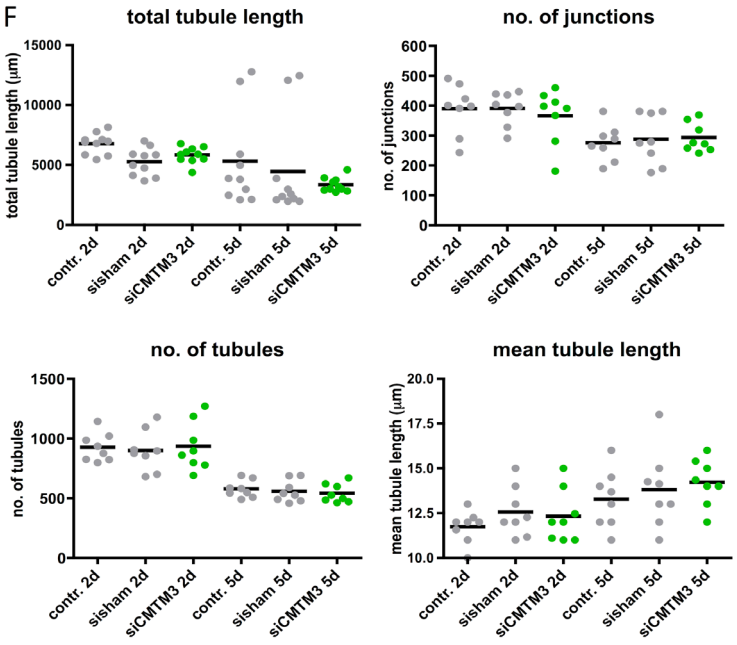

Figure 1. CMTM3 silencing in endothelial cells impairs vascular growth in a 3D collagen matrix vascular co-culture system *in vitro*. (A) Quantitative polymerase chain reaction (qPCR) analysis of *CMTM3* expression levels in HUVECs treated with *CMTM3*-targeting siRNA (siCMTM3) compared with non-targeting siRNA treated cells (sisham) or non-treated controls (contr.). (B) QPCR analysis of mRNA expression levels of CMTM family members in HUVECs treated with siCMTM3 compared with sisham or contr. cells. For A and B, gene expression levels are shown in target gene/house-keeping gene (*ß-actin*) ratio (AU). N≥6. Shown is mean ± SEM; *P<0.05 vs. sisham and control. (C) Schematic figure showing the 3D collagen matrix co-culture set up. Right: representative confocal microscopy images taken at low (upper image) and high magnifications (lower image) at 5 days of co-culture. HUVECS are labelled with GFP (green) and pericytes are labelled with RFP (red). Arrowheads indicate neovascular structures with open lumen. (D) Representative low (upper row) and high (2 lower rows) magnification images of 3D collagen matrix HUVECs-GFP and pericytes-GFP co-cultures in which HUVECs-GFP were treated with siCMTM3 and compared with sisham or contr. cells. Images displayed were taken at day 5. (E) Quantification of total tubule length, number of tubules and junctions, and mean tubule length at day 2 and 5 of co-culture. N≥15 co-cultures. Shown is mean ± SEM; *P<0.05 vs. control and sisham at day 2, $^{\Phi}$P<0.05 vs. control and sisham at day 5. (F) Data from co-culture experiments in which pericytes-RFP were treated with siCMTM3 and compared with sisham or contr. cells. Quantification of total tubule length, number of tubules and junctions, and mean tubule length at days 2 and 5 of co-cultures. N≥8 co-cultures. Shown is mean ± SEM.

expression was not altered in mural cells exposed to endothelial co-stimulation, whereas *CMTM2*, *CMTM4*, and *CMTM8* expressions in mural cells were responsive to co-culture with ECs. These findings indicate that *CMTM3* and CMTM-family

members are upregulated in response to endothelial and mural cell contact.

Silencing of CMTM3 during zebrafish development inhibits intersomitic vessel growth.

To assess the involvement of CMTM3 in angiogenesis *in vivo*, the gene was silenced in developing zebrafish larvae of the transgenic zebrafish lines Tg(fli1:eGFP)^{y1}, using morpholino (MO) knockdown technology. *CMTM3* and its family members are highly conserved in most species including the zebrafish. Two morpholinos were designed for silencing of the zebrafish *CMTM3* orthologue based on the splice modification principle of the pre-mRNA target and were validated to produce (non-functional) alternative splice products (Supplemental Figure 2A-C). The first morpholino construct targeting the splice site located on *CMTM3* exon 3 – intron 3 (E3-I3), diminished intersegmental vessel (ISV) formation at 24 hours post fertilization compared with uninjected controls (UICs). Quantification of zebrafish phenotype showed that in the E3-I3 group, 47% of the larvae displayed the ISV defect phenotype, versus 0% in the control group (Figure 3A,B). Functional validation of the E3-I3 morpholino was shown by PCR analysis of mRNA extracted from injected pools of larvae, indicated by the presence and absence of the non-spliced pre-mRNA band in E3-I3 and UIC groups respectively (Supplemental Figure 2A-C). Similarly, the second morpholino construct targeting the splice site on exon 2 – intron 2 (E2-I2) inhibited the growth of ISVs, with the defect phenotype consistently observed in 67% of the E2-E2 group versus 0% in the UIC group, further validating the negative effect of *CMTM3* silencing on angiogenesis during zebrafish development (Figure 3B and Supplemental Figure 2A-F).

CMTM3 silencing does not affect endothelial cell proliferation and migration.

Previous studies in gastric cancer cells imply that CMTM3 functions as a tumor suppressive gene with overexpression of CMTM3 leading to inhibition of cell proliferation and migration. Here we investigated the effect of CMTM3 silencing on these specific parameters in HUVECs. Knockdown of *CMTM3* mediated by siRNA targeting (siCMTM3) did not affect cell proliferation compared with non-transfected and non-targeting siRNA transfected controls (sisham), indicated by a lack of difference in cell count during HUVEC expansion in the course of 2 days (Figure 4A). In line with these results, no difference in cell cycle progression was observed between the groups (Figure 4B and C). In addition, cell migration capacity

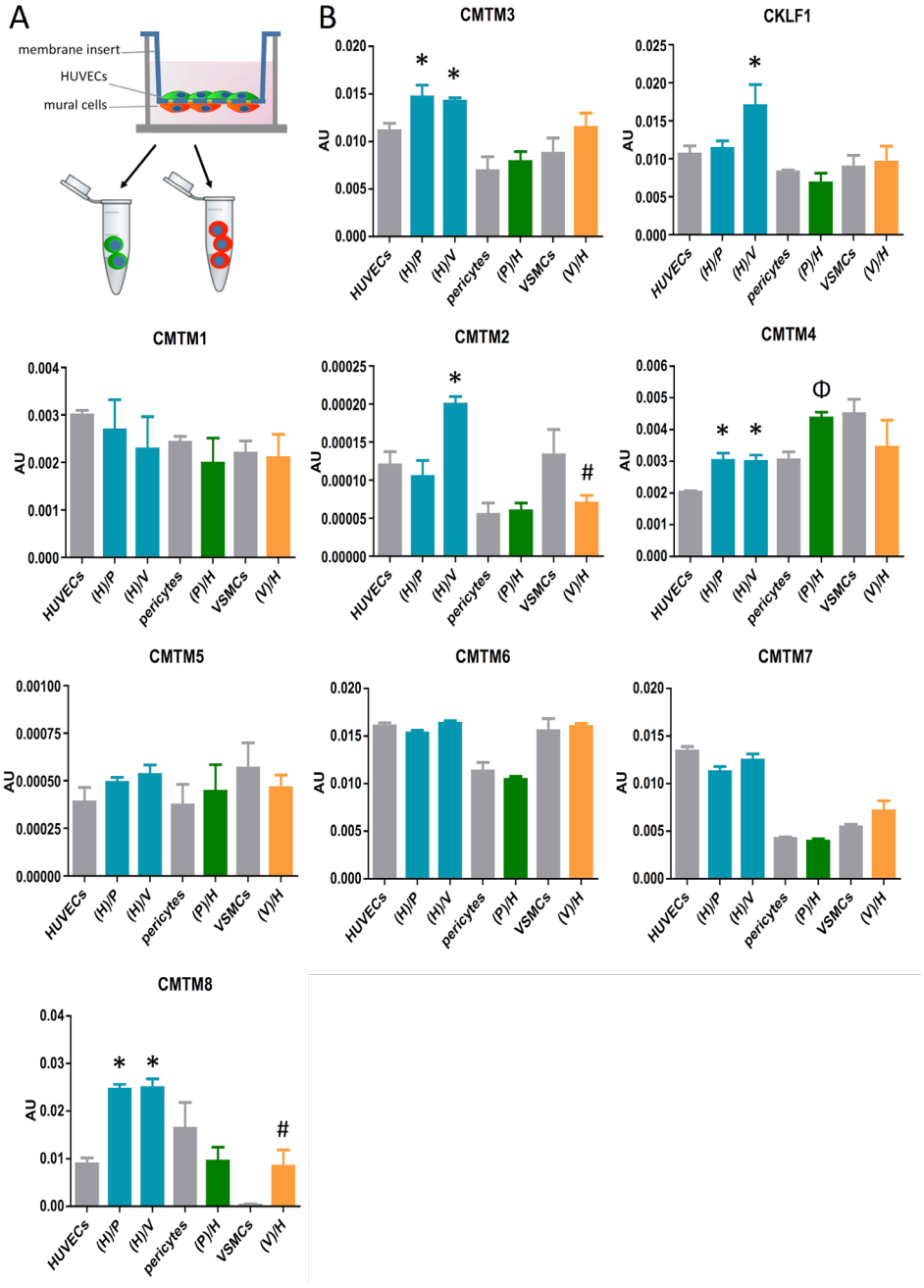

Figure 2. Among the CMTM-family members, *CMTM3*, *CKLF1*, *CMTM2*, *CMTM4*, and *CMTM8* expression in HUVECs respond to mural cell interaction. (A) Schematic representation of the protocol. (B) Quantitative polymerase chain reaction (qPCR) analysis of the expression level of CMTM-family members in monoculture of HUVECs, perycites or VSMCs and

(Figure 2 continued) co-culture conditions. (H)/P: Measured in HUVECs cocultured with pericytes. (H)/V): Measured in HUVECs cocultured with VSMCs. (P)/H: Measured in pericytes cocultured with HUVECs. (V)/H: Measured in VSMCs cocultured with HUVECs. Gene expression levels are shown in target gene/house-keeping gene (*ß-actin*) ratio (AU). N≥6. Shown is mean ± SEM; *P<0.05 vs. other HUVEC single culture, $^{\Phi}$P<0.05 vs. pericyte single culture, $^{\#}$P<0.05 vs. VSMC single culture.

was investigated in a transwell migration assay, but showed no effect of *CMTM3* silencing (Figure 4D and E). Similarly, migration and proliferation was not affected by CMTM3 overexpression in HUVECs, which was induced by transfection with a recombinant adenovirus encoding for human CMTM3 cDNA (adCMTM3) (Supplemental Figure 3). These data indicate that decrease in physiological levels of CMTM3 does not affect the proliferative and migratory capacity of human ECs.

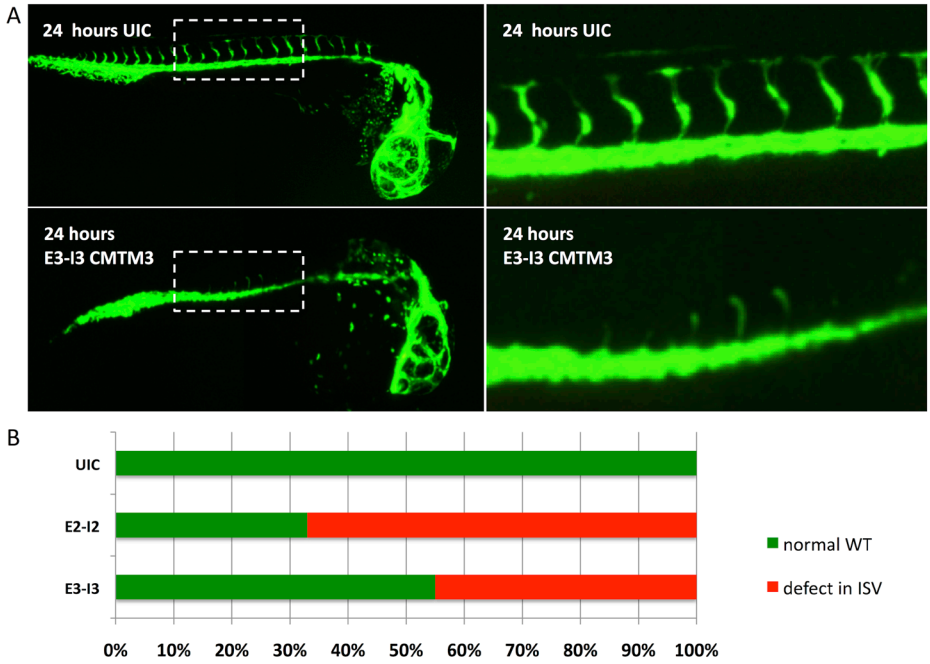

Figure 3. Morpholino-induced silencing of *CMTM3* in zebrafish affects vascular growth of intersomitic vessels. (A) Tg(fli1:eGFP)^{y1} embryos at 24 hpf, lateral view, anterior to the right. Distinct reduction of intersomitic vascular sprouting in the trunk region was observed in *CMTM3* targeting morpholino-injected (morpholino targeting splice site E3-I3 of *CMTM3*, indicated as E3-I3 *CMTM3*) embryos compared with uninjected controls (UIC). The zebrafish vascularture is highlighted by the eGFP marker (green). Right hand panel shows high magnification images showing intersomitic outgrowth in the indicated trunk region. (B) Quantification of the defective intersomitic vasculature (ISV) phenotype and wildtype (normal) phenotype in zebrafish larvae injected with E3-E3 or E2-I2 morpholinos vs. UIC. Data represent percentage of counted larvae.

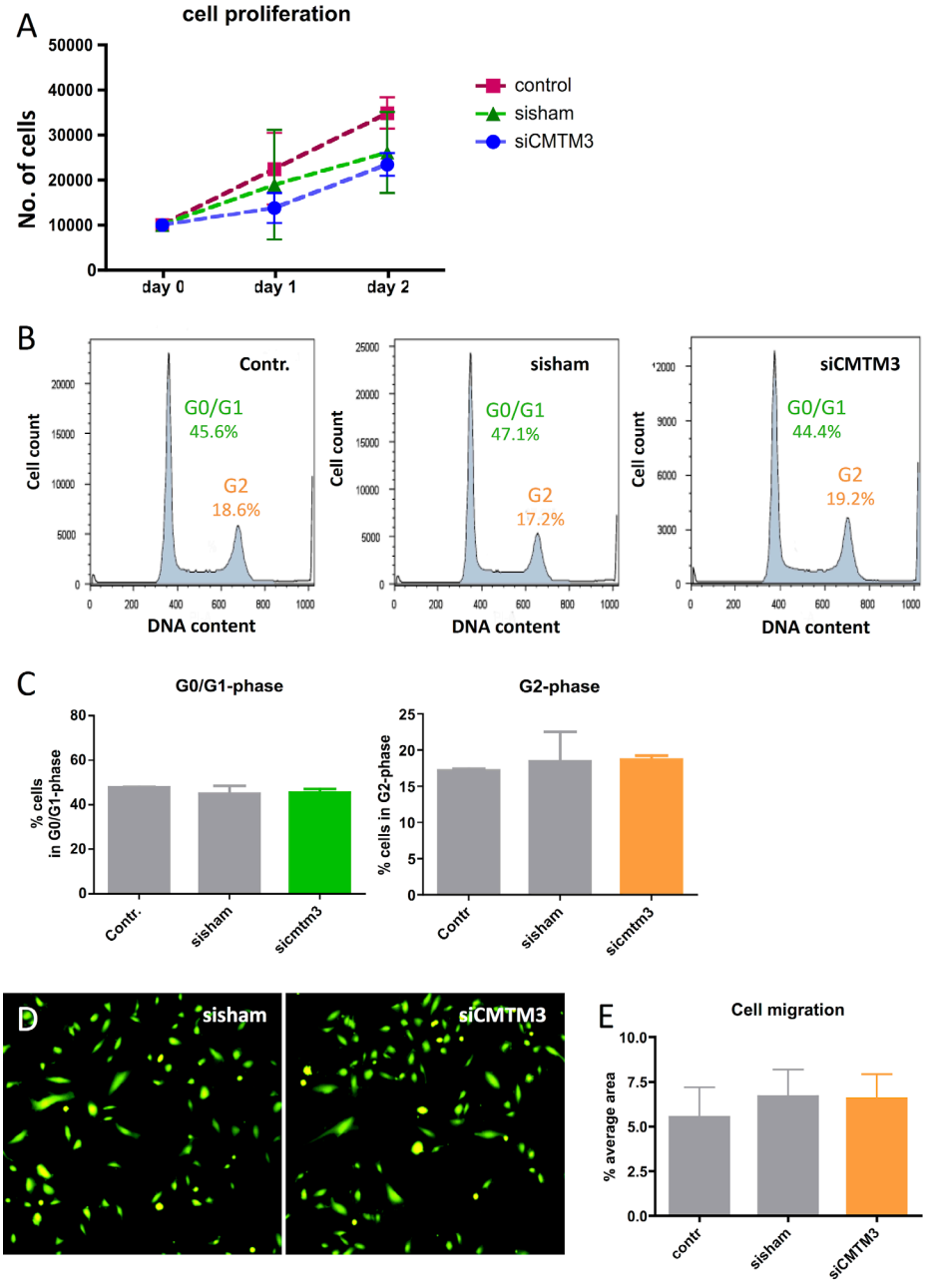

Figure 4. CMTM3 inhibition does not affect endothelial cell proliferation and migration. (A) Number of counted cells at day of seeding (day 0) and after 1 and 2 days of cell proliferation of HUVECs treated with *CMTM3*-targeting siRNA (siCMTM3) compared with non-targeting siRNA treated cells (sisham) and non-treated controls (contr.). N=6. Shown is mean ± SEM.

(Figure 4 continued) (B) Representative flow cytometry profiles showing the distribution of G0/G1 and G2 phase cells at 2 days post seeding of siCMTM3 transfected HUVECs compared with sisham and non-transfected controls stained for DNA content with PI. (C) Quantification of % cells in G0/G1 and % cells in G2 phase of siCMTM3 transfected HUVECs compared with sisham and non-transfected controls. N=6. Shown is mean ± SEM. (D) Representative results of trans-membrane migration assays after 24 hours of migration of siCMTM3 treated HUVECs compared with sisham treated cells. Cells are visualized by Calcein-AM (Green) uptake. (E) Quantification of % area within image field covered by siCMTM3 transfected HUVECs compared with sisham and non-transfected controls. N=8. Shown is mean ± SEM.

CMTM3 localizes in distinct vesicle-like structures and co-localizes with VE-cadherin in the endothelial cytosol.

To further elucidate the mechanistic function of CMTM3, HUVECs were transfected with adCMTM3. Transgene expression was validated by qPCR and compared with HUVECs transfected with sham virus (adsham; Figure 5A). CMTM3 protein was detected by immunofluorescence staining in the cytosol where it accumulated in vesicle-like structures (Figure 5B). Western blot analysis also demonstrated that CMTM3 was present in the soluble cytosolic fraction, and not in the insoluble actin bound fraction of HUVEC lysates (Figure 5C). To further elucidate the intracellular function of CMTM3, we assessed the co-localization of CMTM3 with markers of the different intracellular vesicular transport compartments. Double immunofluorescence staining of EEA1 (a marker of early endosomes) and CMTM3 in HUVECs transfected with adCMTM3 showed significant co-localization between the 2 signals in the larger sized cytosolic vesicles (Figure 5D). Similarly, CMTM3 co-localized with larger vesicles that were positive for Clathrin (Figure 5E). In contrast, co-localizations between CMTM3 and Rab11 or Rab4 (both markers of recycling vesicles), and between CMTM3 and Rab7 (marker for vesicles destined to transport proteins to the lysosomal degradative pathway) or Rab5 (late endosome/lysosome protein) were limited (Figure 5F-I). Intracellular trafficking of endocytic vesicles plays a crucial regulatory role in controlling cell surface presentation of VE-cadherin, a cell-cell AJ protein that is critical for vascular barrier function and angiogenesis[10]. Immunofluorescence staining of VE-cadherin in confluent endothelial monolayers of adCMTM3 transfected HUVECs (adCMTM3) showed that CMTM3 overexpression increased cytosolic localization of VE-cadherin compared with the mainly cell-cell junctional localization that was observed in controls transfected with sham adenovirus (adsham) (Figure 5J). Western blot analysis indicated that total protein levels of VE-cadherin remained unchanged (Figure 5K). Double staining of CMTM3 and VE-cadherin in adCMTM3

HUVECs showed significant co-localization of CMTM3 with cytosolic VE-cadherin (Figure 5L).

Quantification of the co-localization signals represented in Pearson's correlation coefficient values confirms our visual observations, showing higher values for CMTM3/EEA1 and CMTM3/VE-cadherin compared with CMTM3/Rab11, CMTM3/Rab7, CMTM3/Rab4 or CMTM3/Rab5 co-localizations (Figure 5M). CMTM3/

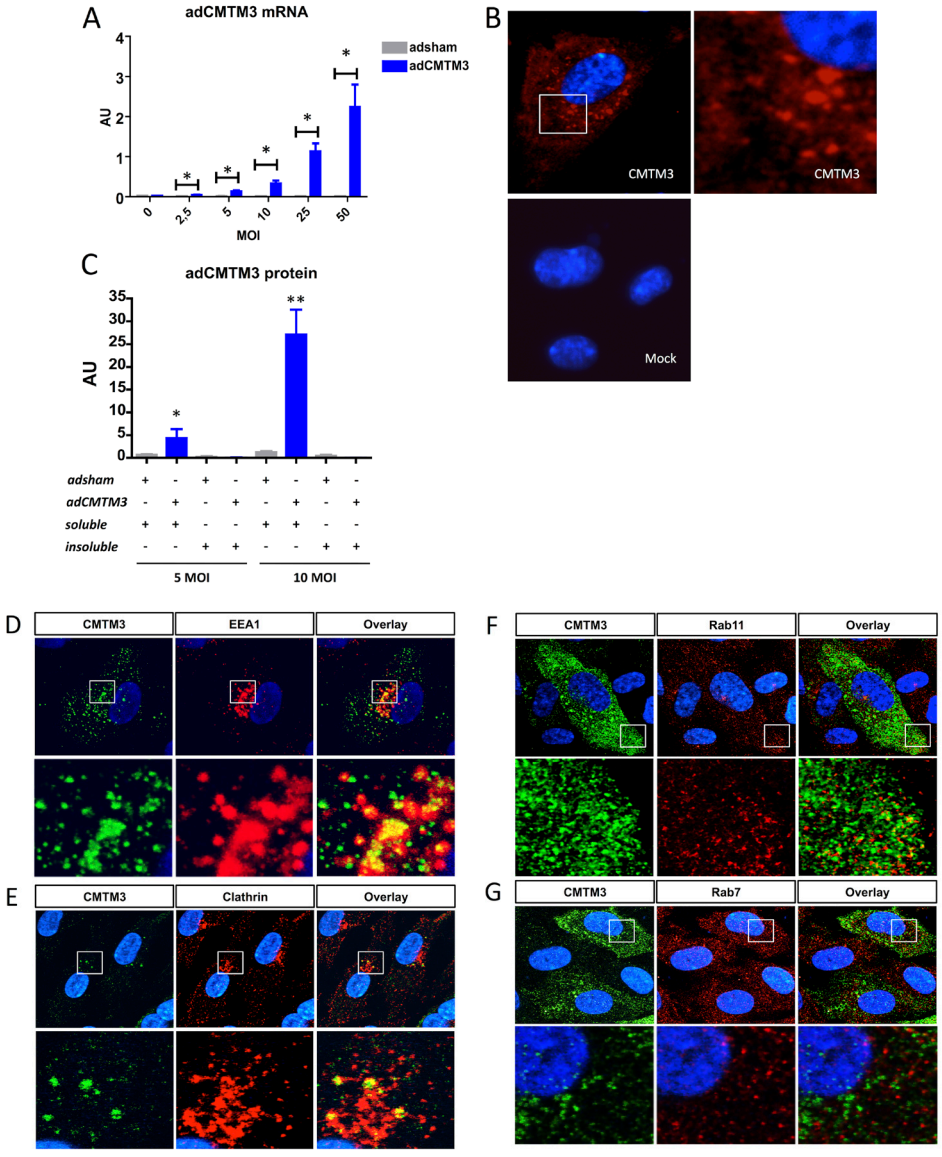

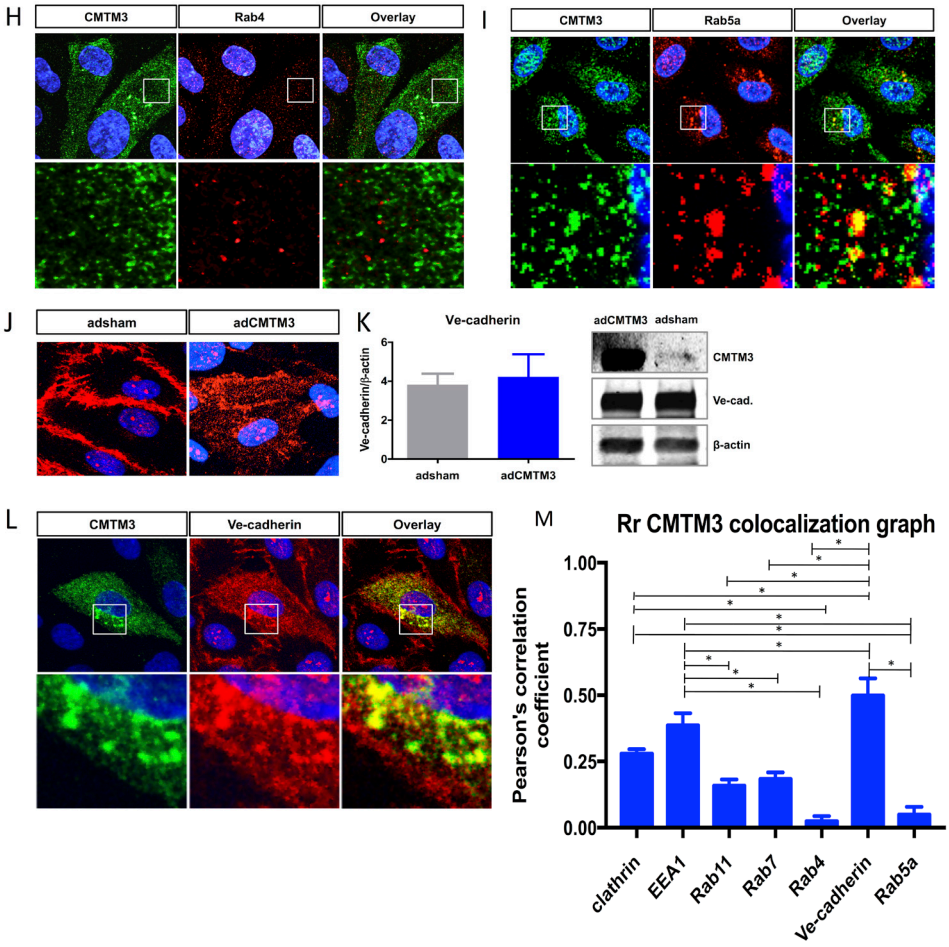

Figure 5. CMTM3 localizes in distinct vesicle-like structures and co-localizes with VE-cadherin in the endothelial cytosol, but not at adherens junctions. (A) Quantitative polymerase chain reaction (qPCR) analysis of human *CMTM3* expression levels in HUVECs transfected with different multiplicity of infection (MOI) of adenovirus containing an expression vector for CMTM3 cDNA (adCMTM3) or with sham virus containing an empty expression vector (adsham). Gene expression levels are shown in target gene/house-keeping gene (*ß-actin*) ratio (AU). N=3. Shown is mean ± SEM; *P<0.05 in Student's t-test comparisons between adsham and adCMTM3 group of equal MOI. (B) Representative low and higher magnification immunofluoresence images of HUVECs transfected with adCMTM3 and immunostained for CMTM3 (red). Mock image shows the background signal of secondary labeling antibody. (C) Western blot quantification of CMTM3 protein levels in adsham and adCMTM3 transfected HUVECs in the soluble (cytosol) and insoluble (actin-cytoskeleton bound) cell lysates fraction at different MOIs. Protein levels are shown in CMTM3/loading control protein (ß-actin) ratio (AU). N=4. Shown is mean ± SEM; *P<0.05 vs. other all other groups, **P<0.01 vs. all other groups. (D) Representative low and higher magnification immunofluorescence images of HUVECs transfected with adCMTM3 MOI 5, immunostained for CMTM3 (green) and EEA1 (red), (E) CMTM3 (green) and Clathrin (red), (F) CMTM3 and Rab11,

(Figure 5 continued) (G) CMTM3 and Rab7, (H) CMTM3 and Rab4. (I) CMTM3 and Rab5. Co-localization of CMTM3 and endocytic compartment protein markers in overlay images in yellow. (J) Representative immunofluoresence images of HUVECs transfected with adsham or adCMTM3, immunostained for VE-cadherin (red). Co-localization in overlay image is in yellow. (K) Western blot quantification of VE-cadherin protein bands in adsham and adCMTM3 transfected HUVECs, protein levels are shown in VE-cadherin/loading control protein (ß-actin) ratio. N=3. Shown is mean ± SEM. Representative Western blot bands for CMTM3, VE-cadherin and ß-actin are shown for adCMTM3 and adsham transfected HUVECs. (L) Representative low and higher magnification immunofluoresence images of HUVECs transfected with adCMTM3 and immunostained for CMTM3 (green) and VE-cadherin (red). (M) Quantificantion of co-localization of CMTM3 with VE-cadherin and endocytic compartment markers in immunofluorescence images based on Pearson's correlation coefficient (Rr). N≥8. Shown is mean ± SEM; *P<0.05.

EEA1 was also significantly more observed compared with CMTM3/Clathrin. For CMTM3/Clathrin, the correlation value was significantly higher compared with CMTM3/Rab4 and CMTM3/Rab5. Colocalization of endogenous CMTM3 with EEA1 was also detected (Supplemental Figure 4).

Quantification of the immunofluorescence signals of Clathrin, EEA1, Rab11, Rab7, Rab5 and Rab4 indicated that Clathrin+, EEA1+, Rab11+, Rab5+ and Rab7+ vesicles were significantly increased in adCMTM3 versus adsham treated HUVECs (Figure 6A-F). Combined, these data indicate that CMTM3 is localized in early endosomes and could be involved in regulating VE-cadherin transport in cytosolic vesicles during endocytosis. Functional involvement of these endocytosis-related proteins in angiogenesis was shown in the 3D collagen matrix vascular co-culture system: Knockdown of Clathrin and Rab5 in GFP-HUVECs mimicked the CMTM3 phenotype, significantly diminishing the numbers of junctions and tubules and decreasing total tubule length (Supplemental Figures 5 and 6 for Clathrin and Rab5, respectively).

CMTM3 mediates VE-cadherin endocytosis and barrier function of endothelial adherens junctions.

To elucidate the role of CMTM3 in the internalization of VE-cadherin, we conducted an internalization assay in which adsham and adCMTM3 transfected confluent HUVEC monolayers were compared. Quantification of the total VE-cadherin+ areas per cell (before acid wash procedure that removes extracellular VE-cadherin signal, see material and methods for details) demonstrates that CMTM3 overexpression did not alter the signal (data not shown). In contrast, assessment of VE-cadherin and cell cytoskeleton actin represented in Pearson's correlation coefficient values shows a significant reduction in VE-cadherin/actin

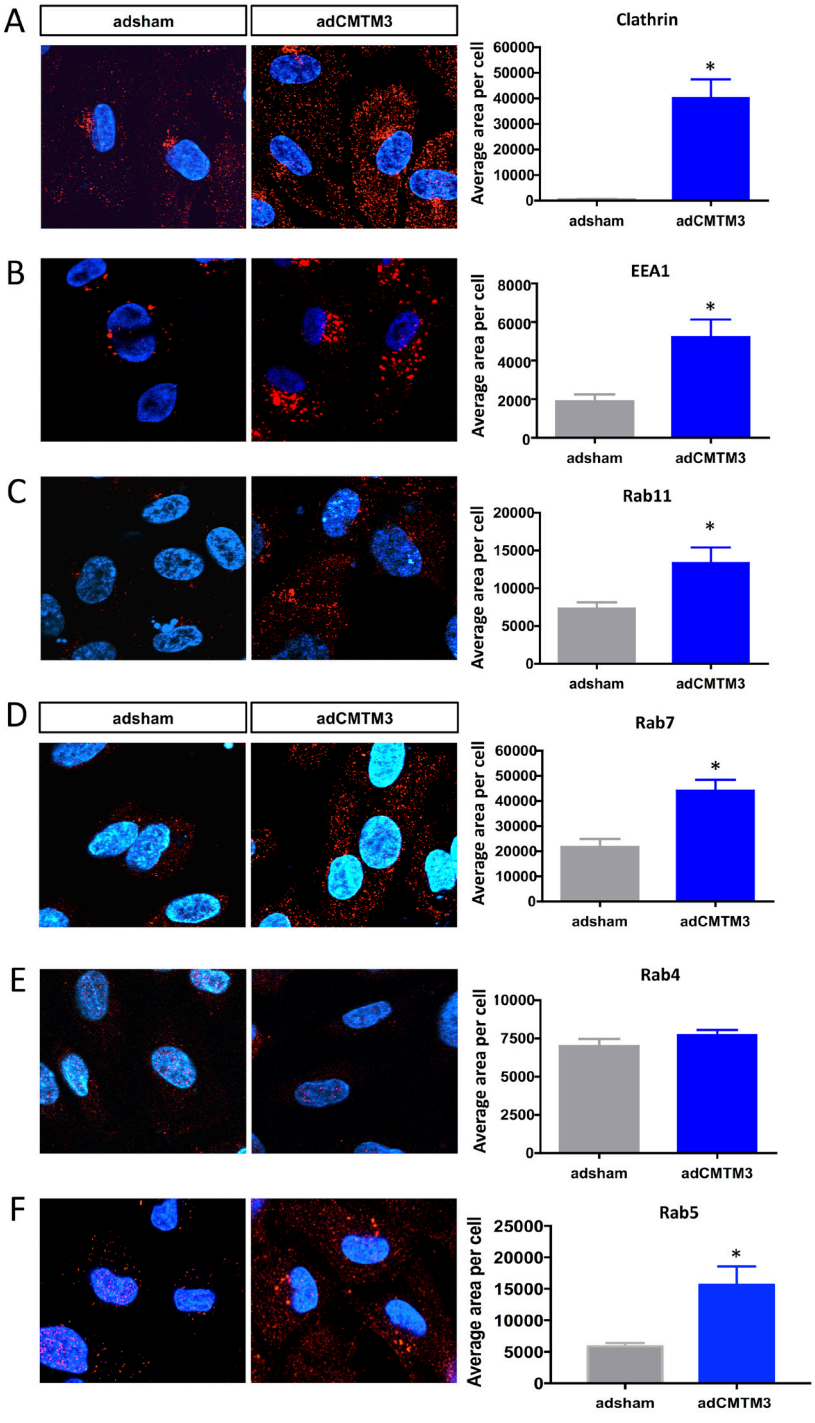
A
adsham
adCMTM3
Clathrin
Average area per cell
60000
50000
40000
30000
20000
10000
0
*
adsham
adCMTM3
B
EEA1
8000
6000
4000
2000
C
Rab11
20000
15000
10000
5000
D
Rab7
E
Rab4
7500
2500
F
Rab5
25000

◀ **Figure 6. CMTM3 overexpression significantly upregulates the endocytic pathway.** (A) Representative immunofluorescence images of HUVECs transfected with adenovirus containing an expression vector for CMTM3 cDNA (adCMTM3) or with sham virus containing an empty expression vector (adsham), immunostained for Clathrin (red). Quantification of Clathrin+ area per cell in adsham and adCMTM3 transfected HUVECs. (B) Representative immunofluorescence images of HUVECs transfected with adsham or adCMTM3 and immunostained for EEA1 (red). Quantification of EEA1+ area per cell in adsham and adCMTM3 transfected HUVECs. (C) Representative immunofluorescence images of HUVECs transfected with adsham or adCMTM3, immunostained for Rab11 (red). Quantification of Rab11+ area per cell in adsham and adCMTM3 transfected HUVECs. (D) Representative immunofluorescence images of HUVECs transfected with adsham or adCMTM3, immunostained for Rab7 (red). Quantification of Rab7+ area per cell in adsham and adCMTM3 transfected HUVECs. (E) Representative immunofluorescence images of HUVECs transfected with adsham or adCMTM3, immunostained for Rab4 (red). Quantification of Rab4+ area per cell in adsham and adCMTM3 transfected HUVECs. (F) Representative immunofluorescence images of HUVECs transfected with adsham or adCMTM3, immunostained for Rab5 (red). Quantification of Rab5+ area per cell in adsham and adCMTM3 transfected HUVECs. N≥8. Shown is mean ± SEM for all data; *P<0.05 vs. adsham.

co-localization in adCMTM3 versus adsham groups (Figure 7A, B), indicating that VE-cadherin connections with the actin cytoskeleton, which are necessary for AJ formation and stabilization, are affected. Furthermore, quantification after acid wash treatment demonstrates that internalization of VE-cadherin is significantly increased in adCMTM3 versus adsham treated HUVECs under both basic conditions and VEGFA stimulation (Figure 7C-E). Visa versa, siRNA mediated knockdown of *CMTM3* (siCMTM3) significantly decreases VE-cadherin internalization compared with sisham treated HUVECs in response to VEGFA

▶ **Figure 7. CMTM3 promotes internalization of cell-surface VE-cadherin.** (A) Representative low and high magnification immunofluorescence images of confluent grown HUVECs transfected with adenovirus containing an expression vector for CMTM3 cDNA (adCMTM3) or with sham virus containing an empty expression vector (adsham), immunostained for actin (red) and VE-cadherin (green). Co-localization in overlay image is in yellow. (B) Quantificantion of co-localization of VE-cadherin and actin in immunofluorescence images based on Pearson's correlation coefficient (Rr). N≥9. Shown is mean ± SEM; *P<0.05. (C) Representative immunofluorescence images of confluent grown HUVECs transfected with adsham or adCMTM3, labelled with VE-cadherin antibodies at 4°C, followed by 37°C incubation for 30 minutes with and without exogenous VEGFA stimulation to track VE-cadherin movement, followed by a low pH wash to remove surface bound antibodies, before proceeding with immunostaining to visualize internalized VE-cadherin (green). (D) Quantification of internalized VE-cadherin+ area per cell in adsham and adCMTM3 HUVECs without VEGFA, and (E) with VEGFA stimulation. N≥8. Shown is mean ± SEM; *P<0.05 vs. adsham, $P<0.1 vs. adsham. (F) Representative immunofluorescence images of confluent grown HUVECs treated with *CMTM3*-targeting siRNA (siCMTM3) or of cells treated with non-targeting siRNA (sisham), showing internalized VE-cadherin (green) following a protocol similar to C. (G) Quantification of internalized VE-cadherin+ area per cell in sisham and siCMTM3 treated HUVECs without VEGFA and (H) with VEGFA stimulation. N≥8. Shown is mean ± SEM; *P<0.05 vs. adsham.

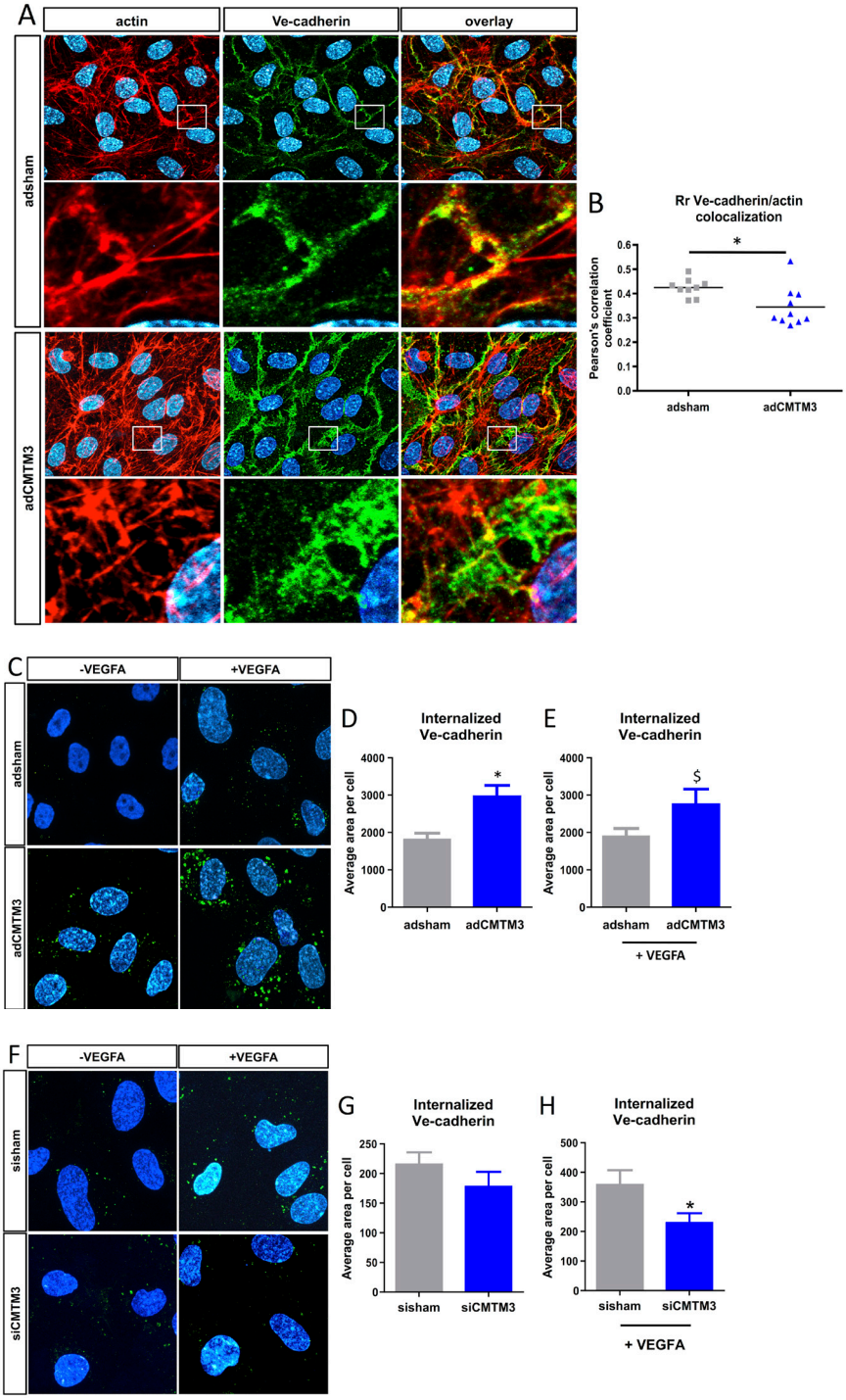
A
actin
Ve-cadherin
overlay
adsham
adCMTM3
B
Rr Ve-cadherin/actin colocalization
Pearson's correlation coefficient
0.6
0.5
0.4
0.3
0.2
0.1
0.0
*
adsham
adCMTM3
C
-VEGFA
+VEGFA
adsham
adCMTM3
D
Internalized Ve-cadherin
Average area per cell
4000
3000
2000
1000
0
*
adsham
adCMTM3
E
Internalized Ve-cadherin
Average area per cell
4000
3000
2000
1000
0
$
adsham
adCMTM3
+ VEGFA
F
-VEGFA
+VEGFA
sisham
siCMTM3
G
Internalized Ve-cadherin
Average area per cell
250
200
150
100
50
0
sisham
siCMTM3
H
Internalized Ve-cadherin
Average area per cell
500
400
300
200
100
0
*
sisham
siCMTM3
+ VEGFA

stimulation (Figure 7F-H). SiRNA or adenoviral transfection did not significantly affect VE-cadherin uptake, as shown by comparison between adsham/sisham versus non-transfected controls (Supplemental Figure 7). Thus, these data confirm that CMTM3 is indeed involved in VE-cadherin internalization. To investigate whether VE-cadherin uptake was mediated by direct binding to CMTM3, co-immunoprecipitation experiments were conducted using magnetic beads coated with an antibody against VE-cadherin to isolate VE-cadherin-complexes in protein lysate of adCMTM3 transfected HUVECs. VE-cadherin protein pull down was successful, but no CMTM3 was detected in the co-immunoprecipitate, implying that direct binding between CMTM3 and VE-cadherin does not take place in HUVECs (Supplemental Figure 8).

Shifts in VE-cadherin endocytosis directly alter cell-surface bio-availability of VE-cadherin to form intercellular homophilic bonds at AJs and may therefore impact endothelial barrier function. To evaluate the effect of CMTM3 on the barrier function, we conducted transendothelial electric resistance (TEER) measurements on HUVEC monolayers exposed to thrombin induced endothelial junction disruption. Basal levels of electrical resistance did not differ between siCMTM3 and sisham groups. However, the thrombin-induced response in CMTM3 knockdown was significantly decreased compared with sisham controls (Figure 8A): The decrease in resistance during the initial phase (0-30 minutes, exposure to thrombin) was less for siCMTM3 ($P<0.1$; Figure 8B), whereas the increase in resistance during the recovery phase (30-120 minutes, after removal of thrombin at 30 minutes) was not significantly different between the 2 groups (Figure 8C). In contrast, whereas basal levels were similarly not affected, CMTM3 overexpression significantly increased the thrombin-induced response (Figure 8D): The decrease in resistance during the initial phase was significantly higher for adCMTM3 compared with adsham controls (Figure 8E). Similarly, the increase in resistance during the restoration phase was more pronounced in the adCMTM3 group (Figure 8F).

Discussion

We have previously found that CMTM3 expression is enriched in endothelial progenitor cells during murine embryonic development. In this study, we assessed the endothelial function of this putative angiogenic regulator. The most important findings of our current study are as follows: (1) CMTM3 in ECs is crucial for new vessel formation, as shown in an *in vitro* 3D collagen based co-culture assay

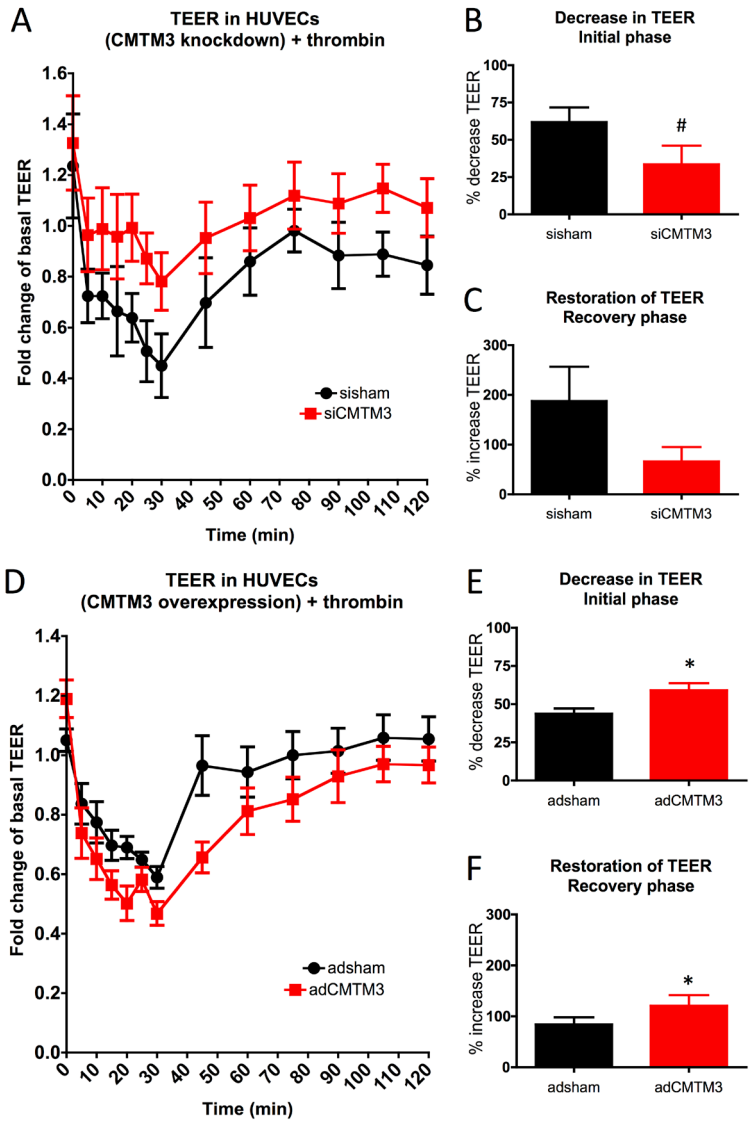

Figure 8. CMTM3 promotes loss of endothelial electric resistance in thrombin-induced response. (A) Thrombin response (presented in fold change compared with basal resistance of the non-transfected group: Y-axes) of confluent HUVEC monolayers treated with *CMTM3*-targeting siRNA (siCMTM3) or treated with non-targeting siRNA (sisham), during (0-30 minutes) and after (30-120 minutes) thrombin (1 U/ml) stimulation. At 0 minutes, thrombin was added and at 30 minutes thrombin was removed. N≥8 per time series. Shown is mean ± SEM. (B) Decrease in resistance during initial phase (0-30 minutes) in sisham and siCMTM3 treated groups. (C) Increase in resistance during recovery phase (30-120 minutes) in sisham and siCMTM3 treated groups. N≥8. Shown is mean ± SEM for B and C; $^{\#}P<0.1$ vs. sisham. (D) Thrombin response (presented in fold change compared with basal resistance of the non-transfected

(Figure 8 continued) group: Y-axes) of confluent HUVEC monolayers transfected with adenovirus containing an expression vector for CMTM3 cDNA (adCMTM3) or with sham virus containing an empty expression vector (adsham), during (0-30 minutes) and after (30-120 minutes) thrombin (1 U/ml) stimulation. At 0 minutes, thrombin was added and at 30 minutes thrombin was removed. N≥8 per time series. Shown is mean ± SEM. (E) Decrease in resistance during initial phase (0-30 minutes) in adsham and adCMTM3 groups. (F) Increase in resistance during recovery phase (30-120 minutes) in adsham and adCMTM3 groups. N≥8. Shown is mean ± SEM in E and F; *P<0.05 vs. adsham.

with human ECs and pericytes by siRNA mediated CMTM3 silencing. (2) CMTM3 inhibition *in vivo* by morpholino injection in developing zebrafish larvae confirms that CMTM3 expression is required for (intersomitic) vascular growth. (3) CMTM3 knockdown does not affect EC proliferation or migration. (4) However CMTM3 is localized in early endosome markers (EEA1 and Clathrin) positive intracellular vesicles. (5) Furthermore, CMTM3 co-localizes with internalized VE-cadherin. (6) CMTM3 overexpression enhances the endothelial endocytic pathway. (7) CMTM3 overexpression enhances whereas CMTM3 knockdown decreases VE-cadherin internalization. (8) Knockdown of CMTM3 increases junctional resistance during exposure to thrombin. This effect is reversed in CMTM3 overexpression conditions.

CMTM3 regulation of VE-cadherin turnover in angiogenesis

Previously, CMTM-family members have been shown to regulate tumor cell growth and migration in different types of cancers[9,12,13]. For CMTM3, it has been reported that the protein was highly expressed in testis, leukocytes and spleen[11]. In cancer cells, CMTM3 was silenced by CpG methylation in carcinomas and restoration of CMTM3 expression inhibited tumor cell growth and promoted apoptosis[17]. CMTM3 silencing or downregulation was also reported for testicular and gastric cancer cells. Similarly, restoration of CMTM3 expression inhibited cancer cell growth by inducing cell cycle arrest and reducing cancer cell migration[15,20]. However, the function of CMTM3 in normal cell types, in particular vascular cells, remained yet to be defined.

In this study, we demonstrated that CMTM3 plays an important role in angiogenesis *in vivo* and *in vitro*. In contrast to the main CMTM3 function in various cancer cell types, our data showed that CMTM3 does not influence cell cycle progression and proliferation in ECs. Furthermore, CMTM3 does not affect EC migration. Rather, our data demonstrated that the angiogenic capacity of CMTM3 is associated with the regulation of cell surface VE-cadherin bio-availability mediated by mechanisms of endocytosis.

Endocytosis-mediated internalization of VE-cadherin removes the protein

from AJ sites and reduces formation of intercellular complexes. This decrease in cell-cell connections is vital for the initial phases of angiogenic sprouting, as destabilization of intercellular contacts promotes EC migration and tip and stalk cell differentiation, followed by vascular expansion from the pre-existing origin vessel. For example, knockdown of VE-cadherin in zebrafish embryos has been shown to increase intersomitic vessel sprouting[21]. Previous studies have also shown that AJ turnover involves endocytic trafficking pathways that essentially control the rate of VE-cadherin turnover: VE-cadherin internalization in response to e.g. VEGFA stimulation, is mediated by VE-cadherin targeting for Clathrin-mediated endocytosis by binding of (β-arrestin) adaptor protein-mediated complexes, which further recruits endocytic machinery protein clusters into Clathrin-coated pits situated in the membrane[4]. This is followed by dynamin-mediated scission of the plasma membrane, followed by inward membrane budding to form Clathrin-coated vesicles[22]. After internalization, these vesicles fuse into early endosomes where VE-cadherins are either sorted into late endosomes and subsequently degraded in lysosomes[23], or are transported back to the cell surface pool directly, or via further processing by recycling endosomes[16,22].

Here we demonstrated that CMTM3 can promote the endocytosis pathway: Clathrin+ subcellular vesicles and early endosomes marked by EEA1 were increased in CMTM3 expressing ECs compared with adsham controls. Furthermore, CMTM3 expression increased recycling endosomes marked by Rab11 and late endosomes marked by Rab7. We also showed that CMTM3 expression promotes internalization of VE-cadherin at basal level and in response to VEGFA stimulation, whereas CMTM3 knockdown inhibited VE-cadherin internalization in response to VEGFA. Furthermore, CMTM3 reduced junctional resistance in endothelial monolayers, indicating that CMTM3 regulates endothelial barrier function and vascular integrity.

In relation to endocytic mechanisms and subcellular vesicles trafficking, Eswaran *et al* reported that the CMTM-family genes were homologous to myelin and lymphocyte (MAL) proteins tricellulins, plasmolipins and occluding families, which contain the tetra-spanin trans-membrane domain (MAL and related protein for vesicle trafficking and membrane linking (MARVEL)). These proteins have been functionally linked to cell communication and intracellular transport[24]. They also demonstrated that CMTM7 interacts with B-cell linker (BLNK) in a membrane protein complex in B-cell precursor acute lymphoblastic leukemia cell lines[24]. Overexpression of CMTM8 in tumor cell lines enhanced the endocytosis rate of

epidermal growth factor receptor (EGFR)[25]. Further studies are required to assess whether the other family members, like CMTM3, are involved in endocytosis regulation.

On the basis of our findings and previous reports, we interpret from our data that CMTM3 is involved in turnover of the cell surface VE-cadherin pool. In an angiogenic environment, formation of vascular sprouts from pre-existing vessels is mediated by VEGFA. Endocytosis of VE-cadherin after VEGFA stimulation is one of the main mechanisms by which VEGFA promotes vascular sprouting[4]. As indicated by our findings, CMTM3 seems to be an important regulator in this process as it significantly enhances VEGFA-mediated VE-cadherin internalization, thereby reducing junctional adhesion strength between the cells. The exact mechanism by which CMTM3 facilitates VE-cadherin internalization remains to be further investigated. Given that our findings also demonstrated that CMTM3 is co-localized with Clathrin, CMTM3 could function as an adaptor protein that is involved in VE-cadherin targeting and positioning in the protein complex of Clathrin-mediated endocytosis. Similarly, CMTM3 could be involved in regulating the fusion of Clathrin coated vesicles into EEA1+ endosomes, as CMTM3 also co-localized with EEA1 in our studies. Currently, we are conducting further studies to elucidate the contribution of CMTM3 in subcellular trafficking of VE-cadherin.

In conclusion, this study identified a regulatory function for CMTM3 in angiogenesis. CMTM3 is involved in VE-cadherin turnover and is a regulator of the cell surface pool of VE-cadherin. Therefore, CMTM3 mediates cell-cell adhesion at AJs and contributes to the control of vascular sprouting. Further studies that elucidate the exact mechanisms by which CMTM3 regulates endocytic transport of plasma membrane proteins in ECs could lead to the identification of new drug targets and contribute to new therapies to block vascular growth in tumor, or enhance angiogenesis in tissue regeneration.

Acknowledgements

We thank the Cell Microscopy Core, Departement of Cell Biology, Center for Molecular Medicine, UMC Utrecht, for excellent technical support. We also thank dr.Klazina Kooiman of the department of Biomedical Engineering for kind permission to use the TEER apparatus. For technical support we would like to thank Esther van de Kamp, Lau Blonden, Pinar Sarikaya, Matthijs Snelders and Stephan David.

The work was supported by Netherlands Foundation for Cardiovascular Excellence [to C.C], NWO VIDI grant [no. 91714302 to C.C.], the ErasmusMC fellowship grant [to C.C.], the RM fellowship grant of the UMC Utrecht [to C.C.] and the Netherlands Cardiovascular Research Initiative: An initiative with support of the Dutch Heart Foundation [CVON2014-11 RECONNECT to C.C. and D.D].

Materials and methods

Cell culture

All cells were cultured at 37^{0}C in a 5% CO_2 humid atmosphere. HUVECs were obtained from Lonza and maintained in EGM2 medium (Lonza) with 100 Uml^{-1} penicillin-streptomycin (PS). Human brain vascular pericytes were obtained from ScienCell and maintained in DMEM supplemented with 10% FCS and 100 Uml^{-1} PS. Human aortic vascular smooth muscle cells (VSMC) were obtained from Lonza and maintained in $SMGM_2$ supplemented with 100 Uml^{-1} PS. All cells were used between passages 3 and 6. Co-culture experiments were performed in basal EBM medium supplemented with 2% FCS, rhFGF-B, ascorbic acid, and 100 Uml^{-1} PS. HUVEC and pericytes were transfected with lentivirus GFP and RFP expression constructs respectively, obtained from Sanbio. For this, cells (passage 1) were plated on gelatine coated culture plates, and transfection was performed when cells reached 60% confluence. Lentivirus was added to the cells at MOI 5 in the presence of 6 µg/ml polybrene in basal medium with 0.2% FCS. After 6 hours of transduction, the cells were incubated for 72 hours in fresh growth medium. Puromycin (2.5 µg/ml) was added to the cells as a selection marker. After 7 days of selection, GFP-positive HUVECs and RFP-positive pericytes were harvested and propagated for storage by cryopreservation.

Trans-membrane co-culture

HUVEC were seeded on top of a 0.4 µM polycarbonate membrane (Transwell$_{®}$ Costar) and mural cells on the downside of the membrane. After 24 hours incubation in serum low condition (EBM+0.2% FCS+PS) cells were separately harvested using a cell-scraper and processed for mRNA isolation.

QPCR analysis

Total RNA was extracted from treated cells using RNAeasy kit (Qiagen) and was checked for quality and quantity by spectrophotometer (Nanodrop; ND-1000) and/or capillary electrophoresis (Agilent 2100 Bioanalyser). Reverse transcription was conducted with iScript synthesis kit (Brad) according to manufacturer instructions. Quantitative real-time PCR was performed using SYBR-Green-Cycler IQ5 detection system (Biorad). All results

were normalised for the expression of the house keeping gene *ß-actin*. The primers of target genes are summarized in Supplemental Table 1.

Short interference RNA

Silencing *CMTM3* in HUVEC and HUVEC-GFP was conducted by using a mixture of 4 complementary siRNA sequences directed against the mRNA of *CMTM3* (Thermo Fisher): 5'-GCCCUCAUCUACUUUGCUA-3'; 5'-GCAACUGAUUUCUACCUGA-3'; 5'-CAAGACAGAAGAAGAGAGAAU-3'; 5'-UUAACGACGUGGCCAAAUU-3' (siCMTM3). A second sequence of siRNA was also tested for CMTM3: siGENOME 1: 5'-UUAACGACGUGGCCAAAUU-3'; siGENOME 2: 5'-CCACAGCCCACAAGA CAGA-3'. As a negative control a pool of 4 non-targeting siRNA sequences were used (siSham). Cells were grown to 60% confluence and transfected with 80 nM siRNA using lipofectamine (Dharmafect, Thermo Scientic) according to manufacturer's instructions. The siRNA silencing was validated 48-72 hours post transfection using qPCR and Western blotting. Optimal *CMTM3* silencing was obtained 72 hours post transfection.

Subcellular fractioning and protein extraction

Cells were harvested 72 hours post siRNA transfection. To distinguish cytoplasmic proteins (soluble fraction) from the membrane proteins (insoluble fraction), cells were washed twice with PBS and harvested in lysisbuffer (140 mM NaCl, 10 mM Tris pH 7.6, 1 mM EDTA, 1% Triton X-100 [TX-100], 0.05% sodium dodecyl sulfate, 1x protease inhibitor cocktail, 1 mM PMSF). The lysates were incubated for 20 minutes on ice and centrifuged at 13000g for 12 minutes to separate the soluble fraction from the insoluble fraction. The insoluble fraction was then solubilised in lysis buffer with 2% SDS. Both fractions were loaded onto SDS-PAGE followed by Western blot analysis.

Western blot

Before protein samples were loaded on sodium dodecyl sulfatepolyacrylamide gel electrophoresis (SDS-PAGE), the protein concentration was determined using Pierce BCA Protein Assay according manufacturer's protocol. Samples were denatured for 10 minutes at 95°C, followed by separation with a 10% or a 4-15% gradient SDS-PAGE gel (Biorad). Subsequently, proteins were transferred to a nitrocellulose membrane (Pierce) and incubated for 1 hour in Odyssey (Li-Cor) blocking buffer (diluted 1:1 in PBS). The membranes were incubated overnight with anti-CMTM3, ß actin, and anti-VE-cadherin (Santa Cruz) in concentrations recommended by the manufacturer. Protein bands were visualized with the Li-Cor detection system (Westburg). See Supplemental Table 2 for

antibody list.

Collagen based 3D co-culture

The microvessel networks were established by seeding HUVEC-GFP and pericyte-RFP at a density of $6X10^4$ HUVEC-GFP and $1.2X10^4$ pericytes-RFP in 50 µl of 2.0 mg/ml type 1 collagen (BD Bioscience). Stem cell factor, stromal-derived factor-1α, and interleukin-3 (BD-Bioscience) were each added at 800 ng/ml in the collagen matrix to promote angiogenesis, followed by collagen cross-linking for 1 hour at 37°C and 5% CO_2 after supplementing the gel with 100 µl EBM_2+2%FCS+ascorbic acid + fibroblast growth factor-2 (obtained from the EGM_2 bulletkit) in a 96-wells plate setup. Co-cultures were recorded by fluorescence microscopy at day 2 and day 5. Total tubule length, mean tubule length and the number of vascular junctions and tubules were quantified using the Angiosys software program.

VE-cadherin internalization assay and immunofluorescence

The internalization assay was performed as described previously by Gavard *et al*[26]. Briefly, HUVECs were grown on coverslips to confluence before incubation in EGM with anti-human VE-cadherin antibody (5 µg/ml) at 4°C for 1 hour to label cell-surface exposed VE-cadherin. Subsequently, cells were placed at 37°C for 30 minutes to track VE-cadherin movement, in either basal medium (control) or basal medium supplemented with VEGFA (50 ng/ml; cat#100-20, Peprotech). Cells were either washed with PBS (PBS supplemented with 1.8 mM $CaCl^2$ and 1 mM $MgCl^2$) and fixed with 4% paraformaldehyde at room temperature for 30 minutes, or exposed to an additional mild acid wash (2mM PBS-glycine [pH 2.0], 15 minutes) prior to washing and fixation to remove membrane bound antibodies. This treatment reveals internalized anti-VE-cadherin antibodies. Blocking and permeabilization was conducted for 30 minutes at room temperature in PBS with 1% BSA and 0.5% Triton-X. Secondary antibody incubation was performed for 2 hours at room temperature, followed by an incubation step with phalloidin-rhodamine for 30 minutes at room temperature to label cytoskeletal F-actin. DAPI was used as a nuclear counterstain. Images of fluorescent-labelled markers were acquired by a ZEISS LSM700 microscope and a 63 oil immersion objective lens. Images were acquired by using the manufacturer's standard software. 3D images were obtained by scanning several XY planes in the Z direction with enough depth to scan the entire cell (±10 µm). Serial pictures along the Z-axis were combined, creating a stacked XY image. The total area of VE-cadherin from multiple stacked images was determined by using imageJ 1.47v. See Supplemental Table 2 for antibody list.

Flow cytometry

CMTM3 silenced HUVEC were seeded at a density of $0.5X10^5$ cells/well in a 6 wells plate in co-culture medium. After 24, 48,and 72 hours cells were harvested for proliferation and apoptosis assay. The single cell suspension for each condition were stained for Propidium Iodide and Annexin V (BD Pharmingen) according to manufacturer's protocol and analyzed by flowcytometry (BD Facs Canto). Cells were counted for 2 minutes at medium speed to determine the average cell amount. Cell cycle analysis was performed after 48 hours incubation at 37°C in 5% CO2 and fixed overnight in 70% ethanol at 4°C. After washing the cells with ice-cold PBS, cells were stained with PI and treated with 0.5mg/ml RNase for 30 min at 37°C and analyzed by flowcytometry.

Migration assay

CMTM3 was silenced in HUVEC and after 24 hours seeded at a density of $5X10^4$ cells/well in a 96 wells plate with cell seeding stoppers of Oris™ Universal Cell Migration (Platypus Technologies). Cells were allowed to adhere for 24 hours and after that the seeding stoppers were removed to reveal a cell-free detection zone into which cells migrate in serum low condition EBM with 2% FCS for 16 hours. The cells were washed and stained with Calcein-AM (BD-Bioscience) according manufacturer's instructions and imaged by fluorescence microscopy. Quantification of the images was assessed by Clemex vision software to measure the percentage of the mean surface area of the migrated cells.

Intracellular immunostaining

24 hours post transfection with siRNA, HUVEC were seeded in a 48 wells plate $1X10^5$ cells/well. Cells adhere for 24 hours after which they were fixed in 4% paraformaldehyde (PFA) for 10 min, followed by 15 min permeabilization in 0.1% Triton-X100. This was followed by overnight 4°C incubation with primary antibody, secondary antibody Alexa Fluor 488 or Alexa Fluor 594, and vectashield with dapi, all according to manufacturer's protocol (see supplemental table 2). In some experiments, cells were also co-stained with phalloidin-rhodamin or a second primary antibody. Samples were imaged by fluorescence or confocal microscopy. For quantification of area and assessment of co-localization, the signal of multiple stacked images was analyzed using imageJ 1.47v. See Supplemental Table 2 for antibody list.

CMTM3 adenovirus

Recombinant adenoviruses were produced using Gateway pAd/CMV/V5-DEST vector and ViraPower™ Adenoviral Expression System, according manufacturer's instructions

(Invitrogen). Fully sequenced Human CMTM3 cDNA clone was obtained from Lifesciences, which contains the coding sequence (cds) of CMTM3 in a pCMV-SPORT6. Full-length cDNAs of CMTM3 with attB-site was amplified by PCR using specific forward oligos: 5`-GGGGACAAGTTTGTACAAAAAAGCAGGCTTCACCATGTGGCCCCCAGACCCCGACC-3` and reverse oligo`s 5`-GGGGACCACTTTGTACAAGAAAGCTGGGTTTCAGTCAGAGTCCGAGTCGGA ATTCTC-3`. Moreover a HIS tag was placed at the C-terminal region of CMTM3 (CMTM3-HA) using the RV primer 5`-GGGGACCACTTTGTACAAGAAAGCT-GGGTGGTCAGAGTCCGAGTCGGAATTCTC-3`. Amplicons of CMTM3 and CMTM3-HA were cloned into a pDONR™ 221 vector via BP Clonase™ II enzyme mix to create an entry clone. The fidelity of CMTM3 and CMTM3-HA was confirmed by DNA sequencing. Subsequently, the CMTM3 expression cassette was cloned from the entry vectors into pAd/CMV/V5-DEST (Invitrogen) expression vectors (pAd CMV) using LR-reaction II (invitrogen). After verification by DNA sequencing, the pAd/CMV plasmids were linearized by Pac1 restriction and subsequently transfected with Lipofectamine 2000 (Invitrogen) in 293A cells. Infected cells were harvested until 80% of the cells detached from plates followed by three cycles of freeze/thawing to get crude viral lysate (CVL).

Immunoprecipitation

Immunoprecipitation on adCMTM3 transfected Huvecs was performed starting with lysis of the cells using RIPA lysis buffer freshly supplemented with 1mM PMSF, β-glycerolphosphate and 1x Complete EDTA-free Protease Inhibitor Cocktail (Roche). After lysis, lysates were centrifuged at 4°C for 13 minutes at 13.000 g and pre-cleared at 4°C for 1 hour with Dynabeads™ protein G (Thermo Scientific). Subsequently the protein concentration of the pre-cleared samples was determined using the BCA-protein assay kit (Thermo Fisher) according manufactures protocol. 50 µg of lysate was used for immunoprecipitation on 1,5 mg of Dynabeads™-coated with a target specific antibody or isotype control antibody according to manufactures protocol. After 48 hours incubation at 4°C with rotation the Dynabeads™-Ab-antigen complex was washed for 5x times and eluted using a non-denaturing elution step. After denaturing the eluated proteins for 10 minutes at 70°C, (lysates) were loaded on a SDS-PAGE gel and transferred using Western-blot analysis.

Transendothelial resistance measurements

HUVEC were transfected with adenovirus or siRNA 24 hours before seeding on a pre-coated (0,1% gelatin) semi-permeable filter insert (0.4um pore size, Falcon). Before seeding, the blank resistance (R_{blank}) of each insert was measured in an Endohm-SNAP chamber (World Precision Instruments, Berlin) filled with 5 ml of EGM-2, which was coupled to an

EVOMX resistance meter (World Precision Instruments). The Transendothelial resistance (TEER) was measured daily for a total of 3 days post transfection. At day 2 the monolayers were treated with 1 U/ml thrombin for 30 minutes and the TEER was recorded every 5 min. After thrombin-induced decrease in TEER the cells were washed with fresh medium and the TEER was recorded every 15 min for 2 hr. The electrical resistance was calculated by Ohm`s law and expressed in $\Omega*cm^2$, (resistance of experimental insert minus resistance of corresponding blank insert) times 4.2 (area of the insert membrane in cm^2).

References

1. Eelen G, de Zeeuw P, Simons M, et al. Endothelial cell metabolism in normal and diseased vasculature. Circ Res. 2015;116(7):1231-1244.
2. Vestweber D. VE-cadherin: the major endothelial adhesion molecule controlling cellular junctions and blood vessel formation. Arterioscler Thromb Vasc Biol. 2008;28(2):223-232.
3. Wallez Y, Huber P. Endothelial adherens and tight junctions in vascular homeostasis, inflammation and angiogenesis. Biochim Biophys Acta. 2008;1778(3):794-809.
4. Gavard J, Gutkind JS. VEGF controls endothelial-cell permeability by promoting the beta-arrestin-dependent endocytosis of VE-cadherin. Nat Cell Biol. 2006;8(11):1223-1234.
5. Lampugnani MG, Orsenigo F, Gagliani MC, et al. Vascular endothelial cadherin controls VEGFR-2 internalization and signaling from intracellular compartments. J Cell Biol. 2006;174(4):593-604.
6. Gory-Faure S, Prandini MH, Pointu H, et al. Role of vascular endothelial-cadherin in vascular morphogenesis. Development. 1999;126(10):2093-2102.
7. Cattelino A, Liebner S, Gallini R, et al. The conditional inactivation of the beta-catenin gene in endothelial cells causes a defective vascular pattern and increased vascular fragility. J Cell Biol. 2003;162(6):1111-1122.
8. Stenmark H. Rab GTPases as coordinators of vesicle traffic. Nat Rev Mol Cell Biol. 2009;10(8):513-525.
9. Xiao K, Garner J, Buckley KM, et al. p120-Catenin regulates clathrin-dependent endocytosis of VE-cadherin. Mol Biol Cell. 2005;16(11):5141-5151.
10. Chiasson CM, Wittich KB, Vincent PA, et al. p120-catenin inhibits VE-cadherin internalization through a Rho-independent mechanism. Mol Biol Cell. 2009;20(7):1970-1980.
11. Zhong J, Wang Y, Qiu X, et al. Characterization and expression profile of CMTM3/CKLFSF3. J Biochem Mol Biol. 2006;39(5):537-545.
12. Gardner H, Kreidberg J, Koteliansky V, et al. Deletion of integrin alpha 1 by homologous recombination permits normal murine development but gives rise to a specific deficit in cell adhesion. Dev Biol. 1996;175(2):301-313.
13. Li H, Li J, Su Y, et al. A novel 3p22.3 gene CMTM7 represses oncogenic EGFR signaling and inhibits cancer cell growth. Oncogene. 2014;33(24):3109-3118.
14. Han W, Ding P, Xu M, et al. Identification of eight genes encoding chemokine-like factor superfamily members 1-8 (CKLFSF1-8) by in silico cloning and experimental validation. Genomics. 2003;81(6):609-617.
15. Stephens LE, Sutherland AE, Klimanskaya IV, et al. Deletion of beta 1 integrins in mice results in inner cell mass failure and peri-implantation lethality. Genes Dev. 1995;9(15):1883-1895.
16. Yan Z, Wang ZG, Segev N, et al. Rab11a Mediates Vascular Endothelial-Cadherin Recycling and Controls Endothelial Barrier Function. Arterioscler Thromb Vasc Biol. 2016;36(2):339-349.
17. Wang Y, Li J, Cui Y, et al. CMTM3, located at the critical tumor suppressor locus 16q22.1, is silenced by CpG methylation in carcinomas and inhibits tumor cell growth through inducing apoptosis. Cancer Res. 2009;69(12):5194-5201.
18. Lei Z, van Mil A, Brandt MM, et al. MicroRNA-132/212 family enhances arteriogenesis after hindlimb ischaemia through modulation of the Ras-MAPK pathway. J Cell Mol Med. 2015;19(8):1994-2005.
19. Stratman AN, Malotte KM, Mahan RD, et al. Pericyte recruitment during vasculogenic tube assembly stimulates endothelial basement membrane matrix formation. Blood. 2009;114(24):5091-5101.
20. Su Y, Lin Y, Zhang L, et al. CMTM3 inhibits cell migration and invasion and correlates with favorable prognosis in gastric cancer. Cancer Sci. 2014;105(1):26-34.
21. Abraham S, Yeo M, Montero-Balaguer M, et al. VE-Cadherin-mediated cell-cell interaction suppresses sprouting via signaling to MLC2 phosphorylation. Curr Biol. 2009;19(8):668-674.

22. Mellman I, Yarden Y. Endocytosis and cancer. Cold Spring Harb Perspect Biol. 2013;5(12):a016949.
23. Xiao K, Allison DF, Kottke MD, et al. Mechanisms of VE-cadherin processing and degradation in microvascular endothelial cells. J Biol Chem. 2003;278(21):19199-19208.
24. Eswaran J, Sinclair P, Nakjang S, et al. Identification of Cmtm Family Proteins As Tumor Suppressor and Membrane Regulator in B Cell Precursor Acute Lymphoblastic Leukemia. Blood. 2014;124(21):3582.
25. Jin C, Ding P, Wang Y, et al. Regulation of EGF receptor signaling by the MARVEL domain-containing protein CKLFSF8. FEBS Lett. 2005;579(28):6375-6382.
26. Gavard J, Patel V, Gutkind JS. Angiopoietin-1 prevents VEGF-induced endothelial permeability by sequestering Src through mDia. Dev Cell. 2008;14(1):25-36.

Supplemental Figures

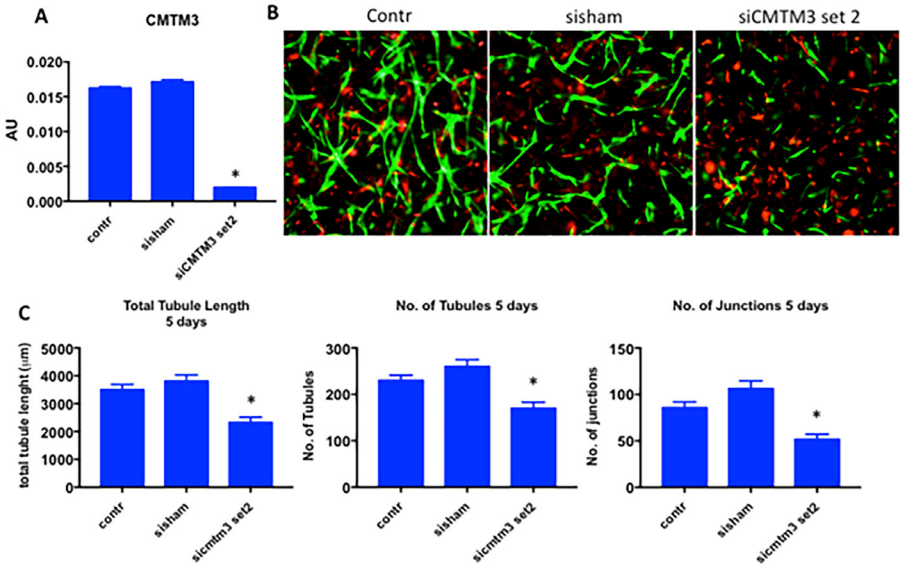

Supplemental Figure 1. CMTM3 silencing using a second siRNA sequence in endothelial cells impairs vascular growth in a 3D collagen matrix vascular co-culture system *in vitro*. (A) Quantitative polymerase chain reaction (qPCR) analysis of *CMTM3* expression levels in HUVECs treated with a second sequence of *CMTM3*-targeting siRNA (siCMTM3) compared with non-targeting siRNA treated cells (sisham) or non-treated controls (contr.). Gene expression levels are shown in target gene/house-keeping gene (*ß-actin*) ratio (AU). N≥3. Shown is mean ± SEM; *P<0.05 vs. sisham and control. (B) Representative images of 3D collagen matrix HUVECs-GFP and pericytes-GFP co-cultures in which HUVECs-GFP were treated with a second sequence of CMTM3-targeting siRNA (siCMTM3) compared with non-targeting siRNA treated cells (sisham) or non-treated controls (contr.). Images displayed were taken at day 5. (C) Quantification of total tubule length, number of tubules and junctions at day 5 of co-culture. N≥15 co-cultures. Shown is mean ± SEM; *P<0.05 vs. control and sisham at day 5.

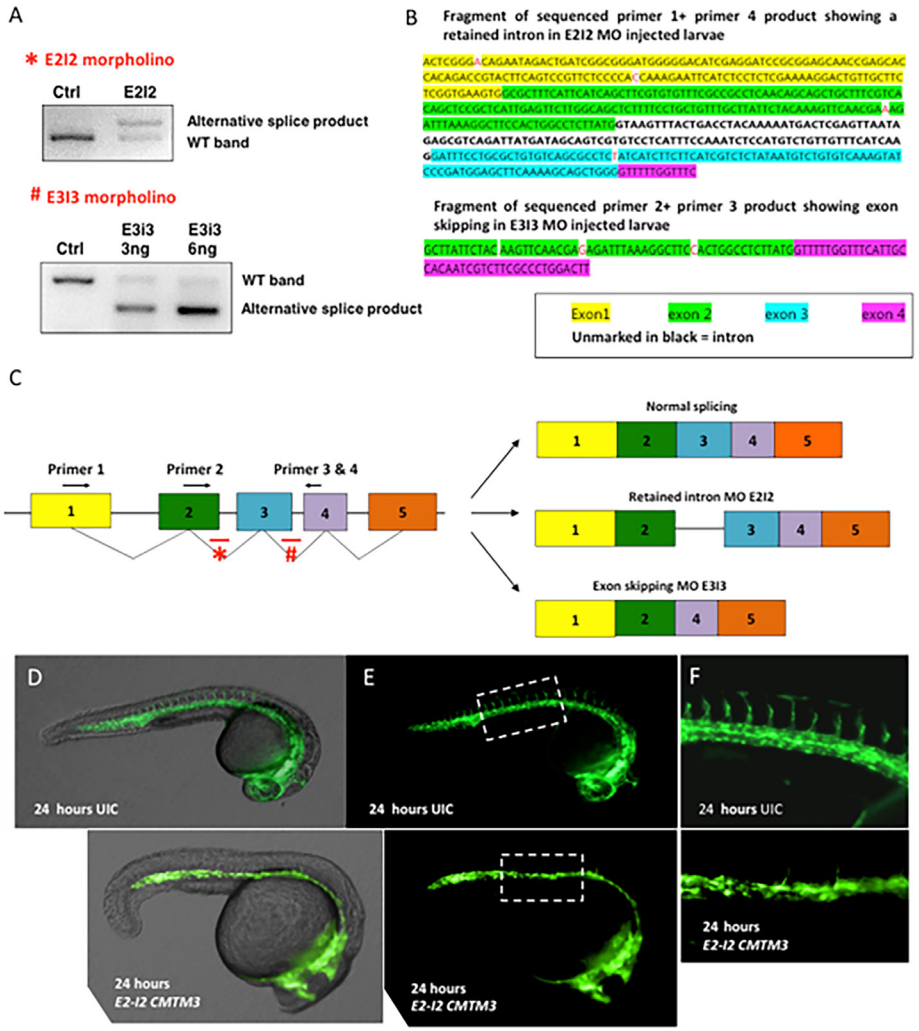

Supplemental Figure 2. Morpholino-induced silencing of CMTM3 in zebrafish affects vascular growth of intersomatic vessels. (A) Polymerase chain reaction (PCR) validation of the morpholino targeting of splice sites E2-I2 and E3-I3. Shown are the PCR bands of wildtype (WT) and alternatively spliced (non-functional) zebrafish CMTM3 mRNAs in uninjected (Ctrl) and E2-I2 or E3-I3 morpholino (MO) treated larvae. (B) PCR bands were isolated from gel and sequenced to reveal the composition of the alternative spliced products. (C) Diagram showing the alternative spliced mRNA products of (1) MO E2I2: Larger product with retained intron compared with WT, and (2) MO E3I3: Smaller product with exon skipping. (D) Tg(fli1:eGFP)^{y1} embryos at 24 hpf, lateral view, anterior to the right. (E) Distinct reduction of intersomatic vascular sprouting in the trunk region was observed in CMTM3 targeting morpholino-injected (morpholino targeting splice site E2-I2 of CMTM3 (indicated as E2-I2 CMTM3) embryos compared with uninjected controls (UIC). The zebrafish vasculature is highlighted by the eGFP marker (green). (F) Panel shows high magnification images of intersomatic outgrowth in the indicated trunk region in UIC and E2-I2 CMTM3 group.

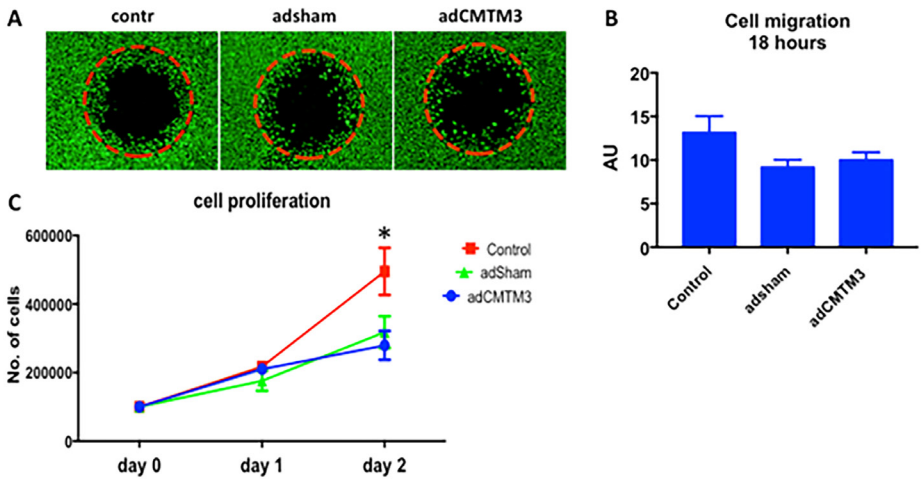

Supplemental Figure 3. CMTM3 overexpression does not affect endothelial cell migration and proliferation. (A) Representative results of plug-based migration assays after 24 hours of migration in HUVECs transfected with adenovirus containing an expression vector for CMTM3 cDNA (adCMTM3) compared with HUVECs transfected with sham virus containing an empty expression vector (adsham) and nontransfected controls. Cells are visualized by Calcein-AM (Green) uptake. The red circle indicates the area occupied by a plug during seeding. Plug was removed to allow free migration of cells into the circle zone for 18 hours. (B) Quantification of % area within circle zone covered by adCMTM3 treated HUVECs compared with sisham and nontransfected controls. N≥4. Shown is mean ± SEM. (C) Number of counted cells at day of seeding (day 0) and after 1 and 2 days of cell proliferation of adCMTM3 treated HUVECs compared with adsham and non-transfected controls. N≥4. Shown is mean ± SEM; *P<0.05 control vs. adsham and adCMTM3.

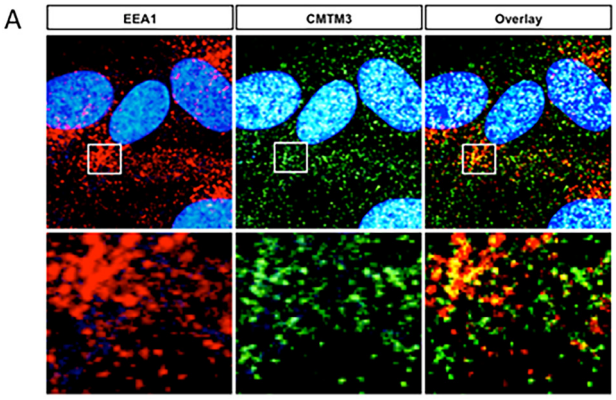

Supplemental Figure 4. Endogenous CMTM3 colocalizes with EEA1. (A) Representative immunofluoresence images of HUVECs immunostained for endogenous CMTM3 (green), EEA1 (red) and DAPI. Co-localization in overlay image is in yellow.

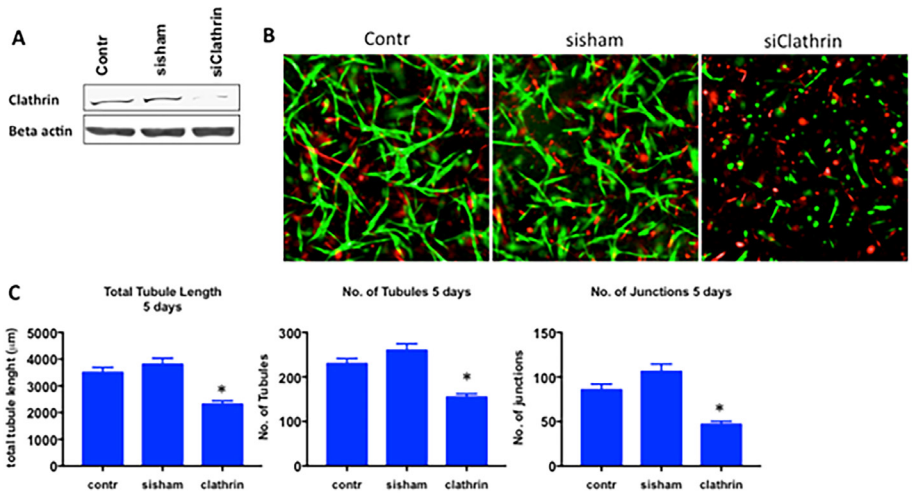

Supplemental Figure 5. Clathrin silencing in endothelial cells impairs vascular growth in a 3D collagen matrix vascular co-culture system *in vitro*. (A) Western blot analysis of clathrin protein levels in HUVECs treated with *clathrin*-targeting siRNA (siclathrin) compared with non-targeting siRNA treated cells (sisham) or non-treated controls (contr). ß-actin was used as a loading control. Shown is a representative blot of 2. (B) Representative images of 3D collagen matrix HUVECs-GFP and pericytes-GFP co-cultures in which HUVECs-GFP were treated with siclatherin or sisham or untreated (contr). Images displayed were taken at day 5. (C) Quantification of total tubule length, number of tubules and junctions at day 5 of co-culture. N≥15 co-cultures. Shown is mean ± SEM; *P<0.05 vs. control and sisham at day 5.

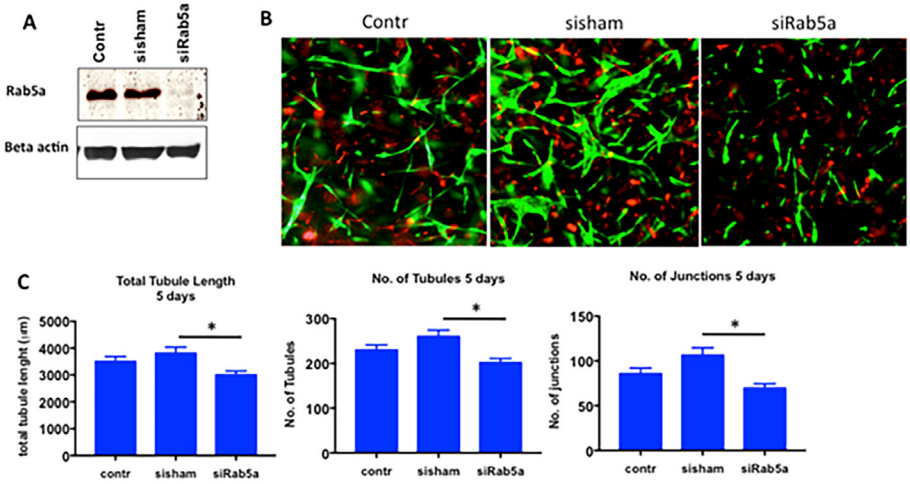

Supplemental Figure 6. Rab5a silencing in endothelial cells impairs vascular growth in a 3D collagen matrix vascular co-culture system *in vitro*. (A) Western blot analysis of Rab5a protein levels in HUVECs treated with *Rab5*-targeting siRNA (siRab5a) compared with non-targeting siRNA treated cells (sisham) or non-treated controls (contr). ß-actin was used as a loading control. Shown is a representative blot of 2. (B) Representative images of 3D collagen matrix HUVECs-GFP and pericytes-GFP co-cultures in which HUVECs-GFP were treated with siRab5 or sisham or untreated (contr.). Images displayed were taken at day 5. (C) Quantification of total tubule length, number of tubules and junctions at day 5 of co-culture. N≥15 co-cultures. Shown is mean ± SEM; *P<0.05 vs. sisham at day 5.

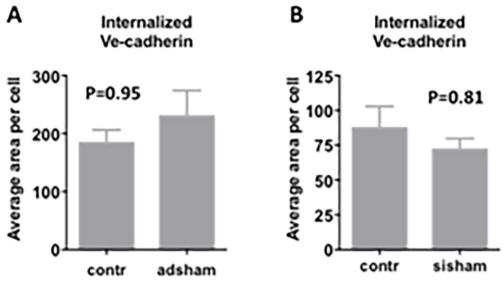

Supplemental Figure 7. Internalization of cell-surface VE-cadherin in sham transfected HUVECs versus non-transfected controls. (A) Quantification of internalized VE-cadherin+ area per cell in HUVECs transfected with sham virus containing an empty expression vector (adsham) and non-transfected cells. N≥6. Shown is mean ± SEM. (B) Quantification of internalized VE-cadherin+ area per cell in non-targeting siRNA treated HUVECs and non-transfected cells. N≥6. Shown is mean ± SEM.

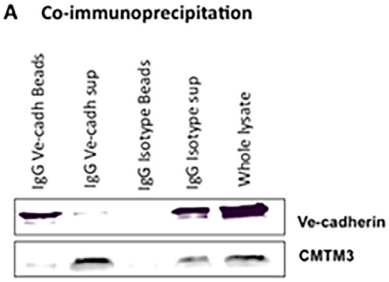

Supplemental Figure 8. Co-immunoprecipitation experiments show successful pull-down of targeted VE-cadherin but no direct binding of VE-cadherin with CMTM3. (A) Western blot analysis of VE-cadherin and CMTM3 bands detected in (from left to right): (1) pull-down lysate of beads coated with an antibody against VE-cadherin, (2) the flush-through lysate of IgG VE-cadherin coated beads condition, (3) pull-down lysate of beads coated with a non-specific IgG isotype, (4) flush-through lysate of IgG isotype coated beads condition, and (5) whole lysate. Blot shows representative result of 3 experiments.

Supplemental Tables

Supplemental Table 1. Primer sequences.

Primer	Sequence	Product size
CKLF1	ccggaagcttctgttcaatc	54bp
CKLF1	tcatgcacaggctttttctg	54bp
***CMTM1* forward**	ctccggttgtttcaagttcc	168bp
***CMTM1* reverse**	ggggaggtagccaacagc	168bp
***CMTM2* forward**	cgtggtctttgctgtgagaa	181bp
***CMTM2* reverse**	gggtccttttttcctttcctg	181bp
***CMTM3* forward**	accatcgtgtttgcaactga	74bp
***CMTM3* reverse**	gcagagtccccttgtttgag	74bp
***CMTM4* forward**	ctggcgtcttgctgattatg	160bp
***CMTM4* reverse**	atttctgctccggctctatg	160bp
***CMTM5* forward**	tctaagcaaggggagggatt	200bp
***CMTM5* reverse**	aggcacttcgagaaacctga	200bp
***CMTM6* forward**	tcatatgccaacaggggaat	223bp
***CMTM6* reverse**	tgcaccttggttgttgatgt	223bp
***CMTM7* forward**	acgcctcacttcaggaaaga	208bp
***CMTM7* reverse**	tgttttctgccttcctgctt	208bp
***CMTM8* forward**	ttggctgggtcatgtttgta	219bp
***CMTM8* reverse**	cccagctgttgaagttgtga	219bp
***β-actin* forward**	tccctggagaagagctacga	194bp
***β-actin* reverse**	agcactgtgttggcgtacag	194bp

Supplemental Table 2. Antibodies.

Antibody	Company
pAb anti-CMTM3 (cell staining)	Sigma-Aldrich
pAb anti-CMTM3 (western blot)	Abcam
pAb anti-Ve-cadhrin (C-19)	Santa Cruz
mAb anti-VE-cadherin (D87F2)	Bioke
mAB anti-VE-cadherin (BVv9 clone)	Abcam
mAb anti-EEA1 clone 14	BD Transduction Laboratories
mAb anti-Rab7	Sigma-Aldrich
mAb anti-Rab11 clone 47	BD Transduction Laboratories
pAb anti-β actin	Abcam
mAb anti-Rab4 clone 4E11	LSBio
mAb anti-Rab5 [3A4]	Abcam
pAb anti-Rab5	Cell Signaling Technology
pAb anti-Clathrin heavy chain clone 23	BD Transduction Laboratories
AffiniPure Fab Fragment goat-anti-rabbit IgG (H+L)	Jackson ImmunoResearch Laboratories inc.
Rhodamine phalloidin	ThermoFisher scientific
Alexa Fluor 488 goat anti mouse IgG	Invitrogen
Alexa Fluor 594 goat anti rabbit IgG	Invitrogen
Alexa Fluor 488 goat anti rabbit IgG	Invitrogen
IRDye 800CW donkey anti-mouse	Li-cor Biosciences
IRDye 800CW goat-anti rabbit	Li-cor Biosciences
IRDye 800CW donkey anti- goat	Li-cor Biosciences
IRDye 680RD donkey anti-goat	Li-cor Biosciences

Angiogenesis – **Chapter 6**

CMTM4 regulates angiogenesis by promoting cell surface recycling of VE-cadherin to endothelial adherens junctions

L. Louzao Martinez*, I. Chrifi*, M.M. Brandt, C.G.M. van Dijk, P.E. Bürgisser, C. Zhu, J.M. Kros, M.C. Verhaar, D.J. Duncker, C. Cheng.

(2019) Angiogenesis, 22(1):75-93

* indicates shared first authorship.

Abstract

Vascular endothelial (VE) cadherin is a key component of endothelial adherens junctions (AJs) and plays an important role in maintaining vascular integrity. Endocytosis of VE-cadherin regulates junctional strength and a decrease of surface VE-cadherin reduces vascular stability. However, disruption of AJs is also a requirement for vascular sprouting. Identifying novel regulators of endothelial endocytosis could enhance our understanding of angiogenesis. Here, we evaluated the angiogenic potential of (CKLF-like MARVEL transmembrane domain 4) CMTM4 and assessed in which molecular pathway CMTM4 is involved during angiogenesis. Using a 3D vascular assay composed of GFP-labeled HUVECs and dsRED-labeled pericytes, we demonstrated *in vitro* that siRNA-mediated CMTM4 silencing impairs vascular sprouting. *In vivo*, CMTM4 silencing by morpholino injection in zebrafish larvae inhibits intersomitic vessel growth. Intracellular staining revealed that CMTM4 colocalizes with Rab4+ and Rab7+ vesicles, both markers of the endocytic trafficking pathway. CMTM4 colocalizes with both membrane-bound and internalized VE-cadherin. Adenovirus-mediated CMTM4 overexpression enhances the endothelial endocytic pathway, in particular the rapid recycling pathway, shown by an increase in early endosomal antigen-1 positive (EEA1+), Rab4+, Rab11+ and Rab7+ vesicles. CMTM4 overexpression enhances membrane-bound VE-cadherin internalization, whereas CMTM4 knockdown decreases internalization of VE-cadherin. CMTM4 overexpression promotes endothelial barrier function, shown by an increase in recovery of trans-endothelial electrical resistance (TEER) after thrombin stimulation. We have identified in this study a novel regulatory function for CMTM4 in angiogenesis. CMTM4 plays an important role in the turnover of membrane-bound VE-cadherin at AJs, mediating endothelial barrier function and controlling vascular sprouting.

Introduction

Angiogenesis is a critical process that occurs during embryonic development, is re-activated in wound healing and is often disturbed in disease. Abnormalities in new vessel formation, represented by either excessive or insufficient growth, contribute to a wide range of disorders, including cancer and cardiovascular diseases[1].

Acquiring and maintaining vascular homeostasis is crucial for the formation and stabilization of new blood vessels during angiogenesis. In order for the endothelial cells (ECs), that form the inner lining of new blood vessels, to function in an integrated manner, specific junctions consisting of cell-adhesion molecules are required. From these junctions, adherens junctions (AJs) are critical for cell-cell adhesion and are tightly regulated by complex molecular pathways. Vascular endothelial (VE) cadherin is the main cell-adhesion molecule found in endothelial AJs and plays an important role in maintaining endothelial barrier function[2,3]. Blocking VE-cadherin by the use of antibodies has a negative effect on endothelial survival and increases vascular permeability[4]. In addition, VE-cadherin-deficient mice suffer from severe vascular defects, including impaired vascular sprouting, limited organization of ECs into large mature vessels and vessel regression, resulting in death at mid-gestation[5,6].

AJs are dynamic structures from which the amount of membrane-bound VE-cadherin that can undergo homophilic interactions with neighboring cells can be actively regulated, thereby modulating the junctional adhesive strength. A reduction in membrane-bound VE-cadherin will result in microvascular destabilization and loss of barrier function. However, a decrease in adhesive strength is required for the disruption of AJs in order to allow EC migration and morphological adaptation into tip and stalk cells during vascular sprouting.

Endocytosis is a form of active transport that is commonly used by cells to take up large secreted molecules or membrane-bound proteins, such as VE-cadherin, into the cytosol for processing. VE-cadherin is taken up in specialized regions called clathrin-coated pits that bud from the membrane to form clathrin-coated vesicles. These vesicles then fuse with early endosomes in which the endocytosed cargo is sorted for recycling, lysosomal or other trafficking routes[7]. Each distinct trafficking step is controlled by a subset of Rab GTPases, making these enzymes ideal markers to monitor the transport route of endocytosed proteins [8]. Rapid endocytosis of VE-cadherin and the subsequent disassembly of AJs is promoted by vascular endothelial growth factor A (VEGF-A), making the ligand for the VEGF

Receptor 1 and 2 (VEGFR1 and 2) an active regulator of vascular permeability[9].

Whereas endocytosis plays a vital role in modulating vascular permeability by controlling the adhesive strength in AJs, little is known about important regulators involved in the early endocytic and subsequent trafficking routes in ECs. Moreover, the exact contribution of endocytosis regulators to the angiogenic process remains to be further elucidated. To identify novel regulators of angiogenesis, we performed a transcriptome analysis of mouse embryos, comparing VEGFR2+ endothelial progenitor cells with the VEGFR2 negative cell population. We identified an enriched expression of several members of the CKLF-like MARVEL Transmembrane domain-containing gene (CMTM) family in the VEGFR2+ population. In humans, this family comprises 9 genes (CKLF and CMTM1-8) that all contain a MAL (myosin and lymphocyte) And Related proteins for Vesicle trafficking and membrane Link (MARVEL) domain[10]. Several studies on CMTM members reveal that they can prevent growth and invasion of different cancer types[11-18]. In a recent study, we revealed that CMTM3 has a specialized function in ECs, where it is involved in regulating the early endocytosis of VE-cadherin during vascular growth[19]. However, the putative function of other CMTM members in endothelial endocytosis, regulation of vascular permeability and angiogenesis remains to be elucidated. Increasing our understanding of other regulators of angiogenesis is highly important for the development of novel therapeutic targets.

In this study, we investigated the angiogenic potential of CMTM4 and assessed in which molecular pathways CMTM4 is involved in ECs. To our knowledge, CMTM4 is until now only known for its potential to act as a tumor suppressor gene[14]. Our data demonstrated that CMTM4 regulates angiogenesis by promoting cell surface recycling of VE-cadherin to endothelial AJs.

Results

CMTM4 expression is essential for vascular growth in an in vitro 3D angiogenesis assay

The function of CMTM4 was investigated *in vitro* using siRNA mediated silencing in HUVECs. Both qPCR and Western blot analysis confirmed efficient silencing of CMTM4 in cells transfected with two different siRNA sets specific for *CMTM4* (siCMTM4 set 1 and set 2), compared to untreated cells (control) and cells transfected with a pool of non-targeting siRNA sequences (siSHAM) (Figure 1A,

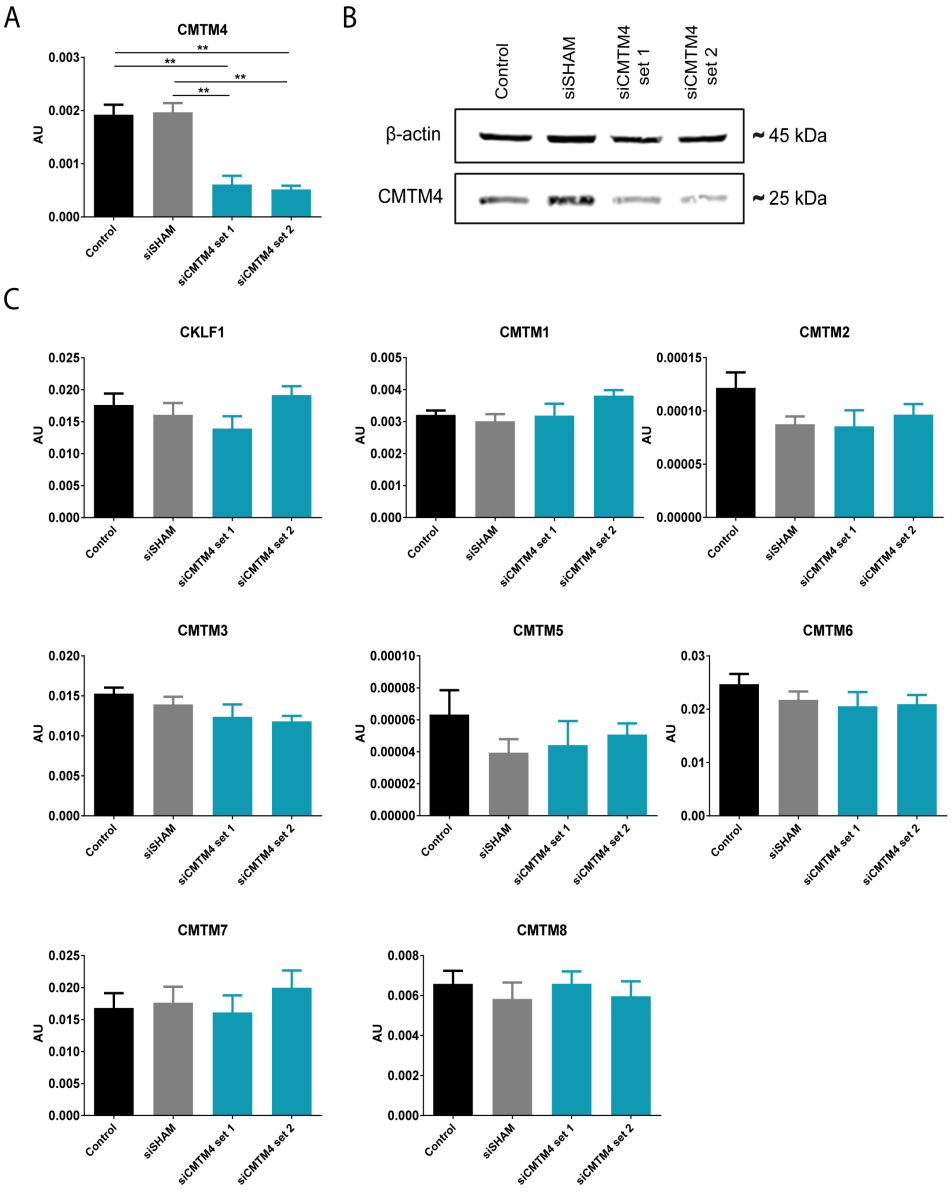

Figure 1. *CMTM4*-targeting siRNA induces significant and specific silencing of *CMTM4* expression. (A) Gene expression levels of *CMTM4* in HUVECs transfected with *CMTM4*-targeting siRNA (siCMTM4), non-targeting siRNA (siSHAM) and in non-transfected HUVECs (control). (B) Representative Western blot of CMTM4 and β-actin protein levels in siCMTM4, siSHAM and control HUVECs. Shown is a representative blot of 3 blots. (C) Gene expression levels of CMTM family members in siCMTM4, siSHAM and control HUVECs. For (A) and (C), gene expression levels were normalized to *β-actin* (AU). N≥8 qPCRs. Shown is mean ± SEM; **P<0.01.

B). The mRNA levels of the other CMTM family members were not significantly downregulated by both *CMTM4* targeting siRNA sets when comparing siCMTM4 versus siSHAM, indicating that the siRNA mediated silencing was specific for *CMTM4* (Figure 1C).

Next, the angiogenic potential of these CMTM4-silenced HUVECs was assessed *in vitro* in a 3D angiogenesis assay developed for studying the formation of lumenized micro-capillary structures[20]. In this assay, GFP-expressing HUVECs and dsRED-expressing pericytes directly interact in a collagen type I matrix. After 1 day of co-culture, EC sprouting and tubule formation can be observed and these neovascular structures are stabilized by perivascular recruitment of pericytes. After 5 days, micro-capillaries with distinct luminal areas and pericyte coverage can be observed. Imaging and quantification of these vascular structures was conducted at day 2 and 5. This assay has been well validated in previous studies[21-23]. Endothelial silencing of CMTM4 severely impaired the formation of neovascular structures in the 3D angiogenesis assay when compared to control and siSHAM (Figure 2A). Quantification revealed a significant reduction in the number of junctions, the number of tubules and the total tubule length of HUVECs after both 2 and 5 days of coculture (Figure 2B). In contrast, CMTM4 silencing in pericytes did not affect tubule formation at 2 or 5 days of coculture (Supplemental Figure 1A-D).

Silencing of CMTM4 in developing zebrafish larvae inhibits intersomitic vessel growth

In order to evaluate CMTM4 function during *in vivo* angiogenesis, the zebrafish orthologue of the gene was silenced in developing larvae of the transgenic zebrafish line Tg(fli1:eGFP)^{y1} by morpholino knockdown. *CMTM4* is highly conserved in the zebrafish genome and two morpholinos were designed to target the *CMTM4* zebrafish orthologue with knockdown based on the splice modification principle of the pre-mRNA target. Injection with a morpholino construct that targeted the

► **Figure 2. CMTM4 is essential for vascular growth *in vitro*.** (A) Representative immunofluorescent images taken at 20x magnification (upper row) and zoomed-in images (3 lower rows) of GFP-labelled HUVECs (green) and dsRED-labelled pericytes (red) cultured for 5 days in a 3D collagen matrix, in which the HUVECs-GFP were transfected with either *CMTM4*-targeting siRNA (siCMTM4) or non-targeting siRNA (siSHAM) or not transfected (control). Scale bar represents 1 mm for the upper row and 0.25 mm for the 3 lower rows. (B) Quantification of the number of junctions, number of tubules and total tubule length of siCMTM4, siSHAM and control HUVECs at day 2 and 5 of co-culture. N≥6 co-cultures, ± 7 images each. Shown is mean ± SEM; **P<0.01 compared to all other conditions.

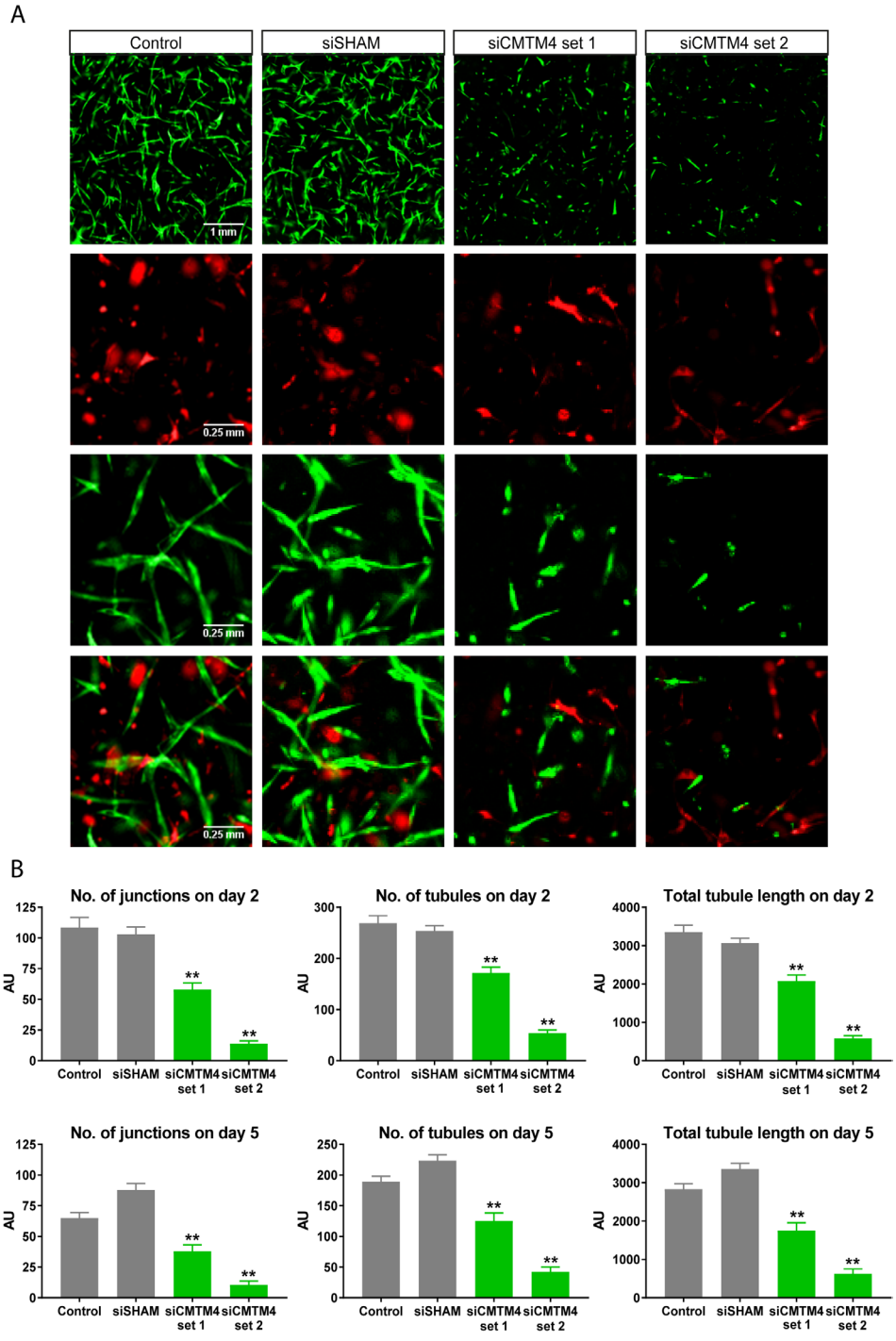
A
Control
siSHAM
siCMTM4 set 1
siCMTM4 set 2
1 mm
0.25 mm
0.25 mm
0.25 mm
B
No. of junctions on day 2
No. of tubules on day 2
Total tubule length on day 2
No. of junctions on day 5
No. of tubules on day 5
Total tubule length on day 5
AU
Control
siSHAM
siCMTM4 set 1
siCMTM4 set 2
**

splice site located on *CMTM4* intron 2 – exon 3 (i2-e3) affected intersomitic vessel (ISV) formation versus uninjected larvae at 24 hours post-fertilization (Figure 3A). Phenotype quantification showed in the 3ng i2-e3 morpholino group that 36% of larvae displayed defects in ISV formation versus 0% in the control group. Injection with 6ng i2-e3 increased the number of larvae with affected ISVs to 48% (Figure 3B). In line with these findings, injection of the second morpholino construct that targeted the splice site on *CMTM4* intron 1 – exon 2 (i1-e2) affected ISV formation in 56% of the larvae in the i1-e2 group versus 0% in the control population (Supplemental Figure 2A, B). These data clearly demonstrate a negative effect of *CMTM4* silencing on angiogenesis in developing zebrafish larvae *in vivo*.

Effect of CMTM4 on cell cycle progression, migration and proliferation

Previous studies in HeLa and clear cell renal cell carcinoma cells imply that CMTM4 functions as a tumor suppressive gene, with expression of CMTM4 leading to cell migration and inhibition of cell proliferation via G2/M phase accumulation[14,15]. We investigated the effects of CMTM4 silencing in HUVECs on these parameters. CMTM4 silencing using either siRNA set 1 or 2 did not affect cell proliferation as shown by comparison with siSHAM treated and non-treated control groups based on cell count and PI analysis of the G0/G1-phase and G2 phase in fixed cells (Supplemental Figure 3A, B). Migration capacity was also assessed by scratch assay and showed a significant decrease in response to CMTM4 silencing by set 2, but not by set 1, in HUVECs compared to siSHAM treated or non-treated controls after 4 and 8 hours of migration (Supplemental Figure 3C-E).

Next, we investigated the effects of CMTM4 overexpression on the same parameters. HUVECs were transfected with a recombinant adenovirus that encodes for human CMTM4 cDNA (adCMTM4). QPCR analysis validated significant transgenic expression of CMTM4 in HUVECs compared to HUVECs transfected with sham virus (adSHAM) (Figure 4A). In contrast with CMTM4 silencing, cell count and cell cycle progression were decreased in adCMTM4 HUVECs versus adSHAM or non-transfected groups, as shown by reduced cell count and an increase of cells in G0/G1 versus G2 phase (Figure 4B, C). However, overexpression of CMTM4 did not affect migration capacity of HUVECs (Figure 4D-F). These findings indicate that increased levels of CMTM4 limit cell proliferation, but do not affect cell migration.

CMTM4 colocalizes with endocytic vesicle structures and VE-cadherin in adherens junctions

In a recent study, we revealed that CMTM3 is mainly localized in the cytosol, where it is involved in regulating the early endocytosis of the AJ protein VE-cadherin[19]. Therefore, we evaluated in this study the intracellular function of CMTM4 in ECs. Western blot analysis demonstrated that CMTM4 was mainly present in the soluble cytosolic fraction and not in the insoluble more actin enriched fraction of the HUVEC lysates (Figure 5A). Similarly, VE-cadherin was mainly enriched in the soluble fraction (Figure 5A).

Double immunofluorescent staining of CMTM4 with different markers of intracellular vesicular transport compartments showed limited colocalization with early endosome markers EEA1 and Clathrin (Figure 5B-D). In contrast, examination of CMTM4 with markers of recycling vesicles showed significant colocalization

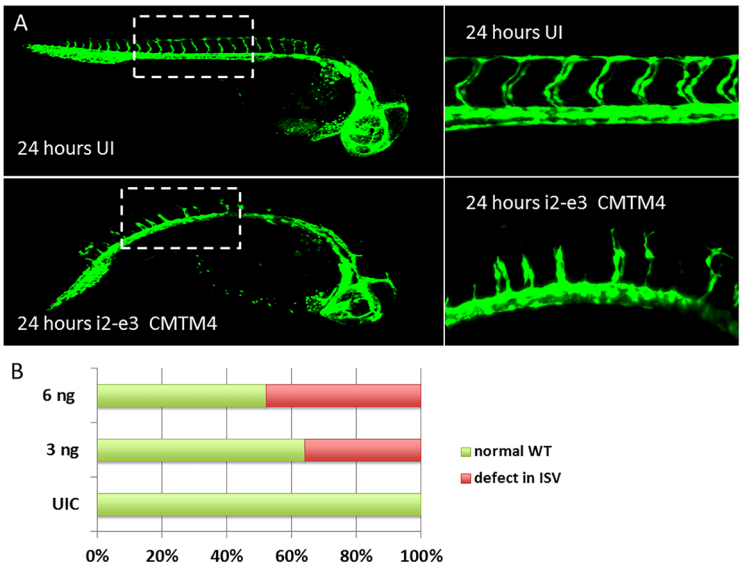

Figure 3. Morpholino silencing of *CMTM4* in developing zebrafish larvae induces defects in intersomitic vessels. (A) Tg(fli1:eGFP)^{y1} larvae at 24 hours post fertilization, anterior to the right, lateral view. Defects in intersomitic vessel (ISV) formation was observed in the trunk region in specimens injected with morpholinos targeting the splice site of i2-e3 of *CMTM4* (indicated as i2-e3 *CMTM4*) compared with uninjected (UI) controls. The vasculature is highlighted by eGFP (green). Left hand panels show 20x magnification images with 0.5 mm scale bar, right hand panels show 100x images with 0.25 mm scale bar. (B) Quantification of ISV defect phenotype versus wildtype (WT) phenotype in i2-e3 injected group at different doses versus UI controls (UIC). Data represent percentage of counted larvae (~100 per group).

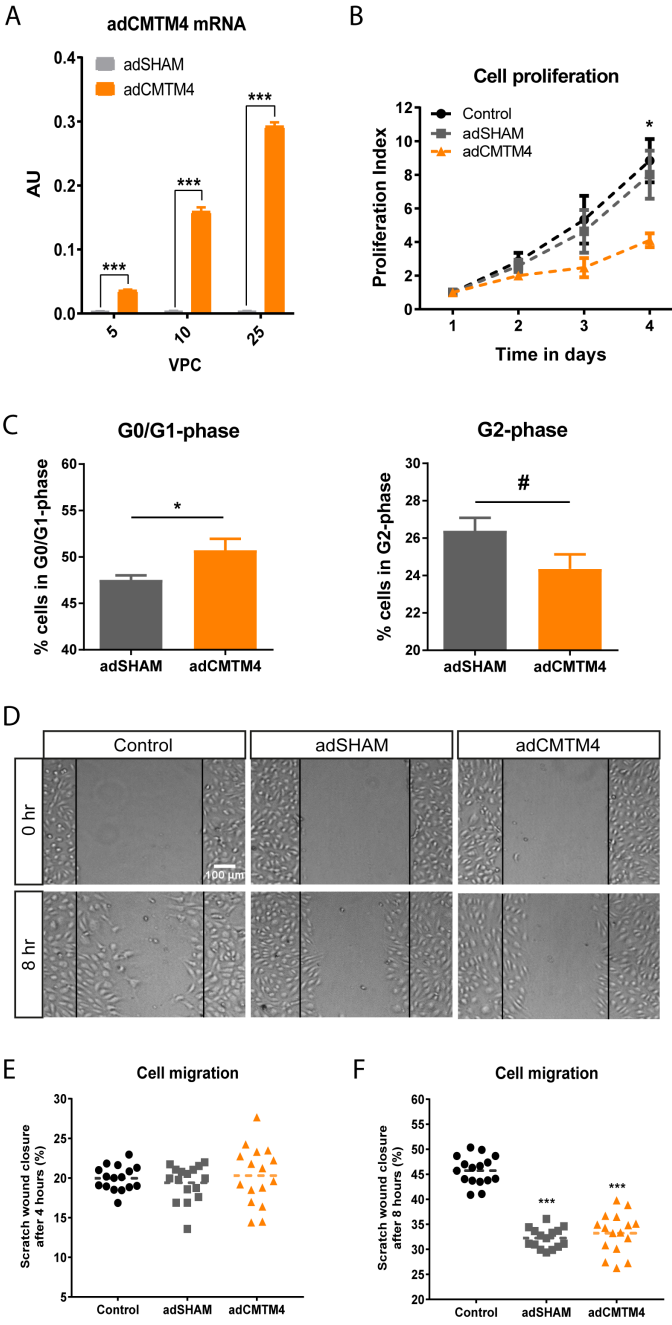

Figure 4. CMTM4 overexpression limits endothelial cell proliferation, but does not affect cell migration. (A) Quantitative polymerase chain reaction (qPCR) of human *CMTM4* expression in HUVECs transfected with different (5, 10, 25) virus particles per cell (VPC) of

(Figure 4 continued) adenovirus containing an expression vector for CMTM4 cDNA (adCMTM4) or with sham virus containing an empty expression vector (adSHAM). Shown are target gene/housekeeping gene (*β-actin*) ratio (AU). N=4 qPCRs. Shown is mean ± SEM; ***P<0.001 in comparison between adSHAM and adCMTM4 group of equal VPC. (B) The number of cells counted at day of seeding (day 1), and at day 2, 3 and 4 of cell proliferation of adCMTM4 HUVECs compared with adSHAM and non-transfected controls. N=6. Shown is mean ± SEM; *P<0.05. (C) Bar graphs showing the % of G0/G1 and G2 phase cells at day 2 after transfection of adCMTM4 versus adSHAM HUVECs. N=4. Shown is mean ± SEM; *P<0.05, #P<0.10. (D) Representative brightfield microscope images (40x magnification) of a scratch migration assay after 8 hours of migration of adCMTM4 HUVECs compared to adSHAM and non-treated controls. Scale bar represents 100 μm. Bar graphs of the quantified results of the scratch migration assay showing the % area within the scratched region covered by adCMTM4 HUVECs compared to adSHAM and non-treated controls after 4 hours (E) and 8 hours (F). N=2, 8 wells each. Shown is a dot plot with the distribution and mean; ***P<0.001.

between CMTM4 and Rab4, but not Rab11 (Figure 5B, E, F). Furthermore, colocalization between CMTM4 and Rab7, a marker for vesicles destined for the lysosome pathway, was also significantly increased compared to EEA1, clathrin, and Rab11 (Figure 5B, G). These findings indicated that CMTM4 was colocalized in (Rab4 marked) recycling and (Rab7 marked) lysosome-destined vesicles and may contribute to recycling and lysosome activity in the process of endocytosis. Further analysis of CMTM4 intracellular localization showed cytosolic and cell-cell junction localization of the protein. Dual immunostaining analysis demonstrated that the CMTM4 signal colocalized with VE-cadherin, both at the AJs and in cytosolic vesicle structures (Figure 5B, H). Transgenic overexpression of CMTM4 in ECs appeared to alter the junctional pattern of VE-cadherin into plaque-like structures (Figure 5I). Studies have shown that Junction-Associated-Intermittent-Lamellipodia (JAIL) structures appear at established endothelial junctions and induce an overlap with the plasma membrane of the neighboring cell, forming subsequent VE-cadherin plaques that, after retraction of JAIL, are incorporated into the junctions[24,25]. Overexpression of CMTM4 did not affect the total VE-cadherin+ area (Figure 5J). Similarly, Western blot analysis of adCMTM4 and adSHAM transfected HUVECs showed no difference in total protein concentration of VE-cadherin (Figure 5K).

Quantification of EEA1, Clathrin, Rab4, Rab11, and Rab7 immunofluorescence signals showed that EEA1+, Rab4+, and Rab11+ vesicles were significantly increased in adCMTM4 versus adSHAM-treated HUVECs and a similar trend was visible for Rab7+ vesicles. In contrast, the amount of Clathrin+ vesicles was not affected (Figure 6A-E). These data indicate that CMTM4 enhances endocytosis processes in ECs.

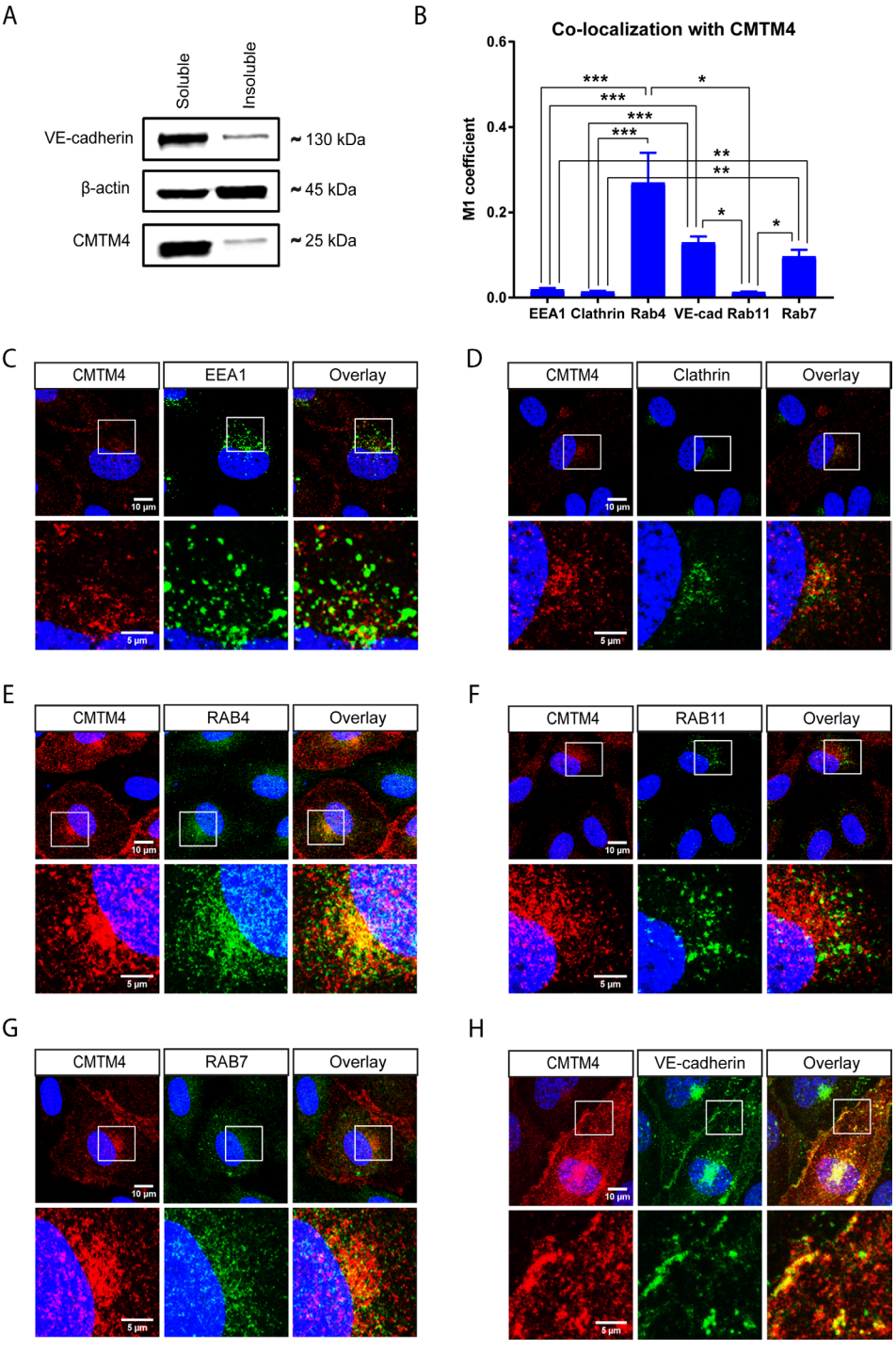
A
Soluble
Insoluble
VE-cadherin
β-actin
CMTM4
~ 130 kDa
~ 45 kDa
~ 25 kDa
B
Co-localization with CMTM4
M1 coefficient
0.6
0.4
0.2
0.0
EEA1 Clathrin Rab4 VE-cad Rab11 Rab7
C
CMTM4
EEA1
Overlay
D
CMTM4
Clathrin
Overlay
E
CMTM4
RAB4
Overlay
F
CMTM4
RAB11
Overlay
G
CMTM4
RAB7
Overlay
H
CMTM4
VE-cadherin
Overlay
10 µm
5 µm

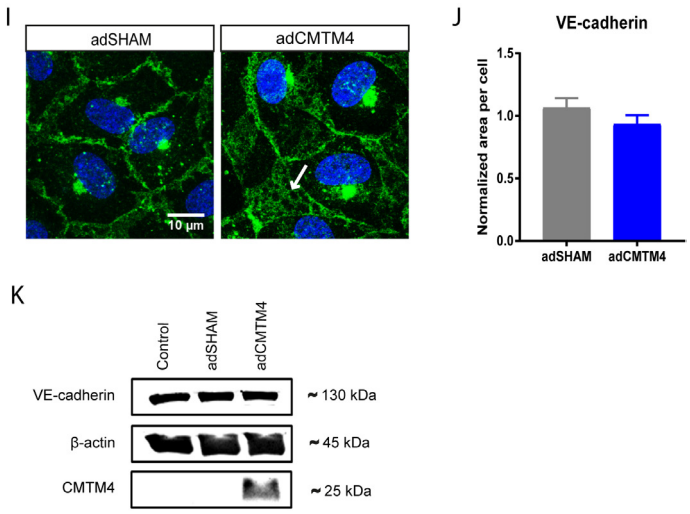

Figure 5. CMTM4 localizes with different vesicle compartments of the intracellular endocytosis pathway and VE-cadherin+ adherens junctions. (A) Representative Western blot of CMTM4, β-actin and VE-cadherin protein levels in the soluble and insoluble cell lysates fraction of HUVECs. (B) Quantification of colocalization of CMTM4 with VE-cadherin and endocytic compartment markers in immunofluorescence images based on M1 coefficient. N=3, 5 fluorescent images each. Shown is mean ± SEM; *P<0.05, **P<0.01, ***P<0.001; Representative 630x magnification (upper row) and zoomed-in (lower row) immunofluorescence images of HUVECs transfected with adenovirus containing an expression vector for CMTM4 cDNA (adCMTM4) (VPC10), immunostained for CMTM4 (red) and EEA1 (green) (C) Clathrin (green) (D), Rab4 (green) (E), Rab11 (green) (F), Rab7 (green) (G) and VE-cadherin (green) (H). Colocalization of CMTM4 and endocytic compartment protein markers or VE-cadherin in overlay images is displayed in yellow. Scale bars represent 10 µm for the upper rows and 5 µm for the lower rows. (I) Representative 630x magnification immunofluorescence images of VE-cadherin (green) in adSHAM and adCMTM4 HUVECs (VPC10). White arrow marks the altered VE-cadherin junctional pattern into a plaque-like structure. Scale bar represents 10 µm. (J) Quantification of total VE-cadherin+ area per cell in adSHAM or adCMTM4 transfected HUVECs (VPC10). N=3, 5 fluorescent Z-stacks each. Shown is mean ± SEM. (K) Representative Western blot bands for total CMTM4, VE-cadherin and β-actin expression in adCMTM4 and adSHAM HUVECs (VPC5). Shown is a representative blot of 2 blots.

CMTM4 regulates VE-cadherin endocytosis and promotes endothelial barrier function of endothelial adherens junctions

The putative role of CMTM4 in endocytosis processing of VE-cadherin was evaluated with an internalization assay, where confluent HUVECs transfected with adSHAM or adCMTM4 were exposed to a low temperature shock (1 hour at 4°C) followed by an 1 hour incubation at 37°C. Assessment of VE-cadherin in relation to the actin cytoskeleton showed a significant increase in colocalization in adCMTM4 treated versus adSHAM confluent HUVEC monolayers, as demonstrated by an

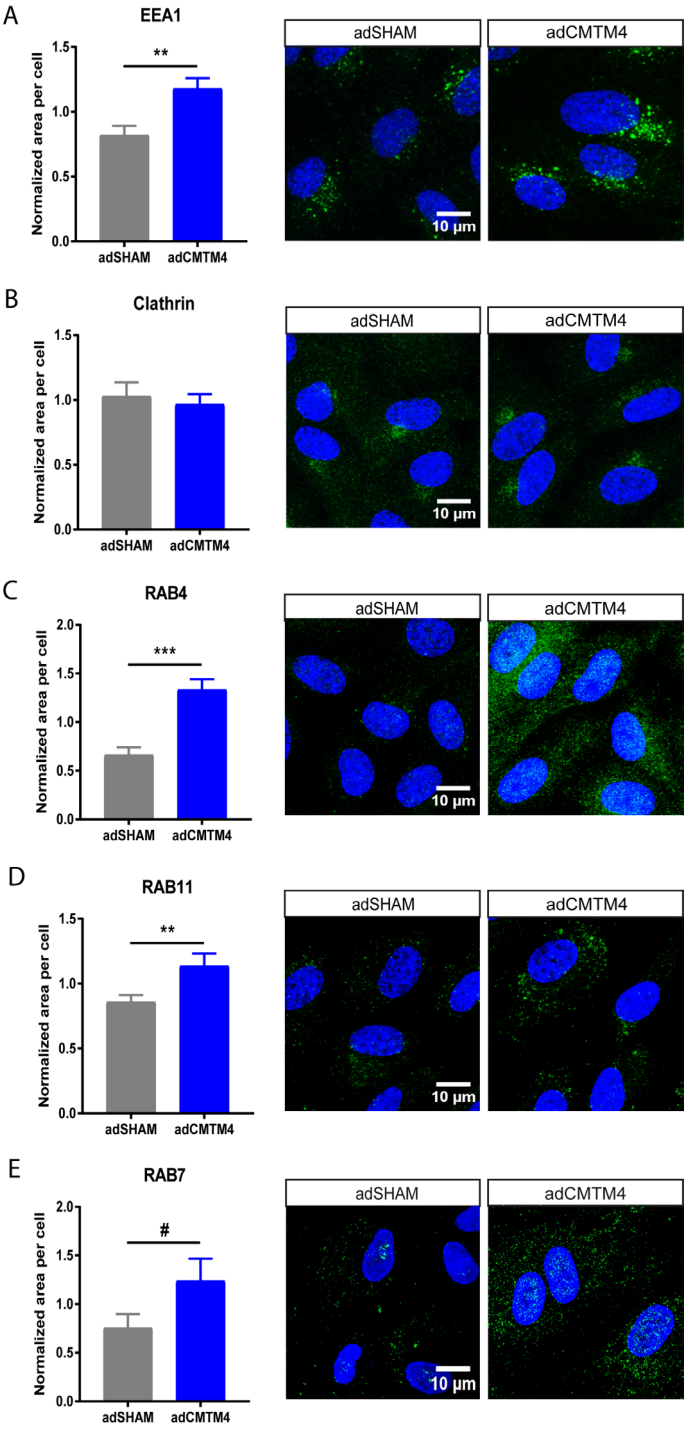
A
EEA1
Normalized area per cell
1.5
1.0
0.5
0.0
**
adSHAM
adCMTM4
adSHAM
adCMTM4
10 µm
B
Clathrin
Normalized area per cell
1.5
1.0
0.5
0.0
adSHAM
adCMTM4
adSHAM
adCMTM4
10 µm
C
RAB4
Normalized area per cell
2.0
1.5
1.0
0.5
0.0
***
adSHAM
adCMTM4
adSHAM
adCMTM4
10 µm
D
RAB11
Normalized area per cell
1.5
1.0
0.5
0.0
**
adSHAM
adCMTM4
adSHAM
adCMTM4
10 µm
E
RAB7
Normalized area per cell
2.0
1.5
1.0
0.5
0.0
#
adSHAM
adCMTM4
adSHAM
adCMTM4
10 µm

◀ **Figure 6. CMTM4 overexpression significantly upregulates the endothelial endocytic pathway.** Quantification of area per cell in HUVECs transfected with adenovirus containing an expression vector for CMTM4 cDNA (adCMTM4) or with sham virus containing an empty expression vector (adSHAM) (VPC10). Representative immunofluorescence images (630x magnification) of HUVECs transfected with adCMTM4 and adSHAM (VPC10), immunostained (green) for EEA1 (A), Clathrin (B), Rab4 (C), Rab11 (D) and Rab7 (E). N=3, 5 Z-stacks each. Shown is mean ± SEM for all data; #P<0.1, **P<0.01, ***P<0.001; scale bars represent 10 μm.

increase in Pearson correlation coefficient (Figure 7A, B). This finding indicates that CMTM4 promotes VE-cadherin connections with the actin cytoskeleton that are vital for AJ stabilization.

Next, the role of CMTM4 in VE-cadherin endocytosis was assessed. For this, confluent adSHAM or adCMTM4 HUVECs were incubated with VE-cadherin antibody at 4°C before an acid wash treatment to remove all extracellular VE-cadherin signal. Subsequent analysis following 1 hour incubation at 37°C with and without VEGFA stimulation showed a significant increase of internalized VE-cadherin in adCMTM4 versus adSHAM conditions (Figure 7C-E). The internalized VE-cadherin upon VEGF stimulation was present in both Rab4+ and Rab7+ vesicles, with significantly more Rab4+ and Rab7+ vesicles loaded with VE-cadherin in adCMTM4 HUVECs when compared to adSHAM HUVECs (Figure 7F-H). In line with these findings, siRNA mediated knockdown of CMTM4 significantly decreased the signal of internalized VE-cadherin in siCMTM4 treated HUVECs with and without VEGFA stimulation (Figure 7I-K). This effect of CMTM4 was dependent on Rab4, since adCMTM4 HUVECs transfected with siRNA specific for Rab4a (siRAB4a) also showed significantly less internalized VE-cadherin when compared to siSHAM HUVECs. The trend was still visible under VEGF stimulation (Figure 7L-N and Supplemental Figure 4A).

Findings so far indicate that CMTM4 could regulate the bio-availability of VE-cadherin at cell-cell AJs, which implies that it could impact endothelial barrier function. We used transendothelial electric resistance (TEER) measurements to evaluate the response of HUVEC monolayers transfected with adSHAM or adCMTM4 to thrombin-induced junction disruption. Basal levels (before thrombin stimulation) of TEER were not affected by CMTM4 overexpression. However, the recovery of TEER post thrombin stimulation was significantly increased in adCMTM4 conditions compared to adSHAM (Figure 8A-C). In line with these findings, basal TEER levels were similarly not affected by siRNA mediated silencing of CMTM4, but TEER recovery after thrombin removal was significantly decreased in siCMTM4 versus siSHAM conditions (Supplemental Figure 5A, B).

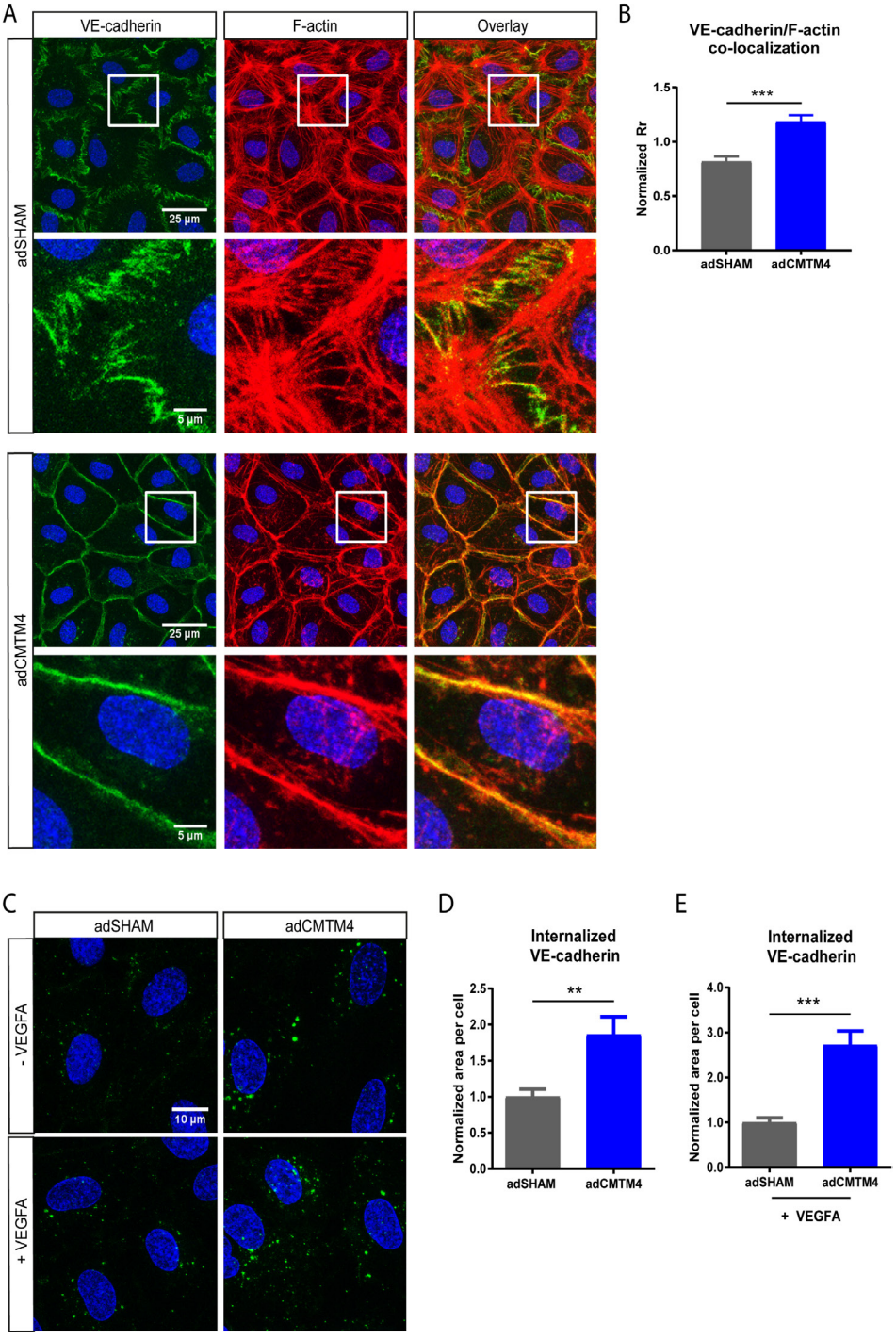
A
VE-cadherin
F-actin
Overlay
adSHAM
adCMTM4
25 µm
5 µm
B
VE-cadherin/F-actin
co-localization
Normalized Rr
1.5
1.0
0.5
0.0
***
adSHAM
adCMTM4
C
adSHAM
adCMTM4
- VEGFA
+ VEGFA
10 µm
D
Internalized
VE-cadherin
Normalized area per cell
2.5
2.0
1.5
1.0
0.5
0.0
**
adSHAM
adCMTM4
E
Internalized
VE-cadherin
Normalized area per cell
4.0
3.0
2.0
1.0
0.0
***
adSHAM
adCMTM4
+ VEGFA

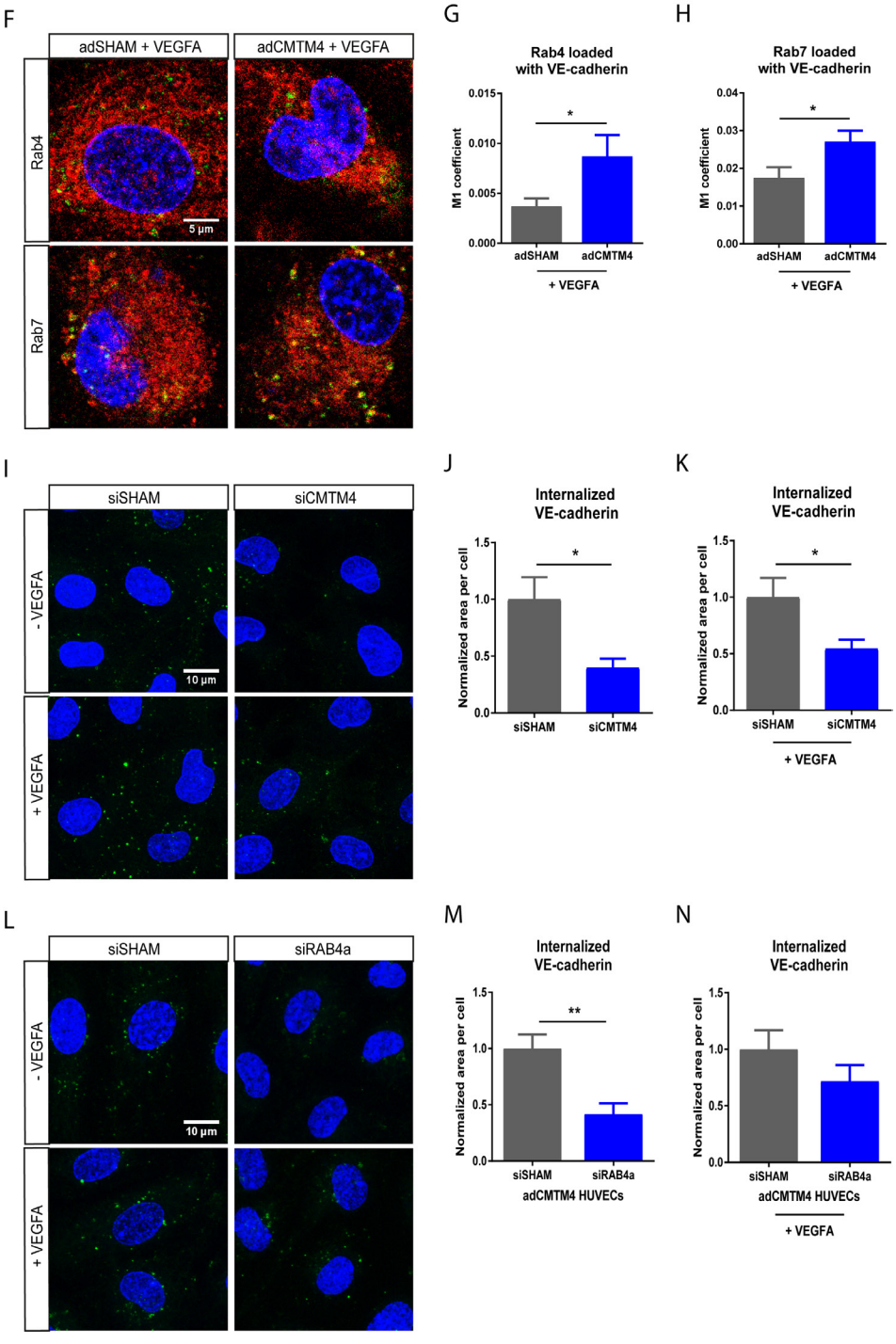
F
adSHAM + VEGFA
adCMTM4 + VEGFA
Rab4
Rab7
5 µm
G
Rab4 loaded with VE-cadherin
M1 coefficient
0.015
0.010
0.005
0.000
*
adSHAM
adCMTM4
+ VEGFA
H
Rab7 loaded with VE-cadherin
M1 coefficient
0.04
0.03
0.02
0.01
0.00
*
adSHAM
adCMTM4
+ VEGFA
I
siSHAM
siCMTM4
- VEGFA
+ VEGFA
10 µm
J
Internalized VE-cadherin
Normalized area per cell
1.5
1.0
0.5
0.0
*
siSHAM
siCMTM4
K
Internalized VE-cadherin
Normalized area per cell
1.5
1.0
0.5
0.0
*
siSHAM
siCMTM4
+ VEGFA
L
siSHAM
siRAB4a
- VEGFA
+ VEGFA
10 µm
M
Internalized VE-cadherin
Normalized area per cell
1.5
1.0
0.5
0.0
**
siSHAM
siRAB4a
adCMTM4 HUVECs
N
Internalized VE-cadherin
Normalized area per cell
1.5
1.0
0.5
0.0
siSHAM
siRAB4a
adCMTM4 HUVECs
+ VEGFA

◀ **Figure 7. CMTM4 upregulates endocytosis and subsequent recycling of VE-cadherin.** (A) Representative 630x magnification (upper row) and zoomed-in (lower row) confocal microscope images of confluent HUVEC cultures that were immunostained for F-actin (red) and VE-cadherin (green) in HUVECs transfected with adenovirus containing an expression vector for CMTM4 cDNA (adCMTM4) or with sham virus containing an empty expression vector (adSHAM) (VPC10). Cells were exposed to low temperature shock (1 hour at 4°C) followed by 1 hour incubation at 37°C. Adherens junctions were quicker restored in adCMTM4 condition versus adSHAM conditions (zigzagged VE-cadherin signal in adSHAM versus linear VE-cadherin junctions in adCMTM4). Colocalization signal in overlay is in yellow. Scale bars represent 25 μm for the upper rows and 5 μm for the lower rows. (B) Quantification of the colocalization signal between VE-cadherin and F-actin in immunofluorescence images based on normalized Pearson correlation coefficient (Rr). N=4, 5 Z-stacks each. Shown is mean ± SEM; ***P<0.001 versus adSHAM. (C) Representative confocal micrographs (630x magnification) of confluent adSHAM and adCMTM4 cultures (VPC10) labeled with VE-cadherin antibodies at 4°C to track VE-cadherin movement, followed by 37°C incubation for 1 hour with and without VEGFA stimulation. Surface bound VE-cadherin antibodies were removed by an acid-wash, before proceeding with immunostaining for visualization of internalized VE-cadherin (green). Scale bar represents 10 μm. Quantification of internalized VE-cadherin area per cell in adSHAM and adCMTM4 HUVECs without VEGFA (D) and with VEGFA (E) stimulation. N=4, 5 Z-stacks each. Shown is mean ± SEM; **P<0.01, ***P0.001 versus adSHAM. (F) Representative zoomed-in confocal micrographs (630x magnification) of confluent adSHAM and adCMTM4 cultures (VPC10) labeled with VE-cadherin antibodies at 4°C to track VE-cadherin movement, followed by 37°C incubation for 1 hour with and without VEGFA stimulation. Surface bound VE-cadherin antibodies were removed by an acid-wash, before proceeding with immunostaining for visualization of internalized VE-cadherin (green) and either Rab4 or Rab7 (red). Scale bar represents 5 μm. Quantification of colocalization of either Rab4 (G) or Rab7 (H) with VE-cadherin in confocal micrographs based on M1 coefficient. N=2, 5 fluorescent images each. Shown is mean ± SEM; *P<0.05. (I) Representative confocal micrographs (630x magnification) of confluent HUVECs transfected with either *CMTM4*-targeting siRNA (siCMTM4) or non-targeting siRNA (siSHAM), labeled with VE-cadherin antibodies at 4°C to track VE-cadherin movement, followed by 37°C incubation for 1 hour with and without VEGFA stimulation. Surface bound VE-cadherin antibodies were removed by an acid-wash, before proceeding with immunostaining for visualization of internalized VE-cadherin (green). Scale bar represents 10 μm. Quantification of internalized VE-cadherin area per cell in siSHAM and siCMTM4 HUVECs without VEGFA (J) and with VEGFA (K) stimulation. N=2, 5 Z-stacks each. Shown is mean ± SEM; *P<0.05 versus adSHAM. (L) Representative confocal micrographs (630x magnification) of confluent siSHAM HUVECs and HUVECs transfected with *Rab4a*-targeting siRNA (siRAB4a) labeled with VE-cadherin antibodies at 4°C to track VE-cadherin movement, followed by 37°C incubation for 1 hour with and without VEGFA stimulation. Surface bound VE-cadherin antibodies were removed by an acid-wash, before proceeding with immunostaining for visualization of internalized VE-cadherin (green). Scale bar represents 10 μm. Quantification of internalized VE-cadherin area per cell in siSHAM and siRAB4a HUVECs without VEGFA (M) and with VEGFA (N) stimulation. N=2, 7 Z-stacks each. Shown is mean ± SEM; **P<0.01 versus adSHAM.

Discussion

In this study, we investigated the angiogenic potential of CMTM4 and evaluated in which molecular pathways CMTM4 is involved in ECs. The most important findings of this study are as follows: 1) CMTM4 silencing impairs vascular growth in an *in*

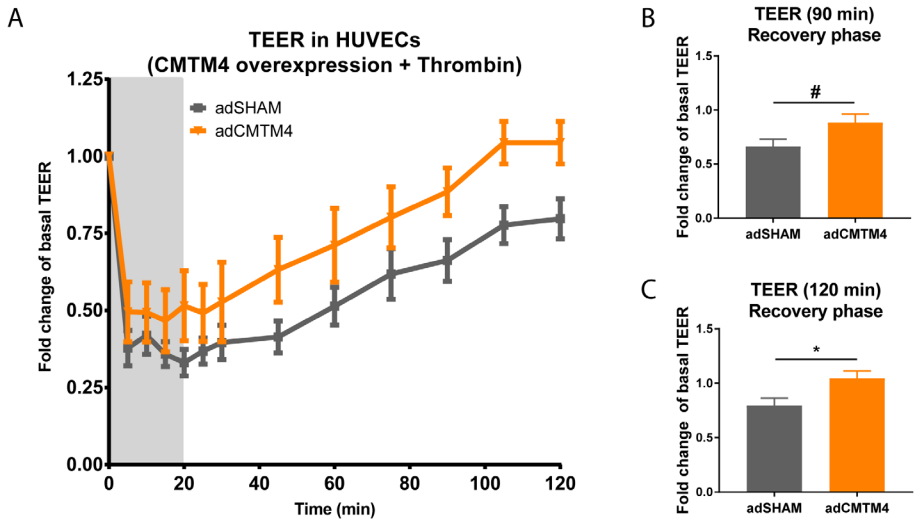

Figure 8. CMTM4 promotes restoration of endothelial electric resistance in thrombin-induced response. (A) Thrombin response (presented in fold change compared with basal resistance of nontransfected group: Y-axes) of confluent HUVECs transfected with adenovirus containing an expression vector for CMTM4 cDNA (adCMTM4) or with sham virus containing an empty expression vector (adSHAM), during (0–20 minutes) and after (20–120 minutes) thrombin (1 U/mL) stimulation. At 0 minutes, thrombin was added and after 20 minutes thrombin was removed (gray area). N≥4 per time series. Shown is mean ± SEM. Increase in resistance during recovery phase at 90 minutes (B) and 120 minutes (C) in adSHAM and adCMTM4 groups. N≥6. Shown is mean ± SEM; #P<0.10 versus adSHAM.

vitro 3D angiogenesis assay. 2) Silencing of CMTM4 in developing zebrafish larvae inhibits intersomitic vessel growth. 3) Intracellular staining reveals that CMTM4 colocalizes with Rab4+ and Rab7+ vesicles, and with both membrane-bound and internalized VE-cadherin. 4) CMTM4 enhances the endothelial endocytic pathway, in particular the Rab4 recycling pathway. 5) CMTM4 also enhances VE-cadherin internalization and increases endothelial barrier function recovery.

Several previous studies have revealed that CMTM family members can prevent growth and invasion of different cancer cell types[11-18]. CMTM4 has been reported to be frequently downregulated in clear cell renal cell carcinoma where it functions as a tumor suppressor. Thus, restoration of CMTM4 suppresses the tumorigenicity of these cancer cells, whereas knockdown of CMTM4 leads to enhanced tumor growth[14]. Furthermore, overexpression of CMTM4 inhibits HeLa cell growth via G2/M phase accumulation[15]. In a recent study, we demonstrated that CMTM3 has a specialized function in ECs, where it is involved in the regulation of early

endocytosis of VE-cadherin during vascular growth[19]. However, the putative function of CMTM4 in endothelial endocytosis and the contribution of CMTM4 to the regulation of vascular permeability have not been elucidated to date.

In the present study, we demonstrate that CMTM4 plays an important role in angiogenesis. Loss of CMTM4, as shown *in vitro* with a 3D vascular assay and *in vivo* with zebrafish larvae, results in a significant reduction of vascular sprouting. ECs can actively modulate their junctional adhesive strength by regulating the amount of bioavailable VE-cadherin on the cell membrane. A reduction in membrane-bound VE-cadherin will result in microvascular destabilization that is required for EC migration and vascular sprouting. Vascular sprouting from pre-existing vessels is mediated by VEGFA by stimulating the endocytosis of VE-cadherin[9]. Similar to CMTM3, we have shown that the angiogenic capacity of CMTM4 is associated with the regulation of cell-surface VE-cadherin. CMTM4 overexpression promotes the internalization of VE-cadherin, both at basal levels and in response to VEGFA stimulation. Vice versa, CMTM4 knockdown inhibits VE-cadherin internalization. In line with our findings, it has been shown that a reduction of VE-cadherin both *in vitro* and *in vivo* increases vascular permeability and stimulates vascular sprouting[4,26].

After these initial stages of neovessel formation, VE-cadherin is eventually required for the formation of a stable vasculature by preventing disassembly. This is demonstrated in VE-cadherin-deficient mice, who suffer from severe vascular defects, resulting in death at mid-gestation[5,6]. In line with those observations, our data indicate that CMTM4 overexpression promotes VE-cadherin connections with the actin cytoskeleton that are vital for AJs stabilization. The VE-cadherin/catenin complex interacts with actin filaments to ensure adequate junction adhesion and barrier function. Usually, the boundaries between adjacent ECs display a stable linear morphology and are regulated by circumferential actin filaments. However, endothelial AJs are highly dynamic and reorganize continuously in response to external stimuli[25]. These linear cell-cell junctions can convert into dynamic discontinuous cell-cell junctions, characterized by the appearance of stress fibers and zigzagged junctions where VE-cadherin aligns with the end of these stress fibers. Discontinuous junctions are characteristic for an activated and permeable endothelium[27]. Our data indicate that AJs are quickly restored in adCMTM4 HUVECs after a cold stimulus, showing a stable resting condition pattern with linear VE-cadherin junctions that colocalize with the circumferential actin filaments. adSHAM HUVECs appear to be at a different stage of cell-cell junction remodeling

in response to the cold stimulus, showing a zigzagged VE-cadherin pattern and stress fibers. This discontinuous pattern seen in adSHAM HUVECs will contribute to a rapid increase in endothelial permeability and subsequently a longer recovery phase. In concordance, TEER measurements reveal a fast recovery after thrombin induced endothelial junction disruption in ECs with overexpression of CMTM4 when compared to sham treated cells, whereas knock-down of CMTM4 results in a lower recovery rate. Taken together, these results are consistent with the concept that CMTM4 is responsible for a fast turn-over of VE-cadherin from the plasma membrane and back, thereby regulating the junctional adhesive strength of ECs and hence the endothelial barrier function.

The turnover of cell surface VE-cadherin involves endocytic trafficking pathways, in which VE-cadherin is transferred into the cytosol in clathrin-coated vesicles and is further sorted for recycling or lysosomal trafficking routes, among others[7]. Cargo proteins can be recycled back to the plasma membrane through two distinct recycling pathways: The Rab4-mediated rapid recycling pathway and the Rab11-mediated slow endosome pathway[28]. Rapid recycling occurs directly from the early endosomal compartment, whereas the slow recycling route involves protein cargo trafficking from either early endosomes or the trans-Golgi network through the pericentriolar recycling endosomal compartment, before returning to the cell surface[29,30].

In the present study, we demonstrate that CMTM4 strongly colocalizes with Rab4 and VE-cadherin, suggesting that CMTM4 is involved in regulating the rapid recycling of VE-cadherin back to the plasma membrane at AJs. Furthermore, overexpression of CMTM4 significantly increases Rab4+ vesicles in the cytosol, but does not increase the total protein amount of VE-cadherin, indicating that CMTM4 regulates the localization, but not the synthesis or degradation of VE-cadherin. It has been shown that overexpression of Rab4 increases the recycling of various receptors back to the cell surface. For example, Rab4 overexpression in CHO (Chinese Hamster Ovary) cells raises the number of transferrin receptors on the cell surface from 20% to 80%[31]. Recycling and activation of the β-Adrenergic receptor is also enhanced by overexpression of Rab4 in cardiac myocytes[32]. Furthermore, Rab4 activation increases the expression of VE-cadherin at the cell surface of lung microvascular endothelial cells (LMVECs), whereas Rab4 inhibition reduces VE-cadherin levels, thereby increasing vascular permeability[33]. More specifically, Rab4 activation enhances EC migration, adhesion and tube formation[34]. As reported by

these studies, silencing of Rab4a in HUVECs overexpressing CMTM4 reduces the internalization of VE-cadherin, indicating that the effect of CMTM4 is dependent on Rab4.

Besides Rab4, we show that CMTM4 overexpression also significantly enhances Rab11+ and EEA1+ vesicles in the cytosol. EEA1 colocalizes exclusively to early endosomes, from which cargo is further sorted into trafficking routes. Silencing of Rab11a in LMVECs prevents VE-cadherin recycling and expression at the plasma membrane and blocks junctional reannealing after vascular inflammation[35]. CMTM4 does not colocalize with either EEA1 or Rab11, however, our findings do imply that the slow endosome pathway is activated as well in response to CMTM4 overexpression. Sorting endosomes leaving the recycling pathways are organized in different Rab domains, created through the recruitment of specific effector proteins[28]. These recycling endosomes are composed of multiple combinations of Rab proteins, creating distinct endosome populations. Fast recycling is achieved by rapid sorting into Rab4+ domains within one endosome and recycling slows down once the cargo arrives to the pericentriolar membranes consisting mainly of Rab4+ Rab11+ domains[28,36]. After Rab4 depletion, Rab11+ vesicles fuse with the plasma membrane to release the protein cargo[36]. Rab4 is not involved in exocytosis, but acts as a regulator in the formation of recycling vesicles from early endosomes, since removal of Rab4 strongly inhibits the formation of these vesicles[37] Our findings imply that CMTM4 may function as an effector protein for creating Rab4+ domains in rapid and slow recycling endosome populations. CMTM4 may also serve as an adaptor protein for targeting and positioning VE-cadherin in these Rab4+ recycling vesicles, since our findings indicate that CMTM4 is also involved in VE-cadherin endocytosis and recycling.

Instead of recycling back to the plasma membrane, VE-cadherin can also be targeted to the lysosomal trafficking route for degradation. In our dataset, CMTM4 also localizes with Rab7, which is involved in the regulation of late endosomal trafficking to lysosomes[38]. Furthermore, overexpression of CMTM4 enhances Rab7+ vesicles in the cytosol, indicating that the lysosomal trafficking route is also activated in response to CMTM4 overexpression. In line with these statements, CMTM4 stimulates the loading of Rab4+ and Rab7+ trafficking vesicles with internalized VE-cadherin.

In a recent paper, we have shown that family-member CMTM3 regulates the endocytosis of VE-cadherin and localizes with EEA1 and Clathrin, both markers of

the early endocytic pathway, but not with Rab4[19]. This generates the perception that the CMTM-family may play an important role in the endocytosis and recycling of VE-cadherin in ECs, with each member of the gene family having their own specialized function along the various endocytic trafficking routes. All 9 CMTM-family members contain a MARVEL domain, which is characterized by a four transmembrane-helix architecture and has been associated with proteins involved in vesicle trafficking[39]. In line with this finding, overexpression of CMTM8 in tumor cell lines enhances the endocytosis of the epidermal growth factor receptor (EGFR), whereas knockdown delays endocytosis[40]. We assessed if there is a functional relationship between CMTM4 and CMTM3. HUVECs overexpressing both CMTM4 and CMTM3 trend toward internalizing more VE-cadherin compared to single CMTM overexpression, but it does not reach statistical significance. Both HUVECs with single and double CMTM overexpression do internalize significantly more VE-cadherin than sham treated cells, implying that CMTM3 and CMTM4 do not hinder each other in their function (Supplemental Figure 6A, B, and G). Normally, CMTM4 localizes both at the cytosol and cell border in ECs, whereas CMTM3 only localizes at the cytosol. This pattern does not change when silencing the other family member, implying that CMTM4 and CMTM3 do not regulate each other's localization (Supplemental Figure 6 C-F and H). Further studies are required to assess if other family members are involved in the endocytosis regulation of ECs.

In conclusion, we have identified in this study for the first time to our knowledge, a regulatory function for CMTM4 in angiogenesis. CMTM4 plays an important role in the turnover of surface VE-cadherin, thereby mediating endothelial barrier function and controlling vascular sprouting. Further studies are needed to elucidate the exact mechanism by which CMTM4 regulates the endocytosis and trafficking of EC surface proteins. Increasing our understanding of the regulators of endothelial endocytosis could help find novel therapeutic targets for the treatment of various diseases associated with vascular leakage, to block vascular growth in tumors or to overcome the problem of poor vascularization in tissue engineering.

Acknowledgements

We would like to thank the Cell Microscopy Core, Department of Cell Biology, Center for Molecular Medicine, UMC Utrecht, for excellent technical support. We also thank dr. Klazina Kooiman of the department of Biomedical Engineering

for kind permission to use the TEER apparatus. For technical support we would like to thank Esther van de Kamp, Lau Blonden, Pinar Sarikaya, Matthijs Snelders and Stephan David.

The work was supported by Netherlands Foundation for Cardiovascular Excellence [to C.C.], NWO VIDI grant [no. 91714302 to C.C.], the Erasmus MC fellowship grant [to C.C.], the RM fellowship grant of the UMC Utrecht [to C.C.] and the Netherlands Cardiovascular Research Initiative: An initiative with support of the Dutch Heart Foundation [CVON2014-11 RECONNECT to C.C. and D.D.].

Material and methods

Cell culture

Primary human umbilical vein endothelial cells (HUVECs) were purchased from Lonza and maintained in EGM2 medium (Lonza) with 100 Uml^{-1} penicillin-streptomycin (PS). Primary human brain derived vascular pericytes were purchased from ScienCell and maintained in DMEM+10%FCS with 100 Uml^{-1} PS. At passage 1, HUVECs were transduced with lentiviral GFP construct (HUVECs-GFP) and pericytes with lentiviral dsRED construct (pericytes-dsRED) and selected for puromycin (2.5µg/ml) resistance as previously described[19]. All cells were used between passages 3 and 6 and cultured at 37°C in a humidified atmosphere containing 5% CO_2.

QPCR analysis

Total RNA was isolated from cultures (single cell monolayers and co-cultured HUVECs and pericytes) using RNeasy kit (Qiagen) according to the manufacturer's instructions. The purity and concentrations of RNA were quantified by using Nanodrop (ND-1000) absorbance measurements at 260/280nm and/or capillary electrophoresis (Agilent 2100 Bioanalyser). The iScript synthesis kit (Biorad) was used for cDNA synthesis according to the manufacturer's instructions. Gene expression was determined using quantitative real-time PCR (qPCR) according to the SYBR-Green-Cycler IQ5 detection protocol (Biorad). The primer sequences are listed in Supplemental Table 1. All results were normalized for the expression of house-keeping gene *β-actin*.

Short interference RNA (siRNA)

CMTM4 or *CMTM3* knockdown in HUVECs and HUVECs-GFP was achieved by using either a mix of 4 complementary siRNA sequences or 2 sets of individual siRNA sequences directed against the mRNA of *CMTM4* or *CMTM3* (ThermoScientific). As a negative

control, cells were either untreated or transfected with a mix of 4 non-targeting siRNA sequences. The sequences are listed in Supplemental Table 2.

Adenoviral transduction

Human recombinant CMTM4 or CMTM3 adenovirus were produced using the Gateway pAd/CMV/V5-DEST vector kit and ViraPower™ Adenoviral Expression System kit, according to the manufacturer's instructions (Invitrogen). Fully sequenced Human CMTM4 or CMTM3 cDNA were obtained from OriGene and Lifesciences, respectively, cloned in a pCMV-SPORT6 vector. To amplify the CMTM4 gene from the obtained clone and simultaneously convert it with *att*B sites, a PCR was conducted with full length *att*B-CMTM4 specific primers: forward oligo's 5`- GGGGACAAGTTTGTACAAAAAAG CAGGCTTCACCATGCGGAGCGGCGAGGAGCTGGACGG-3` and reverse oligo`s 5`- GGGGACCACTTTGTACAAGAAAGCTGGGTTTCACGTGTCCAGGCGCTGGATCT CAGG-3`. The full length attB-CMTM4 amplicons was then cloned into a pDONR™ 221 vector to create an entry clone, according to BP Clonase™ II protocol. Full-length cDNAs of CMTM3 with *att*B-site was amplified by PCR using specific forward oligos 5`- GGGG ACAAGTTTGTACAAAAAAGCAGGCTTCACCATGTGGCCCCCAGACCCCGACC-3` and reverse oligo`s 5`- GGGGACCACTTTGTACAAGAAAGCTGGGTTTCAGTCA GAGTCCGAGTCGGAATTCTC-3`. Moreover a HIS tag was placed at the C-terminal region of CMTM3 (CMTM3-HA) using the RV primer 5`- GGGGACCACTTTGTACAAGAAAGCT GGGTGGTCAGAGTCCGAGTCGGAATTCTC-3`. Amplicons of CMTM3 and CMTM3-HA were cloned into a pDONRTM 221 vector via BP ClonaseTM II enzyme mix to create an entry clone. DNA sequencing validated the obtained CMTM4 or CMTM3 sequence. Using LR-reaction II (Invitrogen), the CMTM4 or CMTM3 reading frame cassettes were cloned into pAd/CMV/V5-DEST (Invitrogen) expression vectors according to the manufacturer's protocol. After verification by DNA sequencing, the pAd/CMV/V5-DEST plasmids were linearized by *Pac1* restriction and transfected with Lipofectamine 2000 (Invitrogen) into 293A cells. When 80% of the infected cells formed crude viral vesicles, the cells were harvested, followed by three cycles of freeze/thawing to get crude viral lysate (CVL), and the virus was purified using cesium chloride gradient.

Subcellular fractioning and protein extraction

To separate cytoplasmic proteins from the membrane-bound proteins, i.e. the soluble and insoluble fraction, respectively, HUVECs received a PBS wash twice and were harvested in lysis buffer (140 mM NaCl, 10 mM Tris [pH 7.6], 1 mM EDTA, 1% Triton X-100, 0.05% SDS, 1X protease inhibitor cocktail, 1 mM PMSF) 48 hours post-transfection. The lysates

were incubated on ice for 20 minutes and were centrifuged at 13,000 g for 12 minutes to separate the soluble from the insoluble fraction. The pellet was then solubilized in lysis buffer with 2% SDS. Both fractions were subjected to SDS-PAGE and immunoblotting.

Western blot

Protein concentration was determined by the Bradford method (Pierce BCA Protein Assay kit). Equal amounts of sample were loaded on a sodium dodecyl sulfate-polyacrylamide gel electrophoresis (SDS-PAGE) and transferred onto a nitrocellulose membrane (Pierce) at 4°C overnight. Membranes were blocked and probed with primary antibodies according to the manufacturer's instructions (Supplemental Table 3). Protein bands were visualized with Li-Cor secondary antibodies and detection system (Westburg) according to the manufacturer`s instructions. The detected protein expressions were normalized with β-actin.

Collagen based 3D co-culture

HUVEC-GFP and pericyte-dsRed were co-cultured at a 5:1 ratio in a 3D bovine collagen type 1 (2 mg/ml) environment (Gibco), supplemented with EBM-2 medium (Lonza), ascorbic acid, fibroblast growth factor, 2% FCS, SCF-1, SDF-1α and IL-3 (i.e. co-culture medium), as previously described[41]. Images were taken 2 days after seeding to assess the sprouting capacities of ECs and at day 5, when lumenized micro-capillary structures are formed. Images were taken with fluorescence microscopy with a 2x objective. Images were analyzed based on the number of junctions, the number of tubules and the tubule length using AngioSys 2.0 software.

VE-cadherin internalization assay and immunofluorescence

The internalization assay was performed at 48 hours post-transfection as previously described[9]. Briefly, HUVECs were grown on coverslips to confluence before labeling the cell-surface exposed VE-cadherin by incubation with mouse anti-human VE-cadherin (Supp. Table 3) at 4°C for 1 hour. Movement of labeled VE-cadherin was monitored by placing the cells at 37°C for 1 hour, in basal medium with or without VEGF (50ng/ml; Preprotech), after which the cells were either washed with PBS (PBS supplemented with 1.8 mM CaCl2 and 1 mM MgCl2) or with a mildly acidic buffer (2mM PBS-glycine [pH 2.0], 15 minutes) to remove membrane bound antibodies and revealing the internalized labeled VE-cadherin. Cells were fixed with 4% paraformaldehyde for 30 min, followed by a blocking and permeabilization step for 30 min in PBS with 1% BSA and 0.5% Triton-X. Secondary antibody (Supplemental Table 3) incubation was performed for 1 hour at room

temperature, followed by a 30 minutes incubation step to label cytoskeletal F-actin with rhodamine phalloidin (Supplemental Table 3). For labeling of Rab proteins (Supp. Table 3), an extra primary antibody step was performed after fixation instead of labeling cytoskeletal F-actin. DAPI was used as a nuclear counterstain. Images of fluorescent-labeled markers were obtained with a Leica TCS SP8 X microscope and a 63x oil immersion objective lens. 3D images were obtained by scanning multiple XY planes in the Z direction with a depth of ±10 µm. Serial pictures along the Z-axis were combined to create a stacked XY image. The total internalized VE-cadherin area was determined by using ImageJ 1.47v.

Morpholino injection in developing zebrafish larvae

Zebrafish (Danio rerio) were maintained under standard laboratory conditions. Morpholinos (MO) against the zebrafish orthologue of *CMTM4* were obtained from Gene Tools (Philomath, USA) and suspended in Danieau buffer (58mM NaCl, 0.7mM KCl, 0.4mM MgSO4, 0.6 mM Ca(NO3)2, 5.0 mM HEPES pH 7.6) containing 0.2% phenol red. Different doses of the MO were injected into single-cell stage zebrafish embryos as previously described[42]. The sequences are listed in Supplemental Table 4.

Flow cytometry

CMTM4 silenced HUVECs were seeded at a density of $50x10^3$ cells/well in co-culture medium. After 24, 48, and 72 hours cells were harvested for proliferation and apoptosis analysis. Each harvested sample was stained with Propidium Iodide (PI) and Annexin V (BD Pharmingen) according to the manufacturer's protocol and analyzed by flowcytometry (BD Facs Canto). Cells were counted for 2 minutes at medium speed to determine the average cell amount. Cell cycle analysis was conducted after the cells were cultured for 48 hours at 37°C in 5% CO2 and fixed overnight in 70% ethanol at 4°C. Cells were washed with ice-cold PBS and were stained with PI and treated with 0.5 mg/ml RNase for 30 minutes at 37°C before analysis by flow cytometry.

Migration assay

HUVECs were seeded at a density of $75x10^3$ cells/well in a 24-well plate and after 24 hours. EC migration was assessed 24 hours post-transfection by scratching the HUVEC layer using a 200 µl pipette tip. Loose cells were removed by a PBS wash. Images were taken at t=0, t=4 and t=8 hours, after which the scratch area reduction was determined using Adobe Photoshop CS6.

Intracellular immunostaining

HUVECs were seeded at a density of $10x10^4$ cells/well 24 hours prior to transfection. Cells were fixed 48 hours post-transfection with 4% paraformaldehyde for 30 minutes, followed by a blocking and permeabilization step for 30 minutes in PBS with 1% BSA and 0.5% Triton-X. This was followed by incubation with a primary and secondary antibody (Supp. Table 3) at room temperature for 1.5 and 1 hour, respectively. Cytoskeletal F-actin was labeled with rhodamine phalloidin and DAPI was used as a nuclear counterstaining. Images of fluorescent-labeled markers were obtained with a Leica TCS SP8 X microscope and a 63x oil immersion objective lens. For quantification of the total area, 3D images were obtained by scanning multiple XY planes in the Z direction with a depth of ± 10 µm. Serial pictures along the Z-axis were combined to create a stacked XY image that was further analyzed using ImageJ 1.47v.

Transendothelial resistance measurements

HUVECs were transfected with CMTM4 siRNA or adenovirus 24 hours prior to seeding on a 0.1% gelatin permeable filter insert (0.4 µm pore, Falcon). Before the experiment, the resistance (R_{blank}) was measured by placing unseeded inserts in an Endohm-SNAP chamber filled with 5 ml of EGM-2 medium (World Precision Instruments, Berlin). The chamber was coupled to an EVOMX resistance meter (World Precision Instruments, Berlin). The trans-endothelial electrical resistance (TEER) was measured daily to monitor resistance buildup during growth towards full confluence. At day 2, confluent monolayers were treated with 1U/ml thrombin for 20 minutes during which the TEER was measured every 5 minutes. After 20 minutes, the thrombin solution was washed away and replaced with normal medium. TEER was measured every 15 minutes during the restoration phase for 2 hours.

Statistical analysis

The statistical analyses were performed using Graphpad Prism version 7.02. To test if values came from a Gaussian distribution, the D'Agostino-Pearson omnibus or Shapiro-Wilk normality test were used. The unpaired t-test and the ordinary one-way ANOVA test were used if the values were normally distributed. In case the values did not pass the normality test, either the Mann-Whitney test or Kruskal-Wallis were used as non-parametric tests. $P \leq 0.05$ was accepted as statistically significant. Values are shown as mean ± SEM.

References

1. Carmeliet P. Angiogenesis in health and disease. Nat Med. 2003;9(6):653-660.
2. Wallez Y, Huber P. Endothelial adherens and tight junctions in vascular homeostasis, inflammation and angiogenesis. Biochim Biophys Acta. 2008;1778(3):794-809.
3. Vestweber D. VE-cadherin: the major endothelial adhesion molecule controlling cellular junctions and blood vessel formation. Arterioscler Thromb Vasc Biol. 2008;28(2):223-232.
4. Corada M, Liao F, Lindgren M, et al. Monoclonal antibodies directed to different regions of vascular endothelial cadherin extracellular domain affect adhesion and clustering of the protein and modulate endothelial permeability. Blood. 2001;97(6):1679-1684.
5. Carmeliet P, Lampugnani MG, Moons L, et al. Targeted deficiency or cytosolic truncation of the VE-cadherin gene in mice impairs VEGF-mediated endothelial survival and angiogenesis. Cell. 1999;98(2):147-157.
6. Gory-Faure S, Prandini MH, Pointu H, et al. Role of vascular endothelial-cadherin in vascular morphogenesis. Development. 1999;126(10):2093-2102.
7. Xiao K, Garner J, Buckley KM, et al. p120-Catenin regulates clathrin-dependent endocytosis of VE-cadherin. Mol Biol Cell. 2005;16(11):5141-5151.
8. Stenmark H. Rab GTPases as coordinators of vesicle traffic. Nat Rev Mol Cell Biol. 2009;10(8):513-525.
9. Gavard J, Gutkind JS. VEGF controls endothelial-cell permeability by promoting the beta-arrestin-dependent endocytosis of VE-cadherin. Nat Cell Biol. 2006;8(11):1223-1234.
10. Han W, Ding P, Xu M, et al. Identification of eight genes encoding chemokine-like factor superfamily members 1-8 (CKLFSF1-8) by in silico cloning and experimental validation. Genomics. 2003;81(6):609-617.
11. Li Z, Xie J, Wu J, et al. CMTM3 inhibits human testicular cancer cell growth through inducing cell-cycle arrest and apoptosis. PLoS One. 2014;9(2):e88965.
12. Wang Y, Li J, Cui Y, et al. CMTM3, located at the critical tumor suppressor locus 16q22.1, is silenced by CpG methylation in carcinomas and inhibits tumor cell growth through inducing apoptosis. Cancer Res. 2009;69(12):5194-5201.
13. Hu F, Yuan W, Wang X, et al. CMTM3 is reduced in prostate cancer and inhibits migration, invasion and growth of LNCaP cells. Clin Transl Oncol. 2015;17(8):632-639.
14. Li T, Cheng Y, Wang P, et al. CMTM4 is frequently downregulated and functions as a tumour suppressor in clear cell renal cell carcinoma. J Exp Clin Cancer Res. 2015;34:122.
15. Plate M, Li T, Wang Y, et al. Identification and characterization of CMTM4, a novel gene with inhibitory effects on HeLa cell growth through Inducing G2/M phase accumulation. Mol Cells. 2010;29(4):355-361.
16. Xiao Y, Yuan Y, Zhang Y, et al. CMTM5 is reduced in prostate cancer and inhibits cancer cell growth in vitro and in vivo. Clin Transl Oncol. 2015;17(6):431-437.
17. Li H, Li J, Su Y, et al. A novel 3p22.3 gene CMTM7 represses oncogenic EGFR signaling and inhibits cancer cell growth. Oncogene. 2014;33(24):3109-3118.
18. Gao D, Hu H, Wang Y, et al. CMTM8 inhibits the carcinogenesis and progression of bladder cancer. Oncol Rep. 2015;34(6):2853-2863.
19. Chrifi I, Louzao-Martinez L, Brandt M, et al. CMTM3 (CKLF-Like Marvel Transmembrane Domain 3) Mediates Angiogenesis by Regulating Cell Surface Availability of VE-Cadherin in Endothelial Adherens Junctions. Arterioscler Thromb Vasc Biol. 2017;37(6):1098-1114.
20. Stratman AN, Malotte KM, Mahan RD, et al. Pericyte recruitment during vasculogenic tube assembly stimulates endothelial basement membrane matrix formation. Blood. 2009;114(24):5091-5101.
21. Jorgensen CB. Nature of moulting control in amphibians: effects of cortisol implants in toads Bufo bufo. Gen Comp Endocrinol. 1988;71(1):29-35.

22. Zhou Z, Chrifi I, Xu Y, et al. Uridine adenosine tetraphosphate acts as a proangiogenic factor in vitro through purinergic P2Y receptors. Am J Physiol Heart Circ Physiol. 2016;311(1):H299-309.
23. Zhu C, Chrifi I, Mustafa D, et al. CECR1-mediated cross talk between macrophages and vascular mural cells promotes neovascularization in malignant glioma. Oncogene. 2017;36(38):5356-5368.
24. Cao J, Ehling M, Marz S, et al. Polarized actin and VE-cadherin dynamics regulate junctional remodelling and cell migration during sprouting angiogenesis. Nat Commun. 2017;8(1):2210.
25. Abu Taha A, Schnittler HJ. Dynamics between actin and the VE-cadherin/catenin complex: novel aspects of the ARP2/3 complex in regulation of endothelial junctions. Cell Adh Migr. 2014;8(2):125-135.
26. Abraham S, Yeo M, Montero-Balaguer M, et al. VE-Cadherin-mediated cell-cell interaction suppresses sprouting via signaling to MLC2 phosphorylation. Curr Biol. 2009;19(8):668-674.
27. Millan J, Cain RJ, Reglero-Real N, et al. Adherens junctions connect stress fibres between adjacent endothelial cells. BMC Biol. 2010;8:11.
28. Sonnichsen B, De Renzis S, Nielsen E, et al. Distinct membrane domains on endosomes in the recycling pathway visualized by multicolor imaging of Rab4, Rab5, and Rab11. J Cell Biol. 2000;149(4):901-914.
29. Van Der Sluijs P, Hull M, Zahraoui A, et al. The small GTP-binding protein rab4 is associated with early endosomes. Proc Natl Acad Sci U S A. 1991;88(14):6313-6317.
30. Ullrich O, Reinsch S, Urbe S, et al. Rab11 regulates recycling through the pericentriolar recycling endosome. J Cell Biol. 1996;135(4):913-924.
31. van der Sluijs P, Hull M, Webster P, et al. The small GTP-binding protein rab4 controls an early sorting event on the endocytic pathway. Cell. 1992;70(5):729-740.
32. Filipeanu CM, Zhou F, Lam ML, et al. Enhancement of the recycling and activation of beta-adrenergic receptor by Rab4 GTPase in cardiac myocytes. J Biol Chem. 2006;281(16):11097-11103.
33. Chichger H, Braza J, Duong H, et al. Select Rab GTPases Regulate the Pulmonary Endothelium via Endosomal Trafficking of Vascular Endothelial-Cadherin. Am J Respir Cell Mol Biol. 2016;54(6):769-781.
34. Chichger H, Braza J, Duong H, et al. Neovascularization in the pulmonary endothelium is regulated by the endosome: Rab4-mediated trafficking and p18-dependent signaling. Am J Physiol Lung Cell Mol Physiol. 2015;309(7):L700-709.
35. Yan Z, Wang ZG, Segev N, et al. Rab11a Mediates Vascular Endothelial-Cadherin Recycling and Controls Endothelial Barrier Function. Arterioscler Thromb Vasc Biol. 2016;36(2):339-349.
36. Ward ES, Martinez C, Vaccaro C, et al. From sorting endosomes to exocytosis: association of Rab4 and Rab11 GTPases with the Fc receptor, FcRn, during recycling. Mol Biol Cell. 2005;16(4):2028-2038.
37. Pagano A, Crottet P, Prescianotto-Baschong C, et al. In vitro formation of recycling vesicles from endosomes requires adaptor protein-1/clathrin and is regulated by rab4 and the connector rabaptin-5. Mol Biol Cell. 2004;15(11):4990-5000.
38. Bucci C, Thomsen P, Nicoziani P, et al. Rab7: a key to lysosome biogenesis. Mol Biol Cell. 2000;11(2):467-480.
39. Sanchez-Pulido L, Martin-Belmonte F, Valencia A, et al. MARVEL: a conserved domain involved in membrane apposition events. Trends Biochem Sci. 2002;27(12):599-601.
40. Jin C, Ding P, Wang Y, et al. Regulation of EGF receptor signaling by the MARVEL domain-containing protein CKLFSF8. FEBS Lett. 2005;579(28):6375-6382.
41. Zhu C, Mustafa D, Zheng PP, et al. Activation of CECR1 in M2-like TAMs promotes paracrine stimulation-mediated glial tumor progression. Neuro Oncol. 2017;19(5):648-659.
42. Nasevicius A, Ekker SC. Effective targeted gene 'knockdown' in zebrafish. Nat Genet.

2000;26(2):216-220.

Supplemental Figures

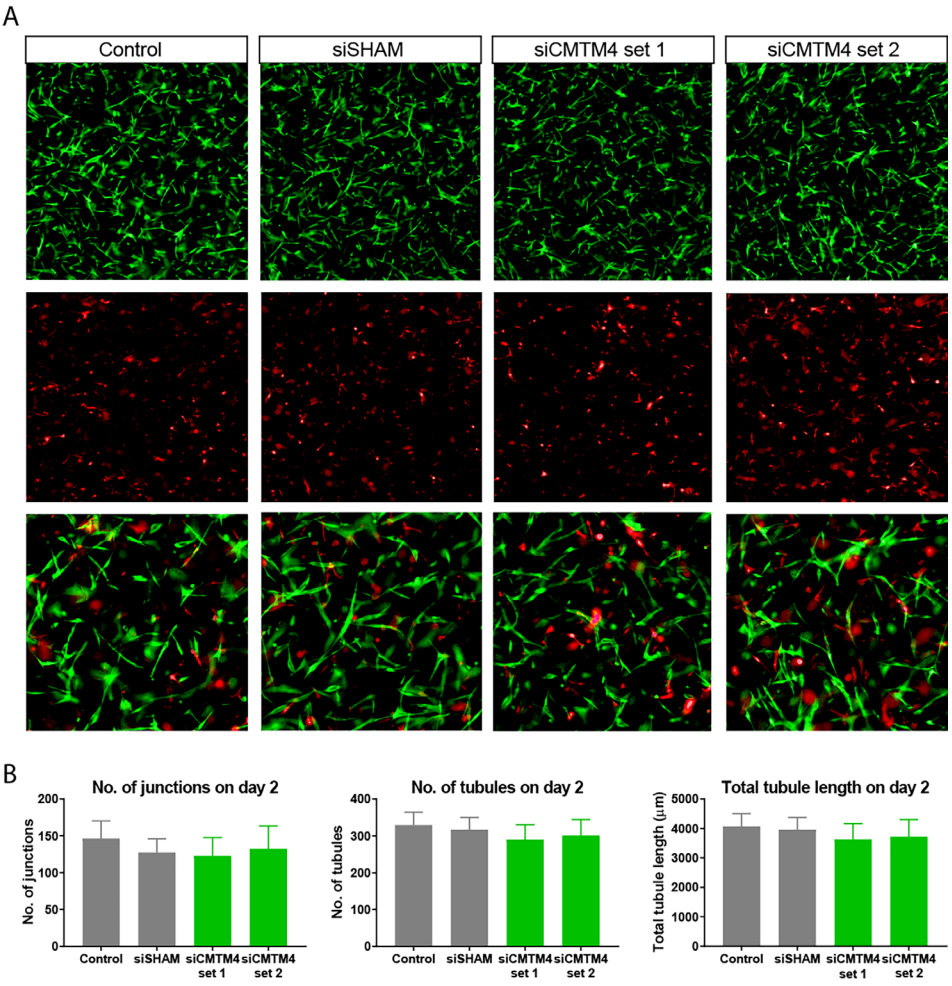

Supplemental Figure 1. CMTM4 silencing in pericytes does not affect vascular growth *in vitro*. (A) Representative immunofluorescent images taken at 2x magnification (upper rows) and zoomed-in images (lower row) of GFP-labelled HUVECs (green) and dsRED-labelled pericytes (red) cultured for 2 days in a 3D collagen matrix, in which the dsRED labeled pericytes were transfected with either *CMTM4*-targeting siRNA (siCMTM4 set 1 or set 2), non-targeting siRNA (siSHAM) or not transfected (control). (B) Quantification of the number of junctions, number of tubules and total tubule length of siCMTM4 set 1 and set 2, siSHAM and control HUVECs at day 2 of co-culture. N=4 co-cultures. Shown is mean ± SEM. (C) Representative immunofluorescent images taken at 20x magnification (upper rows) and zoomed-in images (lower row) of GFP-labelled HUVECs (green) and dsRED-labelled pericytes (red) cultured for 5 days in a 3D collagen matrix, in which the dsRED labeled pericytes were transfected with either *CMTM4*-targeting siRNA (siCMTM4 set 1 or set

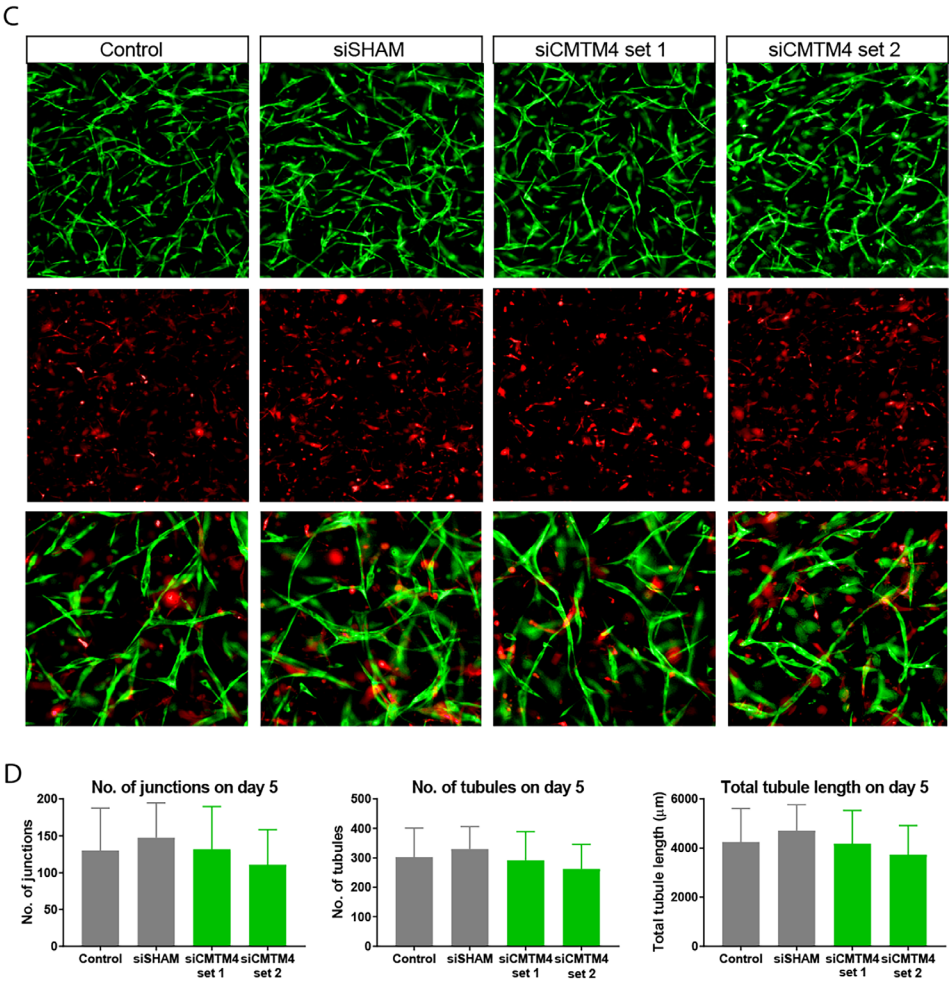

(Supplemental Figure 1 continued) 2), non-targeting siRNA (siSHAM) or not transfected (control). (D) Quantification of the number of junctions, number of tubules and total tubule length of siCMTM4 set 1 and set 2, siSHAM and control HUVECs at day 5 of co-culture. N=4 co-cultures. Values are mean ± SEM.

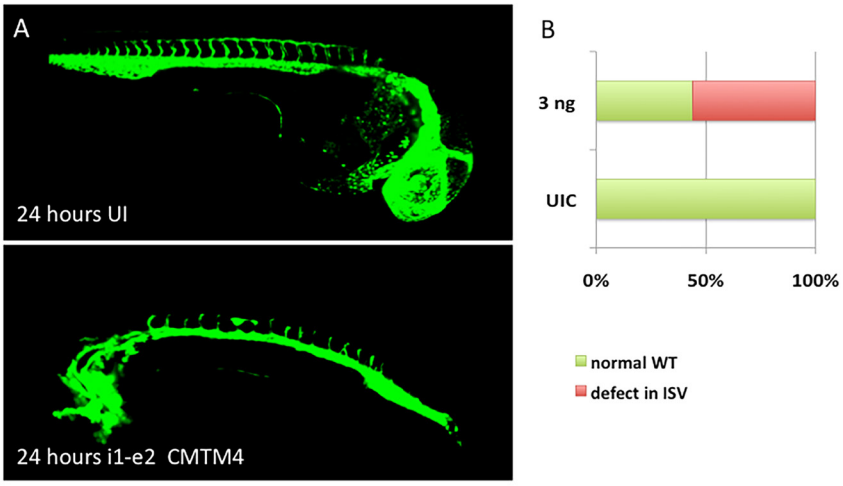

Supplemental Figure 2. Silencing of *CMTM4* by morpholino targeting in developing zebrafish larvae triggers defects in intersomitic vessels. (A) Tg(fli1:eGFP)^{y1} larvae at 24 hours post fertilization. Defects in intersomitic vessel formation were detected in the trunk region in larvae injected with morpholinos targeting the splice site of i1-e2 of *CMTM4* (indicated as i1-e2 *CMTM4*) (lower image) compared to uninjected (UI) controls (upper image). Vasculature is visualized with eGFP (green). 20x magnification (B) Quantification of intersomitic vessel defect phenotype versus wildtype phenotype in i1-e2 injected group versus UI controls (UIC). Data represents percentage of counted larvae (~100 counted per group).

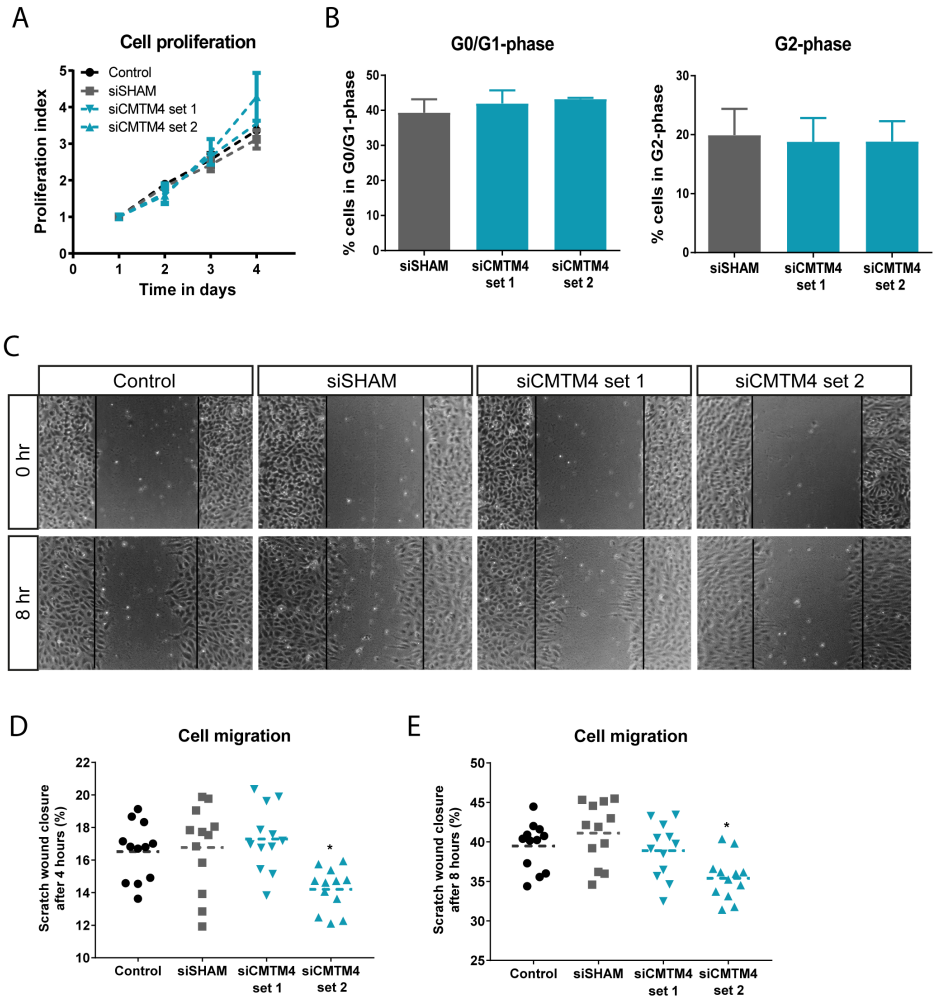

Supplemental Figure 3. CMTM4 silencing does not affect endothelial cell proliferation, but has a small effect on cell migration. (A) The number of cells counted at day of seeding (day 1), and at day 2, 3 and 4 of cell proliferation of HUVECs transfected with either *CMTM4*-targeting siRNA (siCMTM4 set 1 or set 2), non-targeting siRNA (siSHAM) or not transfected (control). N=4. Shown is mean ± SEM. (B) Bargraphs showing the % of G0/G1 and G2 phase cells at day 2 after transfection of siCMTM4 (set 1 and set 2) HUVECs versus siSHAM cells. N≥3. Shown is mean ± SEM. (C) Representative brightfield microscope images (40x magnification) of a scratch migration assay after 8 hours of migration of siCMTM4 HUVECs (set 1 and set 2) compared with siSHAM and non-treated controls. Bargraphs of the quantified results of the scratch migration assay showing the % area within the scratched region covered by siCMTM4 (set 1 and set 2) HUVECs compared with siSHAM and non-treated controls after (D) 4 hours and (E) 8 hours. N=2, 6 wells each. Shown is mean.

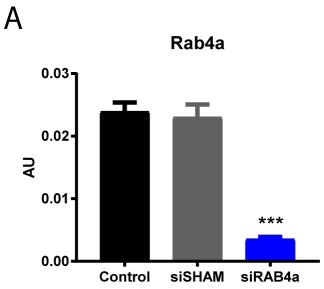

Supplemental Figure 4. *Rab4a*-targeting siRNA induces significant silencing of *Rab4a* expression. (A) Gene expression levels of *Rab4a* in HUVECs transfected with *Rab4a*-targeting siRNA (siRAB4a), non-targeting siRNA (siSHAM) and in non-transfected HUVECs (control). Gene expression levels were normalized to *β-actin* (AU). N=4 qPCRs. Shown is mean ± SEM; ***P<0.001 compared to both control and siSHAM.

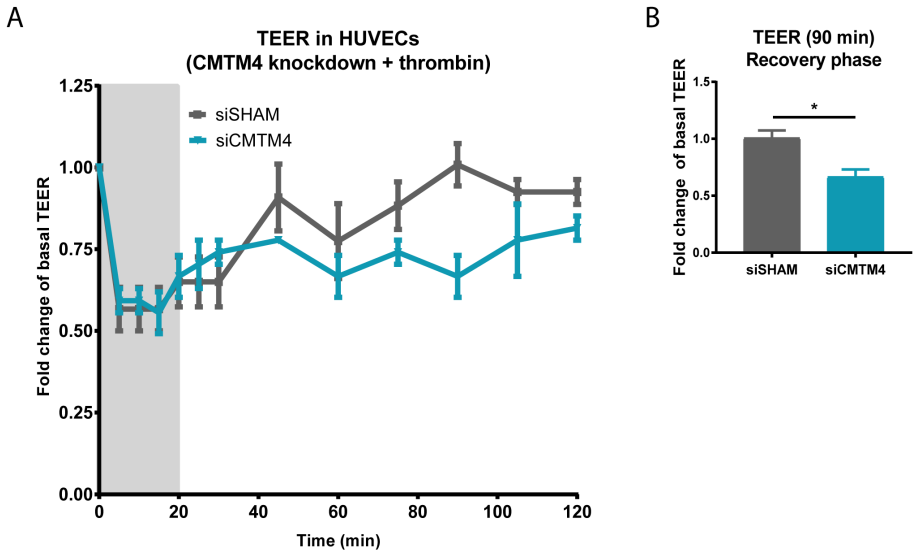

Supplemental Figure 5. CMTM4 promotes restoration of endothelial electric resistance in thrombin-induced response. (A) Thrombin response (presented in fold change compared with basal resistance of nontransfected group: Y-axes) of confluent HUVECs transfected with either *CMTM4*-targeting siRNA or non-targeting siRNA (siSHAM), during (0–20 minutes) and after (20–120 minutes) thrombin (1 U/mL) stimulation. At 0 minutes, thrombin was added and at 20 minutes thrombin was removed (gray area). N=3 per time series. Shown is mean ± SEM. (B) Increase in resistance during recovery phase at 90 minutes in siSHAM and siCMTM4 groups. N=3. Shown is mean ± SEM; *P≤0.05 versus siSHAM.

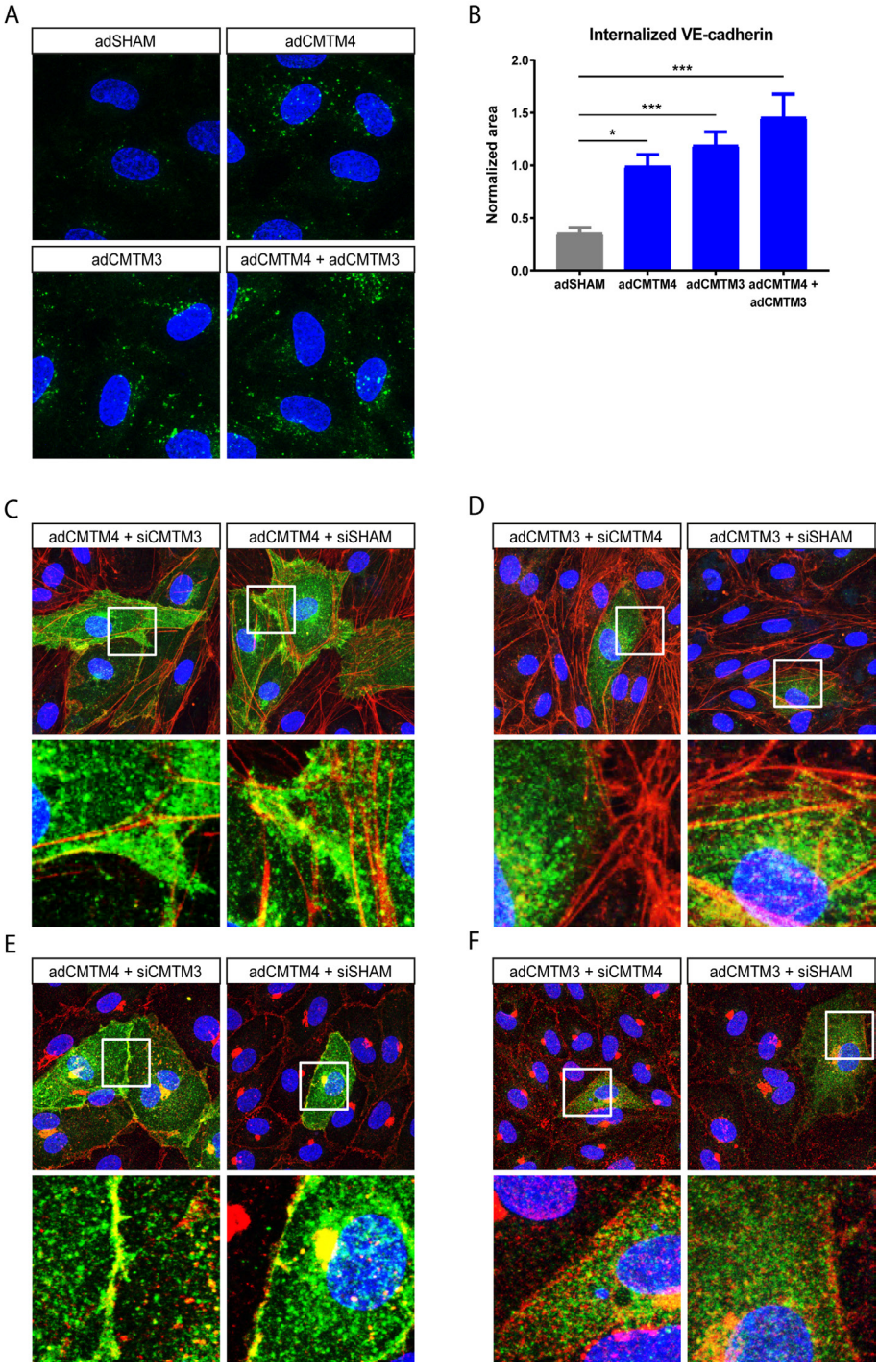
A
adSHAM
adCMTM4
adCMTM3
adCMTM4 + adCMTM3
B
Internalized VE-cadherin
Normalized area
2.0
1.5
1.0
0.5
0.0
***
***
*
adSHAM
adCMTM4
adCMTM3
adCMTM4 + adCMTM3
C
adCMTM4 + siCMTM3
adCMTM4 + siSHAM
D
adCMTM3 + siCMTM4
adCMTM3 + siSHAM
E
adCMTM4 + siCMTM3
adCMTM4 + siSHAM
F
adCMTM3 + siCMTM4
adCMTM3 + siSHAM

G

	CMTM3 (AU)		CMTM4 (AU)	
adSHAM	0.018972	0.019645	0.004082	0.004148
adCMTM4	0.021615	0.023672	0.317889	0.304525
adCMTM3	1.905051	1.902983	0.004664	0.004623
adCMTM4 + adCMTM3	1.007529	1.072234	0.186527	0.182948

H

	CMTM3 (AU)		CMTM4 (AU)	
adCMTM4 + siCMTM3	0.001536	0.001832	0.068990	0.093618
adCMTM4 + siSHAM	0.012848	0.018171	0.073897	0.091932
adCMTM3 + siCMTM4	1.383564	2.560715	0.000740	0.000494
adCMTM3 + siSHAM	1.194415	1.531579	0.004066	0.003358

Supplemental Figure 6. CMTM4 and CMTM3 do not interfere or enhance each other's function and localization. (A) Representative zoomed-in confocal micrographs (630x magnification) of confluent HUVECs transfected with sham virus containing an empty expression vector (adSHAM), with adenovirus containing either an expression vector for CMTM4 cDNA (adCMTM4) (VPC20) or CMTM3 (adCMTM3) (VPC20) and adCMTM4 + adCMTM4 double overexpression (VPC10 each) HUVECs, labeled with VE-cadherin antibodies at 4°C and followed by 37°C incubation for 1 hour to track VE-cadherin movement. Surface bound VE-cadherin antibodies were removed by an acid-wash before proceeding with immunostaining for visualization of internalized VE-cadherin (green). (B) Quantification of internalized VE-cadherin area per cell in adSHAM, adCMTM4 (VPC20), adCMTM3 (VPC20) and adCMTM4 + adCMTM4 double overexpression (VPC10 each) HUVECs. N=2, 5 Z-stacks each. Shown is mean ± SEM; *P<0.05, ***P0.001 versus adSHAM. (C) Representative 630x magnification (upper row) and zoomed-in (lower row) immunofluorescence images of adCMTM4 + siCMTM3 and adCMTM4 + siSHAM HUVECs immunostained for CMTM4 (green) and F-actin (red) (VPC10). (D) Representative 630x magnification (upper row) and zoomed-in (lower row) immunofluorescence images of adCMTM3 + siCMTM4 and adCMTM3 + siSHAM HUVECs immunostained for CMTM3 (green) and F-actin (red) (VPC10). (E) Representative 630x magnification (upper row) and zoomed-in (lower row) immunofluorescence images of adCMTM4 + siCMTM3 and adCMTM4 + siSHAM HUVECs immunostained for CMTM4 (green) and VE-cadherin (red) (VPC10). (F) Representative 630x magnification (upper row) and zoomed-in (lower row) immunofluorescence images of adCMTM3 + siCMTM4 and adCMTM3 + siSHAM HUVECs immunostained for CMTM3 (green) and VE-cadherin (red) (VPC10). (G) Gene expression levels of *CMTM3* and *CMTM4* in adSHAM, adCMTM4, adCMTM3 and adCMTM4 + adCMTM4 double overexpression HUVECs. Gene expression levels were normalized to *β-actin* (AU). N=2 qPCRs; VPC20. (H) Gene expression levels of *CMTM3* and *CMTM4* in adCMTM4 + siCMTM3, adCMTM4 + siSH1AM, adCMTM3 + siCMTM4 and adCMTM3 + siSHAM HUVECs. Gene expression levels were normalized to *β-actin* (AU). N=2 qPCRs; VPC10.

Supplemental Tables

Supplemental Table 1. Primer sequences.

Gene	Forward primer sequence	Reverse primer sequence	Product size
CKLF1	ccggaagcttctgttcaatc	tcatgcacaggctttttctg	54bp
CMTM1	ctccggttgtttcaagttcc	ggggaggtagccaacagc	168bp
CMTM2	cgtggtctttgctgtgagaa	gggtccttttttcctttcctg	181bp
CMTM3	accatcgtgtttgcaactga	gcagagtccccttgtttgag	74bp
CMTM4	ctggcgtcttgctgattatg	atttctgctccggctctatg	160bp
CMTM5	tctaagcaaggggagggatt	aggcacttcgagaaacctga	200bp
CMTM6	tcatatgccaacaggggaat	tgcaccttggttgttgatgt	223bp
CMTM7	acgcctcacttcaggaaaga	tgttttctgccttcctgctt	208bp
CMTM8	ttggctgggtcatgtttgta	cccagctgttgaagttgtga	219bp
β-actin	tccctggagaagagctacga	agcactgtgttggcgtacag	194bp

Supplemental Table 2. siRNA sequences.

Target gene	Target sequence
Non-targeting SMARTpool	UGGUUUACAUGUCGACUAA
	AGGUUUACAUGUUGUGUGA
	UGGUUUACAUGUUUUCUGA
	UGGUUUACAUGUUUUCCUA
CMTM4 siGENOME set 1	AGAAAUUGCUGCCGUGAUA
CMTM4 siGENOME set 2	ACACUGGACUCAGCGUUU
CMTM4 SMARTpool	CAAUCGUACUGGCUGCUUU
	ACUGGCGUCUUGCUGAUUA
	AGAAAUUGCUGCCGUGAUA
	AAACGUAACAGUAAGGAAA
CMTM3 SMARTpool	GCCCUCAUCUACUUUGCUA
	GCAACUGAUUUCUACCUGA
	CAAGACAGAAGAAGAGAGAAU
	UUAACGACGUGGCCAAAUU
Rab4a SMARTpool	GCUCAGGAGUGUGGUUGUU
	UACAAUGCGCUUACUAAUU
	GAUAAUAAAUGUUGGUGGU
	GAACGAUUCAGGUCCGUGA

Supplemental Table 3. Antibodies.

Antibody	Company
Rabbit pAb anti-CMTM4	Sigma Aldrich
Rabbit mAb anti-CMTM4	Santa cruz
Mouse mAb anti-CMTM4	Abcam
Rabbit pAb anti-CMTM3	Sigma-aldrich
Rabbit anti-β-actin	Cell Signaling Technology
Goat anti-β-actin	Abcam
Rhodamin phalloidin	Invitrogen
Rabbit mAb VE-cadherin (D87F2) XP	Cell Signaling Technology
Rabbit (DA1E) mAb IgG XP Isotype control	Cell Signaling Technology
Mouse mAb anti-Rab7	Sigma-aldrich
Rabbit pAb anti-Rab7	Sigma-aldrich
Mouse mAb anti-Rab4 (clone 4E11)	LsBio
Rabbit pAb anti-Rab4	Abcam
Mouse mAb anti-Rab11 (clone 47)	BD Transduction Laboratories
Mouse mAb anti-clathrin Heavy Chain Clone 23	BD Transduction Laboratories
Mouse mAb anti-EEA1 (early endosome antigen 1)	BD Transduction Laboratories
Mouse anti-VE-cadherin	Sigma-aldrich
Alexa Fluor 488 goat anti mouse IgG	Invitrogen
Alexa Fluor 488 goat anti rabbit IgG	Invitrogen
Alexa Fluor 568 donkey anti rabbit	Invitrogen
Alexa Fluor 594 goat anti rabbit IgG	Invitrogen
IRDye 800CW donkey anti-mouse	Li-cor Biosciences
IRDye 800CW goat anti-rabbit	Li-cor Biosciences
IRDye 800CW donkey anti-goat	Li-cor Biosciences
IRDye 680RD donkey anti-goat	Li-cor Biosciences
IRDye 680RD donkey anti-rabbit	Li-cor Biosciences
IRDye 680RD goat anti-mouse	Li-cor Biosciences

Supplemental Table 4. CMTM4 morpholino sequences.

Name	Antisense morpholino sequence
CMTM4 i1-e2	CCAGAACCTGAGAAGAAGGAGGAGA
CMTM4 i2-e3	AAATCCTGCAAATGCGAGGAAGAGA

Angiogenesis – Chapter 7

Chromatin conformation links distal target genes to chronic kidney disease loci

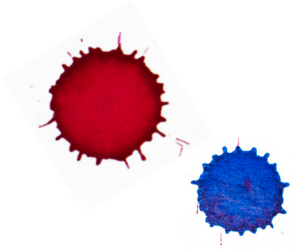

M.M. Brandt*, C.A. Meddens*, L. Louzao Martinez, N.A.M. van den Dungen, N.R. Lansu, E.E. Nieuwenhuis, D.J. Duncker, M.C. Verhaar, J.A. Joles, M. Mokry, C. Cheng.

(2018) Journal of the American Society of Nephrology: JASN, 29(2):462-476

* indicates shared first authorship.

Abstract

Genome-wide association studies (GWASs) have identified many genetic risk factors for chronic kidney disease (CKD). However, linking common variants to genes that are causal for CKD etiology remains challenging. By adapting self-transcribing active regulatory region sequencing, we evaluated the effect of genetic variation on DNA regulatory elements (DREs). Variants in linkage with the CKD-associated single-nucleotide polymorphism rs11959928 were shown to affect DRE function, illustrating that genes regulated by DREs colocalizing with CKD-associated variation can be dysregulated and therefore, considered as CKD candidate genes. To identify target genes of these DREs, we used circular chromosome conformation capture (4C) sequencing on glomerular endothelial cells and renal tubular epithelial cells. Our 4C analyses revealed interactions of CKD-associated susceptibility regions with the transcriptional start sites of 304 target genes. Overlap with multiple databases confirmed that many of these target genes are involved in kidney homeostasis. Expression quantitative trait loci analysis revealed that mRNA levels of many target genes are genotype dependent. Pathway analyses showed that target genes were enriched in processes crucial for renal function, identifying dysregulated geranylgeranyl diphosphate biosynthesis as a potential disease mechanism. Overall, our data annotated multiple genes to previously reported CKD-associated single-nucleotide polymorphisms and provided evidence for interaction between these loci and target genes. This pipeline provides a novel technique for hypothesis generation and complements classic GWAS interpretation. Future studies are required to specify the implications of our dataset and further reveal the complex roles that common variants have in complex diseases, such as CKD.

Introduction

Chronic kidney disease (CKD) is a condition marked by loss of kidney function, which can lead to end-stage renal disease (ESRD) and is associated with a dramatic increase in cardiovascular disease–related morbidity and mortality[1]. On the basis of the latest report of the Center for Disease Control and Prevention (2007–2014), over 15% of the United States population is affected by CKD, and the numbers are expected to rise. CKD incurs substantial rising medical costs in the United States, with similar developments observed globally. Over the last decade, the findings of multiple genome-wide association studies (GWASs) have established common DNA variants as genetic risk factors for CKD[2,3]. However, functional annotation and explanation of these loci remain an issue. Currently, the functional annotation of GWAS data is mainly conducted by linking susceptibility loci by spatial proximity to the nearest gene[4]. For example, well known single-nucleotide polymorphisms (SNPs) that are associated with CKD include SNPs annotated with *ALMS1* and *UMOD*. *ALMS1* is required for medullar collecting duct ciliogenesis[5], whereas *UMOD* is involved in the inhibition of calcium oxalate crystallization in renal fluids[6] and has an evolutionary role in protection from urinary tract infections[7]. Because these SNPs are located in coding regions of genes with important renal protective functions, it is conceivable that the genetic variation marked by these SNPs affects both genes, contributing to CKD pathogenesis. For many of the CKD-associated susceptibility loci that are not directly located in or near protein coding regions, the causal contribution to disease etiology is far less straightforward.

New insights brought by epigenetic research have revealed the prevalence of DNA regulatory elements (DREs), such as enhancers and silencers, located in both coding- and nonprotein-coding DNA regions (Figure 1A)[8]. These DREs play a crucial role in regulating gene expression in a cell-specific manner. Enhancer elements regulate transcription of their target genes through three-dimensional (3D) chromatin interactions with transcriptional start sites (TSSs) (Figure 1B). Importantly, DREs can regulate expression levels of gene targets over a distance up to thousands of kilobase pairs[9], far exceeding the current standard distance for GWAS annotation. Common genetic variation in DREs could be a causative factor in dysregulation of target gene expression, leading to disease or other phenotypes (Figure 1C and D). This was shown previously for the SNP rs12913832, which was shown to modulate human pigmentation by affecting the enhancer regulation of the *OCA2* promoter[10]. Systematic mapping of the target genes of DREs that overlap with known CKD-associated SNPs could greatly improve our understanding of

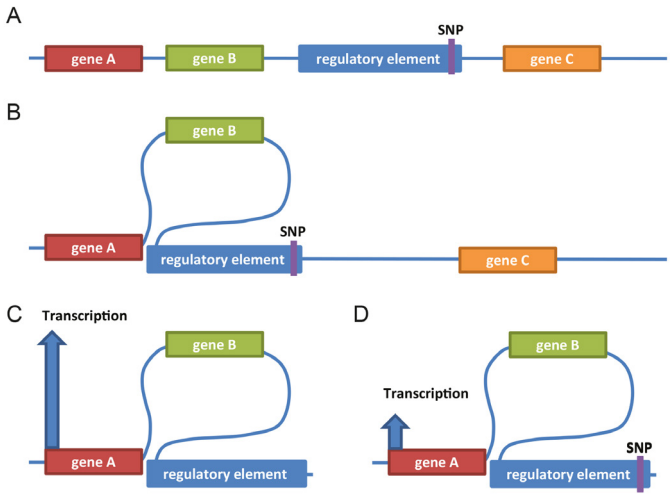

Figure 1. Genetic variation in DREs could be a causative factor in dysregulation of distal target gene expression. (A) Many of the susceptibility loci that are not located in protein coding regions overlap with DREs, such as enhancers and silencers. (B) DREs play a crucial role in regulating gene expression in a cell-specific manner by modulating 3D chromatin interactions and increasing spatial proximity of DREs with TSSs, thereby regulating transcription of genes on a nonlinear DNA scale. (C) Distal transcriptional activity of DREs could be compromised by (D) genetic variation (represented by colocalization with disease-associated SNP).

the complex genetics of CKD.

Here, we used self-transcribing active regulatory region sequencing (STARR-seq) to evaluate the potential effect of CKD-associated genetic variation on transcriptional regulation. In a proof of principle approach, we cloned putative DREs located on the same linkage disequilibrium (LD) block as the CKD-associated SNP rs11959928 from 20 donors in STARR-seq reporter plasmids. This approach enabled us to study the effect of all variants found on this susceptibility region in the donor pool on enhancer activity in primary human renal proximal tubular epithelial cells (HRPTECs), human renal glomerular endothelial cells (HRGECs), and the human embryonic kidney cell line HEK293a. The findings of this experiment illustrated how regulatory function could be affected by common small variants, thereby highlighting the relevance of studying downstream target genes of DREs overlapping with disease-associated susceptibility regions to add an additional layer to post-GWAS analysis. Subsequently, we used circular chromosome conformation capture sequencing (4C-seq) to identify putative candidate genes for CKD by examining 3D interactions between DREs that colocalize with CKD susceptibility loci and their target genes. This allowed us to study long-range

regulation of target gene promoters by crosslinking the folded and interacting DRE segments followed by two restriction-ligation steps of the DNA strands and DNA sequencing. Because transcriptional regulation is cell type specific and because CKD pathogenesis is associated with reduced GFR as a result of tubulointerstitial fibrosis[11] as well as loss of peritubular and glomerular capillaries[12,13], we conducted the 4C-seq in HRPTECs and HRGECs. Chromatin interactions were studied in these primary cells from healthy donors to create an overview of genes interacting with CKD susceptibility loci. We conducted a systematic screen of 39 putative regulatory elements that colocalize with previously reported susceptibility regions for CKD. This led to the identification of 304 target genes that are potentially transcriptionally affected by these CKD-associated SNPs. This study shows, for the first time, a direct interaction between CKD-associated common variant regions and the promoter regions of CKD-associated target genes. Although additional functional studies are needed to determine the exact mechanism of action, in this form, our data presents an extensive overview of potential target genes for the previously reported CKD-associated SNPs, providing new gene candidates for hypothesis-driven future studies.

Results

STARR-seq directly shows the potential of genetic variation to affect regulation of gene expression

To illustrate the effect of genetic variation on regulatory activity of DREs as an additional layer to GWAS interpretation, the STARR-seq reporter setup was used to test the influence of common genetic variants colocalizing with possible DREs positioned on the haploblock marked by the CKD-associated SNP rs11959928. The STARR-seq reporter assay is on the basis of a reporter plasmid containing a minimal promoter followed by an incorporated candidate enhancer sequence[14]. The activity of each enhancer is reflected by its ability to induce the promoter activity, leading to RNA transcription of the enhancers sequence (Figure 2A). The advantage of this approach over luciferase reporter assays is that STARR-seq allows parallel (and thus, "high-throughput") assessment of all genomic variation in the enhancer regions located on this specific haploblock, because the effect of a variant on enhancer strength is reflected by its relative prevalence in transcribed RNA compared with its prevalence in the pool of reporter plasmids. Putative DREs located on the haploblock marked by the CKD-associated SNP rs11959928 (Figure 2B), containing at least three potential regulatory regions (I–

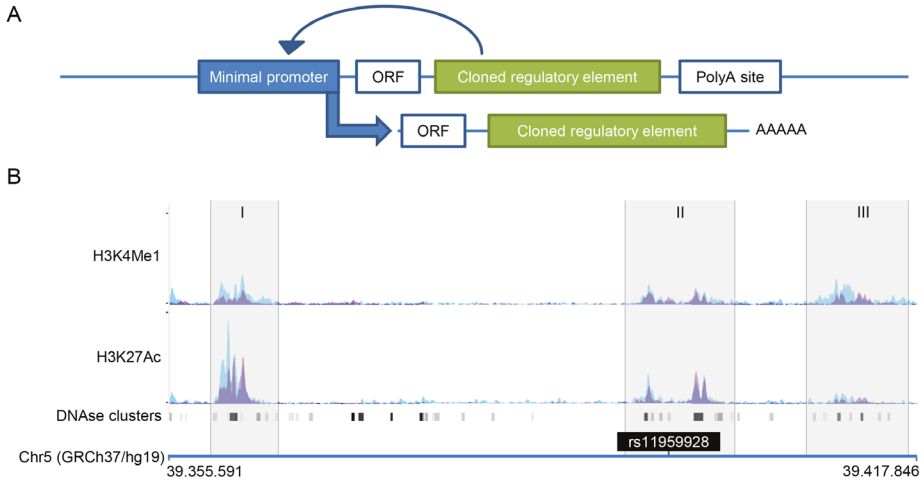

C

variant location	*reference*	*input 1*	*input 2*	*HRGECs 1*	*HRGECs 2*	*Δ HRGECs 1*	*Δ HRGECs 2*
chr5:39361231	A	72.8	69.1	100.0	100.0	27.2	30.9
chr5:39361273	T	74.8	71.2	100.0	100.0	25.2	28.8
chr5:39361303	G	36.5	31.8	17.8	3.2	-18.7	-28.6
chr5:39361359	A	70.2	64.8	100.0	99.1	29.8	34.3
chr5:39361573	A	48.9	45.2	100.0	99.6	51.1	54.4

variant location	*reference*	*input 1*	*input 2*	*HRPTECs 1*	*HRPTECs 2*	*Δ HRPTECs 1*	*Δ HRPTECs 2*
chr5:39361231	A	72.8	69.1	100.0	100.0	27.2	30.9
chr5:39361273	T	74.8	71.2	100.0	100.0	25.2	28.8
chr5:39361303	G	36.5	31.8	8.3	23.2	-28.1	-8.6
chr5:39361359	A	70.2	64.8	100.0	100.0	29.8	35.2
chr5:39361573	A	48.9	45.2	100.0	100.0	51.1	54.8

variant location	*reference*	*input 1*	*input 2*	*HEK293a 1*	*HEK293a 2*	*Δ HEK293a 1*	*Δ HEK293a 1*
chr5:39361231	A	72.8	69.1	100.0	100.0	27.2	30.9
chr5:39361273	T	74.8	71.2	100.0	100.0	25.2	28.8
chr5:39361303	G	36.5	31.8	9.1	19.8	-27.4	-12.1
chr5:39361359	A	70.2	64.8	100.0	100.0	29.8	35.2
chr5:39361573	A	48.9	45.2	98.9	100.0	50.0	54.8

Figure 2. STARR-seq analysis illustrates the effect of chronic kidney disease-associated genetic variation on transcriptional regulation. (A) The STARR-seq reporter principle is on the basis of a reporter plasmid containing a minimal promotor followed by a cloned candidate enhancer sequences. The activity of each enhancer is reflected by its ability to transcribe itself. ORF, Open Reading Frame. (B) Putative DREs, identified by H3K4Me1, H3K27Ac, and DNAse clusters (HUVECs are in blue and HEKs are in pink; overlap is shown in purple; adapted from USCS genome browser), located on the haploblock marked by chronic kidney disease (CKD)-associated SNP rs11959928 (I–III) were cloned into the STARR-seq plasmid from 20 individual donors. (C) The library of STARR-seq plasmids was transformed in HRGECs, HRPTECs, and HEK293a followed by RNA-seq of the produced enhancer RNA strands. Shown in replicate is the percentage of the reference allele in the input library, the percentage of the reference allele in cellular transcribed RNA, and the Δ between the prevalence in the library and transcribed RNA (found in region I).

III) as illustrated by H3K4Me1, H3K27Ac, and DNAse clusters in human umbilical vein endothelial cells and human epidermal keratinocytes (adapted from USCS genome browser), were cloned from 20 individual donors into one combined reporter library (Supplemental Table 1). This library was transformed in HRGECs, HRPTECs and HEK293a (the latter cell type was used an additional control) followed by sequencing of the produced enhancer-derived RNA as well as the library itself, enabling us to compare transcription frequency of each variable allele located in the enhancer sequences on the haploblock with its original frequency in the library (Supplemental Table 2). Via this approach, one particular region containing five variants was found to be strongly affected by allele-specific activity in all three examined cell types (Figure 2C). Four of these variants had a reference allele frequency of 45.2%–74.8% in the library input, but virtually only the reference alleles were transcribed in all three cell types. The other allele had a wild-type penetrance of 31.8%–36.5% in the library input, but its frequency was strongly reduced in the transcribed RNA. This example illustrates that disease-associated SNPs not only may affect gene coding sequences but might also affect the transcriptional regulation of DRE target genes.

4C-seq leads to discovery of new target genes for chronic kidney disease-associated SNPs

Building on the illustrative STARR-seq findings, 39 CKD-associated susceptibility loci that colocalize with DREs were studied in HRGECs and HRPTECs to identify the target genes of putative DREs[2,3]. Activity of these DREs was assessed in renal epithelium and fetal renal tissue for HRPTECs and microvascular endothelium for HRGECs on the basis of DNase hypersensitivity and H3K4me3 chromatin immunoprecipitation data (Supplemental Table 3). Of the 39 studied loci, six colocalize only with active DREs in renal epithelium, five colocalize only with active DREs in microvascular endothelium, and 28 loci colocalize with active DREs in both renal epithelium and microvascular endothelium. For the discovery of target genes of these regulatory elements, the TSSs that interacted with these loci were examined in HRPTECs and HRGECs using 4C-seq (Figure 3A–F). 67 chromatin interaction datasets were generated in twofold, of which only the replicated chromatin interactions were considered as candidate genes. These candidate genes were filtered per cell type for expression in that specific cell type using in-house and public expression datasets (Figure 3G). This led to the discovery of 304 CKD target genes, of which 199 were found in HRGECs (Figure

4, Supplemental Table 4) and 229 were found in HRPTECs (Figure 5, Supplemental Table 5). Among the 199 target genes interacting in HRGECs and 229 target genes interacting in HRPTECs, 124 were identified in both cell types (Figure 3G). These 304 candidate genes all fulfilled the following three criteria. (1) The TSS of the candidate gene colocalizes with a significant 4C-seq signal ($P<10^{-8}$) within 5 kbp. (2) The SNP or any other SNP in LD ($r>0.8$) colocalizes with active regulatory regions. (3) The candidate gene is expressed in the cell types of interest (reads per kilobase million reads sequenced [RPKMs] >−1 and probe intensity

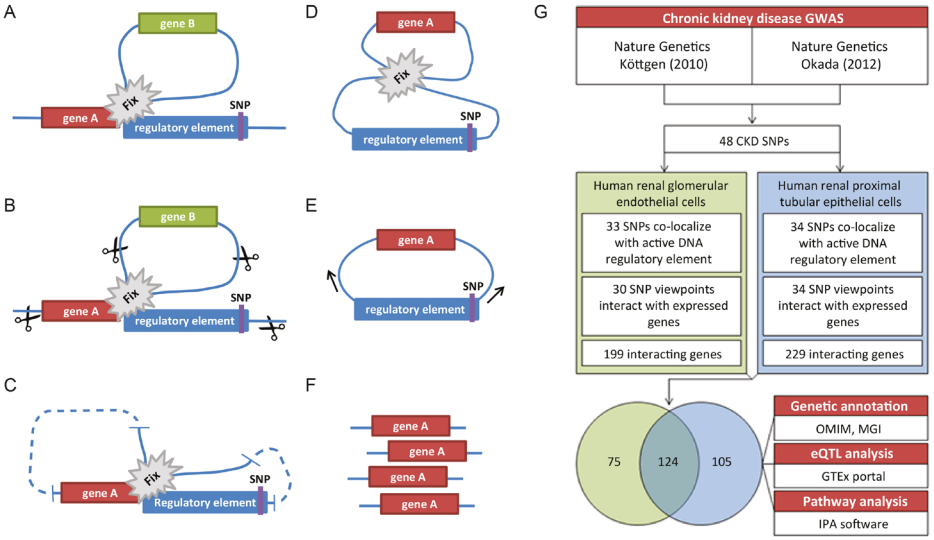

Figure 3. 4C-seq was used to study chromatin interactions, leading to the discovery of 304 chronic kidney disease target genes in total. The 3D chromatin conformation of the DREs was studied in detail on the basis of the 4C template, which was generated by (A) fixing the chromatin structure, followed by (B) enzymatic (DpnI restriction enzyme) digestion of the fixed chromatin. (C) The digested chromatin was ligated into circular fragments in a diluted environment, after which (D) the chromatin was decrosslinked. (E) The circular DNA molecules followed another round of enzymatic (CviQI restriction enzyme) digestion and ligation, after which the 4C-seq library was prepared with primers that target sequences in close proximity of the chronic kidney disease (CKD) susceptibility loci. (F) This library was sequenced to identify genes that were physically interacting with CKD susceptibility loci. (G) The 4C analysis was initially performed on 48 viewpoints on the basis of CKD-associated SNPs, of which, in total, 39 colocalized with active DREs on the basis of mapping with DNase hypersensitivity or H3K04me3 ChIP-seq datasets (33 in HRGECs and 34 in HRPTECs with partial overlap of SNPs). Of these 39 studied viewpoints, only 36 (31 in HRGECs and 34 in HRPTECs with partial overlap of viewpoints) were interacting with a total of 304 target genes with validated expression in the assessed cell types (overlap indicated in the Venn graph). These 304 genes were subsequently processed for genetic annotation to renal failure–associated traits in the OMIM database and the MGI database in addition to eQTL analysis in the GTEx portal database and pathway analysis using IPA software.

>6 for microvascular endothelium RNA-seq data and HRPTECs microarray data, respectively)[15]. The TSSs of the majority of candidate genes found with circular chromosome conformation capture (4C; both expressed and nonexpressed) were positioned within 500 kbp from the lead SNP position (88% in HRGECs and 84% in HRPTECs), but occasionally, interacting genes were found over 1000 kbp from the SNP locus (seven in HRGECs and 23 in HRPTECs) (Supplemental Figure 1).

Genetic annotation of candidates picked up by 4C-Seq in the OMIM and the MGI shows link with chronic kidney disease

We evaluated if the identified candidates were associated with CKD using the Online Mendelian Inheritance in Man (OMIM) and the Mouse Genome Informatics (MGI) databases. The OMIM database is a catalog of human genetic disorders that connects rare gene variants with phenotype. We established the overlap of our HRPTECs and HRGECs gene lists with the genes retrieved from the OMIM Morbid Map by searching for the keywords "kidney," "renal," and "nephro." Monogenetic defects in five CKD candidate genes were directly correlated with a renal disease phenotype, of which two are completely located on a different haploblock than the 4C viewpoint (Table 1, white unpatterned mark). The MGI database contains murine phenotypic information of mutant alleles. Analysis revealed that monogenetic silencing of 23 of the CKD candidate genes in mice caused direct renal failure–related traits, including albuminuria (*ALMS1*, *MPV17*, and *SCARB2*), abnormal renal filtration rate (*SLC14A1*), and glomerular sclerosis (*CCNI*, *MPV17*, and *VEGFA*) (Table 2). Of the 23 renal failure trait–associated target genes found with the MGI, 13 are located entirely on a different haploblock than the 4C viewpoint (Table 2, white unpatterned mark).

EQTL analyses reveal genotype-dependent expression of chronic kidney disease candidate genes

A candidate gene with an expression level that is significantly correlated with co-occurrence of an SNP is likely to be transcriptionally regulated by a DRE affected by the SNP. These loci that contribute to variation in gene expression levels, called expression quantitative trait loci (eQTL), are identified using GWAS and RNA-seq data of the target organ. To date, no large genome-wide eQTL data of the human kidney have been published that allow adequate analysis of all CKD-associated SNPs[16]. To evaluate if the expression levels of the CKD candidate genes are affected by CKD-associated SNPs, we used the Genotype-Tissue Expression (GTEx)

A

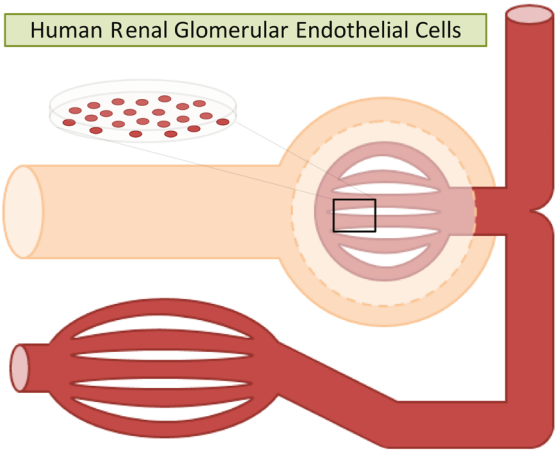

B

rs267734 (chr. 1)	
Target genes	kbps
ANP32E	744
APH1A	710
C1orf51	696
MRPS21	685
PRPF3	658
RPRD2	614
TARS2	492
ECM1	471
ADAMTSL4	430
MCL1	399
ENSA	350
GOLPH3L	282
CTSS	213
CTSK	171
ARNT	102
SETDB1	53
LASS2	4
ANXA9	3
FAM63A	28
PRUNE	29
C1orf56	69
CDC42SE1	81
MLLT11	81
GABPB2	92
SEMA6C	168
LYSMD1	187
SCNM1	187
VPS72	211
PIP5K1A	220
PSMD4	276

rs2049805 (chr. 1)	
Target genes	kbps
EFNA1	95
RAG1AP1	87
DPM3	82
KRTCAP2	49
TRIM46	49
MUC1	32
THBS3	17
MTX1	16
GBAP	2
GBA	16
FAM189B	30
SCAMP3	37
CLK2	48
HCN3	52
FDPS	84
C1orf104	99
RUSC1	96
ASH1L	337
MIR555	121
LOC645676	337
MSTO1	385
YY1AP1	464
DAP3	464

rs1260326 (chr. 2) ns	
Target genes	kbps
GTF3C2	151
EIF2B4	138
SNX17	138
ZNF513	127
PPM1G	98
FTHL3P	114
NRBP1	79
KRTCAP3	66
IFT172	18
FNDC4	13
C2orf16	68
ZNF512	75
CCDC121	121
GPN1	121
SUPT7L	156
SLC4A1AP	155

rs13538 (chr. 2) ns	
Target genes	kbps
ALMS1	255
TPRKB	96
DUSP11	139
STAMBP	188
DGUOK	286
TET3	405
BOLA3	507
MOBKL1B	538
DCTN1	734

rs13069000 (chr. 3)***	
Target genes	kbps
SLC25A26	680
LRIG1	248

rs16853722 (chr. 3)	
Target genes	kbps
MECOM	287
ARPM1	337

rs347685 (chr. 3)	
Target genes	kbps
RASA2	601
RNF7	350
ATP1B3	212
TFDP2	83
GK5	137
XRN1	360
ATR	491

rs10937329 (chr. 3)***	
Target genes	kbps
BCL6	261
LPP	217

rs13146355 (chr. 4)	
Target genes	kbps
NUP54	342
SCARB2	277
STBD1	184
SHROOM3	56
CCNI	585
CCNG2	666

rs2725220 (chr. 4)**	
Target genes	kbps
SPARCL1	509
PKD2	31
ABCG2	120
PPM1K	246
HERC6	340
HERC5	418
PIGY	485

rs17319721 (chr. 4)	
Target genes	kbps
STBD1	141
SHROOM3	13

rs11959928 (chr. 5)	
Target genes	kbps
RICTOR	323
DAB2	28
TTC33	1359

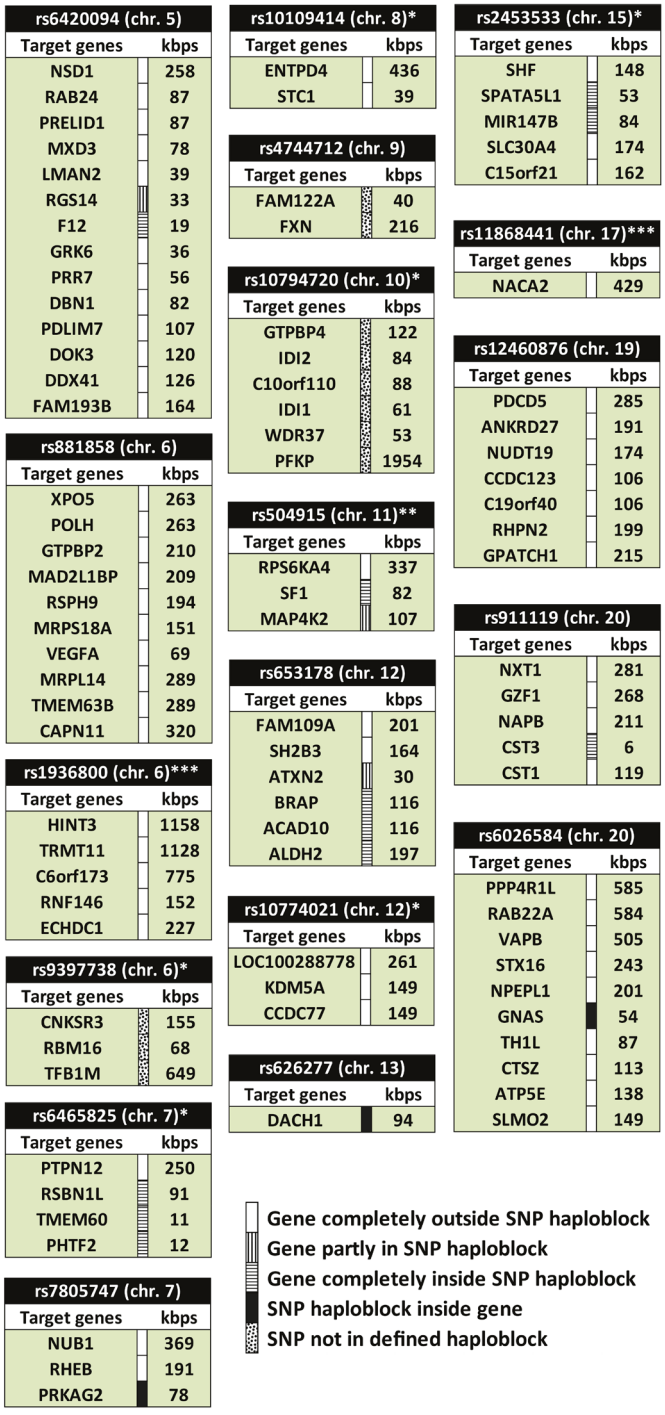

Figure 4. Analysis of chromatin interactions of chronic kidney disease susceptibility loci that colocalize with regulatory elements using 4C-seq led to the discovery of 199 chronic kidney disease target genes in glomerular endothelial cells. (A) Chromatin interactions were studied in cultured HRGECs to define endothelial target genes of chronic kidney disease (CKD) susceptibility loci that colocalize with active regulatory elements. (B) Of a total of 33 replicated 4C datasets, on the basis of CKD susceptibility loci that colocalize with active regulatory elements, 30 interacted with at least one target gene that was expressed in endothelium, which led to the identification of 199 CKD target genes in total. Studied SNPs are displayed ordered on position followed by haploblock information and the SNP-TSS distance in kilobase pairs. ns, Nonsynonymous SNP. *SNP solely associated with serum creatinine (eGFR); **SNP solely associated with serum urate; ***SNP solely associated with BUN.

A

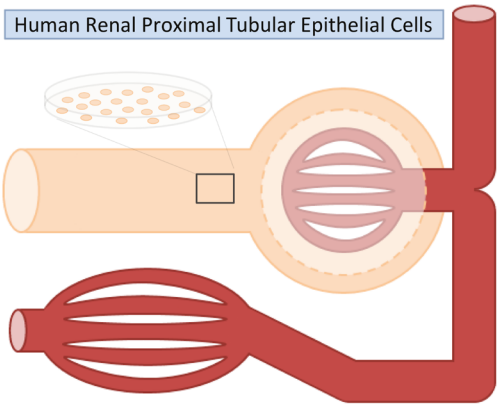

B

rs267734 (chr. 1)	
Target genes	kbps
NBPF10	5658
ANP32E	744
CA14	721
APH1A	710
C1orf54	706
PRPF3	658
RPRD2	614
TARS2	492
ECM1	471
ADAMTSL4	430
MCL1	399
ENSA	350
GOLPH3L	282
CTSS	213
CTSK	171
SETDB1	53
LASS2	4
ANXA9	3
FAM63A	28
PRUNE	29
C1orf56	69
CDC42SE1	81
SEMA6C	168
SCNM1	187
VPS72	211
PIP5K1A	220
PSMD4	276

rs2049805 (chr. 1)	
Target genes	kbps
ADAR	614
PMVK	285
PBXIP1	266
PYGO2	261
SHC1	252
CKS1B	248
FLAD1	239
LENEP	229
ZBTB7B	220
ADAM15	171
EFNA4	159
EFNA3	144
EFNA1	95
RAG1AP1	87
DPM3	82
TRIM46	49
MUC1	32
THBS3	17
MTX1	16
GBAP	2
GBA	16
FAM189B	30
SCAMP3	37
CLK2	48
PKLR	76
FDPS	84
RUSC1	96
ASH1L	337
MSTO1	385
YY1AP1	464
DAP3	464

rs1260326 (chr. 2) ns	
Target genes	kbps
AGBL5	456
SLC30A3	245
UCN	200
MPV17	185
GTF3C2	151
EIF2B4	138
SNX17	138
PPM1G	98
NRBP1	79
FNDC4	13
GCKR	11
GPN1	121
SUPT7L	156
SLC4A1AP	155
RBKS	382
BRE	383

rs13538 (chr. 2) ns	
Target genes	kbps
CCT7	407
FBXO41	370
ALMS1	255
NAT8	1
NAT8B	60
TPRKB	96
DUSP11	139
STAMBP	188
ACTG2	252
TET3	405
SLC4A5	702

rs11123170 (chr. 2)***	
Target genes	kbps
PRPF40A	39595

rs16853722 (chr. 3)	
Target genes	kbps
MECOM	287
MYNN	340

rs13069000 (chr. 3)***	
Target genes	kbps
LRIG1	248

rs347685 (chr. 3)	
Target genes	kbps
RASA2	601
RNF7	350
ATP1B3	212
TFDP2	83
ATR	491

rs10937329 (chr. 3)***	
Target genes	kbps
BCL6	261
LPP	217

rs3775948 (chr. 4)**	
Target genes	kbps
DRD5	212
SLC2A9	28
WDR1	123

rs17319721 (chr. 4)	
Target genes	kbps
NUP54	299
SCARB2	234
STBD1	141
CCNI	628
CCNG2	710

rs13146355 (chr. 4)	
Target genes	kbps
SDAD1	500
CXCL9	484
CXCL10	467
NUP54	342
SCARB2	277
STBD1	184
CCNI	585
CCNG2	666

rs6420094 (chr. 5)	
Target genes	kbps
UIMC1	384
FGFR4	304
NSD1	258
MXD3	78
LMAN2	39
RGS14	33
SLC34A1	6
F12	19
GRK6	36
PRR7	56
DBN1	82
PDLIM7	107
DOK3	120
DDX41	126
FAM193B	164
TMED9	202
B4GALT7	209

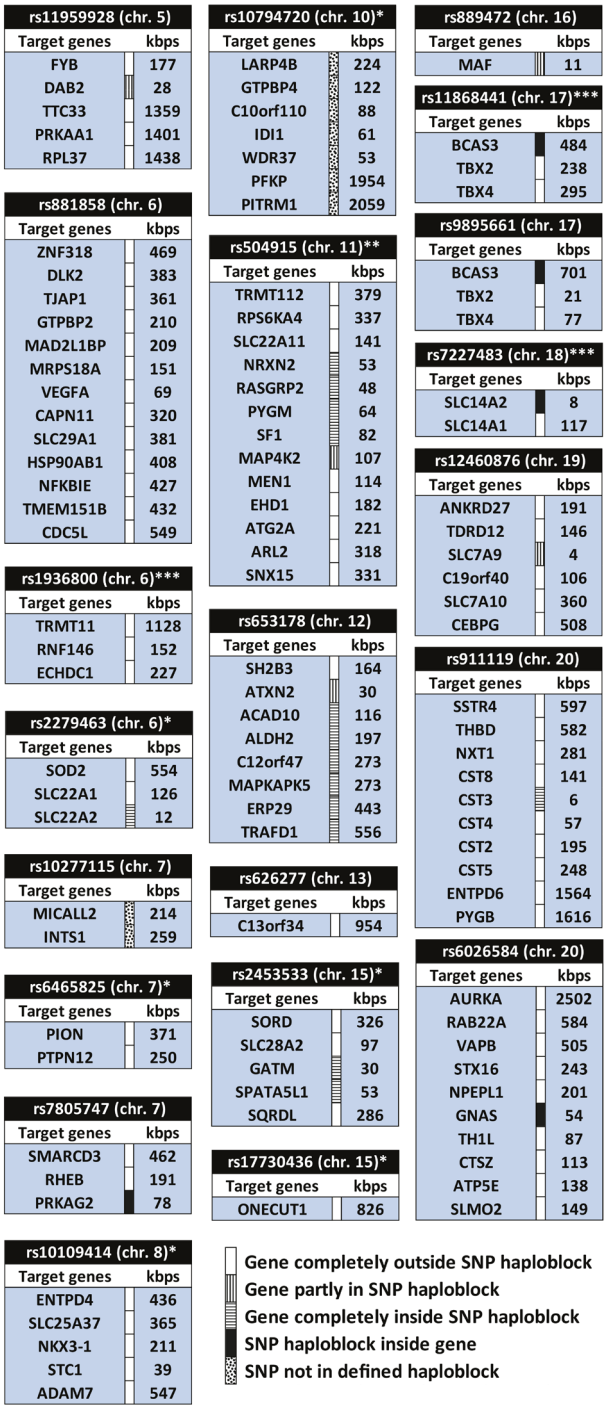

Figure 5. Analysis of chromatin interactions of chonic kidney disease susceptibility loci that colocalize with regulatory elements using 4C-seq led to the discovery of 229 chronic kidney disease target genes in renal proximal tubular epithelial cells. (A) Chromatin interactions were studied in cultured HRPTECs to define epithelial target genes of chronic kidney disease (CKD) susceptibility loci that colocalize with active regulatory elements. (B) Of a total of 34 4C datasets, on the basis of CKD susceptibility loci that colocalize with active regulatory elements, 34 interacted with at least one target gene that was expressed in HRPTECs, which led to the identification of 229 CKD target genes in total. Studied SNPs are displayed ordered on position followed by haploblock information and the SNP-TSS distance in kilobase pairs. ns, Nonsynonymous SNP. *SNP solely associated with serum creatinine (eGFR); **SNP solely associated with serum urate; ***SNP solely associated with BUN.

Table 1. Overlapping genes in 4C-seq retrieved genes and chronic kidney disease associated genes in OMIM.

Gene ID	Phenotype	MIM Number	4C SNP	SNP-TSS (kbp)	HRGECs	HRPTECs
MUC1	Medullary cystic kidney disease 1	158340	rs2049805	32	x	x
PKD2	Polycystic kidney disease 2	173910	rs2725220	31	x	
SCARB2	Epilepsy, progressive myoclonic 4, with or without renal failure	602257	rs13146355	277	x	x
SLC2A9	Hypouricemia	612076	rs3775948	28		x
SLC34A1	Nephrolithiasis/osteoporosis, hypophosphatemic	182309	rs6420094	6		x

Gene completely outside SNP haploblock
Gene completely inside SNP haploblock
SNP haploblock inside gene

database. Although the GTEx so far only contains kidney-specific expression data of 26 genotyped donors, which does not reach the GTEx threshold for eQTL analysis (>70), the database does include genotype- and expression-matched data of 449 donors for which eQTL analysis was conducted in 44 nonrenal tissues, which is large enough to stratify most of the individual CKD SNPs and wild-type alleles assessed in our study. Of the 39 CKD-associated susceptibility loci, 25 were annotated in the GTEx. These 25 SNPs were significantly correlated with the expression of 54 genes, of which 48 physically interacted with the 4C-seq input loci (data not shown). Of these 48 captured target genes, 38 were actually expressed in HRPTECs and/or HRGECs and they included ten genes located on a completely different haploblock than the CKD-associated SNP (Table 3, white unpatterned mark). Thus, although the lack of genotype-kidney expression datasets prohibited us to study these eQTL in renal tissue, this shows the ability of the studied elements to establish an SNP-dependent expression pattern of captured target genes in the 4C-seq approach. Interesting eQTL target genes also picked up by 4C-seq include the solute carriers *SLC28A2* and *SLC30A4* (rs2453533) and in relation to renal fibrosis, the genes encoding for the secreted proteases *CTSS* and *CTSK* (rs267734) (Figure 6).

Pathway analyses reveal potentially disrupted mechanisms and regulators in chronic kidney disease

Other than studying individual loci and interacting genes, we used Ingenuity Pathway Analysis (IPA; QIAGEN) to determine the pathways in which the CKD candidate genes are involved. In both HRGECs and HRPTECs, the 4C candidate genes were most significantly enriched in biosynthesis pathways (Supplemental Tables 6 and 7), including the superpathway of geranylgeranyl diphosphate biosynthesis ($P<0.001$ and $P<0.001$, respectively) and the trans, trans-farnesyl diphosphate biosynthesis

Table 2. Overlapping genes in 4C-seq retrieved genes and chronic kidney disease associated genes in MGI.

Gene ID	Phenotype	4C SNP	SNP-TSS (kbp)	HRGECs	HRPTECs
ALMS1	abnormal kidney morphology, urine-, renal tubules-, and other kidney related abnormalities	rs13538	255	x	x
ASH1L	glomerulus- and other kidney related abnormalities	rs2049805	337	x	x
CCNI	urine-, blood-, glomerulus-, podocyte-, and other kidney related abnormalities	rs13146355	585	x	x
CTSS	abnormal kidney angiogenesis	rs267734	213	x	x
DCTN1	blood abnormalities	rs13538	734	x	
GNAS	urine- and other kidney related abnormalities	rs6026584	54	x	x
GRK6	glomerulus- and other kidney related abnormalities	rs6420094	36	x	x
IFT172	abnormal kidney morphology, glomerulus abnormalities	rs1260326	18	x	
MAF	abnormal kidney morphology, renal tubules abnormalities	rs889472	11		x
MECOM	blood abnormalities	rs16853722	287	x	x
MPV17	abnormal kidney morphology and angiogenesis, urine-, blood-, glomerulus-, renal tubules-, and other kidney related abnormalities	rs1260326	185		x
PKD2	abnormal kidney morphology, kidney cysts, blood-, renal tubules-, and other kidney related abnormalities	rs2725220	31	x	
RNF7	abnormal kidney angiogenesis	rs347685	350	x	x
SCARB2	urine abnormalities	rs13146355	277	x	x
SHC1	abnormal kidney angiogenesis	rs2049805	252		x
SLC14A1	urine- and blood abnormalities, abnormal renal filtration	rs7227483	117		x
SLC14A2	urine abnormalities, abnormal renal filtration	rs7227483	8		x
SLC2A9	kidney cysts, urine-, blood-, renal tubules-, and other kidney related abnormalities	rs3775948	28		x
SLC4A5	urine abnormalities, abnormal renal filtration	rs13538	702		x
SLC7A9	renal tubules abnormalities	rs12460876	4		x
SOD2	blood abnormalities	rs2279463	554		x
THBD	abnormal kidney morphology	rs911119	582		x
VEGFA	abnormal kidney morphology and angiogenesis, blood-, glomerulus-, renal tubules-, and podocyte abnormalities	rs881858	69	x	x

Gene completely outside SNP haploblock
Gene partly in SNP haploblock
Gene completely inside SNP haploblock
SNP haploblock inside gene

pathway (P<0.001 and P=0.001, respectively) (Figure 7A and B). Interestingly, both molecular pathways are linked to the mevalonate pathway (Supplemental Figure 2). 4C-seq identified *FDPS* and *PMVK* (rs2049805) as well as *IDI1* and *IDI2* (rs10794720) as candidate genes in relation to the mevalonate pathway in CKD.

In addition, IPA was used to identify upstream regulators of which the target genes were over-represented among the CKD candidate genes. Targets of the transcription factors ATF6 (P=0.002 and P<0.001) and FOXO4 (P<0.001 and P<0.001) were significantly enriched in the CKD candidates in both HRGECs and HRPTECs, respectively, whereas targets of HNF4α were only enriched in HRPTECs (P=0.04). It was previously shown that HNF4α was crucial for establishing and maintaining transcriptional enhancer elements in the renal proximal tubule and that suboptimal DNA binding properties among others led to transcriptional

dysregulation of a variety of solute carriers[17]. Interestingly, from publically available microarray data (NCBI Gene Expression Omnibus accession no. GSE66494)[18], all three transcription factors were found to be significantly upregulated in renal biopsies from patients with CKD compared with healthy controls (Figure 7C), suggesting that these three factors are potentially key regulators in CKD.

Discussion

The main findings of the study are as follows: (1) CKD-associated variation can

Table 3. Overlapping genes in 4C-seq retrieved genes and eQTL genes derived from GTEx portal.

eQTL	Gene ID	SNP-TSS (kbp)	eQTL in (tissue):	HRGECs	HRPTECs
rs10794720	IDI2	84	Muscle	x	
	NUDT19	174	Artery, Nerve	x	
rs12460876	SLC7A9	4	Adipose, Skin, Thyroid, Nerve, Lung		x
	TDRD12	146	Testis		x
rs1260326	SNX17	138	Muscle	x	x
	FNDC4	13	Thyroid	x	x
	NRBP1	79	Adipose, Testis	x	x
	KRTCAP3	66	Adrenal gland	x	
rs13538	ALMS1	255	Pancreas	x	x
	TPRKB	96	Artery	x	x
	NAT8	1	Adipose, Thyroid, Skin, Esophagus, Pancreas, Artery, Brain		x
rs2049805	THBS3	17	Whole Blood, Thyroid, Esophagus, Colon, Lung, Stomach, Testis, Spleen	x	x
	GBA	16	Esophagus, Nerve, Thyroid	x	x
	MUC1	32	Esophagus	x	x
	FAM189B	30	Thyroid	x	x
	EFNA1	95	Skin	x	x
	HCN3	52	Nerve	x	
rs2453533	SPATA5L1	53	Nerve, Adipose, Esophagus, Thyroid, Whole Blood, Artery, Muscle, Heart	x	x
	SLC30A4	174	Adipose	x	
	GATM	30	Thyroid, Muscle, Esophagus, Lung, Skin, Whole blood		x
	SLC28A2	97	Nerve, Thyroid, Adrenal gland, Colon, Ovary		x
rs267734	ANXA9	3	Skin, Testis	x	x
	CTSS	213	Adipose, Skin, Artery, Muscle, Thyroid, Nerve, Esophagus	x	x
	CTSK	171	Whole blood	x	x
	ARNT	102	Whole blood	x	
rs2725220	PKD2	31	Testis, Esophagus	x	
rs4744712	FAM122A	40	Artery	x	
rs504915	MEN1	114	Testis		x
	NRXN2	53	Lung, Artery, Esophagus, Nerve, Adipose, Muscle, Skin		x
rs6420094	RGS14	33	Skin, Artery, Testis	x	x
	FGFR4	304	Nerve		x
	SLC34A1	6	Esophagus		x
rs6465825	RSBN1L	91	Brain	x	
	TMEM60	11	Artery, Testis	x	
rs653178	ALDH2	197	Skin	x	x
rs911119	CST3	6	Testis, Lung, Whole blood, Nerve	x	x
rs9895661	TBX2	238	Artery		x

Gene completely outside SNP haploblock
Gene partly in SNP haploblock
Gene completely inside SNP haploblock
SNP haploblock inside gene
SNP not in defined haploblock

affect transcriptional regulation as shown in a proof of principle approach for rs11959928 using STARR-seq. (2) CKD-associated loci interact with promoter regions of target genes via 3D chromatin folding. By taking this DNA regulatory information into account in GWAS annotation, we found many novel CKD candidate genes. (3) Multiple SNP target genes sets can be distinguished. (4) The identified target genes can be linked to CKD in human and murine disease databases (the OMIM and the MGI). (5) eQTL analysis reveals that expression

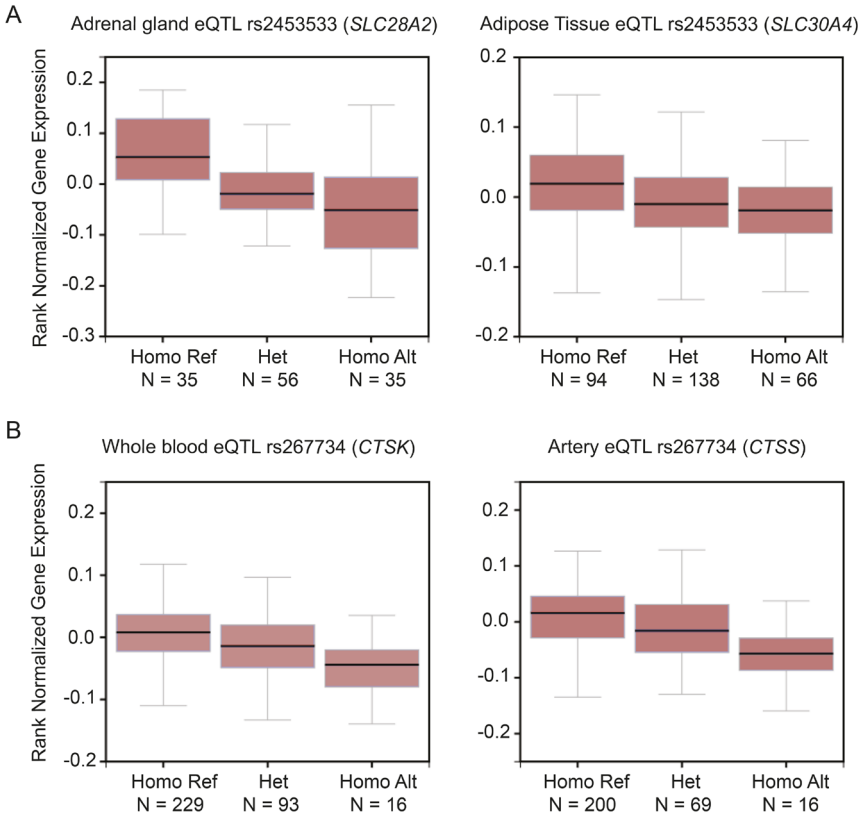

Figure 6. Expression levels of 4C-seq captured genes are correlated with the associated chronic kidney disease SNP. (A) The expression level of solute carriers *SLC28A2* and *SLC30A4* is lower in the presence of the heterozygous (Het) and homozygous alternative (Homo Alt) alleles (rs2453533) compared with the homozygous reference (Homo Ref) "wild-type" allele (P values <0.001 and <0.001, respectively; adjusted from the GTEx portal). (B) Similarly, the expression levels of the secreted proteases *CTSS* and *CTSK* are lower in the presence of the Het and Homo Alt alleles (rs267734) compared with the Homo Ref allele (P values <0.001 and <0.001, respectively; adjusted from the GTEx portal). SNP-target gene pair P values were on the basis of matrix eQTL analysis in linear regression mode as described by the GTEx consortium[39].

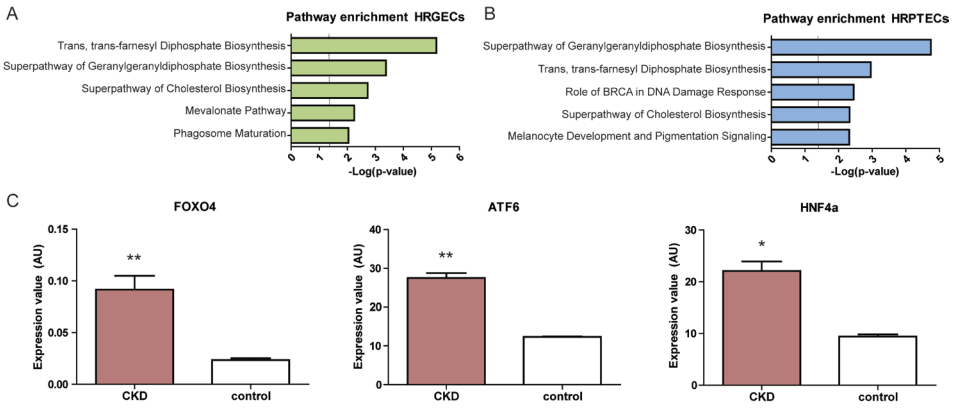

Figure 7. Chronic kidney disease candidate genes are enriched in pathways of biosynthesis, microangiopathy, and molecular transport. IPA revealed that chronic kidney disease (CKD) candidate genes in both (A) HRGECs and (B) HRPTECs were most enriched in biosynthesis pathways, including the superpathway of geranylgeranyl diphosphate biosynthesis and the trans, trans-farnesyl diphosphate biosynthesis pathway. These pathways play crucial roles in protein reuptake in HRPTECs. P-values were calculated by a right-tailed Fisher exact test. (C) Upstream regulators, identified by IPA on the basis of the enrichment of their target genes in the 4C-seq–derived candidates, were significantly higher when expressed in renal biopsy specimens from patients with CKD (derived from GSE66494). P-values were calculated by a nonparametric t-test. *P<0.05; **P<0.001.

of many target genes is genotype dependent. (6) HRGEC- and HRPTEC-derived target genes share the trans, trans-farnesyl diphosphate biosynthesis pathway as a common molecular mechanism. Combined, our data annotated multiple new genes to previously reported CKD-associated SNPs and provided first time evidence for direct interaction between these common variant regions and their targets. Future studies are now required to pinpoint causal genetic variant(s) at each locus, allowing a deeper understanding of their associated disease mechanisms and their relevance in kidney disease.

Previously reported GWASs for CKD-associated SNPs used classic annotation on the basis of spatial proximity principles to identify affected target genes[4]. This includes annotation of SNPs on the basis of location in coding regions or close proximity of TSS (taking into account that the average promotor is 100- to 1000-bp long) but also takes into consideration that these SNPs could be markers for less common variants in gene bodies. Using STARR-seq analysis, variants in LD with the CKD-associated SNP rs11959928 were shown to affect activity of a DRE in an allele-specific manner, emphasizing that not only protein coding variants but

also, variants located in regulatory regions could be at the basis of development or progression of complex diseases. Therefore, we examined the 3D folded state of the chromatin by 4C-seq to list genes that interact with DREs in LD with CKD-associated SNPs. This approach led to the identification of 304 CKD candidate genes, of which many are not directly located near the associated susceptibility loci. Most enhancers are located several hundred kilobase pairs and sometimes, even 1000 kbp from their target genes[9]. In our study, the majority of the SNPs are located between 100 and 500 kbp from the target genes' TSS, supporting the idea that the interactions observed in the 4C-seq approach are enhancer-target gene interactions. The effect of common genetic variants in DREs is relatively low[19]; therefore, it is unlikely that the CKD-associated SNPs in these elements will result in creating new or completely ablating 3D DRE-gene interactions. Rather, dysregulation in the expression of a gene profile that is part of the regulation of kidney homeostasis in healthy individuals is more likely the contributing factor in CKD etiology. The 4C-seq approach helps us to interpret genetic variants as a determining factor of the expression levels of interacting targets in the pathogenesis of CKD.

By overlapping our 304 CKD target genes with datasets provided by the OMIM and the MGI, we confirmed their relevance to kidney disease: Analysis with the MGI database showed that mice deficient for the CKD candidate genes *MPV17*, *CCNI*, *ASH1L*, and *SLC4A5* suffer from renal failure–related traits[20–23]. These genes are located 185 kbp (rs1260326), 585 kbp (rs13246355), 337 kbp (rs2049805), and 702 kbp (rs13538) from the CKD-associated SNP, respectively. In addition, validation of the 4C-seq approach was provided by analysis in the OMIM dataset, which showed that multiple target genes were linked to CKD-associated traits in human. For example, *MUC1* and *PKD2* were identified by 4C-seq as a result of the interaction of their promoter regions with regulatory domains that colocalize with rs2049805 and rs2725220, respectively. *MUC1* encodes the protein mucin-1, which is a membrane anchored mucoprotein involved in providing a protective barrier against pathogens. A frameshift mutation in *MUC1*, leading to a novel stop codon, induced medullar cystic kidney disease type 1 (MIM: 158340)[24]. *PKD2* encodes the polycystin-2 protein, which is involved in renal calcium transport and calcium signaling. Mutations in the gene, leading to loss of function, cause the formation of fluid-filled cysts, eventually leading to progressive destruction of the renal parenchyma (MIM: 173910)[25], but it was recently also shown to be involved in branching and network formation of lymphatic endothelium, which plays a

crucial role in renal function[26,27]. Such examples illustrate the potential relevance of the candidate genes identified by 4C-seq for renal function and provide clear evidence for the functional association between the investigated SNP regions and their corresponding 4C-seq–captured genes in (human) CKD.

Evidence for the transcription regulatory function of the CKD-associated SNP regions was provided by GTEx database analysis. Many of the CKD susceptibility loci were eQTL, showing a significant correlation between SNP genotypes and expression level of linked target genes in a variety of tissues. These eQTL target genes include *CTSS* and *CTSK* coding for cathepsin S and K, respectively, and both are downregulated in the presence of rs267734. Cathepsins are potent proteases and the negative correlation between rs267734 and cathepsin S and K expression might be relevant in relation to renal fibrosis, which is critically involved in CKD progression. In a bleomycin lung fibrosis model, it was shown that cathepsin K–deficient mice had more severe lung fibrosis than wild-type mice[28]. Furthermore, it was observed that pharmacologic inhibition of cathepsin activity in mice with unilateral ureteral obstruction–induced renal fibrosis led to a worse outcome[29], indicating that reduced expression of cathepsin S and K in the presence of rs267734 could contribute to CKD.

Pathway analysis showed enrichment of 4C-seq captured genes in multiple biosynthesis pathways involved in the generation of isoprenoid pyrophosphates. Interestingly, this enrichment was observed in HRGECs and HRPTECs, although with different identified target genes per cell type. Isoprenoid pyrophosphates are indispensable for renal proximal tubular protein reabsorption, because inhibition of 3-hydroxy-3-methylglutaryl CoA reductase in the mevalonate pathway leads to reduced prenylation of GTP binding proteins involved in receptor-mediated endocytosis, eventually resulting in proteinuria[30]. Similarly, altered levels of prenylation of RhoA affect eNOS activity in endothelial cells, resulting in imbalance of ROS levels and contributing to the endothelial dysfunction reported in CKD onset[31].

In our systemic approach, other than the noncoding variants, we also included two nonsynonymous SNPs (SNPs in gene coding regions that alter protein sequence: rs1260326 in *GCKR* and rs13538 in *NAT8*) that were among the studied regions. Presumably, the affected genes are involved in the associated disease phenotype. Especially reports on *NAT8* activity in association with kidney disease seem

convincing[32–34]. However, it was previously shown that DREs can also be located in coding regions[35] and it remains of interest that, by 4C-seq, we found interactions of this locus with TSSs of multiple other genes, of which the expression levels according to GTEx are significantly associated with the occurrence of the variant. The incorporation of regulatory information provides an additional layer in post-GWAS data to aid in our interpretation of these GWAS datasets but certainly does not replace the candidate genes identified on the basis of spatial proximity, such as *NAT8*. Along the same lines, several SNPs associated with a single trait were included. Several SNPs are solely associated with serum creatinine (eGFR). Although these SNPs might be causally associated with CKD, they might also affect creatinine production/secretion independent of renal function. rs91119 is only associated with serum cystatin C (eGFR) and it is located directly within the CST locus. Again, this SNP does not necessarily have to be causally associated with CKD but could also be involved in the dynamics of cystatin C production. The same is true for SNPs solely associated with serum urate or BUN, although the authors who identified SNPs associated with the latter group had corrected for nonrenal factors[3].

In conclusion, taking the 3D structure of chromatin into account, we have identified 304 putative CKD candidate genes of DREs that colocalize with CKD susceptibility loci. In this hypothesis generation–driven approach, we present a new method of GWAS interpretation on the basis of DRE target gene identification by 4C analysis that complements the classic methods of candidate gene identification. In addition, incorporation of the adapted STARR-seq method up- or downstream of the 4C pipeline would further narrow down the identification of causal variants in DNA regulatory function and help us to greatly expand our understanding of the role that common low-risk variants play in the onset of complex diseases, such as CKD.

Acknowledgments

We thank the Utrecht Sequencing Facility for providing the sequencing service and data. The Utrecht Sequencing Facility is subsidized by the University Medical Center (UMC) Utrecht, the Hubrecht Institute, and Utrecht University.

This work was supported by The Netherlands Organisation for Scientific Research Vidi grants 016096359 (to M.C.V.) and 91714302 (to C.C.), The Netherlands

Foundation for Cardiovascular Excellence (C.C.), the Erasmus Medical Center fellowship grant (to C.C.), the Regenerative Medicine fellowship grant of the UMC Utrecht (to C.C.), and The Netherlands Cardiovascular Research Initiative, which is an initiative with support of the Alexandre Suerman Stipendium (the UMC Utrecht; to C.A.M.), the OZF/2012 Wilhelmina Children's Hospital fund (to C.A.M.), and Dutch Heart Foundation grant CVON2014-11 RECONNECT (to D.J.D., M.C.V., J.A.J., M.M., and C.C.).

Concise methods

Cell culture

Primary HRGECs (derived from human donor cell biobank Sciencell) and HRPTECs (Sciencell) were cultured on fibronectin- and gelatin-coated plates on ECM medium (supplemented with the endothelial cell growth kit and penicillin/streptomycin; Sciencell) and EpiCM medium (supplemented with the epithelial cell growth kit and penicillin/streptomycin; Sciencell), respectively. Human embryonic kidney cells (HEK293a) were cultured on gelatin-coated plates on DMEM (Lonza) supplemented with 10% FCS (Gibco) and 100 U/ml penicillin/streptomycin (Lonza). All cells were cultured in 5% CO_2 at 37°C. The experiments with primary cells were conducted with cells at passage 3.

STARR-seq reporter assay

DNA from 20 individual donors was isolated from whole blood obtained from the Mini Donor Service (positive approval from the medical ethics committee of the University Medical Center Utrecht; protocol no. 07/125) via salt precipitation. Regions (approximately 1200 bp in size) containing DNase hypersensitivity sites overlapping with candidate variants (minor allele frequency >0.03) within the susceptibility locus were PCR amplified (primers in Supplemental Table 1), equimolarly pooled, and cloned into pSTARR-seq_human vector (Addgene). The library complexity was verified by dilution series after transformation, and it was estimated to contain 50,000 individual reporter clones; 40 million cells were placed in 1600 µl electroporation buffer (Bio-Rad) supplemented with 120 µg (HEK293a) or 240 µg (HRPTECs and HRGECs) library, after which electroporation mixture was divided over 16 2-mm electroporation cuvettes (Bio-Rad) followed by electroporation with a square wave (110 V/25 ms for HEK293a and 125 V/20 ms for HRPTECs and HRGECs) using Gene Pulser Xcell (Bio-Rad). After electroporation, cells were seeded in normal culture medium for 24 hours followed by RNA extraction using the RNeasy isolation kit (QIAGEN). The polyadenylated fraction of the total RNA was isolated using Dynabeads Oligo dT 25 (Thermo Fisher). The reporter-specific cDNA was synthesized and amplified

according to standard STARR-seq protocols[14]. The amplified cDNA was subsequently fragmented (Covaris S2 ChIP seq program: power peak 40 and duty factor 5 cycle/burst 200) and cleaned followed by sequencing library preparation using NEXTflex ChIP-Seq library prep kit for Illumina sequencing. The libraries were sequenced on the Illumina NextSeq500 platform to produce 75-bp-long single-end reads.

4C-seq

The 4C template was prepared as previously described[36]. In summary, 10 million HRGECs or HRPTECs (both primary cells from healthy donors) were fixed in 2% formaldehyde, after which cells were lysed. The chromatin of the lysed cells was digested with the four-base cutter DpnI (NEB) followed by ligation in a heavily diluted environment with T4 ligase (Roche). The ligated samples were decrosslinked followed by a second digestion with the four-base cutter CviQI (NEB). Next, samples were ligated once more in a diluted environment, after which the chromatin was purified. The efficiency of each digestion and ligation step was validated on agarose gels. Viewpoints were selected on the basis of the CKD susceptibility loci found in the GWASs of Okada *et al*[3] and Köttgen *et al*[2]. If multiple SNPs were found in a genomic region spanning <20 kbp, only the SNP with the lowest P value was selected as the viewpoint. To study the chromatin interactions of CKD-associated susceptibility loci with 4C, primers were designed for each viewpoint as described previously[36]. Briefly, primers were designed within a 5-kbp window surrounding the CKD-associated SNP. Forward primers were designed in the first restriction site, and the reversed primers were designed close to the second restriction site (<100 bp), with a minimum distance of 300 bp between the forward primer and the reversed primer. In the case that no suitable primers could be designed on the basis of these specifications, either the window size surrounding the SNP was increased to 10 kbp or the distance between the forward and reversed primers was reduced (Supplemental Table 8). 4C libraries were sequenced using the NextSeq500 platform (Illumina), producing single-end reads of 75 bp. The raw sequencing reads were then demultiplexed on the basis of viewpoint-specific primer sequences. Reads were trimmed to 16 bases and mapped to an *in silico*–generated library of fragment ends (fragends) neighboring all DpnI sites in human genome (NCBI37/hg19) using the custom Perl scripts[37]. No mismatches were allowed during the mapping. The reads mapping to only one possible fragend were used for additional analysis.

Target gene identification

First, the number of covered fragends within a running window of *k* fragends throughout the whole chromosome was calculated (only the viewpoint's chromosome was taken into

account). The *k* was set separately for every viewpoint, and therefore, it contained, on average, 20 covered fragends in the area around the viewpoint (±100 kbp). Second, we compared the number of covered fragends in each running window with the theoretical random distribution. The windows with significantly higher numbers of covered fragends compared with random distribution ($P<10^{-8}$ on the basis of binominal cumulative distribution function; R pbinom) were considered as a significant 4C signal. The following criteria were defined for the identification of the candidate genes. (1) The TSS colocalizes with a significant 4C-seq signal ($P<10^{-8}$) within 5 kbp. (2) The CKD-associated SNP or other variant in LD colocalizes with at least one of the published datasets that represents candidate regulatory sequences (Supplemental Table 3) in a similar cell type as that from which the 4C signal was. (3) The candidate gene has been validated to be expressed by mRNA datasets.

Identification of gene expression

HRPTECs expression data were used from publically available datasets (NCBI Gene Expression Omnibus accession no. GSE12792)[38]. Expression data from microvascular endothelium were generated via RNA extraction from cultured microvascular endothelial cells in low serum medium (EBM-2 medium supplemented with 0.5% FCS) using the RNeasy isolation kit. Poly(A) Beads (NEXTflex) were used to isolate polyadenylated mRNA, from which sequencing libraries were made using the Rapid Directional RNA-seq Kit (NEXTflex). Libraries were sequenced using the Nextseq500 platform (Illumina), producing single-end reads of 75 bp. Reads were aligned to the human reference genome GRCh37 using STAR, version 2.4.2a. Picard AddOrReplaceReadGroups (v1.98) was used to add read groups to the BAM files, which were sorted with Sambamba v0.4.5, and transcript abundances were quantified with HTSeq-count, version 0.6.1p1, using the union mode. Subsequently, RPKMs were calculated with edgeR RPKM function. Genes were accepted as expressed if probe intensity was >6 or $\log_2$(RPKM) was >−1 in HRPTECs and microvascular endothelium, respectively.

Haploblock localization

Haploview (Broad Institute) was used to download LD plots 500 kb up- and downstream from CKD-associated SNPs (pairwise comparisons of markers <2000 kbp apart). From these LD plots, haploblocks, containing CKD-associated SNPs, were extracted to evaluate target gene localization in relation to the CKD-associated susceptibility region.

Genetic annotation with the OMIM

The OMIM morbid map database was used to find mutant alleles that were associated with CKD. CKD-associated traits were mapped on the basis of the phenotype category queries "renal," "kidney," and "nephro." The gene set found in the OMIM was used to identify known CKD-associated genes in the list of genes generated via the 4C-seq approach.

Genetic annotation with the MGI

The MGI database was used to find monogenic mutant murine alleles that led to CKD-related traits. A data file containing the "approved gene name" and the "mouse genome database ID" was downloaded from the HUGO Gene Nomenclature Committee to identify the mutated murine genes in the MGI database that led to CKD-related traits. CKD related traits were mapped on the basis of the following phenotype categories: abnormal kidney morphology, abnormal kidney angiogenesis, urine abnormalities, blood abnormalities, glomerulus abnormalities, renal tubules abnormalities, podocyte abnormalities, kidney cysts, abnormal renal filtration, and other kidney related traits. The gene set found in the MGI was used to identify known CKD-associated genes in the list of genes generated via the 4C-seq approach.

EQTL Study in the GTEx portal

The GTEx portal database containing data on eQTL in 449 genotyped donors with expression data in 44 different tissues was used to list genes that significantly correlated in their expression with CKD-associated SNPs that colocalized with active DREs. Genes found via this approach were overlapped with the 4C-seq captured gene list to validate whether the 4C-seq approach indeed detected target genes that showed correlations in expression levels with the CKD-associated SNPs.

Pathway Analyses

Datasets were analyzed using QIAGEN IPA. IPA was used to study both enrichment of 4C-seq–identified genes in canonical pathways and upstream regulators of identified candidate genes independently for HRGECs and HRPTECs. P values were calculated on the basis of a right-tailed Fisher exact test calculated by IPA. Expression levels of upstream regulators of which target genes were found enriched in the candidate genes identified by 4C-seq were evaluated in a publically available microarray dataset, which was used to study gene expression in CKD in renal biopsy specimens (NCBI Gene Expression Omnibus accession no. GSE66494)[18].

References

1. Levey AS, Beto JA, Coronado BE, et al. Controlling the epidemic of cardiovascular disease in chronic renal disease: what do we know? What do we need to learn? Where do we go from here? National Kidney Foundation Task Force on Cardiovascular Disease. Am J Kidney Dis. 1998;32(5):853-906.
2. Kottgen A, Pattaro C, Boger CA, et al. New loci associated with kidney function and chronic kidney disease. Nat Genet. 2010;42(5):376-384.
3. Okada Y, Sim X, Go MJ, et al. Meta-analysis identifies multiple loci associated with kidney function-related traits in east Asian populations. Nat Genet. 2012;44(8):904-909.
4. Raychaudhuri S, Plenge RM, Rossin EJ, et al. Identifying relationships among genomic disease regions: predicting genes at pathogenic SNP associations and rare deletions. PLoS Genet. 2009;5(6):e1000534.
5. Li G, Vega R, Nelms K, et al. A role for Alstrom syndrome protein, alms1, in kidney ciliogenesis and cellular quiescence. PLoS Genet. 2007;3(1):e8.
6. Mo L, Huang HY, Zhu XH, et al. Tamm-Horsfall protein is a critical renal defense factor protecting against calcium oxalate crystal formation. Kidney Int. 2004;66(3):1159-1166.
7. Ghirotto S, Tassi F, Barbujani G, et al. The Uromodulin Gene Locus Shows Evidence of Pathogen Adaptation through Human Evolution. J Am Soc Nephrol. 2016.
8. Maurano MT, Humbert R, Rynes E, et al. Systematic localization of common disease-associated variation in regulatory DNA. Science. 2012;337(6099):1190-1195.
9. Williamson I, Hill RE, Bickmore WA. Enhancers: from developmental genetics to the genetics of common human disease. Dev Cell. 2011;21(1):17-19.
10. Visser M, Kayser M, Palstra RJ. HERC2 rs12913832 modulates human pigmentation by attenuating chromatin-loop formation between a long-range enhancer and the OCA2 promoter. Genome Res. 2012;22(3):446-455.
11. Bohle A, Grund KE, Mackensen S, et al. Correlations between renal interstitium and level of serum creatinine. Morphometric investigations of biopsies in perimembranous glomerulonephritis. Virchows Arch A Pathol Anat Histol. 1977;373(1):15-22.
12. Nangaku M. Chronic hypoxia and tubulointerstitial injury: a final common pathway to end-stage renal failure. J Am Soc Nephrol. 2006;17(1):17-25.
13. Kozakowski N, Herkner H, Bohmig GA, et al. The diffuse extent of peritubular capillaritis in renal allograft rejection is an independent risk factor for graft loss. Kidney Int. 2015;88(2):332-340.
14. Arnold CD, Gerlach D, Stelzer C, et al. Genome-wide quantitative enhancer activity maps identified by STARR-seq. Science. 2013;339(6123):1074-1077.
15. Mokry M, Hatzis P, Schuijers J, et al. Integrated genome-wide analysis of transcription factor occupancy, RNA polymerase II binding and steady-state RNA levels identify differentially regulated functional gene classes. Nucleic Acids Res. 2012;40(1):148-158.
16. Keller BJ, Martini S, Sedor JR, et al. A systems view of genetics in chronic kidney disease. Kidney Int. 2012;81(1):14-21.
17. Martovetsky G, Tee JB, Nigam SK. Hepatocyte nuclear factors 4alpha and 1alpha regulate kidney developmental expression of drug-metabolizing enzymes and drug transporters. Mol Pharmacol. 2013;84(6):808-823.
18. Nakagawa S, Nishihara K, Miyata H, et al. Molecular Markers of Tubulointerstitial Fibrosis and Tubular Cell Damage in Patients with Chronic Kidney Disease. PLoS One. 2015;10(8):e0136994.
19. Vernot B, Stergachis AB, Maurano MT, et al. Personal and population genomics of human regulatory variation. Genome Res. 2012;22(9):1689-1697.
20. Viscomi C, Spinazzola A, Maggioni M, et al. Early-onset liver mtDNA depletion and late-onset proteinuric nephropathy in Mpv17 knockout mice. Hum Mol Genet. 2009;18(1):12-26.

21. Griffin SV, Olivier JP, Pippin JW, et al. Cyclin I protects podocytes from apoptosis. J Biol Chem. 2006;281(38):28048-28057.
22. Xia M, Liu J, Wu X, et al. Histone methyltransferase Ash1l suppresses interleukin-6 production and inflammatory autoimmune diseases by inducing the ubiquitin-editing enzyme A20. Immunity. 2013;39(3):470-481.
23. Groger N, Vitzthum H, Frohlich H, et al. Targeted mutation of SLC4A5 induces arterial hypertension and renal metabolic acidosis. Hum Mol Genet. 2012;21(5):1025-1036.
24. Kirby A, Gnirke A, Jaffe DB, et al. Mutations causing medullary cystic kidney disease type 1 lie in a large VNTR in MUC1 missed by massively parallel sequencing. Nat Genet. 2013;45(3):299-303.
25. Koptides M, Hadjimichael C, Koupepidou P, et al. Germinal and somatic mutations in the PKD2 gene of renal cysts in autosomal dominant polycystic kidney disease. Hum Mol Genet. 1999;8(3):509-513.
26. Stolarczyk J, Carone FA. Effects of renal lymphatic occlusion and venous constriction on renal function. Am J Pathol. 1975;78(2):285-296.
27. Outeda P, Huso DL, Fisher SA, et al. Polycystin signaling is required for directed endothelial cell migration and lymphatic development. Cell Rep. 2014;7(3):634-644.
28. Buhling F, Rocken C, Brasch F, et al. Pivotal role of cathepsin K in lung fibrosis. Am J Pathol. 2004;164(6):2203-2216.
29. Lopez-Guisa JM, Cai X, Collins SJ, et al. Mannose receptor 2 attenuates renal fibrosis. J Am Soc Nephrol. 2012;23(2):236-251.
30. Sidaway JE, Davidson RG, McTaggart F, et al. Inhibitors of 3-hydroxy-3-methylglutaryl-CoA reductase reduce receptor-mediated endocytosis in opossum kidney cells. J Am Soc Nephrol. 2004;15(9):2258-2265.
31. Eelen G, de Zeeuw P, Simons M, et al. Endothelial cell metabolism in normal and diseased vasculature. Circ Res. 2015;116(7):1231-1244.
32. Chambers JC, Zhang W, Lord GM, et al. Genetic loci influencing kidney function and chronic kidney disease. Nat Genet. 2010;42(5):373-375.
33. Suhre K, Shin SY, Petersen AK, et al. Human metabolic individuality in biomedical and pharmaceutical research. Nature. 2011;477(7362):54-60.
34. Yu B, Zheng Y, Alexander D, et al. Genetic determinants influencing human serum metabolome among African Americans. PLoS Genet. 2014;10(3):e1004212.
35. Birnbaum RY, Clowney EJ, Agamy O, et al. Coding exons function as tissue-specific enhancers of nearby genes. Genome Res. 2012;22(6):1059-1068.
36. van de Werken HJ, de Vree PJ, Splinter E, et al. 4C technology: protocols and data analysis. Methods Enzymol. 2012;513:89-112.
37. Ji H, Jiang H, Ma W, et al. An integrated software system for analyzing ChIP-chip and ChIP-seq data. Nat Biotechnol. 2008;26(11):1293-1300.
38. Beyer S, Kristensen MM, Jensen KS, et al. The histone demethylases JMJD1A and JMJD2B are transcriptional targets of hypoxia-inducible factor HIF. J Biol Chem. 2008;283(52):36542-36552.
39. Consortium GT. Human genomics. The Genotype-Tissue Expression (GTEx) pilot analysis: multitissue gene regulation in humans. Science. 2015;348(6235):648-660.

Supplemental Figures

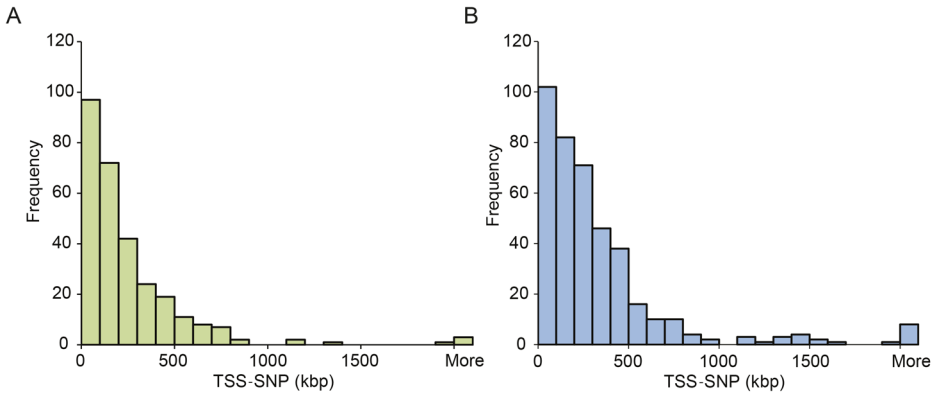

Supplemental Figure 1. The majority of genes identified with 4C-seq were positioned up to 500kbp from the chronic kidney disease (CKD) associated SNP locus. Graph shows the distance from the SNP to the TSS of the target genes found with 4C in HRGECs (X-axis), expressed as the number of target genes (frequency on Y-axis) per 100kbp. The majority of target genes was positioned up to 500kbp from the SNP, but occasionally candidate genes were found at locations over 1.5mb from the SNP locus (A). The TSS of the majority of candidate genes found with 4C in HRPTECs was positioned up to 500kbp from the SNP position, but some candidate genes were found at locations over 1.5mbp from the SNP locus (B).

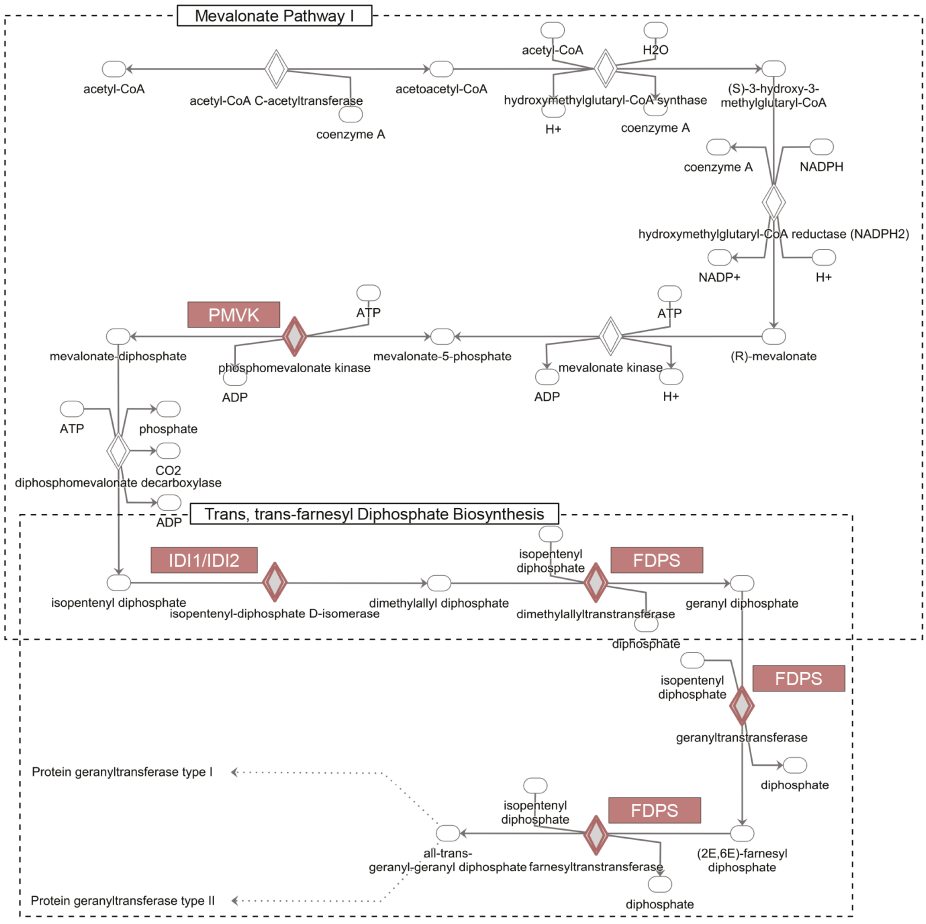

Supplemental Figure 2. Target genes of DREs colocalizing with chronic kidney disease-associated SNPs, highlighted in red, are enriched in the mevalonate pathway and the trans, trans-farnesyl diphosphate biosynthesis pathway (adapted from IPA).

Supplemental Tables

Supplemental tables can be downloaded from: http://bit.ly/36tc2sa

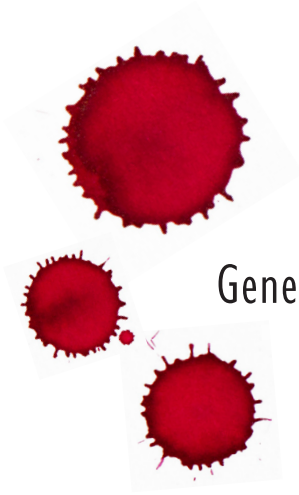

Chapter 8

General discussion

The aim of this thesis was to unravel molecular mechanisms underlying cardiovascular health and disease, focusing on two different research topics where anchoring junctions have a prominent role: (1) extracellular matrix (ECM) and (2) angiogenesis. Vascular cells deposit their own matrix molecules and the composition varies depending on the cell type, making it a tissue-specific structure in which cells are embedded. This process is highly dynamic and the ECM is constant being remodeled, especially during development and disease. Next to cell-matrix adhesion, the interaction between vascular cells plays an even bigger role during angiogenesis. This cell-cell adhesive strength is constant being remodeled in order to allow vessel sprouting and subsequent maturation into a functional network.

Extracellular matrix

The ECM is an essential part of metazoan organization into defined tissue layers. ECM synthesis and secretion already begins at the earliest stages of development by embryonic cells. These secreted components are vital for normal morphogenesis and organ development and their roles go beyond simple adhesive and space filling functions. They are critically important for cell processes including fate decisions, proliferation, differentiation, survival and migration[1,2]. Distinct ECM composition and associated molecular pathways must underlie the formation of each tissue layer, given their unique structure and function. The mature ECM remains highly dynamic, as it undergoes constant controlled remodeling in order to maintain tissue homeostasis. Disrupted tissue homeostasis by aberrant ECM remodeling is associated with many pathological processes, including fibrosis and cancer[2].

Due to the crucial roles played by the ECM in multicellular life, there is an urgent need to characterize the unique ECM composition of different tissues and to describe the compositional changes during development and disease. This spatiotemporal ECM map in both health and disease will aid in the deeper understanding of many developmental and pathological processes.

Proteomic analyses reveal specific extracellular matrix niche important for renal development

The first part of this thesis focused on unraveling the renal ECM composition and associated molecular pathways underlying cell-matrix adhesion. Previous studies focused on unraveling the mature human renal ECM, in particular the glomerular ECM[3-7]. This thesis sought to address a gap in current knowledge about changes

of the human renal ECM during development. ECM proteins overrepresented during renal development could be mechanistically relevant for promoting kidney organogenesis. This active fetal microenvironment matches the environment for tissue growth, adhesion and differentiation needed in 3D renal constructs.

In this thesis, two comprehensive proteomic analyses were performed comparing the ECM proteins present in either the developing kidney (**Chapter 2**) or renal artery (**Chapter 3**) with the corresponding adult tissue. Analyzing these two tissues separately allows for the identification of key ECM proteins involved in either nephrogenesis or angiogenesis. A total of 99 and 101 different ECM proteins were detected in the kidney and renal artery, respectively. The majority of these proteins form an overlapping core, however some ECM proteins were found to be specific for either the human kidney or renal artery during development (Figure 1). For example, specific collagen α chains are linked to the fetal kidney or renal artery. COL2A1 was only detected in the fetal kidney, whereas COL6A6 is specific for the fetal renal artery. *COL6A6* encodes an α chain of a large collagen present in the basal lamina, where it regulates cell-matrix interactions. It has been shown that type VI collagen has pro-angiogenic capacities by stimulating both the survival of endothelial cells (ECs) and pericyte maturation during sprouting, indicating that collagen VI-dependent basal lamina assembly is important for vessel development[8].

Other identified ECM proteins specific for the fetal renal artery have been linked before to angiogenesis as well (Figure 1, **Chapter 3**). For example, EMILIN2 is a glycoprotein involved in both the formation of elastic fibers and cell adhesion[9]. Recently, it has also been linked to angiogenesis by its capacity to directly bind epidermal growth factor receptor (EGFR), thereby enhancing interleukin-8 production and subsequently the proliferation and migration of ECs. *Emilin2* null mice exhibit delayed vascular growth both during embryonic and tumor development, pointing at EMILIN2 as a key ECM cue affecting vessel formation[10]. Furthermore, *ITIH3* encodes a serum carrier protein of hyaluronan and a binding protein between hyaluronan and other ECM proteins. In turn, hyaluronan has a dual function in angiogenesis: depending on its molecular mass, it can either promote or inhibit angiogenesis[11]. Lastly, *ANGPTL6* encodes Angiopoietin-related growth factor (AGF), which has been identified as a direct pro-angiogenic factor that promotes chemotactic activity of ECs and subsequent neovascularization[12]. It plays

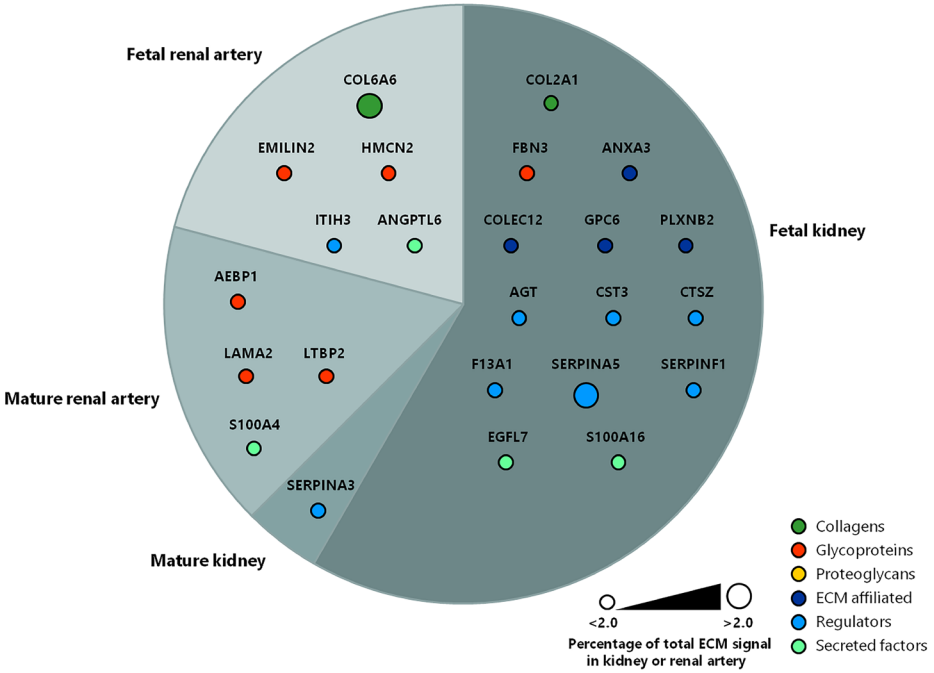

Figure 1. Specific fetal and mature extracellular matrix proteins for the human kidney and renal artery. Extracellular matrix (ECM) proteins were identified in human kidney and renal artery samples of both fetal and mature origin by mass-spectrometry based proteomics. The obtained proteins were classified as collagens, glycoproteins, proteoglycans, ECM affiliated, regulators or secreted factors and colored and arranged accordingly. The pie chart visualizes the ECM proteins only found in either the fetal kidney, mature kidney, fetal renal artery or mature renal artery by comparing the four associated ECM proteomes (for details see Chapters 2 and 3). Each node represents a single protein and is labeled with the gene name. Node size is proportional to the abundance of the protein within either the kidney or renal artery ECM proteome (less than 2% or more than 2% of the total ECM signal in at least one dataset (fetal or mature)).

an important role during murine vascular development, as mice overexpressing AGF show an increase in microvessel density and vascular pearmeability[13]. For the remaining ECM protein specific for the fetal renal artery, HMCN2, a role in angiogenesis has not been described yet. *HMCN2* encodes hemicentin-2, which belongs to the fibulin family of ECM proteins that play a pivotal role during development of various vertebrate tissues. In concordance with the proteomic data of this thesis, hemicentins were detected before in the ECM of blood vessels[14]. Furthermore, family member fibulin-1 is associated with developmental defects of blood vessels[15], making hemicentin-2 an interesting candidate for future research. This validation suggests that ECM enrichment and subsequent mass-

spectrometry-based proteomics is capable of identifying important ECM proteins for renal development.

Even more ECM proteins identified in this thesis are specific for the developing human kidney (Figure 1, **Chapter 2**), of which some have been previously linked to nephrogenesis. For example, *PLXNB2* encodes plexin-B2, which is highly expressed in the developing kidney at the immature glomeruli, metanephric mesenchyme and ureteric epithelium[16]. Deletion of *Plxnb2* during murine development results in hypoplastic kidneys due to reduced cell proliferation in the ureteric epithelium[17]. In more detail, plexin-B2 signaling is needed to correctly orient the mitotic spindle[18]. Another example is AGT, which is the sole precursor of all angiotensin peptides and is cleaved by renin in response to lowered blood pressure. Besides low blood pressure, AGT-deficient mice exhibit impaired kidney development due to hydronephrosis and subsequent atrophy of the renal papilla[19,20]. Direct involvement of GPC6 in nephrogenesis has not been described yet, however in concordance with this thesis, prominent GPC6 expression was found in the developing kidney. This gene encodes glypican-6 that localizes in mesenchymal cells found at the metanephric cap and surrounding the ureteric branches[21]. GPC6 overlaps with the expression pattern of bone morphogenetic protein-7 (BMP-7) and mice deficient in BMP-7 show a gradual cessation of nephrogenesis associated with apoptosis of the metanephric mesenchyme[22,23], making glypican-6 another interesting candidate for future research. In addition, *Serpinf1* and FBN3 were found expressed at elevated levels before in the embryonic kidney[24,25]. In concordance with the kidney matrisome described in this thesis, *SERPINF1* mRNA is expressed in human fetal kidneys and its level declines in adult kidneys[26]. This validation enhances confidence in the remaining identified components of the fetal renal matrisome (Figure 1) and suggests a renal development function for these proteins that have not been previously implicated in this process. Further research is needed to elucidate their putative role in renal development and their potential to be implemented in scaffolds for 3D renal constructs.

The obtained renal matrisome described in **Chapters 2 and 3** has been used to identify major players that could be of potential use in scaffolds for renal tissue engineering. Based on these proteomic analyses, EMILIN1 was proposed as an interesting candidate. There is a striking difference between the expression of EMILIN1 in the fetal matrisome compared to the mature in both the kidney and

renal artery. In the fetal kidney, the EMILIN1 signal comprises 6.8% of the total ECM signal, compared to only 1.5% of the mature ECM. In the fetal renal artery, 3.9% of the total fetal ECM signal is EMILIN1, compared to 0.8% of the mature ECM. These kind of expression levels are more general for space filling ECM components, such as collagens and fibrillins. EMILIN1 is located at elastic fibers, where its main function is to bind integrins[9,27]. Many cell types depend on this interaction for cell adhesion, migration and proliferation[28-31]. Indeed, cell biological analyses described in **Chapter 2** show differences in focal adhesions and migration of renal cells cultured on EMILIN1-depleted ECM compared to cells cultured on ECM containing EMILIN1. In contrast to previous studies, renal epithelial cells grown on EMILIN1-depleted ECM exhibit a weaker adhesion pattern, characterized by a decrease in focal adhesion points and associated stress fibers. This adhesive phenotype promotes renal cell migration. However, ECs cultured on the same EMILIN1-depleted matrix did not show any differences in adhesion and migration compared to control cells (**Chapter 3**). It seems that the effect of EMILIN1 on cell adhesion and migration can either be enhancing, reducing or neutral depending on the interacting cell type, most likely due to cell-specific integrin expression profiles (see Chapter 1, Figure 2). Most cells express several distinct integrins and many integrins are expressed predominantly in certain cell types. The weaker adhesion pattern described in the literature was attributed to the gC1q domain of EMILIN1 interacting with α4/α9/β1 integrins[30-32]. It was speculated in **Chapter 2** that the characteristic adhesive phenotype of renal cells to EMILIN1 involves other integrin α-subunits than α4 or α9. Further research is needed to verify this important contradicting statement that other cellular receptors for EMILIN1 might exist using integrin blocking antibodies. It is also important to further validate that the specific renal adhesion pattern is really due to the direct binding with EMILIN1 and not indirectly via alterations in expression or conformational changes of other ECM components, such as fibronectin. Nevertheless, attention must be given when using cell-based constructs if the selected cells for embedding have a compatible receptor profile with the matrix scaffold. Vice versa, the composition of the ECM is critical for regulating cell phenotype.

Matrigel is by far the most predominant scaffold used in 3D renal cultures. However, Matrigel does not recapitulate the complex renal microenvironment during development, nor does it reflect the exact composition and stiffness of the native renal ECM. Highly-hydrated crosslinked polymer networks, i.e. hydrogels,

are the prime candidate as a basic scaffolding system. These hydrogels can either be based on natural components, such as collagen, fibrin or hyaluronic acid (HA), or on non-natural materials, such as Poly(Ethylene Glycol) (PEG). The mechanical properties of hydrogels can be easily modified and organ-specific ECM cues can be conveniently attached to guide the desired cell behavior. For example, introducing peptide motifs of the ECM-associated protein calponin (CNN) within an elastin polymer triggers integrin-specific EC survival and function, such as adhesion, spreading and migration[33]. Incorporating epidermal growth factor (EGF), a potent mitogen for several cell types, into a collagen hydrogel enhances survival and proliferation of neural cells[34]. Presentation of BMP-2 in gelatin hydrogels enhances osteogenic differentiation of adipose-derived stem cells when compared to free growth factor presented in the media[35]. A collagen hydrogel carrying fibroblast growth factor (FGF) enhances osteogenic differentiation as well and increases the proliferation of mesenchymal stem cells[36]. Lastly, EGF and insulin-like growth factor-1 (IGF-1) polymerized within a fibrin hydrogel promote amylase production in salivary cells[37]. These are all examples of improved biomaterials using ECM cues that mimic more the native microenvironment. Further research is necessary to determine if hydrogels loaded with EMILIN1 might be appropriately bioactive for stimulating tissue growth and adhesion in 3D renal constructs.

Extracellular matrix reflects dilated cardiomyopathy progression

Characterizing ECM components and understanding key ECM remodeling pathways underlying specific diseases offer promising possibilities for therapeutic intervention. Preclinical studies targeting ECM remodeling are promising. For example, injecting an ECM hydrogel derived from decellularized myocardial tissue into porcine and murine models of myocardial infarction improves cardiac healing and function. This ECM hydrogel did not provoke an immune response, providing a strong basis to move towards clinical studies[38,39]. Furthermore, the proteoglycan perlecan has been shown to be neuroprotective after acute stroke by promoting the secretion of VEGF and subsequent angiogenesis in rodents[40]. Strategies to target enzymes involved in ECM remodeling are also promising. For example, inhibiting lysyl oxidase-like 2 (LOXL2) in mouse models of liver and lung fibrosis resulted in a marked reduction of activated fibroblasts, decreased production of growth factors and inhibited the transforming growth factor β (TGF-β) pathway[41]. However, a deeper understanding of the diverse ECM pathways and components involved in specific diseases is needed to uncover new targets for future therapies.

Chapter 4 of this thesis provides a transcriptome-based catalogue of ECM changes associated with dilated cardiomyopathy (DCM). DCM is a relatively common heart muscle disease characterized by left ventricular dilation and dysfunction. Myocardial fibrosis is a major feature of this disease and therefore it is inevitable that corresponding ECM changes are involved. Classical ECM changes in DCM include a consistent increase in collagen type I and III synthesis and deposition[42-48], resulting in a stiffer matrix. Data from this thesis complements these findings, as additional collagen types were found to be overrepresented in the dilated left ventricle. A considerable part of the described DCM matrisome is represented by ECM regulators and secreted factors. Excessive ECM synthesis and stabilization was hypothesized to be the joint outcome from the ECM regulators. This emphasizes, together with the known increase in collagen, that the balance in DCM is shifted towards a stiffer and denser matrix in an attempt to strengthen the dilated heart wall. The combined effect of the secreted factors identified was assumed to alter fibroblast activity. Recent studies have indeed linked fibroblast activation to DCM progression[49-53]. These validate the hypothesis mentioned in **Chapter 4** and show that indeed the DCM microenvironment promotes fibroblast proliferation, contraction and production of growth factors[50-52]. Within the identified core components, the increase of both fibronectin and several regulators of its deposition and in integrin signaling hints towards enhanced cell adhesion in DCM. In line with **Chapter 4**, a recent transcriptome analysis of human heart failure revealed enrichment of cell adhesion pathways in DCM[54].

Overall, the DCM matrisome described in this thesis reflects the causal roles of extracellular matrix synthesis and stabilization, fibroblast activation and cellular adhesion in disease progression. This key ECM remodeling opens possibilities for therapeutic intervention by targeting specific ECM components involved in a complex signaling nexus. Attention must be given to correctly timing the therapy as well, given that the ECM is constantly being remodeled. This ECM catalogue is a static snapshot of the human DCM heart. Focus of future experiments should lie on creating a spatiotemporal map of ECM composition in DCM, as this would yield a more comprehensive story.

Angiogenesis

Angiogenesis is a critical process during development and protective responses, such as wound healing and inflammation. Aberrant angiogenesis occurs in a

wide variety of pathologic settings, such as cancer, psoriasis, arthritis, blindness, cardiovascular disease and nephropathy[55] and these diseases may be alleviated by inhibiting or stimulating angiogenic processes. This hypothesis has prompted many to unravel the molecular mechanisms that underlie angiogenesis with the goal to identify pathways that constitute potential targets for anti- or pro-angiogenic therapies.

Current angiogenic therapies mainly target the vascular endothelial growth factor (VEGF) pathway. Anti-angiogenic therapies targeting VEGF are being employed against metastatic tumors, which need an abundance of nutrients and oxygen to grow. Tumor angiogenesis is widely triggered by high levels of VEGF, therefore VEGF has been targeted in different cancers in combination with chemotherapy. For example, in patients with metastatic renal cell carcinoma, this combination resulted in improvement of the progression-free survival[56]. However, the anti-VEGF treatment did not increase overall survival. Even though a decrease in tumor size was observed, patients experienced disease relapse[57]. Pro-angiogenic therapies targeting the VEGF pathway are being explored as a treatment option for cardiovascular diseases. Here, the VEGF-axis is targeted for alleviating ischemia in either coronary or peripheral artery disease. In several clinical trials, VEGF protein or plasmid was administered to induce therapeutic angiogenesis in the myocardium. However, these clinical trials of VEGF delivery have not proven to be successful, with little to no functional or perfusion improvement[58]. Thus, targeting the VEGF pathway alone is only limitedly effective. Additional targeting of interconnected and compensatory pathways is required to maximize the angiogenic potential. Therefore, focus of current research lies on identifying these additional pathways and their players.

Novel molecular players involved in VE-cadherin turnover across adherens junctions

The second part of this thesis focused on unraveling interconnected angiogenic pathways underlying endothelial cell-cell adhesion, in particular the pathways emanating from adherens junctions (AJs). An important aspect of angiogenesis is the ability of ECs to regulate the availability of VE-cadherin at AJs. A reduction of membrane-bound VE-cadherin decreases the adhesive strength. This disruption of AJs is necessary to allow EC migration during sprouting angiogenesis. When new sprouts are established, the AJs are tightened again by recruiting VE-cadherin back

to the plasma membrane, ensuring vascular stability. Endocytosis and associated recycling or degradation pathways control the rate of VE-cadherin turnover[59,60]. Although endothelial endocytosis plays such a critical role during angiogenesis, the overview of important regulators is far from complete.

Rab GTPases are well known for regulating vesicular transport during the endocytosis process, especially controlling vesicle docking and fusion[61]. Alterations in Rab GTPases have been correlated with the pathogenesis of cancer and cardiovascular diseases[62-64]. For example, Rab25 expression is reduced in esophageal cancer and ectopic overexpression of Rab25 inhibits *in vivo* xenograft tumor development and angiogenesis[64]. Another family of endocytic adaptor proteins has been proposed as a potential target for anti-angiogenic therapy. Epsins are expressed in ECs to attenuate VEGFR2 signaling and subsequent angiogenesis by promoting endocytic degradation of VEGFR2[65]. The tumor vasculature of epsin-knockout mice was found to be enlarged, disorganized, poorly perfused and with insufficient mural cell coverage. Loss of endothelial epsin impairs the lysosomal degradation of VEGFR2, resulting in excessive VEGF signaling and subsequent production of nonfunctional leaky tumor vessels, without affecting the quiescent normal blood vessels[66].

This thesis reports two novel proteins involved in regulating endothelial endocytosis with potential to be implemented in angiogenic therapies: CMTM3 and CMTM4. These proteins are members of the CKLF-like MARVEL transmembrane domain-containing (CMTM) family and are closely located on chromosome 16q22, a main tumor suppressor locus. The results described in this thesis demonstrate that both CMTM3 (**Chapter 5**) and CMTM4 (**Chapter 6**) are essential for angiogenesis. Silencing of either CMTM3 or CMTM4 in ECs severely impairs vascular growth *in vitro* in a 3D angiogenesis assay and *in vivo* in developing zebrafish larvae. The MARVEL transmembrane domain present in all CMTM family members implies that they might be involved in vesicle trafficking[67]. Indeed, colocalization experiments depicted in **Chapters 5 and 6** show that CMTM3 and CMTM4 are part of the endothelial endocytic pathway. CMTM3 seems to be part of the early endocytic machinery, as it colocalizes mainly with clathrin^{+} and EEA1^{+} vesicles and increases their presence. This is in concordance with results published by Yuan *et al*, showing that CMTM3 is involved in early endosome trafficking in gastric cancer[68]. CMTM4 on the other hand shows strong colocalization with Rab4^{+} vesicles and increases their presence, suggesting that CMTM4 functions more downstream at the rapid

recycling route. In addition, both CMTM3 and CMTM4 colocalize with VE-cadherin.

What does this mean for the endothelial barrier function? Internalization assays and TEER experiments described in **Chapters 5 and 6** show that although both CMTM3 and CMTM4 are involved in internalizing VE-cadherin, their impact on endothelial barrier function differs. CMTM3 stimulates VE-cadherin and F-actin reorganization at AJs into a discontinuous activated state characteristic for a permeable endothelium with interrupted AJs along a zigzagged junction line. On the other hand, CMTM4 stimulates a stable linear resting state characteristic for a strong endothelial barrier with non-interrupted AJs along a smooth junction line. Thus, both CMTM3 and CMTM4 regulate angiogenesis, however they participate at a different location along the VE-cadherin endocytosis track. CMTM3 promotes EC barrier permeability by stimulating VE-cadherin internalization to early endosomes, whereas CMTM4 promotes fast recovery of the endothelial barrier by stimulating rapid recycling of endocytosed VE-cadherin back to the plasma membrane (Figure 2). Both these steps are crucial for sprouting angiogenesis and subsequent formation of a mature and stable vessel network.

CMTM3 and CMTM4 seem to collaborate in a novel molecular route involving VE-

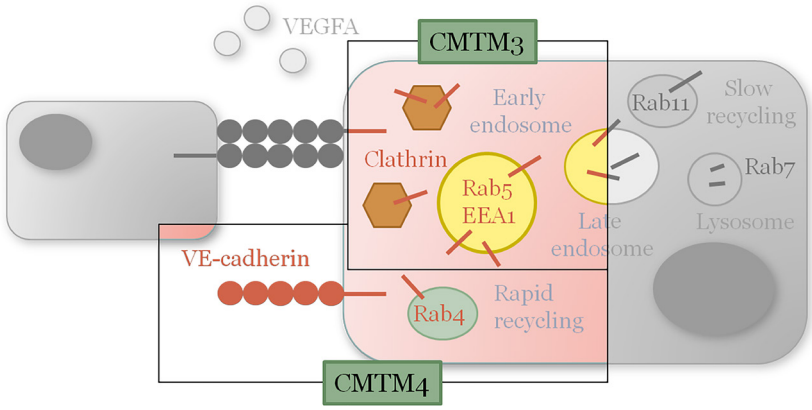

Figure 2. Simplified overview of the working mechanism of CMTM3 and CMTM4 in the endocytosis of VE-cadherin. VEGFA stimulates rapid endocytosis of VE-cadherin and the subsequent disassembly of adherens junctions. CMTM3 is involved in the early stages of VE-cadherin internalization, where VE-cadherin is taken up in clathrin-coated vesicles that fuse with early endosomes. From these vesicles, VE-cadherin is sorted for recycling or degradation. CMTM4 is involved in the rapid recycling of VE-cadherin back to the plasma membrane in order to tighten adherens junctions.

cadherin internalization and recycling, with their own specialized function along the endocytosis track. This raises the question if more CMTM family members are involved. Results described in **Chapter 5** hint towards an additional participation of CMTM8, since mural cell interaction induces expression of *CMTM3*, *CMTM4* and *CMTM8* in ECs. During angiogenesis, the maturation of nascent vessels requires recruitment of mural cells, which together with endothelial cell-cell adhesion, stabilize the neovasculature[69]. In line with this notion, Jin *et al* demonstrated that CMTM8 is involved in the endocytosis of EGFR, thereby regulating its signaling and subsequent cell proliferation[70].

Further research is needed to determine which paracrine factors from pericytes trigger the activation of CMTM family members in the neighboring ECs and if this process can be altered and implemented in angiogenic therapies. The strong paracrine relationship between mural cells and ECs is hypothesized to be part of the problem that targeting the VEGF pathway alone has not been as effective as anticipated. Mural cells play a vital role in supporting developing neovessels. In vascularized tumors, where the aim is to target angiogenesis to promote neoplasm decline[71], mural cell-covered vessels are considered mature and stable as opposed to the unstable and immature vessels that lack this coverage. It is plausible that these supporting cells protect the neighboring ECs from the VEGF therapy by secreting paracrine factors, such that only the immature vessels are susceptible for treatment[72]. In support of this hypothesis, blocking both VEGF and Platelet Derived Growth Factor β (PDGF-β), a mural cell recruiting factor expressed by ECs, results in a more effective therapy for certain tumors compared to blocking VEGF alone[73]. To complement this hypothesis, it is plausible that mural cells stimulate the production of CMTMs in the neighboring ECs, thereby counteracting anti-VEGF therapy by activating a compensatory pathway. Like VEGF, activating the CMTM pathway in ECs promotes angiogenesis by stimulating VE-cadherin turnover. This underscores the importance of targeting mural cells as well to enforce the desired behavior from the neighboring ECs.

Emerging angiogenic molecular pathways associated with chronic kidney disease from 4C-seq hits

Genome wide association studies (GWASs) hold a great potential in unraveling molecular mechanisms and their players. Traditionally, the most straightforward approach in interpreting a GWAS signal is to link the single nucleotide

polymorphism (SNP) to the nearest gene. However, it is estimated that two thirds of the predicted target genes are not the nearest annotated gene to the associated GWAS SNP[74]. In **Chapter 7**, a new method of GWAS interpretation is presented based on SNPs colocalizing with DNA regulatory elements (DREs) to complement the traditional method and to enhance the value of GWAS findings. DREs activate or repress gene transcription and many are situated up to a million base pairs from their target genes, often in large gene-poor areas to help ensure regulatory specificity[75]. Combining SNP and DRE data will aid in unraveling novel DNA regulatory mechanisms linked to disease onset and progression.

Multiple GWASs have established SNPs as genetic risk factors for chronic kidney disease (CKD) and linked various of these to genes involved in nephrogenesis, podocyte function, angiogenesis, solute transport and metabolic functions of the kidney[76,77]. These SNPs are located in coding regions. For many of the identified CKD associated SNPs that are not directly located in or near coding regions, the causal contribution to CKD onset and progression is difficult to interpret. The study described in **Chapter 7** complements these GWAS findings by using circular chromosome conformation capture-sequencing (4C-seq) to identify potential target genes associated through 3D genomic interactions with DREs that contain CKD-associated SNPs. Importantly, DREs regulate gene expression in a cell-specific manner and since CKD is associated with both tubulointerstitial damage and loss of peritubular and glomerular capillaries[78-80], 4C-seq was performed to study chromatin interactions in both human renal proximal tubular epithelial cells (HRPTECs) and glomerular endothelial cells (HRGECs).

4C analyses indentified direct interactions of CKD associated SNPs with the transcription start site of 304 target genes. 124 of these genes were identified in both cell types. In regard to angiogenesis, *VEGFA* is among the overlapping interacting genes, which encodes a major regulator of angiogenesis and vascular permeability[81]. In the kidney, podocytes produce large amounts of VEGFA required for the development and maintenance of the glomerular filtration barrier. Inhibition of VEGF leads to glomerular endothelium damage in animal models and to proteinuria in patients[82]. Even more interesting are the 75 target genes detected only in HRGECs, underscoring the cell type specific activity of DREs and the importance of sequencing multiple renal cell types. Among these endothelium-related genes, the most remarkable finding is the target gene *PKD2*,

which encodes polycystin-2 that together with polycystin-1 functions as a channel spanning the cell membrane of renal tubular epithelial cells to transports ions, particularly calcium ions, into the cell[83]. Mutations in the *PKD2* gene lead to the formation of fluid-filled cysts in the renal tubules[84]. Besides this well-know tubular epithelial consequence, *PKD2* mutations have been linked to a vascular phenotype as well. *Pkd2* mutant mouse embryos exhibit reduced lymphatic vascular branching and density, eventually causing profound edema[85]. At the core of this phenotype is an EC defect in directional migration due to failure of developing a front-rear polarity[85]. This renal lymphatic vasculature is needed for proper renal urea handling[86] and interestingly, the SNP linked to *PKD2* is also associated with high serum urate concentrations. It has been shown that serum urate is not only a readout for renal dysfunction, but that high levels of uric acid are also linked to oxidative stress and EC dysfunction[87,88]. Altogether, these studies confirm the endothelial link of *PKD2* identified by 4C-seq.

Another interesting endothelium related-finding is the target gene *MIR147B* that has recently been linked to angiogenesis. This microRNA is able to decrease the expression of disintegrin and metalloproteinase domain-containing protein 15 (ADAM15), a regulator of endothelial barrier function[89]. During inflammation and sepsis, ADAM15 induces endothelial barrier permeability and promotes neutrophil and monocyte transendothelial migration. The underlying molecular mechanism involves dissociation of endothelial AJ molecules, such as VE-cadherin and γ-catenin. Upregulation of ADAM15 has been linked to atherosclerotic lesion development and pulmonary edema following septic injury[90-92]. These characteristics make ADAM15 an attractive therapeutic target in angiogenic diseases, which could be accomplished by using ADAM15-targeting microRNAs such as MIR147B. Thus, the compromised expression of *MIR147B* identified by 4C-seq could contribute to the endothelial dysfunction associated with CKD.

These examples illustrate the potential relevance of the candidate genes indentified by 4C-seq for unraveling angiogenic pathways underlying CKD. Further functional research is needed to elucidate the consequences of other associated target genes and turn the hypotheses that emerge from GWAS in CKD to clinically useful information.

Concluding remarks

Overall, the data generated in this thesis forms a platform for future studies on the extracellular matrix and angiogenesis. In the first part of this thesis, several ECM datasets were generated using "-omic" approaches that are powerful resources for the research community. A comparison between the human fetal and mature ECM in both kidney and renal artery revealed a specific ECM niche during development (Figure 1). The resulting tissue-specific ECM catalogues provide valuable knowledge for improving current scaffolds in 3D renal constructs to better mimic the native tissue. EMILIN1 was highlighted as a promising component by its capacity to stimulate renal cell adhesion. Further studies are required to unravel the potential of other identified ECM proteins for the tissue engineering field. Furthermore, a DCM matrisome is presented in this thesis reflecting disease progression through key ECM remodeling pathways. It is likely that among these ECM components are novel diagnostic markers or therapeutic targets.

The second part of this thesis described two different approaches for unraveling angiogenic pathways and their players. Firstly, a novel angiogenic pathway is identified involving CMTM3 and CMTM4 that seem to possess angiogenic properties by stimulating VE-cadherin turnover (Figure 2). This novel fundamental finding holds promising therapeutic perspectives to understand and treat angiogenic diseases, which may require a broader approach of inhibiting or stimulating multiple pathways simultaneously. Unraveling which paracrine factors from pericytes trigger the activation of CMTM family members in the neighboring ECs and if this process can be altered would be the next important step. Secondly, an extensive overview of DREs harboring a CKD-associated SNP and their target genes in different renal cell types is presented in this thesis, including genes that potentially influence angiogenesis. These results further our understanding of the molecular mechanisms underlying CKD that can aid in the development of future biomarkers or therapies.

References

1 Rozario, T. & DeSimone, D. W. The extracellular matrix in development and morphogenesis: a dynamic view. Developmental biology 341, 126-140 (2010).

2 Bonnans, C., Chou, J. & Werb, Z. Remodelling the extracellular matrix in development and disease. Nature reviews. Molecular cell biology 15, 786-801 (2014).

3 Hobeika, L., Barati, M. T., Caster, D. J., McLeish, K. R. & Merchant, M. L. Characterization of glomerular extracellular matrix by proteomic analysis of laser-captured microdissected glomeruli. Kidney international 91, 501-511 (2017).

4 Lennon, R. et al. Global analysis reveals the complexity of the human glomerular extracellular matrix. Journal of the American Society of Nephrology : JASN 25, 939-951 (2014).

5 Yoshida, Y. et al. Two-dimensional electrophoretic profiling of normal human kidney glomerulus proteome and construction of an extensible markup language (XML)-based database. Proteomics 5, 1083-1096 (2005).

6 Cui, Z. et al. Profiling and annotation of human kidney glomerulus proteome. Proteome science 11, 13 (2013).

7 Byron, A. et al. Glomerular cell cross-talk influences composition and assembly of extracellular matrix. Journal of the American Society of Nephrology : JASN 25, 953-966 (2014).

8 You, W. K., Bonaldo, P. & Stallcup, W. B. Collagen VI ablation retards brain tumor progression due to deficits in assembly of the vascular basal lamina. The American journal of pathology 180, 1145-1158 (2012).

9 Colombatti, A. et al. The EMILIN/Multimerin family. Frontiers in immunology 2, 93 (2011).

10 Paulitti, A. et al. The ablation of the matricellular protein EMILIN2 causes defective vascularization due to impaired EGFR-dependent IL-8 production affecting tumor growth. Oncogene 37, 3399-3414 (2018).

11 Pardue, E. L., Ibrahim, S. & Ramamurthi, A. Role of hyaluronan in angiogenesis and its utility to angiogenic tissue engineering. Organogenesis 4, 203-214 (2008).

12 Oike, Y., Yasunaga, K. & Suda, T. Angiopoietin-related/angiopoietin-like proteins regulate angiogenesis. International journal of hematology 80, 21-28 (2004).

13 Oike, Y. et al. Angiopoietin-related growth factor (AGF) promotes angiogenesis. Blood 103, 3760-3765 (2004).

14 Xu, X., Dong, C. & Vogel, B. E. Hemicentins assemble on diverse epithelia in the mouse. The journal of histochemistry and cytochemistry : official journal of the Histochemistry Society 55, 119-126 (2007).

15 Kostka, G. et al. Perinatal lethality and endothelial cell abnormalities in several vessel compartments of fibulin-1-deficient mice. Molecular and cellular biology 21, 7025-7034 (2001).

16 Perala, N. M., Immonen, T. & Sariola, H. The expression of plexins during mouse embryogenesis. Gene expression patterns : GEP 5, 355-362 (2005).

17 Perala, N. et al. Sema4C-Plexin B2 signalling modulates ureteric branching in developing kidney. Differentiation; research in biological diversity 81, 81-91 (2011).

18 Xia, J. et al. Semaphorin-Plexin Signaling Controls Mitotic Spindle Orientation during Epithelial Morphogenesis and Repair. Developmental cell 33, 299-313 (2015).

19 Taniguchi, K. et al. Pathologic characterization of hypotensive C57BL/6J-agt: angiotensinogen-deficient C57BL/6J mice. International journal of molecular medicine 1, 583-587 (1998).

20 Kakinuma, Y. et al. Developmental stage-specific involvement of angiotensin in murine nephrogenesis. Pediatric nephrology (Berlin, Germany) 13, 792-799 (1999).

21 Veugelers, M. et al. Glypican-6, a new member of the glypican family of cell surface heparan sulfate proteoglycans. The Journal of biological chemistry 274, 26968-26977 (1999).

22 Dudley, A. T., Lyons, K. M. & Robertson, E. J. A requirement for bone morphogenetic

protein-7 during development of the mammalian kidney and eye. Genes & development 9, 2795-2807 (1995).
23 Luo, G. et al. BMP-7 is an inducer of nephrogenesis, and is also required for eye development and skeletal patterning. Genes & development 9, 2808-2820 (1995).
24 Schwab, K. et al. A catalogue of gene expression in the developing kidney. Kidney international 64, 1588-1604 (2003).
25 Corson, G. M., Charbonneau, N. L., Keene, D. R. & Sakai, L. Y. Differential expression of fibrillin-3 adds to microfibril variety in human and avian, but not rodent, connective tissues. Genomics 83, 461-472 (2004).
26 He, X., Cheng, R., Benyajati, S. & Ma, J. X. PEDF and its roles in physiological and pathological conditions: implication in diabetic and hypoxia-induced angiogenic diseases. Clinical science (London, England : 1979) 128, 805-823 (2015).
27 Verdone, G. et al. NMR-based homology model for the solution structure of the C-terminal globular domain of EMILIN1. Journal of biomolecular NMR 43, 79-96 (2009).
28 Verdone, G. et al. The solution structure of EMILIN1 globular C1q domain reveals a disordered insertion necessary for interaction with the alpha4beta1 integrin. The Journal of biological chemistry 283, 18947-18956 (2008).
29 Danussi, C. et al. EMILIN1-alpha4/alpha9 integrin interaction inhibits dermal fibroblast and keratinocyte proliferation. The Journal of cell biology 195, 131-145 (2011).
30 Danussi, C. et al. EMILIN1/alpha9beta1 integrin interaction is crucial in lymphatic valve formation and maintenance. Molecular and cellular biology 33, 4381-4394 (2013).
31 Spessotto, P. et al. beta 1 Integrin-dependent cell adhesion to EMILIN-1 is mediated by the gC1q domain. The Journal of biological chemistry 278, 6160-6167 (2003).
32 Spessotto, P. et al. EMILIN1 represents a major stromal element determining human trophoblast invasion of the uterine wall. Journal of cell science 119, 4574-4584 (2006).
33 Ravi, S., Haller, C. A., Sallach, R. E. & Chaikof, E. L. Cell behavior on a CCN1 functionalized elastin-mimetic protein polymer. Biomaterials 33, 2431-2438 (2012).
34 Egawa, E. Y., Kato, K., Hiraoka, M., Nakaji-Hirabayashi, T. & Iwata, H. Enhanced proliferation of neural stem cells in a collagen hydrogel incorporating engineered epidermal growth factor. Biomaterials 32, 4737-4743 (2011).
35 Samorezov, J. E., Headley, E. B., Everett, C. R. & Alsberg, E. Sustained presentation of BMP-2 enhances osteogenic differentiation of human adipose-derived stem cells in gelatin hydrogels. Journal of biomedical materials research. Part A 104, 1387-1397 (2016).
36 Oh, S. A. et al. Collagen three-dimensional hydrogel matrix carrying basic fibroblast growth factor for the cultivation of mesenchymal stem cells and osteogenic differentiation. Tissue engineering. Part A 18, 1087-1100 (2012).
37 McCall, A. D. et al. Growth factors polymerized within fibrin hydrogel promote amylase production in parotid cells. Tissue engineering. Part A 19, 2215-2225 (2013).
38 Seif-Naraghi, S. B. et al. Safety and efficacy of an injectable extracellular matrix hydrogel for treating myocardial infarction. Science translational medicine 5, 173ra125 (2013).
39 Wassenaar, J. W. et al. Evidence for Mechanisms Underlying the Functional Benefits of a Myocardial Matrix Hydrogel for Post-MI Treatment. Journal of the American College of Cardiology 67, 1074-1086 (2016).
40 Lee, B. et al. Perlecan domain V is neuroprotective and proangiogenic following ischemic stroke in rodents. The Journal of clinical investigation 121, 3005-3023 (2011).
41 Barry-Hamilton, V. et al. Allosteric inhibition of lysyl oxidase-like-2 impedes the development of a pathologic microenvironment. Nature medicine 16, 1009-1017 (2010).
42 Okada, H. et al. Alteration of extracellular matrix in dilated cardiomyopathic hamster heart. Mol Cell Biochem 156, 9-15 (1996).
43 Woodiwiss, A. J. et al. Reduction in myocardial collagen cross-linking parallels left ventricular

dilatation in rat models of systolic chamber dysfunction. Circulation 103, 155-160 (2001).
44 Bishop, J. E., Greenbaum, R., Gibson, D. G., Yacoub, M. & Laurent, G. J. Enhanced deposition of predominantly type I collagen in myocardial disease. Journal of molecular and cellular cardiology 22, 1157-1165 (1990).
45 Khan, S., Joyce, J., Margulies, K. B. & Tsuda, T. Enhanced bioactive myocardial transforming growth factor-beta in advanced human heart failure. Circulation journal : official journal of the Japanese Circulation Society 78, 2711-2718 (2014).
46 Klotz, S. et al. Mechanical unloading during left ventricular assist device support increases left ventricular collagen cross-linking and myocardial stiffness. Circulation 112, 364-374 (2005).
47 Pauschinger, M. et al. Dilated cardiomyopathy is associated with significant changes in collagen type I/III ratio. Circulation 99, 2750-2756 (1999).
48 Sivakumar, P., Gupta, S., Sarkar, S. & Sen, S. Upregulation of lysyl oxidase and MMPs during cardiac remodeling in human dilated cardiomyopathy. Molecular and cellular biochemistry 307, 159-167 (2008).
49 Burke, M. A. et al. Molecular profiling of dilated cardiomyopathy that progresses to heart failure. JCI insight 1 (2016).
50 Wu, L. et al. Cardiac fibroblasts mediate IL-17A-driven inflammatory dilated cardiomyopathy. The Journal of experimental medicine 211, 1449-1464 (2014).
51 Jin, B., Zhu, J., Shi, H. M., Wen, Z. C. & Wu, B. W. YAP activation promotes the transdifferentiation of cardiac fibroblasts to myofibroblasts in matrix remodeling of dilated cardiomyopathy. Brazilian journal of medical and biological research = Revista brasileira de pesquisas medicas e biologicas 52, e7914 (2018).
52 Blyszczuk, P. et al. Transforming growth factor-beta-dependent Wnt secretion controls myofibroblast formation and myocardial fibrosis progression in experimental autoimmune myocarditis. European heart journal 38, 1413-1425 (2017).
53 Xie, Y. et al. Endothelialtomesenchymal transition in human idiopathic dilated cardiomyopathy. Molecular medicine reports 17, 961-969 (2018).
54 Sweet, M. E. et al. Transcriptome analysis of human heart failure reveals dysregulated cell adhesion in dilated cardiomyopathy and activated immune pathways in ischemic heart failure. BMC genomics 19, 812 (2018).
55 Carmeliet, P. Angiogenesis in health and disease. Nature medicine 9, 653-660 (2003).
56 Escudier, B. et al. Bevacizumab plus interferon alfa-2a for treatment of metastatic renal cell carcinoma: a randomised, double-blind phase III trial. Lancet (London, England) 370, 2103-2111 (2007).
57 Escudier, B. et al. Phase III trial of bevacizumab plus interferon alfa-2a in patients with metastatic renal cell carcinoma (AVOREN): final analysis of overall survival. Journal of clinical oncology : official journal of the American Society of Clinical Oncology 28, 2144-2150 (2010).
58 Mac Gabhann, F., Qutub, A. A., Annex, B. H. & Popel, A. S. Systems biology of pro-angiogenic therapies targeting the VEGF system. Wiley interdisciplinary reviews. Systems biology and medicine 2, 694-707 (2010).
59 Gavard, J. & Gutkind, J. S. VEGF controls endothelial-cell permeability by promoting the beta-arrestin-dependent endocytosis of VE-cadherin. Nature cell biology 8, 1223-1234 (2006).
60 Szymborska, A. & Gerhardt, H. Hold Me, but Not Too Tight-Endothelial Cell-Cell Junctions in Angiogenesis. Cold Spring Harbor perspectives in biology 10 (2018).
61 Gonzalez, L., Jr. & Scheller, R. H. Regulation of membrane trafficking: structural insights from a Rab/effector complex. Cell 96, 755-758 (1999).
62 Wu, G. et al. Increased myocardial Rab GTPase expression: a consequence and cause of cardiomyopathy. Circulation research 89, 1130-1137 (2001).

63 He, H. et al. Identification and characterization of nine novel human small GTPases showing variable expressions in liver cancer tissues. Gene expression 10, 231-242 (2002).

64 Tong, M. et al. Rab25 is a tumor suppressor gene with antiangiogenic and anti-invasive activities in esophageal squamous cell carcinoma. Cancer research 72, 6024-6035 (2012).

65 Song, K. et al. Endothelial epsins as regulators and potential therapeutic targets of tumor angiogenesis. Cellular and molecular life sciences : CMLS 74, 393-398 (2017).

66 Pasula, S. et al. Endothelial epsin deficiency decreases tumor growth by enhancing VEGF signaling. The Journal of clinical investigation 122, 4424-4438 (2012).

67 Sanchez-Pulido, L., Martin-Belmonte, F., Valencia, A. & Alonso, M. A. MARVEL: a conserved domain involved in membrane apposition events. Trends in biochemical sciences 27, 599-601 (2002).

68 Yuan, W. et al. CMTM3 decreases EGFR expression and EGF-mediated tumorigenicity by promoting Rab5 activity in gastric cancer. Cancer letters 386, 77-86 (2017).

69 Jain, R. K. Molecular regulation of vessel maturation. Nature medicine 9, 685-693 (2003).

70 Jin, C., Ding, P., Wang, Y. & Ma, D. Regulation of EGF receptor signaling by the MARVEL domain-containing protein CKLFSF8. FEBS letters 579, 6375-6382 (2005).

71 Raza, A., Franklin, M. J. & Dudek, A. Z. Pericytes and vessel maturation during tumor angiogenesis and metastasis. American journal of hematology 85, 593-598 (2010).

72 Emmett, M. S., Dewing, D. & Pritchard-Jones, R. O. Angiogenesis and melanoma - from basic science to clinical trials. American journal of cancer research 1, 852-868 (2011).

73 Shaheen, R. M. et al. Tyrosine kinase inhibition of multiple angiogenic growth factor receptors improves survival in mice bearing colon cancer liver metastases by inhibition of endothelial cell survival mechanisms. Cancer research 61, 1464-1468 (2001).

74 Zhu, Z. et al. Integration of summary data from GWAS and eQTL studies predicts complex trait gene targets. Nature genetics 48, 481-487 (2016).

75 Williamson, I., Hill, R. E. & Bickmore, W. A. Enhancers: from developmental genetics to the genetics of common human disease. Developmental cell 21, 17-19 (2011).

76 Kottgen, A. et al. New loci associated with kidney function and chronic kidney disease. Nature genetics 42, 376-384 (2010).

77 Okada, Y. et al. Meta-analysis identifies multiple loci associated with kidney function-related traits in east Asian populations. Nature genetics 44, 904-909 (2012).

78 Bohle, A., Grund, K. E., Mackensen, S. & Tolon, M. Correlations between renal interstitium and level of serum creatinine. Morphometric investigations of biopsies in perimembranous glomerulonephritis. Virchows Archiv. A, Pathological anatomy and histology 373, 15-22 (1977).

79 Nangaku, M. Chronic hypoxia and tubulointerstitial injury: a final common pathway to end-stage renal failure. Journal of the American Society of Nephrology : JASN 17, 17-25 (2006).

80 Kozakowski, N. et al. The diffuse extent of peritubular capillaritis in renal allograft rejection is an independent risk factor for graft loss. Kidney international 88, 332-340 (2015).

81 Carmeliet, P. et al. Abnormal blood vessel development and lethality in embryos lacking a single VEGF allele. Nature 380, 435-439 (1996).

82 Eremina, V., Baelde, H. J. & Quaggin, S. E. Role of the VEGF--a signaling pathway in the glomerulus: evidence for crosstalk between components of the glomerular filtration barrier. Nephron. Physiology 106, p32-37 (2007).

83 Zhang, P. et al. The multimeric structure of polycystin-2 (TRPP2): structural-functional correlates of homo- and hetero-multimers with TRPC1. Human molecular genetics 18, 1238-1251 (2009).

84 Koptides, M., Hadjimichael, C., Koupepidou, P., Pierides, A. & Constantinou Deltas, C. Germinal and somatic mutations in the PKD2 gene of renal cysts in autosomal dominant polycystic kidney disease. Human molecular genetics 8, 509-513 (1999).

85 Outeda, P. et al. Polycystin signaling is required for directed endothelial cell migration and lymphatic development. Cell reports 7, 634-644 (2014).
86 Stolarczyk, J. & Carone, F. A. Effects of renal lymphatic occlusion and venous constriction on renal function. The American journal of pathology 78, 285-296 (1975).
87 Sanchez-Lozada, L. G. et al. Mild hyperuricemia induces vasoconstriction and maintains glomerular hypertension in normal and remnant kidney rats. Kidney international 67, 237-247 (2005).
88 Sanchez-Lozada, L. G. et al. Role of oxidative stress in the renal abnormalities induced by experimental hyperuricemia. American journal of physiology. Renal physiology 295, F1134-1141 (2008).
89 Chatterjee, V. et al. MicroRNA-147b regulates vascular endothelial barrier function by targeting ADAM15 expression. PloS one 9, e110286 (2014).
90 Sun, C. et al. ADAM15 deficiency attenuates pulmonary hyperpermeability and acute lung injury in lipopolysaccharide-treated mice. American journal of physiology. Lung cellular and molecular physiology 304, L135-142 (2013).
91 Sun, C. et al. ADAM15 regulates endothelial permeability and neutrophil migration via Src/ERK1/2 signalling. Cardiovascular research 87, 348-355 (2010).
92 Sun, C., Wu, M. H., Lee, E. S. & Yuan, S. Y. A disintegrin and metalloproteinase 15 contributes to atherosclerosis by mediating endothelial barrier dysfunction via Src family kinase activity. Arteriosclerosis, thrombosis, and vascular biology 32, 2444-2451 (2012).

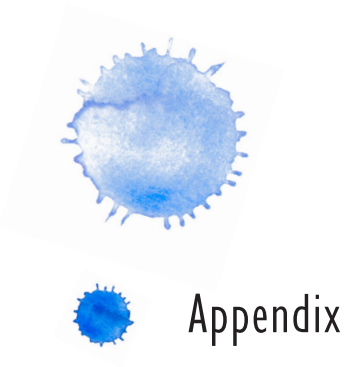

Appendix

SCIENTIFIC SUMMARY

In multicellular organisms, a crucial role of cells junctions is to combine groups of cells with related specializations into tissues. These specific structures are formed between cells or anchor cells to components of the extracellular matrix (ECM). They not only allow the formation and maintenance of distinct tissues, but also the transfer of bidirectional information between the interior and the exterior of cells. Such information transfer is essential for many biological processes, including cell survival, proliferation, differentiation and migration. A main class of cell junctions consists of anchoring junctions, which are strong plasma membrane connections that mechanically attach the cytoskeleton of a cell to either neighboring cells or to the ECM, thereby providing stability and rigidity to tissues. Anchoring junctions can be classified into two main forms, each involved in a distinct type of adhesion: (1) cell-matrix adhesion and (2) cell-cell adhesion.

The extracellular matrix

Cell-matrix adhesion is a key force-sensing interaction of a cell with the surrounding ECM that controls the shape, behavior and fate of a cell. A main type of cell-matrix adhesion anchoring junctions consists of focal adhesions (FAs), which are widely distributed among tissues and anchor the actin filaments of cells to the surrounding ECM via integrins. Besides being an adhesive substrate for cell attachment and migration, the ECM also provides structural and mechanical support and sequestrates biochemical cues, such as growth factors. Resident cells of each tissue are responsible for the composition and structural integrity of the surrounding ECM, making it a tissue-specific 3D scaffold in which cells are embedded. This unique ECM composition is generated during early embryonic development, where ECM remodeling accompanies the migration and differentiation events guiding cell division and the subsequent formation of distinct tissues and organs.

Due to its evolutionarily conserved composition and impact on both embryonic development and cellular homeostasis, the ECM represents an ideal scaffolding system for the use in tissue engineering. This field of research uses a combination of cells and a scaffolding system based on biomaterials and bioactive factors to improve or replace biological tissues or to implement in complex *in vitro* 3D cell models. Selection of the appropriate matrix for tissue engineering is crucial, as it will profoundly affect cell viability and behavior. Often used natural matrices are

hydrogels based on endogenous ECM components, however, these ECM matrices are not tissue-specific nor do they focus on specific matrix factors for guiding the desired cell behavior. Improved matrices, such as synthetic matrices containing tissue-specific ECM components, appear to hold the best potential for mimicking the desired physiological setting. In order to create such a scaffolding system, it is necessary to fully characterize the unique and complex ECM composition of specific organs and tissues. Research until now focused on mapping the adult ECM, however, during development, the ECM undergoes extensive remodeling associated with assembly and growth of tissues, matching with the microenvironment needed in 3D tissue constructs.

In chapters 2 and 3 of this thesis, the differences between the developing fetal and the more static mature human ECM were characterized in both the kidney and renal artery. This comparison between human renal fetal and mature ECM revealed a specific ECM niche during development. This is valuable knowledge for improving current scaffolds to better mimic the native renal tissue. A critical difference found is the abundance of Elastin Microfibril Interfacer 1 (EMILIN1) in the fetal ECM of both tissues. EMILIN1 is a glycoprotein that is located in elastic fibers and plays an important role in the development of elastic tissues, including large blood vessels and the heart. Furthermore, the chemical structure of EMILIN1 hints towards cell adhesive capacities. Indeed, this thesis shows that EMILIN1 can regulate renal cell adhesion and its absence from the ECM stimulates a more migratory phenotype in renal cells. Further studies are required to unravel the potential of EMILIN1 and other identified ECM proteins for the tissue engineering field.

The ECM is tightly regulated by a delicate balance between synthesis, degradation, reassembly and chemical modifications. These complex processes need to be tightly regulated in order to maintain tissue homeostasis, especially during growth and repair. Dysregulation of ECM remodeling is associated with the development and progression of numerous pathological conditions. Many of these diseases are characterized by fibrosis at the end stage, including dilated cardiomyopathy (DCM). This heart muscle disease is characterized by the dilation of the left ventricle and presence of ventricular systolic dysfunction. Myocardial fibrosis is a major feature of DCM and therefore it is inevitable that complex ECM remodeling is involved in DCM onset and progression. Chapter 4 of this thesis focuses on the changes in ECM composition in DCM. Next to summarizing the existing literature,

a catalogue of ECM genes associated with DCM was created using published transcriptome-based datasets. This DCM matrisome reflects disease progression through key ECM remodeling pathways and it is likely that among these identified ECM components are novel diagnostic markers or therapeutic targets.

Angiogenesis

Cell-cell adhesion forms a continuum between cells and their linked cytoskeleton, providing them with mechanical support and positional information. A main type of cell-cell adhesion anchoring junctions consists of adherens junctions (AJs), which are found in epithelial and endothelial cells (ECs) and anchor the actin filaments of neighboring cells together via cadherins. Many events during embryonic development are associated with changes in cell-cell adhesion strength, predominantly during vascular development. Angiogenesis is the process through which new blood vessels are formed from pre-existing vessels by sprouting new branches that connect and remodel into a functional network. Here, endothelial AJs must allow dynamic cellular rearrangements for EC sprouting, while also providing stable connections that prevent leakage of the newly formed vessels.

VE-cadherin is indispensable for proper angiogenesis and the amount of VE-cadherin at the plasma membrane is directly linked to endothelial barrier function. This bioavailability is regulated by endocytosis in a tightly controlled manner. Membrane-bound VE-cadherin is taken up into the cytosol in specialized regions called clathrin-coated vesicles. These vesicles then fuse with early endosomes in which VE-cadherin is further sorted for recycling, lysosomal, or other trafficking routes. Members of the Rab family of small GTPases regulate distinct steps along these trafficking routes. VE-cadherin can be recycled back to the plasma membrane through either the Rab4-mediated rapid recycling pathway or the Rab11-mediated slow endosome pathway. Instead of recycling back to the plasma membrane, VE-cadherin can also be targeted to the Rab7-mediated lysosomal trafficking route for degradation. The balance between VE-cadherin recycling and degradation determines the degree of cell-cell adhesion.

Whereas endocytosis plays a vital role in modulating vascular permeability by controlling the adhesive strength in AJs, little is known about the exact contribution of endocytic regulators to the angiogenic process. Chapters 5 and 6 of this thesis report two novel proteins involved in regulating endocytosis during angiogenesis:

CMTM3 and CMTM4. These proteins are members of the CKLF-like MARVEL transmembrane domain-containing (CMTM) family and were only known for their potential to act as tumor suppressor genes. However, the chemical structure of CMTM family members links them to vesicle trafficking. This thesis describes a novel function for both CMTM3 and CMTM4 in endothelial cell-cell adhesion by regulating the bioavailability of VE-cadherin on the plasma membrane: CMTM3 stimulates VE-cadherin internalization, whereas CMTM4 stimulates the recycling of VE-cadherin back to the cell membrane. This novel fundamental finding holds promising therapeutic perspectives to understand and treat angiogenic diseases, which may require a broader approach of inhibiting or stimulating multiple pathways simultaneously. Unraveling which factors trigger the activation of CMTM family members in ECs and if this process can be altered would be the next important step.

Angiogenesis is a normal process during embryonic development and is re-activated during wound healing and inflammation. However, when dysregulated, angiogenesis contributes to a wide range of disorders and genetic alterations have been linked to many of these diseases. A common method for the discovery of gene-disease relationships is a genome-wide association study (GWAS). This tool is aimed at determining the statistical relationship between an observable disease trait and common DNA variants, mostly single nucleotide polymorphisms (SNPs). For chronic kidney disease (CKD), recent GWASs identified over a hundred SNPs associated with CKD traits. Unfortunately, ±90% of these SNPs lie within the non-coding genome. Non-coding SNPs associated with CKD traits could be located within DNA regulatory regions (DREs). These DREs activate or repress transcription of genes over large genomic distances (up to a million base pairs) by looping out the intervening chromosomal region. Thus, common DNA variants in DREs could lead to dysregulation of target gene expression and thereby contribute to disease. In chapter 7 of this thesis, circular chromosome conformation capture-sequencing (4C-seq) was used to examine the 3D interactions between DREs harboring a CKD-associated SNP and their target genes. Since DREs regulate gene expression in a cell-specific manner and CDK is associated with both tubulointerstitial damage and loss of peritubular and glomerular capillaries, 4C-seq was conducted in both human renal proximal tubular epithelial cells and glomerular endothelial cells. The resulting overview of CKD-associated SNPs and their target genes includes genes that potentially influence angiogenesis. These results further our understanding

of the molecular mechanisms underlying CKD that can aid in the development of future biomarkers or therapies.

Overall, the data generated in this thesis forms a platform for future studies on the extracellular matrix and angiogenesis. The several ECM datasets generated using "-omic" approaches are powerful resources for the research community and the novel angiogenic pathways and their players presented in this thesis aid in the development of future therapies for angiogenic diseases.

WETENSCHAPPELIJKE SAMENVATTING

Een cruciale rol van celverbindingen in meercellige organismen is het combineren van groepen cellen met verwante specialisaties tot weefsels. Deze specifieke structuren worden gevormd tussen cellen of ankeren cellen aan componenten van de extracellulaire matrix (ECM). Ze zijn niet alleen nodig voor de vorming van en het onderhoud aan verschillende weefsels, ze zijn ook nodig voor de overdracht van informatie tussen de binnenkant en de buitenkant van cellen. Een dergelijke informatieoverdracht is essentieel voor veel biologische processen, zoals celoverleving, proliferatie, differentiatie en migratie. Een hoofdklasse van celverbindingen bestaat uit verankeringsverbindingen, wat sterke celmembraan verbindingen zijn die het cytoskelet van een cel mechanisch verbinden met aangrenzende cellen of met de ECM en zo stabiliteit en stijfheid aan het weefsel geven. Verankeringsverbindingen worden ingedeeld in twee hoofdvormen, die elk betrokken zijn bij een specifiek soort adhesie: (1) cel-matrix adhesie en (2) cel-cel adhesie.

De extracellulaire matrix

Cel-matrix adhesie is een belangrijke krachtgevoelige interactie van een cel met de omringende ECM die de vorm, het gedrag en de bestemming van een cel regelt. Een hoofdtype van cel-matrix adhesie verankeringsverbindingen bestaat uit focale adhesies (FAs), die in veel verschillende weefsels voorkomen en daar het actine skelet van cellen verbindt met het omringende ECM via zogenoemde integrines. De ECM is niet alleen een klevend substraat dat cellen nodig hebben om te hechten, maar het biedt ook structurele en mechanische ondersteuning en het houdt biochemische signalen vast, zoals groeifactoren. Cellen zijn zelf verantwoordelijk voor de samenstelling en structurele integriteit van het omliggende ECM, waardoor dit ECM een weefselspecifieke 3D stellage is waarin cellen zijn ingebed. Deze unieke samenstelling van het ECM wordt tijdens de vroege embryonale ontwikkeling gegenereerd, waarbij remodelering van het ECM gepaard gaat met cel migratie, differentiatie en proliferatie dat nodig is voor de uiteindelijke vorming van afzonderlijke weefsels en organen.

Vanwege de evolutionair geconserveerde samenstelling en de impact op zowel de embryonale ontwikkeling als de cellulaire homeostase, vormt de ECM een ideale stellage voor het gebruik bij weefselkweek. Dit onderzoeksgebied maakt

gebruik van een combinatie tussen cellen en een stellagesysteem bestaande uit biomaterialen en bioactieve factoren ter vervanging of verbetering van weefsels of om te implementeren in complexe *in vitro* 3D cel modellen. Het selecteren van de juiste matrix voor weefselkweek is cruciaal, omdat dit de levensvatbaarheid en het gedrag van de cellen uiterst zal beïnvloeden. Vaak gebruikte natuurlijke matrices zijn hydrogelen op basis van endogene ECM-componenten, echter zijn deze ECM matrices niet weefselspecifiek, noch bevatten deze specifieke biochemische signalen om het gewenste gedrag van de cellen te leiden. Verbeterde matrices, zoals synthetische matrices die weefselspecifieke ECM-componenten bevatten, lijken de meeste potentie te hebben voor het nabootsen van de gewenste fysiologische setting. Om een dergelijk stellagesysteem te creëren is het noodzakelijk om de unieke en complexe ECM samenstelling van specifieke organen en weefsels volledig te karakteriseren. Onderzoek tot nu toe richtte zich op het in kaart brengen van de mature ECM, maar tijdens de ontwikkeling ondergaat de ECM een uitgebreide hermodellering die geassocieerd is met de groei van weefsels. Dit matcht met de micro-omgeving die nodig is in 3D weefselkweken.

In hoofdstuk 2 en 3 van dit proefschrift zijn de verschillen tussen de ontwikkelende immature en de meer statische mature ECM van zowel de humane nier als de nierslagader gekarakteriseerd. Deze vergelijking tussen de humane immature en mature renale ECM heeft een specifieke ECM-niche tijdens de ontwikkeling onthuld. Dit is waardevolle kennis voor het verbeteren van de huidige stellages om het natuurlijke nierweefsel beter na te bootsen. Een interessant gevonden verschil is de overvloed van *Elastin Microfibril Interfacer 1* (EMILIN1) in het immature ECM van beide weefsels. EMILIN1 is een glycoproteïne dat zich in elastische vezels bevindt en een belangrijke rol speelt bij de ontwikkeling van elastische weefsels, waaronder de grote bloedvaten en het hart. Verder verwijst de chemische structuur van EMILIN1 naar een aanleg voor adhesie. Dit proefschrift laat inderdaad zien dat EMILIN1 de adhesie van niercellen kan reguleren en ECM zonder EMILIN1 stimuleert een meer migrerend fenotype in niercellen. Verder onderzoek is nodig om de potentie van EMILIN1 en ook van andere geïdentificeerde ECM-eiwitten te ontrafelen voor het gebruik in weefselkweek.

De ECM wordt strak gereguleerd door een gevoelig evenwicht tussen synthese, afbraak, hermontage en chemische modificaties. Deze complexe processen moeten strak worden gereguleerd om de homeostase van het weefsel te

handhaven, vooral tijdens groei en herstel. Dysregulatie van ECM remodellering wordt geassocieerd met de ontwikkeling en progressie van tal van pathologische aandoeningen. Veel van deze ziekten worden gekenmerkt door fibrose tijdens het eindstadium, waaronder ook de ziekte gedilateerde cardiomyopathie (DCM). Deze hartspierziekte wordt gekenmerkt door de verwijding van de linkerventrikel en de aanwezigheid van ventriculaire systolische dysfunctie. Myocardiale fibrose is een belangrijk kenmerk van DCM en het is daarom onvermijdelijk dat complexe ECM remodellering betrokken is bij de ontwikkeling en progressie van DCM. Hoofdstuk 4 van dit proefschrift richt zich op de veranderingen in de samenstelling van de ECM tijdens DCM. Naast een samenvatting van de huidige literatuur is er een catalogus gecreëerd van ECM genen die geassocieerd zijn met DCM met behulp van gepubliceerde datasets van transcriptoom analyses. Deze DCM matrisoom weerspiegelt de ziekteprogressie via belangrijke ECM remodelleringsroutes en het is hoogstwaarschijnlijk dat zich onder deze geïdentificeerde ECM-componenten nieuwe diagnostische markers of therapeutische targets bevinden.

Angiogenese

Cel-cel adhesie vormt een continuüm tussen cellen en hun aan elkaar gekoppeld cytoskelet en biedt hen mechanische ondersteuning en positionele informatie. Een hoofdtype van cel-cel adhesie verankeringsverbindingen bestaat uit adherente juncties (AJs), die in epitheel- en endotheelcellen voorkomen en daar het actine skelet van aangrenzende cellen met elkaar verbindt via zogenoemde cadherines. Veel gebeurtenissen tijdens de embryonale ontwikkeling worden geassocieerd met veranderingen in de sterkte van cel-cel adhesies, voornamelijk tijdens de vasculaire ontwikkeling. Angiogenese is het proces waarbij nieuwe bloedvaten worden gevormd uit bestaande bloedvaten, doordat nieuwe takken ontkiemen en zich weer verbinden tot een functioneel netwerk. Hierbij moeten endotheel AJs dynamische cellulaire herschikkingen mogelijk maken zodat endotheelcellen kunnen ontkiemen, terwijl ze ook stabiele verbindingen moeten bieden aan de nieuwgevormde vaten om lekkage te voorkomen.

VE-cadherine is onmisbaar voor correcte angiogenese en de hoeveelheid VE-cadherine op de celmembraan is direct gekoppeld aan de barrièrefunctie van het endotheel. Deze beschikbaarheid wordt strak gereguleerd door endocytose. Membraangebonden VE-cadherine wordt opgenomen in het cytosol in gespecialiseerde gebieden die clathrine-gecoate vesikels worden genoemd. Deze

vesikels fuseren vervolgens met vroege endosomen waarin VE-cadherine verder wordt gesorteerd voor recycling, degradatie of andere transport routes. Leden van de Rab familie bestaande uit zogenoemde kleine GTPases reguleren specifieke stappen langs deze transport route. VE-cadherine kan teruggevoerd worden naar de celmembraan via zowel de Rab4-gemedieerde snelle recyclingroute of via de Rab11-gemedieerde langzame endosoom route. In plaats van terug te gaan naar de celmembraan kan VE-cadherine ook via de Rab7-gemedieerde lysosomale transportroute afgebroken worden. De balans tussen VE-cadherine recycling en afbraak bepaalt de mate van cel-cel adhesie.

Ondanks dat endocytose een essentiële rol speelt bij het moduleren van de vasculaire permeabiliteit door de adhesie kracht van AJs te beheren, is er weinig bekend over de exacte bijdrage van regulatoren van het endocytose proces aan angiogenese. De hoofdstukken 5 en 6 van dit proefschrift beschrijven twee nieuwe eiwitten die betrokken zijn bij het reguleren van het endocytose proces tijdens angiogenese: CMTM3 en CMTM4. Deze eiwitten zijn onderdeel van de *CKLF-like MARVEL transmembrane domain containing* (CMTM) familie en stonden tot nu toe alleen bekend om hun rol als tumorsuppressorgenen. Echter, de chemische structuur van CMTM-familieleden koppelt hun aan het transport van vesikels. Dit proefschrift beschrijft een nieuwe functie voor zowel CMTM3 als CMTM4 in de cel-cel adhesie van endotheelcellen doordat ze de beschikbaarheid van VE-cadherine op de celmembraan kunnen reguleren: CMTM3 stimuleert VE-cadherine opname, terwijl CMTM4 de terugvoer van VE-cadherine naar de celmembraan stimuleert. Deze nieuwe en fundamentele bevinding biedt veelbelovende therapeutische perspectieven om in ziektes waarbij angiogenese een belangrijke factor is te begrijpen en te behandelen, aangezien deze wellicht een bredere aanpak nodig hebben door meerdere moleculaire routes tegelijkertijd te remmen of te stimuleren. Het ontrafelen van welke factoren leiden tot de activering van CMTM-familieleden in endotheelcellen en of dit proces kan worden veranderd is de volgende belangrijke stap.

Angiogenese is een normaal proces die plaats vindt tijdens de embryonale ontwikkeling en wordt opnieuw geactiveerd tijdens de wondgenezing of een ontsteking. Wanneer angiogenese echter ontregelt raakt, draagt het bij aan een breed scala van aandoeningen waarvan veel gekenmerkt worden door genetische veranderingen. Een veel voorkomende methode voor het ontdekken van gen-

ziekte relaties is een zogenoemde *genome-wide association study* (GWAS). Deze tool is erop gericht om de statistische relatie te bepalen tussen een waarneembare eigenschap van een ziekte en veelvoorkomende DNA varianten, voornamelijk enkel-nucleotide polymorfieën (SNPs). Voor chronische nierziekte (CKD) hebben recente GWAS meer dan honderd SNPs geassocieerd met specifieke CKD kenmerken. Helaas liggen ±90% van deze SNPs binnen het niet-coderende DNA. Niet-coderende SNPs die geassocieerd zijn met CKD kenmerken kunnen zich bevinden in DNA-regulerende regio's (DREs). Deze DREs activeren of onderdrukken de transcriptie van doelwit-genen over grote genomische afstanden (tot aan een miljoen basenparen) door het tussenliggende chromosomale gebied als een lus te verwijderen. Dus, veelvoorkomende DNA varianten in DREs kunnen leiden tot de ontregeling van de genexpressie van doelwit-genen en daarmee bijdragen aan het ziekte proces. Voor hoofdstuk 7 van dit proefschrift werd de techniek *circular chromosome conformation capture-sequencing* (4C-seq) toegepast om de 3D-interacties te onderzoeken tussen DREs die een CKD-geassocieerde SNP bevatten en hun doelwit-genen. Aangezien DREs de genexpressie op een celspecifieke manier reguleren en CKD wordt geassocieerd met zowel tubulo-interstitiële schade als verlies van peritubulaire en glomerulaire capillairen, is de 4C-seq uitgevoerd met zowel humane proximale tubulaire epitheelcellen als glomerulaire endotheelcellen. Het resulterende overzicht van DREs die een CKD-geassocieerde SNP bevatten gelinkt aan hun doelwit-genen bevat genen die potentieel angiogenese kunnen beïnvloeden. Deze resultaten vergroten ons inzicht in de moleculaire mechanismen die ten grondslag liggen aan CKD en kunnen helpen bij de ontwikkeling van toekomstige biomarkers of therapieën.

Algeheel vormen de resultaten beschreven in dit proefschrift een platform voor toekomstige studies over de extracellulaire matrix en angiogenese. De verschillende ECM-datasets verkregen met "*-omic*" technieken zijn veelvermogende bronnen voor de onderzoeksgemeenschap en de nieuwe angiogene routes en hun spelers beschreven in dit proefschrift bevorderen de ontwikkeling van toekomstige therapieën voor angiogenese gerelateerde ziektebeelden.

DANKWOORD

Mijn proefschrift is dan eindelijk een feit, maar dat was niet gelukt zonder hulp van vele anderen. In dit dankwoord wil ik dan ook de mensen bedanken die dit proefschrift mede mogelijk hebben gemaakt.

Te beginnen met mijn promotor, Prof. Marianne Verhaar, bedankt voor de mogelijkheid om onderzoek te doen bij de afdeling Nefrologie en Hypertensie, ik heb deze tijd als een waar genoegen ervaren. Ook al hebben wij elkaar maar een enkele keer gesproken, deze gesprekken waren zeer waardevol.

Dr. Caroline Cheng, mijn copromotor, bedankt voor de begeleiding tijdens mijn promotieonderzoek. De afgelopen vier jaar heb ik onder jouw begeleiding een zelfstandige manier van werken ontwikkeld en het vermogen om mijn bevindingen te delen met het wetenschappelijk veld. Bedankt voor alle interessante discussies en adviezen; jouw creativiteit, oplossingsgerichtheid en grote kennis op celbiologisch gebied heb ik erg gewaardeerd. Je bent een inspirerende wetenschapper en ik hoop dat in de toekomst onze wegen elkaar nog eens zullen kruizen.

Daarnaast wil graag de leden van mijn beoordelingscommissie, Prof. Dirk Duncker, Prof. Roos Masereeuw, Prof. Folkert Asselbergs, Prof. Paul Coffer en Prof. Dorien Peters hartelijk danken voor de tijd die zij hebben genomen voor de beoordeling van dit proefschrift. Dr. Michal Mokry wil ik bedanken voor zijn deelname in de oppositie. Dorien, jou wil ik ook bedanken voor de mogelijkheid om binnen jouw groep mijn wetenschappelijke carrière voort te kunnen zetten als postdoc, ondanks dat ik dit proefschrift nog deels op papier moest zetten. De rest van de PKD squad: Anish, Hans D, Wouter, Elena, Chiara, Sevtap, Romy, Kyra, Hans B, Hester en Sosha, bedankt dat jullie mij met open armen hebben ontvangen en voor alle gezelligheid het afgelopen jaar.

Natuurlijk wil ik graag mijn collega's binnen de Cheng groep bedanken. Allereerst Chris, die het deel van de Cheng groep in Utrecht draaiende houdt. In het begin moet het wel gevoeld hebben alsof je nog een extra master student moest begeleiden. Bedankt voor al jouw hulp en geduld, ondanks dat je het zelf ook druk had. Ik heb veel bewondering voor jouw inzet, gedrevenheid en kennis. Bedankt voor de samenwerking aan de verschillende ECM projecten en dat ik altijd naar

jou toe kon komen om even te sparren of te overleggen. Veel succes met het afronden van je PhD en tegelijkertijd werken aan je postdoc projecten! Jiayi, it was great starting my PhD the exact same day as you did. We have grown so much in our research together. Thank you for all the fun and support, and for the delicious snacks you bring back from China. I also enjoy occasionally bumping into you at Olympos, where we force ourselves to work out in order to deserve that big piece of chocolate afterwards. Good luck with wrapping up your PhD! I hope we keep seeing each other, for example during a well-deserved drink after a work-out or catching up with the other 4th year PhD members, Femke, Merle and Laura, with a nice dinner! Elana, je bent de nieuwste aanwinst binnen de Cheng groep in Utrecht, heel veel succes met het overleven van je PhD!

Ook wil ik ook graag het Rotterdamse deel van de Cheng groep bedanken. Maarten, ik bewonder hoe goed jij alles kan combineren met het jonge gezinsleven. Je bent nu al een geweldige onderzoeker en ik wil je graag bedanken voor de samenwerking tijdens die sporadische momenten dat jij in Utrecht was. Ihsane, bedankt voor de samenwerking aan het CMTM project. Mede door jouw inzet en energie hebben we twee mooie papers gepubliceerd. Ik wens jullie beiden veel succes met jullie carrière in de wetenschap!

Lieve paranimfen, Femke en Merle, ik vind het een eer dat jullie tijdens mijn verdediging aan mijn zijde willen staan! Ik vond het ontzettend leuk om gelijkertijd het hele PhD traject in te gaan en zo van elkaar te leren en elkaar te helpen. Femke, ik heb enorme bewondering voor jouw kunde om altijd het positieve van iets in te zien als bij mij het glas half leeg is (zo heeft Teddy inderdaad nu een groter aaibaar oppervlak). Bedankt voor al jouw oprechte interesse, gezelligheid en gesprekken vol interessante medische feitjes, zeker als we weer eens met z'n tweeën nog 's avonds laat over waren op het RMCU. Ik ben blij dat we de etentjes en bordspelletjesavonden nog steeds voortzetten! En natuurlijk ben je een wel gewaardeerd onderdeel van de patisseriefreaks. Veel succes met de laatste loodjes en met je nieuwe aanstelling als AIOS bij de reumatologie! Inherent verbonden aan Femke is natuurlijk Jon-Ruben, jij ook bedankt voor alle gezellige bordspelletjesavonden en jouw bijzondere gave om spelregels perfect uit te leggen. Ik ben nog steeds onder de indruk van jouw prachtige collectie aan exotische dieren! Merle, ik heb bewondering voor jouw toewijding, gedrevenheid en doorzettingsvermogen als alles even tegenzit. Ik kan niemand bedenken die de

uitdagingen van het onderzoek beter aan zou kunnen. Ook bewonder ik hoe goed jij je carrière weet te combineren met de zorg van de kleine Ana. Je was echt een fijne collega en ik waardeer al onze leuke gesprekken, vooral onze gedeelde passie voor katten. Bedankt voor alles en veel succes met het afronden van jouw PhD! Ik hoop dat we de etentjes en bordspelletjesavonden blijven voortzetten.

Diënty, bedankt dat wij allemaal jouw zogenoemde misbaksels en prachtige bakcreaties keer op keer mochten proeven. Met het organiseren van Heel RMCU Bakt heb je jouw bakkriebels een beetje aan de hele afdeling overgedragen. Ik heb erg genoten van al onze leuke gesprekken (variërend van daadwerkelijk werk gerelateerd tot aan allerlei lekkernijen) en natuurlijk van jou als de captain van de patisseriefreaks! Ik hoop dat we in de toekomst, naast Parijs en Amsterdam, nog meer steden zullen bezoeken om van alles te proeven. Veel plezier met jouw Heidelberg avontuur!

Verder wil ik alle andere (oud) collega's van de Nefrologie afdeling bedanken voor al hun hulp en leuke gesprekken. Petra dG, Bas, Joost, Rachel, Jaap en Silvia, bedankt voor de vele kennis waarmee jullie hebben bijgedragen aan het Nefro lab. Isabel, Paul, Tobias, Maaike, Thijs en Fjodor, de nieuwe generatie, veel succes met jullie PhD. Ook de oude generatie PhD-studenten, Gisela, Dimitri, Olivier, Hendrik, Tim, Frans, Glenn, Laura, Tonja en Sjaak, bedankt, jullie waren stuk voor stuk goede voorbeelden! Petra dB, Krista, Juan, Adele, Melanie, Arda en iedereen die ik nog vergeet, bedankt voor jullie hulp.

Ik heb tijdens mijn PhD het geluk gehad om zes fantastische studenten te mogen begeleiden. Ik wil dan ook graag Merel, Eduard, Niek, Amber, Romi en Novella bedanken voor hun inzet en enthousiasme. Ook wil ik Liana bedanken voor haar hulp. Jullie hebben allemaal veel werk verzet, wat heeft geleid tot mooie data voor mijn publicaties. Op mijn beurt heb ik ook veel van jullie kunnen leren. Ik wens jullie al het beste voor de toekomst.

Ook gaat mijn dank uit naar alle collega's van het Experimentele Cardiologie lab. In het bijzonder Iris en Corina. Iris, jij bent een wel gewaardeerd lid van de patisseriefreaks, bedankt voor alle gezelligheid! Corina, wat een prachtige foto's maak jij toch, bedankt voor alle leuke gesprekken!

Verder wil ik Sandra en Thamar bedanken voor de gezelligheid tijdens onze etentjes. Ook wil ik iedereen van tennis en squash bedanken voor de afleiding die ik kon vinden in de trainingen en de vriendschappelijke partijen.

Lieve Ai, we zien elkaar veel te weinig maar onze vriendschap slijt gelukkig niet. Bedankt dat je er al zo lang voor mij bent!

Lieve papa en mama, zonder jullie zou ik nooit zijn waar ik nu ben. Jullie hebben mij altijd gestimuleerd om het beste uit mijzelf te halen en geleerd dat hard werken loont (dat ging niet altijd even makkelijk). Door jullie liefde, steun, vertrouwen, geduld en bemoedigende woorden heb ik mijn interesse voor de natuur kunnen omzetten naar een mooie carrière en ik kan jullie daar niet genoeg voor bedanken. ¡Os quiero mucho!

Verder wil ik zeker mijn schoonouders, Alex en Marjan, en Hans, Ina, Stefan en Annemay niet vergeten. Bedankt voor alle mooie en leuke momenten samen. ¡Y mi familia en Madrid, Leo, Mariví, Álvaro y Marta, gracias por todo!

Tot slot natuurlijk de belangrijkste: Guido. Ik ben zeer blij dat jij mijn man bent. We hebben al zoveel leuke momenten samen meegemaakt in de afgelopen 13 jaar en ik hoop in de toekomst nog vele mooie avonturen met jou te mogen beleven. Ondanks dat je mij met de inhoud van mijn onderzoek en proefschrift niet zoveel hebt kunnen helpen, ben je in alle andere opzichten een geweldige steun voor mij! Ik ben daar intens dankbaar voor. Ik houd van je!

CURRICULUM VITAE

Laura Louzao Martinez was born on November 13th, 1989 in Arnhem, The Netherlands. In 2009, Laura completed her VWO secondary education with the profile "Nature and Health" at the Arentheem College in Arnhem. She continued her study path with the Bachelor Biology including a minor in Medical Biology at the Radboud University in Nijmegen. As part of her Bachelor's program, she conducted a small research internship at the department of Pathology from the Radboud UMC under the supervision of Dr. Konnie Hebeda on the histology of IgG4-related lymphadenopathy. This work resulted in a first-author publication. After receiving her Bachelor's degree in 2012 (*Bene Meritum*), she continued with her Master's degree in Medical Biology at the Radboud University and performed two large research internships as part of the curriculum. The first internhsip she conducted at the department of Organismal Animal Physiology from the Radboud University under the supervision of Prof. dr. Gert Flik and Dr. Jeroen Boerrigter. Here she studied the effect of Pro-Tex on the stress physiology of common carp and this work resulted in a co-author publication. At the same department she wrote a literature thesis on fish scale cortisol as retrospective calendar of stress under the supervision of Prof. dr. Gert Flik. During her last internship, she went to the Hubrecht Institute in Utrecht, where she conducted research at the group of Prof. dr. Eelco de Koning on improving the expansion and differentiation of human pancreatic organoids under the supervision of Dr. Nerys Williams. At this group she also wrote a second literature thesis on linking the gut microbiome to type 1 diabetes under the supervision of Dr. Gitanjali Dharmadhikari. After her Master's graduation (*Bene Meritum*), Laura moved to Utrecht in 2015 and started her PhD research under the supervision of Dr. Caroline Cheng and Prof. dr. Marianne Verhaar at the department of Nephrology and Hypertension from the University Medical Center Utrecht, which resulted in this thesis. Since April 2019, Laura is working as a postdoc researcher at the department of Human Genetics from the Leiden University Medical Center within the group of Prof. dr. Dorien Peters that focuses on polycystic kidney disease.

LIST OF PUBLICATIONS

L. Louzao Martinez, C.G.M van Dijk, Y.J. Xu, A. Korn, N. Bekker, R. Brouwhuis, M.N. Nicese, J.A.A. Demmers, M.T.H. Goumans, R. Masereeuw, D.J. Duncker, M.C. Verhaar, C. Cheng. (**2019**) "A Proteome Comparison Between Human Fetal and Mature Renal Extracellular Matrix Identifies EMILIN1 as a Regulator of Renal Cell Adhesion" *Matrix Biology Plus*. [Epub ahead of print]

L. Louzao Martinez*, I. Chrifi*, M.M. Brandt, C.G.M. van Dijk, P.E. Bürgisser, C. Zhu, J.M. Kros, M.C. Verhaar, D.J. Duncker, C. Cheng. (**2019**) "CMTM4 regulates angiogenesis by promoting cell surface recycling of VE-cadherin to endothelial adherens junctions" *Angiogenesis*. 22(1):75-93

M.M. Brandt, C.G.M. van Dijk, I. Chrifi, H.M. Kool HM, P.E. Bürgisser, **L. Louzao Martinez**, J. Pei, R.J. Rottier, M.C. Verhaar, D.J. Duncker, C. Cheng. (**2018**) "Endothelial loss of Fzd5 stimulates PKC/Ets1-mediated transcription of Angpt2 and Flt1" *Angiogenesis*. 21(4):805-821

M.M. Brandt*, C.A. Meddens*, **L. Louzao Martinez**, N.A.M. van den Dungen, N.R. Lansu, E.E. Nieuwenhuis, D.J. Duncker, M.C. Verhaar, J.A. Joles, M. Mokry, C. Cheng. (**2018**) "Chromatin Conformation Links Distal Target Genes to CKD Loci" *Journal of the American Society of Nephrology: JASN*. 29(2):462-476

I. Chrifi, **L. Louzao Martinez**, M.M. Brandt, C.G.M. van Dijk, P.E. Bürgisser, C. Zhu, J.M. Kros, D.J. Duncker, C. Cheng. (**2017**) "CMTM3 (CKLF-Like Marvel Transmembrane Domain 3) Mediates Angiogenesis by Regulating Cell Surface Availability of VE-Cadherin in Endothelial Adherens Junctions" *Arteriosclerosis Thrombosis and Vascular Biology*. 37(6):1098-1114

L. Louzao Martinez, A. Vink, M. Harakalova, F.W. Asselbergs, M.C. Verhaar, C. Cheng. (**2016**) "Characteristic adaptations of the extracellular matrix in dilated cardiomyopathy" *International Journal of Cardiology*. 1(220):634-646

L. Louzao Martinez, E. Friedländer, J.A.W.M. van der Laak, K.M. Hebeda. (**2014**) "Abundance of IgG4+ plasma cells in isolated reactive lymphadenopathy is no indication of IgG4-related disease" *American Journal of Clinical Pathology*.

142:459-466

J.G.J. Boerrigter, H.W. van de Vis, R. van den Bos, W. Abbink, T. Spanings, J. Zethof, **L. Louzao Martinez**, W.F.M. van Andel, J. Lopez-Luna, G. Flik. (**2014**) "Effects of Pro-Tex on zebrafish (Danio rerio) larvae, adult common carp (Cyprinus carpio) and adult yellowtail kingfish (Seriola lalandi)" *Fish Physiology and Biochemistry*. 40(4):1201-1212

In preparation or under review:

C.G.M. van Dijk, **L. Louzao Martinez**, E. van Mulligen, B. Boermans, J.A.A Demmers, T.P.P. van den Bosch, M.T.H. Goumans, D.J. Duncker, M.C. Verhaar, C. Cheng. "Extracellular matrix analysis of human renal arteries in both quiescent and active vascular state" [In preparation]

C.G.M. van Dijk, M.M. Brandt, N. Poulis, J. Anten, M. van der Moolen, L. Kramer, **L. Louzao Martinez**, J. Pei, M.M. Krebber, P. de Graaf, D.J. Duncker, M.C. Verhaar, R. Luttge, C. Cheng. "A new microfluidics model for complex vascular structures in full 3D biological matrix environment that allows confocal monitoring of pericyte, endothelial cell, and circulating cell interactions" [Under review]

* *indicates shared first authorship.*